

AD-A162 348

GENERALIZED PHENOMENOLOGICAL CYCLIC  
STRESS-STRAIN-STRENGTH CHARACTERIZATI  
GAINESVILLE DEPT OF CIVIL ENGINEERING  
D SEEREERAM ET AL 27 JUN 85

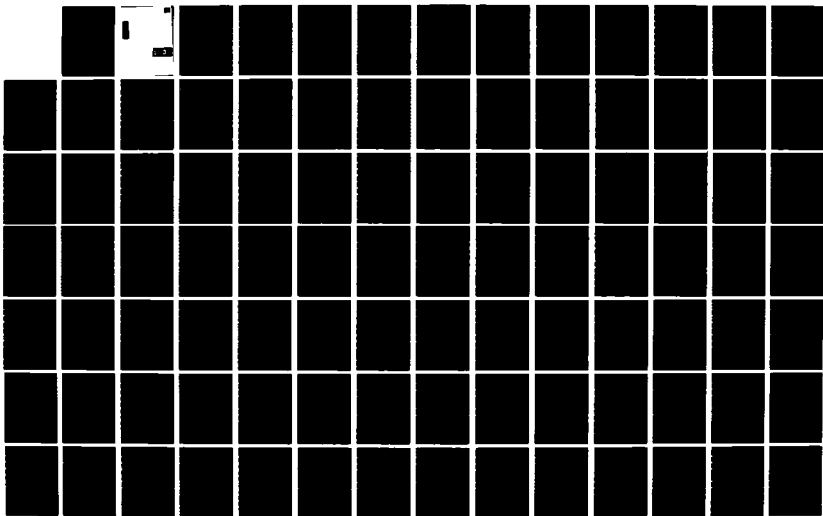
(U) FLORIDA UNIV

1/3

UNCLASSIFIED

F/G 8/13

NL





UNCLASSIFIED

SECURITY CLASSIFICATION OF THIS PAGE

AD A162348

## REPORT DOCUMENTATION PAGE

1. REPORT SECURITY CLASSIFICATION UNCLASSIFIED		1b. RESTRICTIVE MARKINGS													
2. SECURITY CLASSIFICATION AUTHORITY		3. DISTRIBUTION/AVAILABILITY OF REPORT Approved for Public Release; Distribution Unlimited													
4. DECLASSIFICATION/DOWNGRADING SCHEDULE		5. MONITORING ORGANIZATION REPORT NUMBER(S) AFOSR-TR. 85-1023													
6. PERFORMING ORGANIZATION REPORT NUMBER(S)		7a. NAME OF MONITORING ORGANIZATION AFOSR/NA													
6a. NAME OF PERFORMING ORGANIZATION UNIVERSITY OF FLORIDA		7b. ADDRESS (City, State and ZIP Code) Bolling AFB, DC 20332-6448													
8. ADDRESS (City, State and ZIP Code) 346 WEIL HALL		9. PROCUREMENT INSTRUMENT IDENTIFICATION NUMBER AFOSR - 84 - 0108													
10. NAME OF FUNDING/SPONSORING ORGANIZATION AIR FORCE OFFICE OF SCIENTIFIC RESEARCH		10b. OFFICE SYMBOL (If applicable) AFOSR/NA													
11. ADDRESS (City, State and ZIP Code) BOLLING AFB, DC 20332		10. SOURCE OF FUNDING NOS. <table border="1"><thead><tr><th>PROGRAM ELEMENT NO.</th><th>PROJECT NO.</th><th>TASK NO.</th><th>WORK UNIT NO.</th></tr></thead><tbody><tr><td>61102F</td><td>2307</td><td>C1</td><td></td></tr></tbody></table>		PROGRAM ELEMENT NO.	PROJECT NO.	TASK NO.	WORK UNIT NO.	61102F	2307	C1					
PROGRAM ELEMENT NO.	PROJECT NO.	TASK NO.	WORK UNIT NO.												
61102F	2307	C1													
1. TITLE (Include Security Classification) (See Back) (UNCLASSIFIED)															
2. PERSONAL AUTHOR(S) SEEREERAM, DEVO MCVAY, MICHAEL C. LINTON, PAUL F.															
3a. TYPE OF REPORT Annual		13b. TIME COVERED FROM 5-1-85 TO 6-1-85													
14. DATE OF REPORT (Yr., Mo., Day) 6-27-85		15. PAGE COUNT 261													
6. SUPPLEMENTARY NOTATION															
7. COSATI CODES <table border="1"><thead><tr><th>FIELD</th><th>GROUP</th><th>SUB. GR.</th></tr></thead><tbody><tr><td></td><td></td><td></td></tr><tr><td></td><td></td><td></td></tr><tr><td></td><td></td><td></td></tr></tbody></table>		FIELD	GROUP	SUB. GR.										18. SUBJECT TERMS (Continue on reverse if necessary and identify by block number)	
FIELD	GROUP	SUB. GR.													
9. ABSTRACT (Continue on reverse if necessary and identify by block number) <p>This study was an analytical and experimental investigation into the influences of material anisotropy and principal plane rotation on the stress-strain and strength behavior of granular soil (Reid-Bedford Sand).</p> <p>The laboratory investigation entailed the performance of approximately fifteen triaxial tests under conventional compression and extension loading, and five through initial shear, followed by hydrostatic compression. The initial tests with an additional fifteen hollow cylinder experiments, at similar densities obtained from Case Western Reserve were used in characterizing the influence of inherent anisotropy and principal plane rotations on material response. The latter were employed to delineate the affects of stress-induced anisotropy.</p> <p>(continued on back)</p>															
10. DISTRIBUTION/AVAILABILITY OF ABSTRACT UNCLASSIFIED/UNLIMITED <input checked="" type="checkbox"/> SAME AS 4PT. <input type="checkbox"/> DTIC USERS <input type="checkbox"/>		21. ABSTRACT SECURITY CLASSIFICATION UNCLASSIFIED													
22a. NAME OF RESP. INDIVIDUAL LAWRENCE D HOKANSON, Lt Col, USAF		22b. TELEPHONE NUMBER (Include Area Code) 202-767-4935													
		22c. OFFICE SYMBOL AFOSR/NA													

11. "GENERALIZED PHENOMENOLOGICAL CYCLIC STRESS-STRAIN-STRENGTH CHARACTERIZATION OF ANISOTROPIC GRANULAR MEDIA"

19. A review of existing elasto-plastic theory as related to soil mechanics showed only a few models of a phenomenological nature which explicitly account for material anisotropy when subject to cyclic loading. One of the multi-surface isotropic/kinematic hardening characterizations, Prevost's pressure sensitive model, was used in the prediction of the hollow cylinder tests. Although the model reasonably reproduced the response along its calibration path, it did not quantitatively or qualitatively predict the laboratory results along other stress paths which involved principal plane rotations.

The report concludes with a discussion on the significant influence of anisotropy on the stiffness, strength, and plastic flow rate direction of granular media, and the need for improved analytical representation.



# PREFACE

This research was sponsored by the Air Force Office of Scientific Research, Air Force System Command, USAF, under Grant Number AFOSR 84-0108. The U.S. Government is authorized to reproduce and distribute reprints for Governmental purposes notwithstanding any copyright notation thereon.

The study was conducted at the University of Florida in the Division of Soil Mechanics. The principal investigator was Dr. Michael McVay, and the USAF Technical Monitor was Lt. Col. Lawrence D. Hokanson. The graduate student assistants were Devo Seereeram (Ph.D.) and Paul Linton (M.E.). Technical consultation on laboratory testing was provided by Dr. Frank Townsend and Dr. David Bloomquist.

Accession For	
NTIS GRA&I	<input checked="" type="checkbox"/>
DTIC TAB	<input type="checkbox"/>
Unannounced	<input type="checkbox"/>
Justification	
By	
Distribution/	
Availability Codes	
Dist	Avail and/or special
A-1	



AIR FORCE OFFICE OF SCIENTIFIC RESEARCH (AFOSR)  
 NOTICE OF TRANSFER  
 This technical report is being transferred to the  
 appropriate agency for distribution and/or special  
 handling.  
 MATTHEW J. HARRIS  
 Chief, Technical Information Division

# TABLE OF CONTENTS

Section	Title	Page
I	INTRODUCTION.....	1
	A. THE NATURE AND ROLE OF THEORY.....	1
	B. STATEMENT OF PROBLEM.....	2
	C. APPROACH.....	4
II	PRELIMINARIES AND FUNDAMENTAL CONCEPTS.....	7
	A. TENSORS.....	8
	1. Introduction.....	8
	2. The Stress Tensor.....	14
	3. The Strain Tensor.....	26
	B. STRESS-STRAIN EQUATIONS AND CONSTITUTIVE THEORY.	31
	C. A NOTE ON STRESS AND STRAIN IN GRANULAR MEDIA...	36
	D. FABRIC IN GRANULAR MATERIAL.....	41
	E. ELASTICITY.....	48
	1. Cauchy Type Elasticity.....	49
	2. Hyperelasticity or Green Type Elasticity....	53
	3. Hypoelasticity or Incremental Type Elasticity.....	54
	F. PLASTICITY.....	56
	1. Yield Surface.....	57
	2. Incremental Plastic Stress-Strain Relation..	67
	3. Drucker's Stability Postulate.....	76
	4. Applicability of the Normality Rule to Soil Mechanics.....	79
	5. Hardening Rules for Soils.....	81
	6. Incremental Elasto-Plastic Stress-Strain Relation.....	86
III	ELASTO-PLASTIC ANISOTROPIC HARDENING RULE OF PREVOST	89
	A. INTRODUCTION.....	89
	B. FIELD OF WORK-HARDENING MODULII CONCEPT.....	90
	C. MODEL CHARACTERISTICS.....	94
	D. YIELD FUNCTION.....	95
	E. FLOW RULE.....	96

TABLE OF CONTENTS  
(CONTINUED)

Section	Title	Page
III (CONTINUED)		
	F. HARDENING RULE.....	97
	G. MODEL CALIBRATION.....	105
IV	BOUNDING SURFACE PLASTICITY FORMULATION FOR GRANULAR MATERIAL.....	111
	A. GENERAL.....	111
	B. DETAILS OF FUNCTION.....	112
	1. Consolidation Portion of Piecewise Continuous Surface.....	113
	2. Dilatation Portion of Piecewise Continuous Surface.....	116
	3. Range of the Parameters "Q" and "b".....	119
	4. Inclusion of Bounding Surface Variation on $\pi$ plane.....	122
	C. COMPUTATION OF THE GRADIENT TENSOR TO THE BOUNDING SURFACE.....	124
	D. MAPPING RULE LINKING ARBITRARY STRESS STATE TO CONJUGATE POINT.....	127
	E. THE LOADING FUNCTION.....	132
	F. THE FLOW RULE.....	133
	G. BACK CALCULATION OF THE PARAMETERS "Q" AND "b".	135
	H. THE CONSISTENCY CONDITION.....	136
	I. SELECTION OF PLASTIC INTERNAL VARIABLES.....	137
	1. Combined Hardening (Strain).....	138
	2. Combined Hardening (Work).....	142
	3. Two Parameter Hardening.....	144
	J. LINK BETWEEN THE PLASTIC MODULUS ( $K_p$ ) AND THE PLASTIC MODULUS AT THE BOUND ( $K_p$ ).....	151
V	LABORATORY INVESTIGATION OF SOIL ANISOTROPY.....	155
	A. INTRODUCTION.....	155

TABLE OF CONTENTS  
(CONCLUDED)

Section	Title	Page
V (CONTINUED)		
	B. HOLLOW CYLINDER TEST.....	156
	C. DIRECTIONAL SHEAR CELL.....	160
	D. IN-HOUSE 'TRIAxIAL' TESTS.....	166
VI	DISCUSSION OF RESULTS.....	174
	A. GENERAL.....	174
	B. IN-HOUSE 'TRIAxIAL' TESTS.....	175
	C. HOLLOW CYLINDER TEST RESULTS.....	193
	D. PREDICTIONS OF HCA TESTS USING PREVOST'S MODEL..	200
	E. PREDICTION OF SOME TESTS USING THE BOUNDING SURFACE MODEL.....	213
	F. ANALYTICAL STUDY OF THE MOVING WHEEL STRESS PATH	221
VII	CONCLUSIONS.....	226
	REFERENCES.....	228
APPENDIX		
A	PLOTS OF HCA MEASURED RESPONSE.....	236
B	PLOTS OF PREVOST MODEL PREDICTIONS OF HCA RESULTS...	243

# LIST OF FIGURES

Figure	Title	Page
1	Representation of Plane Stress State at a "Point".....	18
2	Typical Stress-Strain Response of Soil During Conventional 'Triaxial' Shear (left) and Hydrostatic Compression (right).....	38
3	Typical Stress Paths Used to Investigate Stress-Strain Response of Solid Cylindrical Soil Specimens.....	39
4	Common Symmetry Types - Triclinic, Monoclinic, Orthorhombic, and n-fold axis (Reference 31).....	42
5	Idealizations of Rate Independent Stress-Strain Behavior.....	58
6	Yield Surface in Heigh-Westergaard Cylindrical Coordinate System.....	62
7	Diagrams Illustrating the Modifying Effects of the Coefficients $A_1$ and $A_2$ : (a) $A_1 = A_2 = 1$ ; (b) $A_1 \neq A_2$ ; (c) $A_1 = A_2 = A$ (Reference 26).....	82
8	Field of Nesting Surfaces in $p'$ - $q$ (top) and $Cp'$ - $q$ subspaces (bottom) (Reference 7).....	99
9	Meridional Section (top) and Octahedral Projection (bottom) of the Bounding Surface Representation.....	115
10	Depiction of the McVay-Taesiri Hardening Rule (Reference 6) in Invariant Stress Space.....	150
11	Stress State in Hollow Cylinder Apparatus (Reference 5).....	157
12	Hollow Cylinder Test Stress Paths (Reference 9).....	161
13	Diagram of Method Used to Apply Normal and Shear Stresses in the Directional Shear Cell (Reference 10).	162
14	Directional Stress Paths for Jump Rotation Loading Tests; $\psi_A = 0^\circ$ (Reference 10).....	164
15	Directional Stress Paths for Jump Rotation Loading Tests; $\psi_A > 0^\circ$ (Reference 10).....	165
16	Photograph of Localized Failure of a Solid Cylindrical Specimen after an RTE test.....	167

LIST OF FIGURES  
(CONTINUED)

Figure	Title	Page
17	Photograph of specimen fitted with LVDT deformation measurement devices.....	169
18	Schematic Illustration of 'Triaxial' Test Apparatus with LVDTs in-place.....	170
19	Photograph of test apparatus with LVDTs attached to specimen in confining chamber filled with oil.....	172
20	Grain Size Distribution Curve for Reid-Bedford Sand...	177
21	Stress Paths for CTC Tests.....	179
22	'Shear' Stress vs. 'Shear' Strain for CTC tests.....	183
23	Volumetric Strain vs. Mean Stress for CTC tests.....	184
24	Stress Paths for RTE Tests.....	186
25	'Shear' Stress vs. 'Shear' Strain for RTE tests.....	188
26	Volumetric Strain vs. Mean Stress for RTE tests.....	189
27	Vertical Strain vs. Horizontal Strain for Hydrostatic Loading on Inherently Anisotropic Specimen.....	190
28	Vertical Strain vs. Horizontal Strain for Hydrostatic Loading on Specimens with Stress-Induced Anisotropy...	192
29	Strength Variation due to Relative Orientation of Eigenvectors of Stress With Respect to those of Fabric (Reference 91).....	197
30	Normalized Shear Stress vs. Shear Strain for the following HCA tests: DC 0, DCR 15, DCR 31.75, and R45 (data from Reference 9).....	198
31	Volume Strain vs. Normalized Mean Stress for the following HCA tests: DC 0, DCR 15, and DCR 31.75 (data from Reference 9).....	199
32	Postdiction of CTC test using Prevost's Model.....	203
33	Initial and Final Configuration of Yield Surfaces for CTC simulation.....	204

LIST OF FIGURES  
(CONTINUED)

Figure	Title	Page
34	Postdiction of RTE test using Prevost's Model.....	205
35	Initial and Final Configuration of Yield Surfaces for RTE simulation.....	206
36	Prediction of RTC test using Prevost's Model.....	207
37	Initial and Final Configuration of Yield Surfaces for RTC simulation.....	208
38	Prediction of GC 0 (or TC) test using Prevost's Model.	209
39	Initial and Final Configuration of Yield Surfaces for GC 0 (or TC) simulation.....	210
40	Prediction of GT 90 (or TE) test using Prevost's Model	211
41	Initial and Final Configuration of Yield Surfaces for GT 90 (or TE) simulation.....	212
42	Postdiction of the Load-Unload HC test using the Bounding Surface Model.....	216
43	Postdiction of the CTC test @35 psi using the Bounding Surface Model.....	217
44	Prediction of the CTC test @25 psi using the Bounding Surface Model.....	218
45	Prediction of the CTC test @30 psi using the Bounding Surface Model.....	219
46	Prediction of the CTC test @45 psi using the Bounding Surface Model.....	220
47	Stresses in a Layered Linear Elastic Medium with a Simulated Wheel Load.....	223
48	Moving Wheel Stress Path (Linear Elastic Assumption).	224
A-1	Normalized Shear Stress vs. Shear Strain for the following HCA tests: R 45, DTR 58.25, DTR 75, and DT 90 (data from Reference 9).....	237

LIST OF FIGURES  
(CONCLUDED)

Figure	Title	Page
A-2	Volume Strain vs. Normalized Mean Stress for the following HCA tests: DTR 58.25, DTR 75, and DT 90 (data from Reference 9).....	238
A-3	Normalized Shear Stress vs. Shear Strain for the following HCA tests: GC 0, GCR 15, GCR 31.75, and R 45 (data from Reference 9).....	239
A-4	Volume Strain vs. Normalized Shear Stress for the following HCA tests: GC 0, GCR 15, GCR 31.75, and R 45 (data from Reference 9).....	240
A-5	Normalized Shear Stress vs. Shear Strain for the following HCA tests: R 45, GTR 58.25, GTR 75, and GT 90 (data from Reference 9).....	241
A-6	Volume Strain vs. Normalized Shear Stress for the following HCA tests: R 45, GTR 58.25, GTR 75, and GT 90 (data from Reference 9).....	242
B-1	Prediction of DCR 15 test using Prevost's Model.....	244
B-2	Prediction of DCR 32 test using Prevost's Model.....	245
B-3	Prediction of DTR 58 test using Prevost's Model.....	246
B-4	Prediction of DTR 75 test using Prevost's Model.....	247
B-5	Prediction of GCR 15 test using Prevost's Model.....	248
B-6	Prediction of GCR 32 test using Prevost's Model.....	249
B-7	Prediction of R 45 test using Prevost's Model.....	250
B-8	Prediction of GTR 58 test using Prevost's Model.....	251
B-9	Prediction of GTR 75 test using Prevost's Model.....	252



# LIST OF TABLES

Table	Title	Page
1	PHYSICAL DESCRIPTION OF REID-BEDFORD SAND.....	176
2	INFLUENCE OF PRINCIPAL STRESS AXES ROTATION ON STRENGTH.....	180
3	SIMPLE MODEL OF FABRIC'C INFLUENCE ON STRENGTH.....	181
4	PREVOST MODEL PARAMETERS FOR REID-BEDFORD SAND.....	201
5	BOUNDING SURFACE MODEL PARAMETERS FOR REID-BEDFORD SAND.....	215

# LIST OF ABBREVIATIONS

CSL	Critical (or Characteristic) State Line
H/D	Height to Diameter Ratio of Specimen
HCA	Hollow Cylinder Apparatus
SCA	Solid Cylinder Apparatus
CTC	Conventional Triaxial Compression
RTE	Reduced Triaxial Extension

## SECTION I

### INTRODUCTION

#### A. THE NATURE AND ROLE OF THEORY

In most fields of knowledge, from physics to political science, it is essential to use a hypothesis to make sense of a complex reality. The complex reality we seek to model in this study is the load-deformation response of a statistically homogenous assemblage of particles. More specifically, we will attempt to use the mathematical theory of plasticity to determine the history of the state of stress and strain at all points in a partially or totally plastic body of sand when the the history of the boundary loadings and displacements are specified.

To explain or model the complex phenomenon of particles crushing, distorting, sliding, and rolling past each other under load, a theory must simplify and abstract from reality, but these simplifications and idealizations must lie within the framework of physically and mathematically permissible stress-strain relations. The test of any scientific theory is whether it explains or predicts what it is designed to explain or predict, and not whether its assumptions exactly mirror reality. On the other hand, the most useful theory (or stress-strain relation in this case) is the simplest one which will work for the problem at hand. A theory can consider only a few of the many factors that influence real events; the trick is to incorporate the most important factors into the theory and ignore the rest.

The mathematical theories of plasticity presented here should be clearly distinguished from the physical or microstructural plasticity theories which attempt to model geometrically the local interaction of the granules. The mathematical (or phenomenological) theory is only a formalization of known experimental results and does not inquire very deeply into their physical basis; it is essential, however, to the solution of problems in stress analysis and also for the correlation of experimental data (Reference 1).

#### B. STATEMENT OF PROBLEM

The structural degradation of a flexible pavement is normally associated with cracking of the bituminous surface course and the development of ruts in the wheel paths (Reference 2). In this report, we focus on the latter aspect which involves considerations of the accumulation of permanent deformation during the repeated application of moving wheel loads at the surface. The conventional design procedure (Reference 2) assumes that rutting occurs only in the subgrade and is controlled by limiting the value of the vertical compressive strain at the top of this layer. The stiffness of the material in this design procedure is characterized by the resilient modulus and Poisson's ratio, the resilient modulus of a cohesionless soil being defined as a mean stress-dependent secant modulus obtained after 200 repetitions at various deviatoric levels of undrained axial loading. Is this modulus appropriate for design? This is the question we will ultimately try to answer in this investigation.

The study of rutting in roadway and runway structural support systems is one of fundamental interest in soil mechanics. First, the elements of underlying soil are subjected to three dimensional, cyclically varying loading paths which, from the theoretical point of view, implicate the subaspects of material anisotropy coupled with rotation of the principal stress axes during loading. The studies of anisotropy and principal stress axes rotation, however, go hand in hand; if, for instance, a material is idealized to possess directional stiffness and strength isotropy, the circumstance of principal stress axes rotation during loading is irrelevant.

Nevertheless, it is common knowledge that the fabric of earthen materials are intimately related to the mechanical processes during their formation. Cohesionless base or subbase courses, constructed by vibratory compaction in the direction of deposition, are prime examples of material which may exhibit significant strength and stiffness anisotropy. The conventional empirical design approach for characterizing the soil's stress-strain relations presently neglect: a) the trajectory of the loading path in invariant stress space, b) the accompanying principal stress axes rotation during loading, and c) the inherent as well as induced anisotropy of the material. Therefore, in the specification of cyclic material behavior using the standard resilient modulus test, there are several assumptions which may prove to be over-simplified and unconservative analogues of real behavior.

A broader perspective on the importance of this study can be proffered by quoting a recent comment of Dr. Salkind (Reference 3),

The relevance is extraordinarily high for this nation. There is the obvious deterioration of our highway system including potholes. The Air Force has 3700 miles of runways around the world designed for a 20 year life. Ninety-two percent are more than 20 years old and 25 percent are significantly deteriorated. The anticipated replacement cost with today's technology is \$1.9 billions.....The underlying methodology is empirical and should be put on a sound analytical basis.....The pavement system, consisting of supporting soil, underpavement, and paving material should be analyzed for loads and moments (and loading spectrum) recognizing the differing response of the various layers with different material properties. A basic science need is the lack of measuring techniques for fundamental soil properties and descriptions of soil constitutive properties. Design is based on empirical values such as the penetration of a standard cone. As soil is a multi-phase mixture of solid particles, water, and air, the challenge is to define what are the basic fundamental properties (eg. soil "fabric" or spatial arrangement of particles) and how such properties change with loading.....

#### C. APPROACH

The methodology used in this study is intimately linked to the development of phenomenological, cyclic, elasto-plastic model for granular materials which explicitly (or implicitly) accounts for the influence of anisotropy on: 1) the direction of the plastic flow rate vector, 2) the plastic modulus, and 3) the strength and stiffness variation due to the relative orientation of the major symmetry axes of stress with respect to those of fabric. This model will be based on the formalism of cyclic plasticity as put forward by Dafalias and Popov (Reference 4). Although it is unlikely that a truly generalized

description of soil response can be developed given the present state-of-the-art in conventional laboratory testing (Reference 5), it is envisioned that the model which evolves from this research effort will at least be able to remedy the numerical anomalies observed in a previous attempt to simulate the moving wheel stress path (Reference 6).

Attention, however, will not be restricted to this particular class of cyclic elasto-plastic formulation. What is perhaps the most analytically complete multi-surface model for soil - the pressure sensitive isotropic/kinematic hardening model of Prevost (Reference 7) - is also evaluated and serves as an interesting supplement to this study of soil behavior.

Although one such apparatus is reportedly under construction (Reference 8), a laboratory device which can subject specimens of sand to the six independent components of stress is, to our knowledge, non-existent. This is, of course, a major constraint to the formulation of generalized constitutive stress-strain relations since there is no way to experimentally validate these models under general paths of loading. At present, however, two unconventional laboratory tests provide useful data for studying the influence of anisotropy on the stress-strain response of sand: the hollow cylinder apparatus and the directional shear cell (see, for example, References 9 and 10). The results of recent studies in both these devices have been acquired, and we hope that these data will form the mainstay of our study of anisotropy in granular media. Simple exploratory tests in the 'triaxial' environment also provide basic manifestations of stress-induced and inherent

anisotropy on the plastic flow rate direction, the stiffness, and the strength for no rotation or ninety degree jump rotations of the principal stress axes.

In summary, the methodology centers on: a) collecting and analyzing homogenous stress-strain data on anisotropic sand specimens from both in-house and external sources, b) using these data to modify the bounding surface plasticity model to permit simulation of the observed anisotropic response, and c) implementing a popular anisotropic hardening multi-surface model for comparison to the predictions of the bounding surface model.

Our objectives here have been clearly defined, but it is fitting to venture briefly into the prospects of future research which may emanate directly from this present investigation. We recognize that the scope of the effort herein is only a part of the broader picture of the study of the moving wheel stress path and its impact on pavement rutting. Once a model has been formulated to capture the essential aspects of this stress path, the step that follows naturally is the incorporation of such a model into a finite element computer code to generate predictions of the stresses and displacements in a typical pavement structure. We also foresee a parallel experimental study in which a small scale model of a loaded pavement system will provide a data base of measured response for comparison to the analytic predictions. In all likelihood, such an apparatus may take the form of the experimental set-up used by Professor Yong at McGill University to study the compactability of soil (Reference 11).



## SECTION II

### PRELIMINARIES AND FUNDAMENTAL CONCEPTS

It is the primary objective of this chapter to present and discuss in a methodical fashion the key concepts which form the foundation of this dissertation. At the risk of composing this section in a format which is perhaps unduly elementary and prolix to the mechanistic, the authors strive herein to fill (what they consider) a conspicuous void in the soil mechanics literature: a discussion of plasticity theory which is comprehensible to the vast majority of geotechnical engineers who do not have a full and working knowledge of classical plasticity or tensor analysis. A similar sentiment does not, however, apply to metal plasticity where many profound expositions on the subject have been published (see, for example, References 1, 12, 13, 14, 15, and 16).

The sequence in which the relevant concepts are introduced is motivated solely by the writers' personal biases as geotechnical engineers - accustomed to the many empirical correlations and conventional plane strain, limit equilibrium methods of analysis - venturing into the decidedly rigorous field of generalized, elasto-plastic stress-strain relations; the terms "generalized" and "elasto-plastic" will be clarified in the sequel. At the beginning, it should also be mentioned that, although an attempt will be made herein to include as many of the basic precepts of soil plasticity as possible, this chapter will only give a very condensed and selected treatment of

an extensive and complex body of knowledge. In a less formal setting, this chapter may have been titled "Plain Talk About Plasticity For The Soils Engineer."

## A. TENSORS

### 1. Introduction

Lack of an intuitive grasp of tensors and tensor notation is perhaps the foremost reason that many geotechnical engineering practitioners and students shun the theoretical aspects of work-hardening plasticity and its potentially diverse computer-based applications in geomechanics. In an effort to make the substance of this thesis comprehensible to a wider audience, it is pedagogical to briefly and simply review the mathematical theory in terms of which physical laws could be described and their universality checked.

In the ensuing discussion, the following terms and elementary operations are used without definition: scalar, vector, linear functions, rectangular Cartesian coordinates, orthogonality, components (or coordinates), base vectors (or basis), domain of definition, and the rules of a vector space such as the axioms of addition, scalar multiple axioms and scalar product axioms. Additionally, it is helpful to point out that rectangular Cartesian coordinates are used exclusively throughout this dissertation; this particular set of base vectors forms an orthonormal basis, simply meaning that the unit vectors comprising this basis are mutually orthogonal (i.e., mutually perpendicular).

Quoting from Malvern (Reference 17, p.7),

Physical laws, if they really describe the physical world, should be independent of the position and orientation of the observer. That is, if two scientists using different coordinate systems observe the same physical event, it should be possible to state a physical law governing the event in such a way that if the law is true for one observer, it is also true for the other.

Assume, for instance, that the physical event recorded is a spatial vector  $\underline{t}$  acting at some point P in a mass of sand which is in equilibrium under a system of boundary forces. This vector represents some geometrical or physical object acting at P and we can instinctively reason that this "tangible" entity,  $\underline{t}$ , does not depend on the coordinate system in which it is viewed. Further, we can intuitively reason that any operations or calculations involving this vector must always have a physical interpretation. The validity of this statement should not be surprising since many of the early workers in vector analysis (Hamilton for example) actually sought these tools to mathematically describe real events; an excellent historical summary of the development of vector analysis can be found in the work published by Wrede (Reference 18).

Having established that the entities typically observed, such as the familiar stress and strain vectors, are immutable with changes in perspective of the viewer, we must now ask: How does one formulate propositions involving geometrical and physical objects in a way free from the influence of the underlying arbitrarily chosen coordinate system? The manner in which this invariance requirement is automatically fulfilled rests on the representation of physical objects

by tensors, the properties of tensors being such as to ensure the desired invariance. To avoid any loss of clarity that may arise from using the word "tensor" prior to its elucidation, it is didactic to record the following: a vector is one of the possible classes of tensors, and thus, the term "vector" may be interchanged with the term "tensor" whenever the use of the latter leads to conceptual problems. There are several excellent references which deal with the subject of vector and tensor analysis in considerably more detail than the mere overview presented in the following passages; some examples of these references include the books by Akivis and Goldberg (Reference 19), Hay (Reference 20), Jaunzemis (Reference 21), Malvern (Reference 17), Synge and Schild (Reference 22) and Wrede (Reference 18).

Although the necessity to free our physical law from the arbitrariness implicit in the selection of a coordinate system has been set forth, it is important to realize that this assertion is meaningless without the existence of coordinate systems and transformation equations relating them. The transformation idea plays a major role in the present-day study of physical laws, and, in fact, the use of tensor analysis as a descriptive language for theoretical physics is largely based on the invariant properties of tensor relations under certain types of transformations. For example, we can imagine that the vector  $\underline{t}$  was viewed by two observers using different rectangular Cartesian coordinate systems (say rotated about the origin with respect to each other), and, as a result, a different set of the vector components were recorded by each scientist. Nonetheless, we should expect that the length of the vector - a frame indifferent

quantity - computed by both these observers to be identical. The transformation rules which guarantee the invariant properties of vectors and tensors are actually quite simple but are very important in deciding whether or not a quantity does indeed possess tensorial characteristics. To illustrate how a vector is converted from one rectangular Cartesian coordinate system to another, let us consider the following example where the "new" coordinate components and base vectors are primed (') for distinction. The transformation from the old basis ( $\underline{i}_1, \underline{i}_2, \underline{i}_3$ ) to the new basis ( $\underline{i}'_1, \underline{i}'_2, \underline{i}'_3$ ) can be written in matrix form as:

$$[\underline{i}'_1, \underline{i}'_2, \underline{i}'_3] = [\underline{i}_1, \underline{i}_2, \underline{i}_3] \begin{bmatrix} \cos(\underline{i}_1, \underline{i}'_1) & \cos(\underline{i}_2, \underline{i}'_1) & \cos(\underline{i}_3, \underline{i}'_1) \\ \cos(\underline{i}_1, \underline{i}'_2) & \cos(\underline{i}_2, \underline{i}'_2) & \cos(\underline{i}_3, \underline{i}'_2) \\ \cos(\underline{i}_1, \underline{i}'_3) & \cos(\underline{i}_2, \underline{i}'_3) & \cos(\underline{i}_3, \underline{i}'_3) \end{bmatrix} \quad (1)$$

where  $\cos(\underline{i}_1, \underline{i}'_2)$ , for example, represents the cosine of the angle between  $\underline{i}_1$  and  $\underline{i}'_2$ . This is an ideal juncture to digress and introduce two notational conventions which can save an enormous amount of equation writing.

The range convention states that when a small Latin suffix occurs unrepeated in a term, it is understood to take all the values 1,2,3 while the summation convention specifies that when a small Latin suffix is repeated in a term, summation with respect to that term is understood, the range of summation being 1,2,3. To see the economy of this notation, observe that equation 1 is completely expressed as

$$\underline{i}'_m = Q_{mk} \underline{i}_k, \quad (2)$$

where  $Q_{mk}$  is equal to  $\cos(\underline{i}_k, \underline{i}'_m)$ . The index "m" in this equation is known as the free index since it occurs only once in each summand while

the index "k" is designated the dummy index because it appears twice in the summand and implies summation over its admissible values (i.e., 1,2,3). The corresponding transformation formulas for the vector components ( $t_r$  to  $t'_k$ ) can now be derived from the information contained in equation 2 and the condition of invariance which requires that the representations of the vector in the two systems to have exactly the same form; i.e.,

$$t = t_k \underline{i}_k = t' = t'_m \underline{i}'_m \quad . \quad (3)$$

Substituting the inverse relation of equation 2 (i.e.,  $\underline{i}_k = Q_{kr} \underline{i}'_r$ ) into equation 3 leads to

$$t_k Q_{kr} \underline{i}'_r = t'_r \underline{i}'_r ,$$

or

$$(t'_r - t_k Q_{kr}) \underline{i}'_r = 0$$

from which we find

$$t'_r = t_k Q_{kr} \quad . \quad (4)$$

With the invariance discussion and the vector transformation example as background information, the following question can now be asked: What actually is a tensor? It is best perhaps to bypass the involved mathematical definition of a tensor and proceed with a heuristic introduction (modified from References 17 and 21) giving rise to the particular type of tensor in which we are most interested: second order (or second rank), orthogonal tensors.

Scalars and vectors are fitted into the hierarchy of tensors by identifying scalars with tensors of rank (or order) zero and vectors of rank (or order) one. Within the framework of indicial notation, we can say that the rank of the tensor corresponds to the number of indices

appearing in the variable; scalars quantities possess no indices, vectors have one index, second order tensors have two indices while higher rank tensors possess three or more indices. Every variable that can be written in index notation is not a tensor, however. Remember that a vector has to obey certain rules of addition, etc. as well as transform according to equation 4. These requirements for first order tensors (i.e., vectors) can be generalized and extended to the higher order tensors.

To introduce the tensor concept, let us characterize the state at the point P (of, say, the representative sand mass) in terms of the nature of the variable under scrutiny. An absolute scalar state can be categorized as a state in which the measured quantity possesses a magnitude which does not depend on the orientation of the observer (i.e., a scalar variable); examples include mass, density, temperature, and work. The magnitude of this type of variable is invariant under all transformations of coordinates, and, as mentioned previously, it is identified as a tensor of zero order. Suppose now that there exists a scalar  $v^{(n)}$  (such as speed) associated with each direction at the point P, the directions being described by the variable unit vector  $\underline{n}$ . This multiplicity of scalars depicts a scalar state, and, if we proceed by associating this scalar with speed for instance, we can write

$$v^{(n)} = \underline{v} [\underline{n}] = v_i n_i \quad (5)$$

where  $v^{(n)}$  is the speed in direction  $\underline{n}$ , and the square brackets are used to emphasize that  $\underline{v}$ , the velocity vector, is a linear operator on  $\underline{n}$ . Deferring a more general proof until later, it can be said that the totality of scalars  $v^{(n)}$  associated with all possible directions is

fully known if the components of  $y$  are known for any three mutually orthogonal directions. At the point  $P$ , therefore, the scalar state is completely represented by a first order tensor, otherwise known as a vector. The argument for a second order tensor suggests itself by considering the existence of a vector state at  $P$ ; that is, a different vector,  $\underline{t}^{(n)}$ , is associated with each direction  $\underline{n}$ .

## 2. The Stress Tensor

The prize example of second order tensors in solid mechanics is the stress tensor, the complete set of data needed to predict the totality of stress (or load intensity) vectors associated with all planes passing through point  $P$ .

By recalling the routinely used Mohr circle stress representation in soil mechanics, we generally expect different magnitudes of shear stress and normal stress to act on an arbitrary plane through  $P$ , and, consequently, the resulting stress vector is unique on each of these planes. Immediately, we recognize that the stress vector (which is also called the traction)  $\underline{t}^{(n)}$  is a function of  $\underline{n}$  at the point  $P$  where  $\underline{n}$  is the unit vector normal to an arbitrary plane. In order to fully describe the state of stress at  $P$ , we need then to derive a relationship between the vectors  $\underline{t}^{(n)}$  and  $\underline{n}$ ; in other words, we seek a vector function of a single vector argument,  $\underline{n}$ . It turns out that we are in fact seeking a linear vector function, say  $\underline{g}$ , which can be described as a rule associating the vector  $\underline{t}^{(n)}$  with each vector  $\underline{n}$  in the domain of definition. A linear vector function is also called a linear transformation of the domain or a linear operator acting in the



domain of definition of the function  $g$ . In analogy to equation 5, we can now write

$$\underline{t}^{(n)} = g[\underline{n}] \quad (6)$$

where again, as in equation 5, the square brackets are used to imply a linear operation. The linearity assumption of the function  $g$  infers the following relationships:

$$g[\underline{n}_1 + \underline{n}_2] = g[\underline{n}_1] + g[\underline{n}_2] \quad (7)$$

for arbitrary vectors  $\underline{n}_1$  and  $\underline{n}_2$ , and

$$g[\alpha \underline{n}] = \alpha g[\underline{n}] \quad , \quad (8)$$

for arbitrary vector  $\underline{n}$  and real number  $\alpha$ .

Geometrically, equation 7 means that the operator  $g$  carries the diagonal of the parallelogram constructed on the vectors  $\underline{n}_1$  and  $\underline{n}_2$  into the diagonal of the parallelogram constructed on the vectors  $\underline{t}_1 = g[\underline{n}_1]$  and  $\underline{t}_2 = g[\underline{n}_2]$ . Equation 8, on the other hand, means that if the length of the vector  $\underline{n}$  is multiplied by a factor  $\alpha$ , then so is the length of the vector  $\underline{t}^{(n)} = g[\underline{n}]$ .

Using a rectangular Cartesian coordinate system, the traction vector,  $\underline{t}^{(n)}$ , and the normal vector,  $\underline{n}$ , can each be resolved into their components  $t_1^{(n)}$ ,  $t_2^{(n)}$ ,  $t_3^{(n)}$  and  $n_1$ ,  $n_2$ ,  $n_3$  respectively, and the linear relationship between  $\underline{t}$  and  $\underline{n}$  can be written in matrix form as

$$[t_1^{(n)}, t_2^{(n)}, t_3^{(n)}] = [n_1, n_2, n_3] \begin{bmatrix} \sigma_{11} & \sigma_{12} & \sigma_{13} \\ \sigma_{21} & \sigma_{22} & \sigma_{23} \\ \sigma_{31} & \sigma_{32} & \sigma_{33} \end{bmatrix} \quad , \quad (9)$$

or alternatively, in indicial notation,

$$t_i^{(n)} = \sigma_{ji} n_j \quad , \quad (10)$$

where the components of the  $3 \times 3$  matrix  $g$  is the stress tensor acting at point P. Note that the wavy underscore under symbols such as  $\sigma$  are used to denote tensorial quantities in this chapter and throughout the remainder of this report. In general, tensors can vary from point to point within the illustrative sand sample, depicting a tensor field or a tensor function of position. If the components of the stress tensor are identical at all points in the granular mass, a homogenous state of stress is said to exist; this concept of homogeneity of stress (and likewise, strain) is particularly important in laboratory soil tests where such an assumption is of fundamental importance in the interpretation of test data (Reference 5).

Second order tensors undergo coordinate transformations in an equivalent manner to vectors (see equation 4). The transformation formula (for a rotation of base vectors) is derived by employing a series of previous equations. Recall from equation 4 that

$$t'_r = t_k Q_{kr} \quad ,$$

and by combining this equation with equation 10, we find

$$t'_r = \sigma_{jk} n_j Q_{kr} \quad ,$$

from which it can be further seen that  $\underline{n}$  can be transformed to  $\underline{n}'$  resulting in

$$t'_r = \sigma_{jk} Q_{js} n'_s Q_{kr} \quad . \quad (11)$$

The left hand side of equation 11 can also be replaced by the linear transformation such that

$$\sigma'_{pr} n'_p = \sigma_{jk} Q_{js} n'_s Q_{kr} \quad ,$$

which when rearranged yields

$$\sigma'_{pr} n'_p - \sigma_{jk} Q_{js} n'_s Q_{kr} = 0 \quad . \quad (12)$$

All the indices in equation 12 are dummy indices except "r" which is the free index. A step that frequently occurs in derivations is the interchange of summation indices, and it can be shown that the set of equations compactly expressed in equation 12 is unchanged if the dummy index "p" is replaced by the dummy index "s". This manipulation allows us to rewrite equation 12 as:

$$\sigma'_{sr} n'_s - \sigma_{jk} Q_{js} n'_s Q_{kr} = 0 ,$$

and by factoring out the common term  $n'_s$ , we obtain

$$(\sigma'_{sr} - \sigma_{jk} Q_{js} Q_{kr}) n'_s = 0 ,$$

from which we can at once deduce the tensor transformation rule to be

$$\sigma'_{sr} = \sigma_{jk} Q_{js} Q_{kr} , \quad (13)$$

or in tensor notation,

$$\underline{\sigma}' = \underline{Q}^T \underline{\sigma} \underline{Q} . \quad (14)$$

It was previously stated (without verification) that a vector is completely defined once its components along three mutually orthogonal directions have been specified; the reciprocal declaration for a second order tensor will therefore quite naturally be that the components of a second order tensor are determined once the vectors acting on three mutually orthogonal planes are given. In actuality, this statement is correct and it can be substantiated by inspecting the free body diagram of figure 1 in which a soil prism is subject to a plane stress state. Plane stress simply means that there is no resultant stress vector on one of the three orthogonal planes, and, as a result, the stress tensor can be represented by a 2x2 matrix instead of the generalized 3x3 matrix. Generalized, in this context, signifies a situation where the full array of the stress tensor is considered in the problem; moreover,

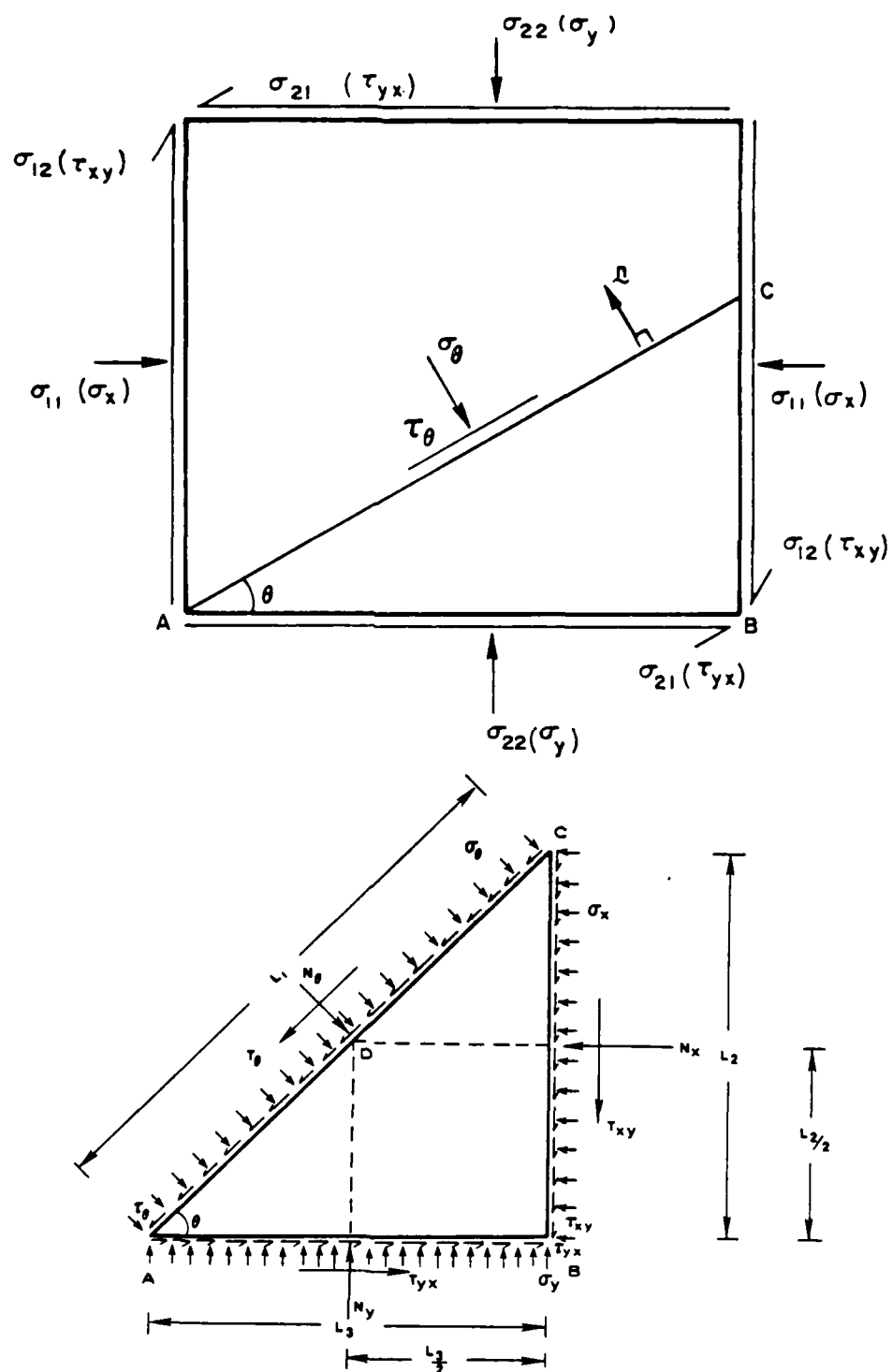


Figure 1. Representation of Plane Stress State at a "Point".

when the adjective "generalized" is used to qualify a stress-strain relationship, it is tacitly assumed that the law should relate all the components of the strain (or strain increment) tensor to the tensor components of stress (or stress increment) under any arbitrary loading program.

Figure 1 shows the two-dimensional free body diagram of the material prism with a uniform distribution of stress vectors acting on each of the mutually perpendicular planes. By taking moments about the point D, it can be shown that  $\tau_{xy} = \tau_{yx}$  and this is known as the theorem of conjugate shear stresses, a relationship which is valid whenever there are no distributed body or surface couples acting on the element. This two dimensional result can be generalized to three dimensions where it can easily be seen that the  $3 \times 3$  stress tensor matrix is symmetric as a consequence of this theorem. Symmetry has another important implication in that there are now only six independent components of the stress matrix tensor necessary to describe the stress state at the point P. By invoking force equilibrium in the x and y-directions of figure 1, the two resulting equations can be solved simultaneously for the unknowns  $\tau_\theta$  and  $\sigma_\theta$ , proving that the shear and normal stress (or the stress vector in this case) on an arbitrary plane can be computed once the stress vectors on a set of mutually perpendicular planes are given. Extension of this two-dimensional result to three dimensions shows that the components of three mutually perpendicular traction vectors are, in actuality, the rows of the stress tensor matrix.

Most geotechnical engineers are familiar with the Mohr-Coulomb strength theory for granular soils which specifies a limit state (i.e., failure with infinite deformations) based on a combination of principal stresses ( $\sigma_1$ ,  $\sigma_2$ , and  $\sigma_3$ ). Even the more complicated failure criteria for soils which have been recently proposed (see subsection II.F.1) embody only mathematical functions of the principal stresses. This underscores the need for a simple procedure to compute the principal stresses once the frame-dependent components of the stress tensor are specified. Note that, although the scalar principal values are invariant, the vectorial description of the planes on which each principal stress acts (say  $\underline{n}_1$ ,  $\underline{n}_2$ , and  $\underline{n}_3$ ) depends on the reference coordinate system chosen.

A principal plane is a plane on which there are no shear stresses. This implies that the normal stress is the sole component of the traction vector acting on a principal plane, and the geometric interpretation is that the traction vector and the unit normal vector to the plane,  $\underline{n}$ , both act in the same direction. Mathematically, the principal plane requirement can be written as:

$$\underline{t}^{(n)} = \lambda \underline{n} \quad , \quad (15)$$

or in indicial notation,

$$t_i^{(n)} = \lambda n_i \quad (16)$$

where  $\lambda$  is the numerical value sought; remember that there are generally three principal planes and therefore three principal values.

Substitution of equation 16 into equation 10 and rearranging leads to

$$\sigma_{ji} n_j - \lambda n_i = 0 \quad . \quad (17)$$

As an aid to solving equation 17, it is fitting at this stage to introduce an extremely useful algebraic device known as the Kronecker delta. The Kronecker delta,  $\delta_{ij}$ , is a second order tensor defined by

$$\delta_{ij} = \begin{cases} 1 & \text{if } i = j \\ 0 & \text{if } i \neq j \end{cases} \quad (18)$$

By writing out the terms in long form, it may be easily verified that

$$n_i = \delta_{ij} n_j \quad (19)$$

Now, we can substitute equation 19 into equation 17 to find that

$$\sigma_{ji} n_j - \lambda \delta_{ij} n_j = 0,$$

and by proceeding to factor out  $n_j$ , we see

$$(\sigma_{ji} - \lambda \delta_{ij}) n_j = 0 \quad (20)$$

For clarity, equation 20 can be written in long form as:

$$\begin{aligned} (\sigma_{11} - \lambda) n_1 + \sigma_{12} n_2 + \sigma_{13} n_3 &= 0 \\ \sigma_{21} n_1 + (\sigma_{22} - \lambda) n_2 + \sigma_{23} n_3 &= 0, \\ \sigma_{31} n_1 + \sigma_{32} n_2 + (\sigma_{33} - \lambda) n_3 &= 0 \end{aligned} \quad (21)$$

or written in matrix form as

$$\begin{bmatrix} \sigma_{11} - \lambda & \sigma_{12} & \sigma_{13} \\ \sigma_{21} & \sigma_{22} - \lambda & \sigma_{23} \\ \sigma_{31} & \sigma_{32} & \sigma_{33} - \lambda \end{bmatrix} \begin{Bmatrix} n_1 \\ n_2 \\ n_3 \end{Bmatrix} = \begin{Bmatrix} 0 \\ 0 \\ 0 \end{Bmatrix}, \quad (22)$$

where it can be seen to represent a homogenous system of three linear equations in four unknowns ( $n_1$ ,  $n_2$ ,  $n_3$  and  $\lambda$ ). The fourth equation for solving this system is derived from the fact that  $\underline{n}$  is a unit vector and hence we automatically know that its magnitude is unity; that is,

$$\underline{n} \cdot \underline{n} = n_i n_i = 1 \quad (23)$$

Also, equation 20 has a nontrivial solution if and only if the determinant of the coefficient matrix in equation 22 is equal to zero (see, for example, Reference 23, p.188). Based on this requirement for

the existence of non-trivial solutions, we can solve for  $\lambda$  by using the property

$$\begin{vmatrix} \sigma_{11}-\lambda & \sigma_{12} & \sigma_{13} \\ \sigma_{21} & \sigma_{22}-\lambda & \sigma_{23} \\ \sigma_{31} & \sigma_{32} & \sigma_{33}-\lambda \end{vmatrix} = 0 . \quad (24)$$

This determinant can be written out term by term to yield a cubic equation which takes the form

$$\lambda^3 - I_1 \lambda^2 - I_2 \lambda - I_3 = 0 , \quad (25)$$

where

$$I_1 = \sigma_{11} + \sigma_{22} + \sigma_{33} = \sigma_{kk} , \quad (26)$$

$$\begin{aligned} I_2 &= -(\sigma_{11}\sigma_{22} + \sigma_{22}\sigma_{33} + \sigma_{33}\sigma_{11}) + \sigma_{23}^2 + \sigma_{31}^2 + \sigma_{12}^2 \\ &= (\sigma_{ij}\sigma_{ij} - I_1^2) + 2 \end{aligned} \quad (27)$$

and

$$I_3 = \begin{vmatrix} \sigma_{11} & \sigma_{12} & \sigma_{13} \\ \sigma_{21} & \sigma_{22} & \sigma_{23} \\ \sigma_{31} & \sigma_{32} & \sigma_{33} \end{vmatrix} . \quad (28)$$

It has previously been mentioned that the principal stresses are independent of the observer's choice of coordinate axes, and since the cubic relation of equation 25 is to yield the same answer for principal stresses irregardless of the imposed reference frame, it is evident that the coefficients of this cubic equation -  $I_1$ ,  $I_2$ , and  $I_3$  - will also be independent of the coordinate system. These coefficients are the so-called invariants of the stress tensor  $\sigma$ ;  $I_1$ ,  $I_2$ , and  $I_3$  are the first, second, and third invariants respectively. It will be shown later in the discussion that it is much simpler to compute the invariants as an intermediate step in the calculation of the principal stresses when given a stress tensor which occupies all elements in a  $3 \times 3$  stress matrix. However, this intermediate computation step can be



circumvented by writing or directly formulating the failure criteria in terms of the invariants, but, in any event, it should be kept in mind that the stress invariants and principal stresses can be interchangeably used in a failure criterion. The following discussion centers on the mathematical aspects of a typical methodology to replace the invariants with the principal values of stress; the inverse procedure of computing the invariants from the principal stresses has already been explicitly stated in equations 26, 27, and 28.

The stress tensor can be decomposed additively into two components: 1) the spherical or hydrostatic stress tensor ( $p \delta_{ij}$ ), and 2) the deviatoric stress tensor ( $s_{ij}$ ). The first of these tensors represents the average pressure or "bulk" stress ( $p$ ) which causes a pure volumetric strain on an isotropic continuum, while the second tensor,  $s$ , is associated with the components of stress which bring about shape changes in an ideal isotropic continuum. The spherical stress tensor is defined as being equal to  $p \delta_{ij}$  where  $p$  is the mean normal pressure ( $\sigma_{kk}/3$  or  $I_1/3$ ) and  $\delta_{ij}$  is the Kronecker delta. Since, by definition, we know the spherical and deviatoric stress tensors combine additively to give the stress tensor, we can write the components of the stress deviator (or deviatoric stress tensor) as:

$$s_{ij} = \sigma_{ij} - p \delta_{ij} , \quad (29)$$

where compressive stresses are taken as positive, as it is throughout this report. The development for the principal values and the invariants of  $g$  apply equally well to the stress deviator,  $s$ , but, two important points should be emphasized in this comparison: a) the principal directions of the stress deviator are the same as those of

the stress tensor since both represent directions perpendicular to planes having no shear stress (see, for example, Reference 17, p.91), and b) the first invariant of the stress deviator (say  $J_1$ ) is equal to zero; i.e.,

$$J_1 = s_{11} + s_{22} + s_{33} \\ = \sigma_{11} - \frac{1}{3} I_1 + \sigma_{22} - \frac{1}{3} I_1 + \sigma_{33} - \frac{1}{3} I_1 ,$$

and recalling the relation of equation 26, clearly

$$J_1 = 0.$$

The invariants of the deviatoric stress tensor are denoted by  $J_1$ ,  $J_2$  and  $J_3$  respectively, and since, as we have shown,  $J_1$  is equal to zero, the cubic expression for the stress deviator, in analogy to equation 25 of the stress tensor  $\underline{g}$ , lacks the quadratic term; i.e.,

$$\lambda^3 - J_2 \lambda - J_3 = 0 , \quad (30)$$

where the roots,  $\lambda$ , are now the principal values (or more formally, the eigenvalues) of the stress deviator:  $s_1$ ,  $s_2$ , and  $s_3$ . The absence of the quadratic term renders the solution of equation 30 more tractable than that of equation 25. As a result, it is more convenient to solve for the principal values of  $\underline{s}$  and then compute the principal values of  $\underline{g}$  using the relations

$$\sigma_1 = s_1 + p , \quad \sigma_2 = s_2 + p , \quad \text{and} \quad \sigma_3 = s_3 + p . \quad (31)$$

The direct evaluation of the roots,  $\lambda$ , of equation 30 is not easy until the similarity of equation 30 to the following trigonometric identity is observed:

$$\sin 3\theta = 3 \sin\theta - 4 \sin^3\theta$$

which when divided through by four gives

$$\sin^3 \theta - \frac{3}{4} \sin \theta + \frac{1}{4} \sin 3\theta = 0 . \quad (32)$$

The mathematical manipulation is achieved by replacing  $\lambda$  with  $r \sin \theta$  in equation 30; this substitution results in

$$r^3 \sin^3 \theta - J_2 r \sin \theta - J_3 = 0 ,$$

and dividing through by  $r^3$  effects

$$\sin^3 \theta - \frac{J_2}{r^2} \sin \theta - \frac{J_3}{r^3} = 0 . \quad (33)$$

By equating equations 32 and 33, we record the following equalities:

$$\frac{J_2}{r^2} = \frac{3}{4}$$

or

$$r = \pm \frac{2}{\sqrt{3}} \sqrt{J_2} , \quad (34)$$

and

$$\frac{J_3}{r^3} = -\frac{1}{4} \sin 3\theta ,$$

or

$$\sin 3\theta = -\frac{4 J_3}{r^3} . \quad (35)$$

Substitution of the negative root of 34 into equation 35 leads to

$$\sin 3\theta = \frac{[3\sqrt{3} (J_3/\sqrt{J_2^3})]}{2} , \quad (36)$$

or

$$\theta = \frac{1}{3} \sin^{-1} \left[ \frac{3\sqrt{3} (J_3/\sqrt{J_2^3})}{2} \right] \quad (37)$$

where  $\theta$  is known as the Lode angle (Reference 24), and it represents an alternative invariant which frequently replaces the  $J_3$  invariant in

failure criteria because of its straightforward geometric interpretation (see section II.F.1).

Owing to the periodic nature of the sine function, the angles  $3\theta$ ,  $3\theta + 2\pi$ , and  $3\theta + 4\pi$  all give the same sine in terms of the calculated invariants of the deviator in equation 36. If we further restrict  $3\theta$  to the range  $\pm\pi$  (i.e.,  $-\pi \leq \theta \leq +\pi$ ), the three independent roots of the stress deviator are furnished (Reference 25),

$$s_1 = -\frac{2}{\sqrt{3}} \sqrt{J_2} \sin(\theta + \frac{4}{3} \pi) \quad , \quad (38)$$

$$s_2 = -\frac{2}{\sqrt{3}} \sqrt{J_2} \sin(\theta) \quad , \quad (39)$$

and,

$$s_3 = -\frac{2}{\sqrt{3}} \sqrt{J_2} \sin(\theta + \frac{2}{3} \pi) \quad . \quad (40)$$

Finally, the relations of equations 38, 39 and 40 can be combined with those of equation 31 to yield the principal values of the stress tensor  $\underline{\sigma}$ ,

$$\begin{Bmatrix} \sigma_1 \\ \sigma_2 \\ \sigma_3 \end{Bmatrix} = -\frac{2}{\sqrt{3}} \sqrt{J_2} \begin{Bmatrix} \sin(\theta + 4/3 \pi) \\ \sin \theta \\ \sin(\theta + 2/3 \pi) \end{Bmatrix} + \frac{1}{3} \begin{Bmatrix} I_1 \\ I_1 \\ I_1 \end{Bmatrix} \quad . \quad (41)$$

### 3. The Strain Tensor

The mathematical interpretation of the concept of strain is considerably more difficult than the development just presented for stress. Nevertheless, a brief introduction to the small strain tensor is attempted herein while it is recommended that the interested reader refer to a continuum mechanics textbook to better understand the

concept and implications of finite deformation. The presentation that follows has been modified from Synge and Schild (Reference 22).

Most soils engineers are familiar with the geometrical measure of unit extension,  $e$ , which is defined as the change in distance between two points divided by the distance prior to straining ( $L_0$ ); i.e.,

$$e = (L_1 - L_0) / L_0, \quad (42)$$

where  $L_1$  is the distance between particles P and Q, for instance, after the deformation. If the coordinates of P and Q are denoted by  $x_r(P)$  and  $x_r(Q)$  respectively, we can write, from geometric considerations, that

$$L_0^2 = [x_r(P) - x_r(Q)] [x_r(P) - x_r(Q)]. \quad (43)$$

Further, if the particles P and Q receive displacements  $u_r(P)$  and  $u_r(Q)$  respectively, we can state that

$$x'_r(P) = x_r(P) + u_r(P), \quad (44)$$

and

$$x'_r(Q) = x_r(Q) + u_r(Q), \quad (45)$$

where the primed coordinates represent the position of the particles P and Q (which retain their identity) after deformation. The notation  $u_r(P)$  and  $u_r(Q)$  indicates that the particles receive a displacement which is a function of their coordinates; if the displacement vector,  $\underline{u}$ , is the exactly the same for each particle in the medium, the whole medium is then translated without deformation (i.e., a rigid body motion). From equations 44 and 45, we have

$$\begin{aligned} L_1^2 &= [x'_r(P) - x'_r(Q)] [x'_r(P) - x'_r(Q)], \\ &= [x_r(P) + u_r(P) - x_r(Q) - u_r(Q)] \\ &\quad [x_r(P) + u_r(P) - x_r(Q) - u_r(Q)], \end{aligned} \quad (46)$$

and by subtracting equation 43 from equation 46, we obtain

$$L_1^2 - L_0^2 = [x_r(P) + u_r(P) - x_r(Q) - u_r(Q)][x_r(P) + u_r(P) - x_r(Q) - u_r(Q)] - [x_r(P) - x_r(Q)][x_r(P) - x_r(Q)] ,$$

which simplifies to

$$L_1^2 - L_0^2 = [u_r(Q) - u_r(P)][u_r(Q) - u_r(P)] + 2 [x_r(Q) - x_r(P)][u_r(Q) - u_r(P)] . \quad (47)$$

If we fix our attention on the point P and let the neighboring particle Q be located at some arbitrary direction but infinitesimal distance from P, we can proceed to generalize the state of strain at the point P. Since the distance between P and Q is assumed small, it is apparent that the term  $[x_r(Q) - x_r(P)][x_r(Q) - x_r(P)]$  is also infinitesimal and we have approximately

$$u_r(Q) = u_r(P) + \partial u_r / \partial x_s |_P [x_s(Q) - x_s(P)] ,$$

from which we can write

$$u_r(Q) - u_r(P) = \partial u_r / \partial x_s |_P [x_s(Q) - x_s(P)] . \quad (48)$$

Substitution of equation 48 into equation 47 leads to

$$L_1^2 - L_0^2 = \partial u_r / \partial x_s |_P [x_s(Q) - x_s(P)] \partial u_r / \partial x_t |_P [x_t(Q) - x_t(P)] + 2 [x_r(Q) - x_r(P)] \partial u_r / \partial x_m |_P [x_m(Q) - x_m(P)] . \quad (49)$$

We also know that

$$[x_r(Q) - x_r(P)] = L_0 n_r \quad (50)$$

where  $n_r$  are the components of the unit vector directed from P to Q.

Substitution of the relation in 50 into 49 results in

$$\begin{aligned} L_1^2 - L_0^2 &= \partial u_r / \partial x_s |_P L_0 n_s \partial u_r / \partial x_t |_P L_0 n_t + \\ &+ 2 L_0 n_r \partial u_r / \partial x_m |_P L_0 n_m \\ &= L_0^2 [\partial u_r / \partial x_s |_P n_s \partial u_r / \partial x_t |_P n_t + \\ &+ 2 n_r \partial u_r / \partial x_m |_P n_m] , \end{aligned} \quad (51)$$

and upon rearranging equation 51, we see that

$$\frac{L_1^2 - L_0^2}{L_0^2} = \left[ \frac{\partial u_r}{\partial x_s} \Big|_P n_s \frac{\partial u_r}{\partial x_t} \Big|_P n_t + 2 n_r \frac{\partial u_r}{\partial x_m} \Big|_P n_m \right] . \quad (52)$$

If an assumption is made that the character of the strain is small, this means that  $\partial u_r / \partial x_t \Big|_P$  and hence the term  $(\partial u_r / \partial x_s \Big|_P \partial u_r / \partial x_t \Big|_P)$  in equation 52 is negligible; this equation may thus be rewritten as:

$$\frac{L_1^2 - L_0^2}{L_0^2} = 2 n_r \frac{\partial u_r}{\partial x_m} \Big|_P n_m . \quad (53)$$

Moreover, we have identically

$$\begin{aligned} \frac{L_1^2 - L_0^2}{L_0^2} &= \frac{L_1 - L_0}{L_0} \frac{L_1 + L_0}{L_0} , \\ &= \frac{L_1 - L_0}{L_0} \frac{L_1 - L_0 + 2 L_0}{L_0} , \\ &= \frac{L_1 - L_0}{L_0} \left[ \frac{L_1 - L_0}{L_0} + 2 \right] , \\ &= e ( e + 2 ) ; \end{aligned} \quad (54)$$

and with the assumption of small strain,  $e^2$  is negligible, and equation 54 reduces to

$$\frac{L_1^2 - L_0^2}{L_0^2} = 2 e . \quad (55)$$

Replacing the small strain approximation of equation 55 into equation 53 yields

$$e = n_r \frac{\partial u_r}{\partial x_m} \Big|_P n_m . \quad (56)$$

If the components of the small strain tensor at point P are now defined as:

$$\epsilon_{rs} = \frac{1}{2} \left[ \frac{\partial u_r}{\partial x_s} + \frac{\partial u_s}{\partial x_r} \right] , \quad (57)$$

it is easy to see from equation 56 that the unit extension of every infinitesimal element emanating from P in the arbitrary direction  $\underline{n}$  is determined by

$$e = \epsilon_{rs} n_r n_s . \quad (58)$$

Soil engineers may wonder how the traditional shear strain concept fits into this definition of strain, but it can be shown (see, for example, Reference 17, p.121) that the off-diagonal terms of the tensor  $\underline{\epsilon}$  is approximately equal to half the decrease,  $\gamma_{rs}$ , in the right angle initially formed by the sides of an element initially parallel to the directions specified by the indices r and s. This only holds for the small strain assumption where the angles are small compared to one radian. Another important geometrical measure is the volume change or dilatation, and, if second order effects can be neglected (i.e. terms such as  $[\partial u_r / \partial x_s]_P \partial u_r / \partial x_t|_P]$  are small), the reader can easily verify that the volume strain ( $dV/V_0$ ) is equal to the first invariant (or trace) of the strain tensor  $\underline{\epsilon}$  (or in indicial notation,  $\epsilon_{mm}$ ). Throughout this report, the strain deviator (in analogy to the stress deviator  $\underline{s}$ ) is denoted by  $\underline{e}$  so we can write its components as:

$$e_{ij} = \epsilon_{ij} - \frac{1}{3} \epsilon_{mm} \delta_{ij} . \quad (59)$$

Since, like stress, strain is a symmetric second order tensor, the whole development of principal strains and invariants parallels the previous discussion for the stress tensor.



## B. STRESS-STRAIN EQUATIONS AND CONSTITUTIVE THEORY

In order to solve statically indeterminate problems, the engineer relies upon: a) the equations of equilibrium, b) the kinematic compatibility conditions, and c) a knowledge of the load-deformation response (or stress-strain constitution) of the engineering material under consideration. As an aside, it may be useful to remind the soils engineer of two elementary definitions which are not part of the everyday soil mechanics vocabulary: first, kinematics is the study of the motion of a system of material particles without reference to the forces which act on the system, and secondly, dynamics is that branch of mechanics which deals with the motion of a system of material particles under the influence of forces, especially those which originate outside the system under consideration. For general applicability, the load-deformation characterization of the solid media is usually expressed in the form of a constitutive law relating the force-type measure (stress) to the measure of change in shape and/or volume (strain) of the medium. A constitutive law therefore expresses an exact correspondence between a man-made action (force) and an effect (deformation) which is due to nature. The correspondence is functional - it is a mathematical representation of the physical processes which take place in a material as it passes from one state of equilibrium to another (Reference 26). This is an appropriate point to interject and briefly clarify the meaning of the adjective functional.

Let us return to the sand mass which contains particle P and extend the discussion to include M discrete granules ( $P_M$ ) contained in the mass. Say that the sand mass was subjected to a system of boundary

loads which induced a motion of the granular assembly while a scientist painstakingly recorded, at  $N$  prescribed time intervals, the location of each of the  $M$  particles using a spatial reference frame  $x$ . The data log therefore consists of the location of each particle  $M$  ( $x_M$ ) and the time at which each measurement was made ( $t'$ ). At the current time  $t$  ( $\geq t'$ ), we are interested in formulating a constitutive relationship which gives us the stress at point  $P$ , and, in our attempt to construct a model of nature, we propose to derive such a relation based on the  $MN$  discrete vector variables we have observed; i.e., the  $M$  locations  $x_M$  at  $N$  different times  $t'$  ( $\leq t$ ). In other words, stress at  $P$  is a function of these  $MN$  variables. This function converges to the definition of a functional as the number of particles  $M$  and the discrete events in time set  $t'$  approach infinity.

In this investigation, we are solely interested in the following:

a) evaluating the performance of certain recently proposed constitutive postulates, and, if necessary, b) proposing and implementing modifications to these existing models such that the influence of principal stress axes rotation on material response is captured.

Without too much intellectual effort, we can tender a simple stress-strain relation of the form

$$\sigma_{ij} = C_{ijkl} \epsilon_{kl}, \quad (60)$$

or inversely,

$$\epsilon_{kl} = D_{klij} \sigma_{ij}, \quad (61)$$

where the fourth order tensors (with 81 components)  $C_{ijkl}$  and  $D_{klij}$  are called the stiffness and compliance tensors respectively. Note that the number of components necessary to define a tensor of arbitrary order

"n" is equal to  $3^n$ . Alternatively, we may view the stress-strain formulation on an incremental basis and write

$$\dot{\sigma}_{ij} = C_{ijkl} \dot{\epsilon}_{kl}, \quad (62)$$

or inversely,

$$\dot{\epsilon}_{kl} = D_{klij} \dot{\sigma}_{ij}, \quad (63)$$

where the superposed dot above the stress and strain tensors symbolizes that these tensors are differentiated with respect to time.  $\dot{\sigma}$  and  $\dot{\epsilon}$ , as they appear in equations 62 and 63, are termed the stress rate and strain rate respectively. If the "step by step" load-deformation model is further idealized to exclude the influence of rate of loading, we can then write the resulting rate-independent equations as:

$$d\sigma_{ij} = C_{ijkl} d\epsilon_{kl}, \quad (64)$$

or inversely,

$$d\epsilon_{kl} = D_{klij} d\sigma_{ij}, \quad (65)$$

where  $d\sigma$  and  $d\epsilon$  are the stress increments and strain increments respectively. The constitutive equations considered in this report are all of the rate-independent type.

In the formulation of general, rate independent, incremental stress-strain formulations, our objective is one of identifying the variables which influence the instantaneous magnitudes of the components of the  $C$  or  $D$  fourth order tensors. Such a study bears resemblance to many other specialized disciplines of civil engineering; the econometrician, for instance, may determine by a selective process that the following variables influence the price of highway construction in a state for any given year: cost of labor, cost of equipment, material costs, business climate, and a host of other

tangible and intangible factors. The soils engineer, perhaps using the econometrician's techniques of regression analysis and some of his personal experience, can easily identify several factors influencing soil behavior. Some of these more important variables in soil mechanics which come to mind are: the history of the stress,  $\underline{g}^t$ ; the magnitude of the stress increment,  $d\underline{g}$ ; the history of the strain,  $\underline{\epsilon}^t$ ; and the "n" so-called internal variables,  $\underline{g}_n$ , that contain information regarding: a) the microstructural properties of the material, and b) discrete events such as abrupt changes in the loading process. We can therefore write a general functional, rate-independent, incremental stress-strain relationship in the form

$$d\underline{\epsilon} = \hat{d\underline{\epsilon}}(\underline{g}^t, \underline{\epsilon}^t, d\underline{g}, \underline{g}_n), \quad (66)$$

and our study in this report centers around the use of special cases of the relation in equation 66 to model soil behavior.

A basic difference between the econometrician's model and the mechanician's load-deformation model must be highlighted: the mechanician is dealing with dependent and independent variables which are physically significant while the econometrician is concerned with variables which may frequently be intangible. Therefore, in the selection of constitutive variables (such as stress and strain), and in the actual formulation of the stress-strain equations, certain physical and mathematical considerations have to be satisfied. These conditions are embodied in the so-called axioms or principles of constitutive theory. Since geotechnical engineers are, for the most part, interested in isothermal processes, the principles which concern thermomechanical events will be suppressed in the sequel.

The Axiom of Causality states that the motion of the material points of a body is to be considered a self-evident, observable effect in the mechanical behavior of the body; any remaining quantities (such as the stress) that enter the entropy production and the balance equations - i.e., the equations of conservation of mass, balance of momentum, and conservation of energy - are the causes or dependent variables.

The Principle of Determinism infers that the stress in a body is determined by the history of the motion of that body; this axiom excludes the dependence of the stress at P on any point outside of the body and any future events.

In the purely mechanical sense, the Axiom of Neighborhood or Local Action rules out any appreciable effects on the stress at P that may be caused by the motion of points distant from P.

During the discussion of stress and strain, it was made quite clear that the tensor measures should be independent of the perspective of the observer, and it is therefore instinctive to suggest a similar constraint for the constitutive equations. This requirement that the constitutive equations be form-invariant with respect to rigid motions of the spatial frame of reference is known as the Principle of Material Frame Indifference or Objectivity.

Finally, the Axiom of Admissibility states that all constitutive equations must be consistent with the basic principles of continuum mechanics; i.e., they are subject to the principles of conservation of mass, balance of momenta, conservation of energy, and the Clausius-Duhem inequality.

### C. A NOTE ON STRESS AND STRAIN IN GRANULAR MEDIA

The concepts of stress and strain discussed in the previous sections are closely associated to the concept of a continuum which effectively disregards the molecular structure of matter and mathematically treats the medium as if there were no holes or gaps. The following quotation from Lambe and Whitman (Reference 27, p.98) succinctly summarizes the applicability of the continuum stress measure to granular materials:

.....when we speak of the stress acting at a point, we envision the forces against the sides of an infinitesimally small cube which is composed of some homogenous material. At first sight we may therefore wonder whether it makes sense to apply the concept of stress to a particulate system such as soil. However, the concept of stress as applied to soil is no more abstract than the same concept applied to metals. A metal is actually composed of many small crystals, and on the submicroscopic scale the magnitude of the forces vary randomly from crystal to crystal. For any material, the inside of the infinitesimally small cube is thus only statistically homogenous. In a sense all matter is particulate, and it is meaningful to talk about macroscopic stress only if this stress varies little over distances which are of the order of magnitude of the size of the largest particle. When we talk about about stresses at a "point" within a soil, we often must envision a rather large "point".

Local strains within a statistically homogenous mass of sand are the result of distortion and crushing of individual particles and the relative sliding and rolling velocities between particles. These local strains are much larger than the overall (continuum) strain described in subsection II A.3. The magnitude of strain caused by a stress will in general depend on the composition, void ratio, past stress history, and the manner in which the stress is applied. In soil mechanics terminology, composition is a descriptive term that includes the

average particle size, gradation of the particle sizes, angularity of the particles, and the mineral type.

Figure 2 illustrates typical qualitative load-deformation behavior for loose and dense soil media subject to two conventional laboratory stress paths: hydrostatic compression, and conventional triaxial compression. Figure 3 shows these paths together with an assortment of other 'triaxial' stress paths used for research as well as routine purposes. Note that, in this context, the adjective 'triaxial' is somewhat ambiguous since this particular test scenario dictates that the circumferential stress always be equal to the radial stress. The stress state is therefore not truly triaxial, but biaxial. As we can gather from figure 2, the stress-strain behavior of soil is quite complicated, and, in order to approximately model the real behavior, drastic idealizations and simplifications are necessary. The major presuppositions in most popular postulates are that a) soil response is independent of the rate of loading, b) the interaction between the mechanical and thermal processes are negligible, and c) the strain tensor can be decomposed into an elastic or recoverable part ( $\epsilon^e$ ) and a plastic or irrecoverable conjugate ( $\epsilon^p$ ) without any interaction between the two simultaneously occurring strain types; i.e.,

$$\epsilon = \epsilon^e + \epsilon^p, \quad (67)$$

or on an incremental basis,

$$d\epsilon = d\epsilon^e + d\epsilon^p. \quad (68)$$

The elastic or recoverable behavior ( $\epsilon^e$  or  $d\epsilon^e$ ) is treated within the framework of elasticity concepts while the irrecoverable part ( $\epsilon^p$

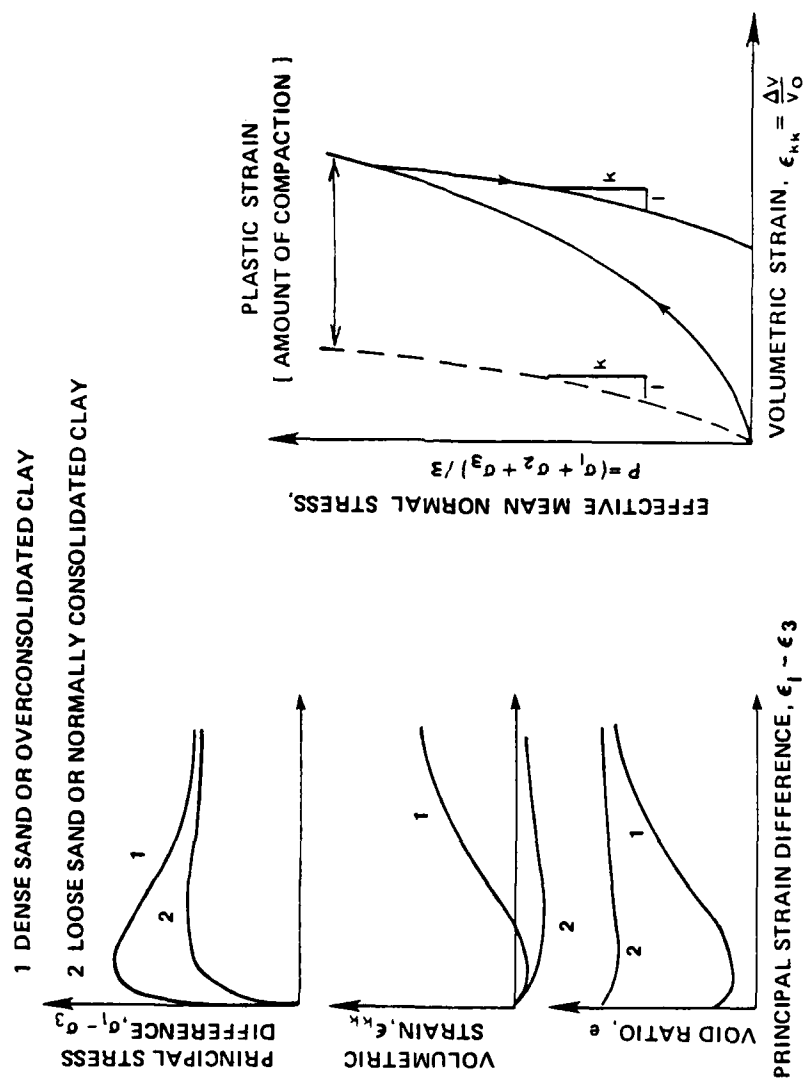


Figure 2. Typical Stress-Strain Response of Soil During Conventional 'Triaxial' Shear (left) and Hydrostatic Compression (right).



NAME OF TEST	Standard Designation	DESCRIPTION
Conventional Triaxial Compression	CTC	$\Delta\sigma_x = \Delta\sigma_z = 0; \Delta\sigma_y > 0$
Hydrostatic Compression	H C	$\Delta\sigma_x = \Delta\sigma_z = \Delta\sigma_y > 0$
Conventional Triaxial Extension	CTE	$\Delta\sigma_x = \Delta\sigma_z > 0; \Delta\sigma_y = 0$
Mean Normal Pressure Triaxial Compression	T C	$\Delta\sigma_x + \Delta\sigma_z + \Delta\sigma_y = 0;$ $\Delta\sigma_y > \Delta\sigma_x (= \Delta\sigma_z)$
Mean Normal Pressure Triaxial Extension	T E	$\Delta\sigma_x + \Delta\sigma_z + \Delta\sigma_y = 0;$ $\Delta\sigma_x = \Delta\sigma_z > \Delta\sigma_y$
Reduced Triaxial Compression	RTC	$\Delta\sigma_x = \Delta\sigma_z < 0; \Delta\sigma_y = 0$
Reduced Triaxial Extension	RTE	$\Delta\sigma_y < 0; \Delta\sigma_x = \Delta\sigma_z = 0$

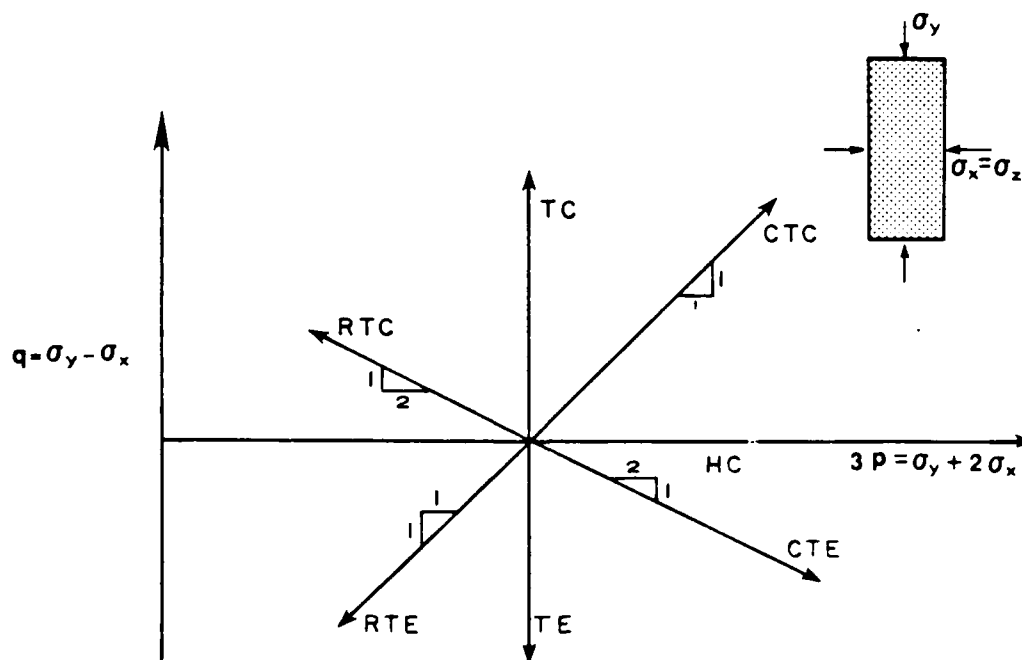


Figure 3. Typical Stress Paths Used to Investigate Stress-Strain Response of Solid Cylindrical Soil Specimens.

or  $d\epsilon^p$ ) is based on plasticity theory; both these theories will be capsulized in later sub sections.

Three broad classes of continuum theories have evolved in the development and advancement of soil stress-strain models (Reference 28): 1) the kinematically ambiguous theories, 2) the phenomenological theories, and 3) the microstructural theories.

The kinematically ambiguous hypotheses employ the stress equations of equilibrium in conjunction with the Coulomb yield condition to form a system of equations relating the components of the stress tensor. This class of theories is referred to as kinematically ambiguous because displacements and strains do not appear in the basic equations of the theory. These theories assume the entire medium is in a state of incipient yielding. The information obtained from these theories is useful, but limited because the theories do not predict strains or any results that follow from a specific stress-strain relation. An example of this type of formulation can be found in Cambou's work (Reference 29).

Phenomenological continuum theories endeavor to devise constitutive relations based on experimentally determined stress-strain curves. This class of theory is presently the most popular and focuses on the macroscopically observable and controllable stress and strain variables without inquiring too deeply into the detailed mechanisms which control the process of deformation. A controversial assumption of the phenomenological continuum theories is that the test procedures for granular materials, such as the conventional triaxial test, achieve homogenous states of strain and stress, and therefore determine local

stress-strain relations. Research attention in the study described herein is targeted toward this type of model.

The microstructural theories attempt to incorporate geometric measures of local granular structure into the continuum theory; this theory is then used to predict the influences of the microstructure on the stress-strain relations. This local granular structure is also called fabric and is defined as the spatial arrangement and contact areas of the solid granular particles and associated voids. An example of this type of formulation can be found in the Nemat-Nasser and Menrabadi reference (Reference 30). The next major topic heading is dedicated to elaborating the concept and significance of fabric anisotropy in granular material.

#### D. FABRIC IN GRANULAR MATERIAL

The fabric of earthen materials are intimately related to the mechanical processes occurring during their natural formation (or test sample preparation) and the subsequent application of boundary forces. We can look at process of fabric evolution in terms of the deformation that occurs (kinematics) or the stresses that are acting (dynamics). Strains that accompany the stresses are influenced by the symmetry of the applied stress system, and, to some extent, by the symmetry of the sand's directional stiffness or fabric. If straining is continued to a relatively high level, we may expect that the initial fabric will develop such that its orientation aligns itself with the symmetry pattern of the applied stress system. Before introducing and discussing a select group of microscopic fabric measures, some of the pertinent

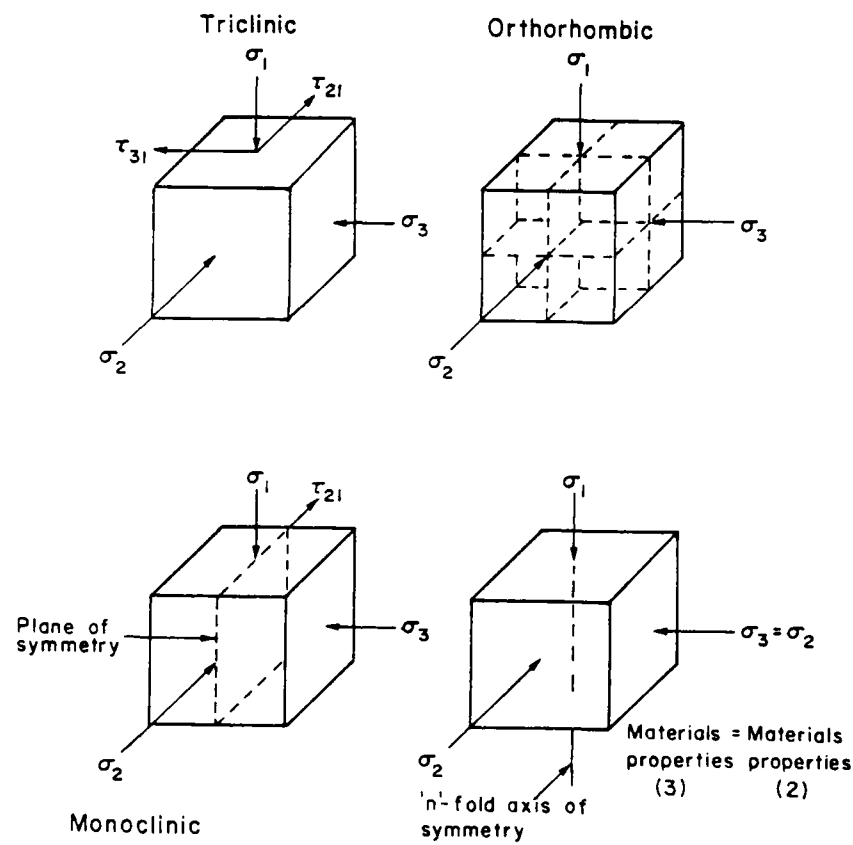


Figure 4. Common Symmetry Types - Triclinic, Monoclinic, Orthorhombic, and  $n$ -fold axis (Reference 31).

symmetry patterns generated by combined kinematic and dynamic boundary conditions will be addressed.

Triclinic symmetry implies that the media possesses no plane or axis of symmetry, and is produced during complex deformations. Gerrard (Reference 31) presents a simple example of how this most general and least symmetric system may arise: triclinic symmetry may develop from compression in direction 1 (see upper left sketch in figure 4), with differential restraint in directions 2 and 3, coupled with shear components acting in directions 2 and 3 on the plane having its normal to axis 1. Geometrically, this fabric configuration may be referred to by three non-mutually perpendicular axes of different length.

In the monoclinic system, there is a single plane of symmetry such that any two directions symmetric with respect to this plane are equivalent. An example of this type of symmetry is shown in the lower left of figure 4 where the anisotropic structure may be created by the following concurrent events: a) compression acting in direction 1, b) deformation being prevented in the 2 and 3 directions, and c) application of a shear stress component in the direction 2 acting on the plane having its normal to axis 1. By slightly modifying this monoclinic symmetry example, we can demonstrate an instance of n-fold axis symmetry, more commonly known as cross-anisotropy in soil mechanics. This can be accomplished by excluding the shear stress application in the previous example with the result that an axis of symmetry is produced such that any direction normal to the axis is equivalent (see bottom right of figure 4).

The orthorhombic symmetry group can best be described by bringing to mind the true triaxial device. Here, for example (top right of figure 4), three mutually perpendicular planes of symmetry can originate from pure compressions of different magnitudes on the faces of the cubical sand specimen. Lastly, the rarest natural case (but most common idealization) is spherical symmetry or material isotropy which implies that all directions in the material are equivalent, and therefore, there are no dominant directions with regards to deformation.

The selection of the internal variables,  $g_n$ , to characterize the mechanical state of a sand medium (see equation 66) has been one of the major themes provoking much discussion at two recently organized symposia on the load-deformation response of granular materials: 1) the IUTAM Conference on Deformation and Failure of Granular Materials held in 1982 at Delft, Netherlands (Reference 32), and 2) the U.S.-Japan Seminar on Continuum Mechanical and Statistical Approaches in the Mechanics of Granular Materials which took place in 1978 at Sendai, Japan (Reference 33). There is no doubt that the initial void ratio ( $e = V_v/V_s$ , where  $V_v$  = volume of voids, and  $V_s$  = volume of solids) is the most dominant geometric measure, but as Cowin (Reference 28) poses: "Given that porosity is the first measure of local granular structure or fabric, what is the best second measure of local granular structure or fabric?". This important topic will be examined briefly in the following paragraphs.

An anthropomorphic description is perhaps ideal for introducing the reader to the concept of fabric in granular material. Let us assume for

illustrative purposes that, through detailed experimental investigation, we have identified a microscopic geometric or physical measure (say variable X) which serves as the secondary controlling factor to the void ratio in interpreting the stress-strain response of sand. Some of the suggestions for the variable X have been: 1) gradient of the void ratio  $\frac{\partial e}{\partial X}$  (Reference 34), 2) orientation of the long axes of the particles (Reference 35), 3) distribution of the magnitude and orientation of the inter-particle contact forces (Reference 29), 4) distribution of the inter-particle contact normals (for example, Reference 36), 5) distribution of branches; note: a branch is defined as the vector connecting the centroids of neighboring particles and it is thus possible to replace a granular mass by a systems of lines or branches (Reference 37), 6) mean projected solid path (Reference 38), and 7) mathematical representations in the form of second order tensors (Reference 39).

A commander (mother nature) of an army (the set representing the internal variable of the sand medium) always stations his troops (variable X) in a configuration which provides maximum repulsive effort to an invading force (boundary tractions). This means that the highest concentration of variable X will point in the direction of the imposed major principal stress. If the invading army (boundary tractions) withdraws (an unloading event), we should expect the general (mother nature) to keep his distribution of soldiers (X) practically unaltered. It is an experimental fact that there is always some strain recovery upon unloading, and this rebound is caused partly by elastic energy

stored within individual particles as the soil was loaded and partly by inelastic reverse sliding between particles. Traditionally, it has been convenient to regard this unloading strain as purely elastic, but, in reality, it stems from microstructural changes due to changes of the fabric and should be considered as a dissipative thermodynamically irreversible process (Reference 40). Returning to our anthropomorphic description, we can therefore say that the general (mother nature) has a built-in command to slightly modify the arrangement of troops (X) once the offensive army (boundary tractions) has been removed. The configuration of the defensive forces (distribution of X) after complete or partial withdrawal of the aggressor (complete or partial removal of the boundary loads) still however reflects the intensity and direction of the earlier attack (initial application of the system of boundary loads). This represents an induced fabric or stress induced anisotropy in our granular material.

We can create additional scenarios with our anthropomorphic model to manifest other features and considerations of fabric anisotropy. During the initial placement of the forces (initial distribution of the variable X during sample preparation or during natural formation of the soil deposit) under the general's command, there is a bias in this arrangement which is directly related to the general's personality (gravity as a subset of mother nature). This is the so-called inherent anisotropy (Reference 41) of soil which differs from the stress-induced anisotropy mentioned previously. Say, by chance, the invading army (boundary tractions) attacks the defensive fortress (sand mass) with a uniform distribution of troops (uniform distribution of stress



vectors), we will expect the maximum penetration (strain) at the weakest locations (smallest concentration of X), but our wise general (mother nature) should take corrective measures to prevent intrusion by the enemy forces (boundary tractions) through the inherently vulnerable sites (points of initially low X concentration). We can relate this situation to the effect of increasing hydrostatic pressure on an inherently cross-anisotropic sand specimen; the results of such a test carried out by Parkin et al. (Reference 35) shows that the ratio of the incremental horizontal strain to incremental vertical strain decreases from about 6 to 2.5. This shows that the influence of increasing hydrostatic pressure is to decrease the degree of anisotropy, but it does not completely wipe out the inherent anisotropic fabric. We can also therefore see that the general (mother nature) cannot reorient his forces at will since he is faced by the annoying internal constraints (particles obstructing each other) which plague most large and complex organizations (the microscopic world of particles sliding and rolling past each other). These very same impediments are also manifest in the case of stress-induced anisotropy.

We can now investigate the more complex situation of a virgin loading with its accompanying fabric induction followed by unloading and then a reloading event with rotated principal stress directions. This is useful in extending the discussion of the progressive development of anisotropy during the application of deviator stress as opposed to the situation for hydrostatic compression described in the preceding paragraph. Experimental evidence indicates that the principal directions of fabric (i.e., principal directions of the distribution of

X or the second order tensor representation) match the principal directions of the applied stress tensor during a virgin or prime loading event, even with the continuous rotation of the principal directions of stress (Reference 42). Again, the question of the influence of microscopic hindrances to the realignment of particles and hence fabric inductivity is one of fundamental research interest. Oda et al. (Reference 43) has shown, through microscopic studies, that the distribution function describing the orientation of contact normals does not change significantly once the material starts to dilate. So, if we can isolate the contact normal density function as a representative measure of fabric, it is safe to assume that fabric induction ceases when the granular material starts to distend.

Of the range of earthen materials, the influence of inherent as well as induced anisotropy on uncemented granular deposits (like sand) is greatest. Based on the discussion presented in this subsection, we can now identify two of the internal state variables ( $g_n$  of equation 66) which provide information regarding the stress-strain-strength response of sand: 1) the initial void ratio, and 2) the fabric measure which may be phenomenological or micromechanical, depending on the level of observation.

#### E. ELASTICITY

We now turn our attention to the mathematical models used to simulate the stress-strain response of soil. In this section, we summarize the essential features of the three broad classes of elasticity-based constitutive models (References 44 and 45): 1) the

Cauchy type, 2) the Hyperelastic (or Green) type, and 3) the incremental (or Hypoelastic) type. Although, in the strict sense, the definition of an elastic body implies fully recoverable behavior, we can, for mathematical convenience in some instances, suppose that all strains are "elastic" and thus disregard the decomposition set forth in equations 67 and 68. This assumption has been applied extensively in the modeling of soil behavior, but we should note that this idealization is only suitable for a limited class of problems wherein a monotonically increasing load prevails.

#### 1. Cauchy Type Elasticity

Recall from equation 66 that we can select the strain increment to be a function of several variables

$$d\epsilon = d\hat{\epsilon}(\underline{g}^t, \underline{\epsilon}^t, d\underline{g}, \underline{g}_n) ;$$

if we assume that this relationship is not a functional (i.e. not a function of a function such as  $\underline{g}^t$  or  $\underline{\epsilon}^t$ ) but merely a function of its independent variables (i.e., the current state of stress,  $\underline{g}$ , or strain,  $\underline{\epsilon}$ ), then the incremental relationship is not dependent on the stress path or strain path followed to get to the current state of stress or strain. With this assumption, we can restate this idealized stress-strain relationship as:

$$d\epsilon = d\hat{\epsilon}(\underline{g}, d\underline{g}, \underline{g}_n) . \quad (69)$$

If we then further presuppose the nonexistence of any significant internal variables, equation 69 can be simplified to obtain a Cauchy type formulation of the form

$$d\epsilon = d\hat{\epsilon}(\underline{g}, d\underline{g}) , \quad (70)$$

or inversely,

$$d\bar{g} = d\hat{g}(\bar{\epsilon}, d\bar{\epsilon}) \quad , \quad (71)$$

where the current state of stress depends only on the current state of strain or vice-versa. The stress-strain behavior described by equations 70 and 71 is reversible, but it has been shown that this type of formulation may generate energy during a load-unload cycle (Reference 44), thus violating the axiom of admissibility stated in section II B.

A comparison of equation 71 with equation 64 shows that we may write an incremental Cauchy elastic stress-strain relation in the form

$$d\sigma_{ij} = C_{ijkl} d\epsilon_{kl}$$

where the components of the fourth order, elastic stiffness tensor,  $\underline{C}$ , is only dependent on the present components of the strain tensor,  $\bar{\epsilon}$ . In order to provide some insight into the formulation of this type of elasticity relation, the most uncomplicated elastic constitutive relation will now be derived.

Let us proceed by first assuming that the body is isotropic (i.e., it has spherical symmetry as described in section II D). This implies that the fourth order stiffness tensor  $\underline{C}$  is also isotropic in the sense that its components are equivalent for all rectangular Cartesian coordinate systems. By generalizing the second order tensor transformation formula (equation 13) to its fourth order equivalent, we obtain

$$C'_{ijkl} = Q_{ip} Q_{jq} Q_{kr} Q_{ls} C_{pqrs} \quad (72)$$

as the transformation rule for the "elastic" stiffness tensor  $\underline{C}$ . With the isotropy assumption, we expect the response to be indifferent to the orientation of the observer and hence we must also insist that  $\underline{C}$  be

equal to  $\underline{C}'$ . A fourth order isotropic tensor - which obeys this transformation rule and satisfies the requirement that  $\underline{C} = \underline{C}'$  - can be constructed from Kronecker deltas,  $\delta$ , defined earlier in equation 18 (see, for example, Reference 22, p.211). The most general isotropic tensor of the fourth order that can be built up from the Kronecker delta is

$$C_{ijkl} = \lambda \delta_{ij} \delta_{kl} + \mu \delta_{ik} \delta_{jl} + \nu \delta_{il} \delta_{jk} , \quad (73)$$

where  $\lambda$ ,  $\mu$ , and  $\nu$  are invariants. Since  $\underline{\delta} = \underline{\delta}'$ , equation 73 transforms according to the rule stated in equation 72 to give  $\underline{C}$  equal to  $\underline{C}'$ . To simplify the solution still further, we must mention the fact that, by definition, the strain tensor,  $\underline{\epsilon}$ , is symmetric (see equation 57); i.e.,  $\epsilon_{kl} = \epsilon_{lk}$ . Consequently, there is no loss of generality in writing

$$C_{ijkl} = C_{ijlk} , \quad (74)$$

and by substituting equation 73 into equation 74, we have

$$\begin{aligned} \lambda \delta_{ij} \delta_{kl} + \mu \delta_{ik} \delta_{jl} + \nu \delta_{il} \delta_{jk} = \\ \lambda \delta_{ij} \delta_{lk} + \mu \delta_{il} \delta_{jk} + \nu \delta_{ik} \delta_{jl} , \end{aligned} \quad (75)$$

which simplifies to

$$(\mu - \nu) (\delta_{ik} \delta_{jl} - \delta_{il} \delta_{jk}) = 0 , \quad (76)$$

such that  $\mu = \nu$ . With this equality, equation 73 then becomes

$$C_{ijkl} = \lambda \delta_{ij} \delta_{kl} + \mu (\delta_{ik} \delta_{jl} + \delta_{il} \delta_{jk}) , \quad (77)$$

where  $\lambda$  and  $\mu$  are the elastic Lamé constants. If we utilize the deviatoric stress and strain tensors ( $\underline{s}$  and  $\underline{e}$ ) together with the volumetric strain ( $\epsilon_{mm}$ ) measure, we can compare these Lamé constants to the more familiar elastic constants such as the bulk modulus  $K$  ( $= d\sigma_{kk}/[3 d\epsilon_{mm}]$ ), and the shear modulus  $G$  ( $= ds_{ij}/[2de_{ij}]$ ). This can be effected by writing out the isotropic elastic stress-strain relation

$$\begin{aligned}
d\sigma_{ij} &= [ \lambda \delta_{ij} \delta_{kl} + \mu (\delta_{ik} \delta_{jl} + \delta_{il} \delta_{jk}) ] d\epsilon_{kl} \\
&= \lambda \delta_{ij} d\epsilon_{mm} + 2 \mu d\epsilon_{ij} ,
\end{aligned} \tag{78}$$

where  $d\epsilon_{mm}$  is the incremental volumetric strain or dilatation (section II.A.3). By multiplying both sides of equation 78 by the Kronecker delta,  $\delta_{ij}$ , we obtain the bulk modulus in terms of  $\lambda$  and  $\mu$  as follows:

$$d\sigma_{kk} = 3 \lambda d\epsilon_{mm} + 2 \mu d\epsilon_{mm} , \tag{79}$$

or

$$d\sigma_{kk} / 3 d\epsilon_{mm} = K = \lambda + \frac{2}{3} \mu . \tag{80}$$

We can determine the expression for the shear modulus by substituting

$$d\sigma_{ij} = ds_{ij} + \frac{1}{3} d\sigma_{kk} \delta_{ij}$$

and

$$d\epsilon_{ij} = de_{ij} + \frac{1}{3} d\epsilon_{kk} \delta_{ij}$$

into equation 78; this leads to

$$ds_{ij} + \frac{1}{3} d\sigma_{kk} \delta_{ij} = \lambda \delta_{ij} d\epsilon_{mm} + 2 \mu (de_{ij} + \frac{1}{3} d\epsilon_{kk} \delta_{ij}),$$

and upon substitution of the relation in equation 79 into the expression above, we obtain

$$ds_{ij} / 2 de_{ij} = G = \mu . \tag{81}$$

This rather lengthy discussion of the Cauchy elastic formulation is justified since it has been, and still is, extensively used in soil mechanics to simulate nonlinear behavior (see, for example, References 46 and 47). The technique usually involves making  $K$  and  $G$  scalar functions of the stress or strain state.

## 2. Hyperelasticity or Green Type Elasticity

Green defined an elastic material as one for which a strain energy function,  $W$ , (or a complementary energy function,  $\Omega$ ) exists (see, for example, Reference 17). The development of this category of elasticity models was motivated by the need to satisfy thermodynamic admissibility, a drawback of the Cauchy elastic model. Stresses or strains in this idealized material class are computed as follows:

$$\sigma_{ij} = \frac{\partial W}{\partial \epsilon_{ij}} \quad , \quad (82)$$

or

$$\epsilon_{ij} = \frac{\partial \Omega}{\partial \sigma_{ij}} \quad . \quad (83)$$

For an initially isotropic material, the strain energy function,  $W$ , can be written as

$$\sigma_{ij} = \frac{\partial W}{\partial \bar{I}_1} \frac{\partial \bar{I}_1}{\partial \epsilon_{ij}} + \frac{\partial W}{\partial \bar{I}_2} \frac{\partial \bar{I}_2}{\partial \epsilon_{ij}} + \frac{\partial W}{\partial \bar{I}_3} \frac{\partial \bar{I}_3}{\partial \epsilon_{ij}} \quad (84)$$

$$= \phi_1 \delta_{ij} + \phi_2 \epsilon_{ij} + \phi_3 \epsilon_{im} \epsilon_{mj} \quad , \quad (85)$$

where

$$\begin{aligned} W = W(\bar{I}_1, \bar{I}_2, \bar{I}_3) = & A_0 + A_1 \bar{I}_1 + A_2 \bar{I}_2 + A_3 \bar{I}_1^2 + A_4 \bar{I}_1^3 + \\ & A_5 \bar{I}_1 \bar{I}_2 + A_6 \bar{I}_3 + A_7 \bar{I}_1^4 + A_8 \bar{I}_1^2 \bar{I}_2 + A_9 \bar{I}_1 \bar{I}_3 + A_{10} \bar{I}_2^2, \end{aligned} \quad (86)$$

$$\bar{I}_1 = \epsilon_{kk}, \quad \bar{I}_2 = \frac{1}{2} \epsilon_{ij} \epsilon_{ij},$$

$$\bar{I}_3 = \frac{1}{3} \epsilon_{km} \epsilon_{kn} \epsilon_{mn} \quad ,$$

and  $\phi_i$  ( $i = 1, 2, 3$ ) are the response functions which satisfy the condition  $\partial \phi_i / \partial \bar{I}_j = \partial \phi_j / \partial \bar{I}_i$ ; this last condition ensures the symmetry of the predicted stress tensor. To complete the model formulation, the constants  $A_k$  ( $k = 1, 2, \dots, 10$ ) are determined from experimental results.

Different orders of hyperelastic models can be obtained by retaining higher order terms in equation 84; if, for instance, we keep terms up to the third power, we obtain a second-order hyperelastic law. Various aspects of soil behavior can be accounted for in this formulation by using different orders of the model; for example, dilatancy can be realistically simulated by including the third term of equation 86. A detailed description of a hyperelastic formulation can be found in Saleeb and Chen (Reference 44).

### 3. Hypoelasticity or Incremental Type Elasticity

This type of formulation is used to describe a class of materials in which the current state of stress depends on the current state of strain and the history of the stress  $\underline{g}^t$  (or the stress path). The incremental constitutive relation is generally written in the form

$$d\underline{g} = \underline{f}(\underline{g}, d\underline{\varepsilon}) \quad , \quad (87)$$

where  $\underline{f}$  is a tensor valued function of the current stress,  $\underline{g}$ , and the strain increment,  $d\underline{\varepsilon}$ . The principle of material frame indifference (or objectivity) imposes the restriction that  $\underline{f}$  obey the transformation (see equation 14)

$$\underline{Q} \underline{f}(\underline{g}, d\underline{\varepsilon}) \underline{Q}^T = \underline{f}(\underline{Q} d\underline{\varepsilon} \underline{Q}^T, \underline{Q} \underline{g} \underline{Q}^T) \quad (88)$$

for any rotation,  $\underline{Q}$ , of the spatial reference frame. When  $\underline{f}$  satisfies the stipulation of equation 88, it is known as a hemitropic function of  $\underline{g}$  and  $d\underline{\varepsilon}$ . A polynomial representation of  $\underline{f}$  can be expressed in the form (see, for example, Reference 45, p.256):



$$\begin{aligned}
d\bar{g}' = \bar{f}(\bar{g}, d\bar{\epsilon}) = & \alpha_0 \operatorname{tr}(d\bar{\epsilon}) \bar{\delta} + \alpha_1 d\bar{\epsilon} + \alpha_2 \operatorname{tr}(d\bar{\epsilon}) \bar{g}' + \\
& \alpha_3 \operatorname{tr}(\bar{g}' d\bar{\epsilon}) \bar{\delta} + \frac{1}{2} \alpha_4 (d\bar{\epsilon} \bar{g}' + \bar{g}' d\bar{\epsilon}) + \alpha_5 \operatorname{tr}(d\bar{\epsilon}) \bar{g}'^2 + \\
& \alpha_6 \operatorname{tr}(\bar{g}' d\bar{\epsilon}) \bar{g}' + \alpha_7 \operatorname{tr}(\bar{g}'^2 d\bar{\epsilon}) \bar{\delta} + \\
& \frac{1}{2} \alpha_8 (d\bar{\epsilon} \bar{g}'^2 + \bar{g}'^2 d\bar{\epsilon}) + \alpha_9 \operatorname{tr}(\bar{g}' d\bar{\epsilon}) \bar{g}'^2 + \\
& \alpha_{10} \operatorname{tr}(\bar{g}'^2 d\bar{\epsilon}) \bar{g}' + \alpha_{11} \operatorname{tr}(\bar{g}'^2 d\bar{\epsilon}) \bar{g}'^2, \quad (89)
\end{aligned}$$

where  $\bar{g}'$  is a nondimensional stress ( $\bar{g}/2\mu$ ),  $\mu$  being the Lamé shear modulus of equation 78,  $\alpha_k$  ( $k = 1, 2, \dots, 11$ ) are the eleven constitutive constants, and "tr" denotes the trace operator of a matrix (i.e., the sum of the diagonal terms). The constants  $\alpha_k$  are usually dimensionless analytic functions of the three invariants of  $\bar{g}'$  which are determined by experimentation and by curve fitting.

The general form of the expression in equation 66 can be further classified according to the powers of the dimensionless stress tensor  $\bar{g}'$  occurring on the right hand side of this equation. A hypoelastic body of grade zero is independent of  $\bar{g}'$  (i.e., dependent on  $\bar{g}'^0$ ), and, in this case, equation 89 reduces to

$$d\bar{g}' = \bar{f}(\bar{g}, d\bar{\epsilon}) = \alpha_0 \operatorname{tr}(d\bar{\epsilon}) \bar{\delta} + \alpha_1 d\bar{\epsilon} \quad ; \quad (90)$$

by comparing this equation to equation 99, we find that

$$\alpha_0 = \frac{\lambda}{2\mu} \quad \text{and} \quad \alpha_1 = 1 \quad .$$

Similarly, we can construct a hypoelastic constitutive equation of grade one by including only the terms to the first power of  $\bar{g}'$  in equation 89. The hypoelastic body of grade one is thus represented by

$$\begin{aligned}
d\bar{g}' = \bar{f}(\bar{g}, d\bar{\epsilon}) = & \alpha_0 \operatorname{tr}(d\bar{\epsilon}) \bar{\delta} + \alpha_1 d\bar{\epsilon} + \alpha_2 \operatorname{tr}(d\bar{\epsilon}) \bar{g}' + \\
& \alpha_3 \operatorname{tr}(\bar{g}' d\bar{\epsilon}) \bar{\delta} + \frac{1}{2} \alpha_4 (d\bar{\epsilon} \bar{g}' + \bar{g}' d\bar{\epsilon}),
\end{aligned}$$

and, as we can see, the description can be extended up to grade two with the penalty being the task of having to fit a larger number of parameters  $\alpha_k$  to the experimental data. These parameters must be determined from representative laboratory tests using curve fitting and regression analysis; this procedure often leads to questions of uniqueness because it may be possible to fit more than one set of parameters to a set of laboratory data.

#### F. PLASTICITY

Having outlined the theory used in computing the elastic, or sometimes pseudo-elastic, component of the total strain increment (see equation 68), we now turn to the unarguably more difficult subject of the plastic or irreversible component of strain,  $d\epsilon^P$ . This topic embraces the theory of plasticity, a mathematical tool which until 1952 (Reference 48) remained strictly in the domain of the metal physicist. Over the last thirty years, the role of plasticity in soil mechanics has increased in unison with the functional importance of electronic computers as an engineer's working tool. Nevertheless, plasticity still remains a mystery to many geotechnical engineers, and there is no doubt that a newcomer to this field will encounter some difficulty in sifting through the esoterically written literature on the subject. One of the chief objectives of this section is to provide a feel for plasticity theory by highlighting the fundamental postulates with emphasis on its application to granular material.

## 1. Yield Surface

Perhaps the best place to start talking about plasticity is to introduce, or rather draw attention to, the concept of a yield surface in stress space. To aid in this objective, the following notation is adopted:  $\tau^n$  and  $\sigma^n$  are the shear stress and normal stress components respectively on a plane identified by a unit normal vector  $\underline{n}$ .

In the calculation of the stability of earth structures, geotechnical engineers frequently rely on the Mohr-Coulomb failure envelope drawn in  $\tau^n - \sigma^n$  space. This straight line is a failure surface (or more precisely, a failure curve) drawn in two-dimensional stress space while the particular solution technique is known as limit equilibrium analysis, a method which provides no information on the deformation prior to reaching the critical  $\tau^n/\sigma^n$  ratio. Failure can be interpreted as the limiting combination of shear and normal stresses to cause "unrestrained flow" in a soil mass. Yield (or a yield surface), on the other hand, is the locus of stress component points in stress space that mark the onset of plastic (or irreversible) deformation; this description contrasts with the typical strain off-set definitions used in metal plasticity. Correspondingly, we can construct a yield curve in  $\tau^n - \sigma^n$  space to enclose a domain called the elastic range (i.e., the totality of elastic states in which an infinitesimal change of stress  $d\sigma$  produces no permanent strain  $d\epsilon^p$ ). If we construct a very simple model where we assume the soil to remain elastic until its stress state (i.e.  $\tau^n$  and  $\sigma^n$ ) reaches failure, then the yield curve coincides with the failure curve and we have what is called elastic-perfectly plastic behavior (see figure 5e). Until the anomalies which

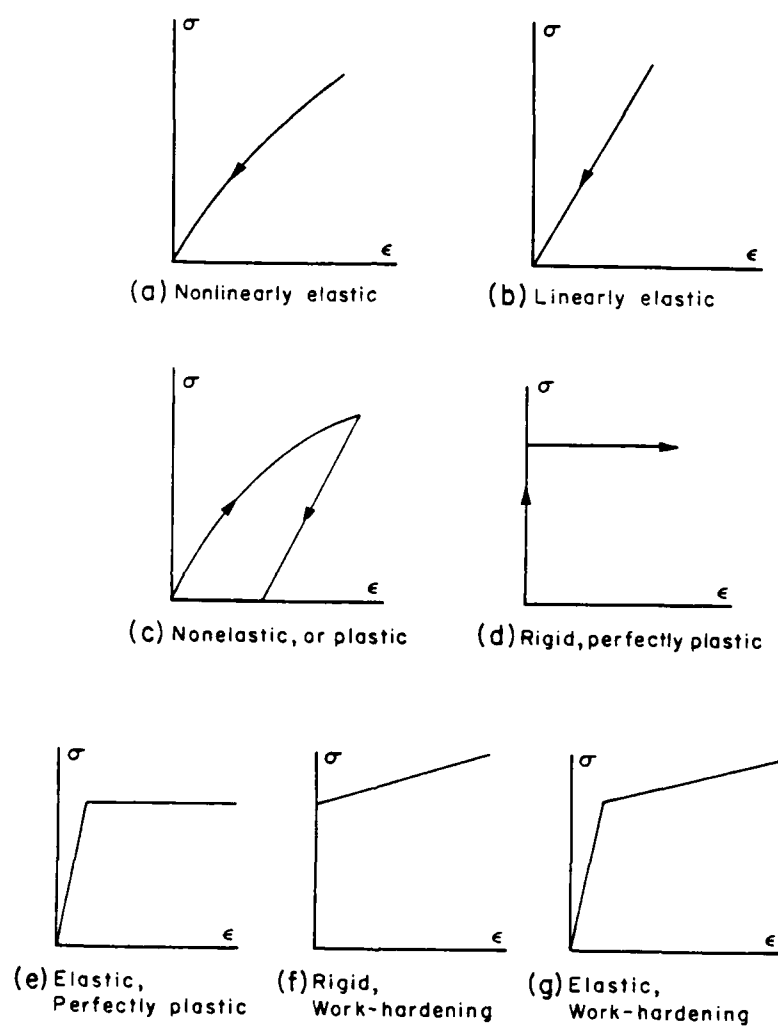


Figure 5. Idealizations of Rate Independent Stress-Strain Behavior.

result from the assumption of yield/failure locii coincidence can be pointed out, it is helpful to think of both these concepts in terms of a single surface.

In section II A.2, we established the fact that the stress state at a point is represented by the nine components of the stress tensor  $\underline{g}$ . Therefore, it is necessary to generalize the representation of the yield/failure surface from this two dimensional picture into a nine-dimensional space. Although such a space need not be regarded as having an actual physical existence, it is an extremely valuable concept because the language of geometry may be applied with reference to it (Reference 22). We can call the set of values  $\sigma_{11}, \sigma_{12}, \sigma_{13}, \sigma_{21}, \sigma_{22}, \sigma_{23}, \sigma_{31}, \sigma_{32}$  and  $\sigma_{33}$  a point, and the variables  $\sigma_{ij}$  the coordinates. The totality of points corresponding to all values of say N coordinates within certain ranges constitute a space of N dimensions denoted by  $V_N$ ; other terms commonly used for  $V_N$  are hyperspace, manifold, or variety.

Before studying the analytical depiction of yield and failure locii in hyperspace, it is advantageous to review the relevant elementary geometric concepts of the familiar Euclidean space of two or three dimensions. If we are concerned with only two coordinates  $\sigma^n$  and  $\tau^n$ , a curve in this space is then specified by a series of connected pairs  $[\tau^n, \sigma^n]$ . The two coordinates of a point in  $V_2$  are given as functions of a real parameter  $u$  ( $a \leq u \leq b$ ); i.e.,

$$\tau^n = f_1(u), \quad \text{and} \quad \sigma^n = f_2(u), \quad (91)$$

where  $f_i(u)$  are the two functions of the parameter "u" used in characterizing the curve. If, for example, we assign the functions  $f_i(u)$  the following forms:

$$f_1 = \tan \phi \ u, \text{ and } f_2 = u, \quad (92)$$

we see that this parametric representation of a portion of the curve plots as a Mohr-Coulomb failure envelope in  $\tau^n - \sigma^n$  space within the limits:  $a \leq \sigma^n \leq b$ . For the general nine dimensional stress space, we can extend this description and define a curve as the totality of points given by the equations

$$\sigma_r = f_r(u) \quad (r = 1, 2, \dots, 9) \quad (93)$$

The parametric representation of a surface in three dimensional space is an extension of the idea of a curve; instead of the dependency of the three coordinate variables on a single constant  $u$ , the points describing a surface are assumed to be functions of two parameters:  $u_1$  and  $u_2$ . A fundamental property of a surface is the division of neighboring portions of space into two parts (such as elastic and plastic regions). Note that, in the definition of a surface, the number of parameters,  $u$ , is one less than the number of space dimensions; this observation allows us to carry the surface definition to nine-dimensional stress space by writing

$$\sigma_r = f_r(u_1, u_2, u_3, \dots, u_8) \quad (r = 1, 2, \dots, 9) \quad (94)$$

where the  $u$ 's are parameters and  $f_r$  are nine functions. By writing out the nine equations expressed indicially in equation 94, one may verify that the eight parameters  $u_i$  ( $i = 1, 2, 3, \dots, 8$ ) can be eliminated to give a single equation of the form

$$F(\sigma_{ij}) = 0 \quad (95)$$

which represents a hypersurface in  $V_9$ . The theoretician is therefore confronted with the task of fitting an analytical function of the type

shown in equation 95 to the experimentally determined locii of stress states which bring about yield or failure.

If an existing testing device had the capability to subject sand specimens to the six independent components of stress, the yield function representation (of equation 95) could be stated in terms of the nine stress components. Unfortunately, such equipment is not available at the present time, and the analytic functions proposed to represent the yield hypersurface of soil are founded on experimental stress-strain data obtained from restrictive classes of test paths (such as the true triaxial device and the conventional triaxial test). These yield/failure surface representations are therefore either generalized to nine-dimensional space or are assumed to model idealized isotropic materials. The latter assumption permits us to state a failure/yield criteria solely in terms of the three principal stresses ( $\sigma_1$ ,  $\sigma_2$ , and  $\sigma_3$  axes), thus, in effect, disregard any directional stiffness or strength properties present in the medium. This leads to an interesting geometrical consequence: in principal stress space, the yield surface may be sketched using a piecewise smooth surface to which we can attach direct physical interpretation of the stress intensity (or stress invariants).

Figure 6 depicts a yield surface in principal stress space. The hydrostatic axis is defined by  $\sigma_1 = \sigma_2 = \sigma_3$  while the other geometric feature of importance, the deviatoric (or octahedral or  $\pi$ ) plane, is specified by the condition that the sum ( $\sigma_1 + \sigma_2 + \sigma_3$ ) be equal to a constant; this plane, it turns out, is perpendicular to the hydrostatic axis. If we perform a constant "p" test (i.e., a mean normal pressure

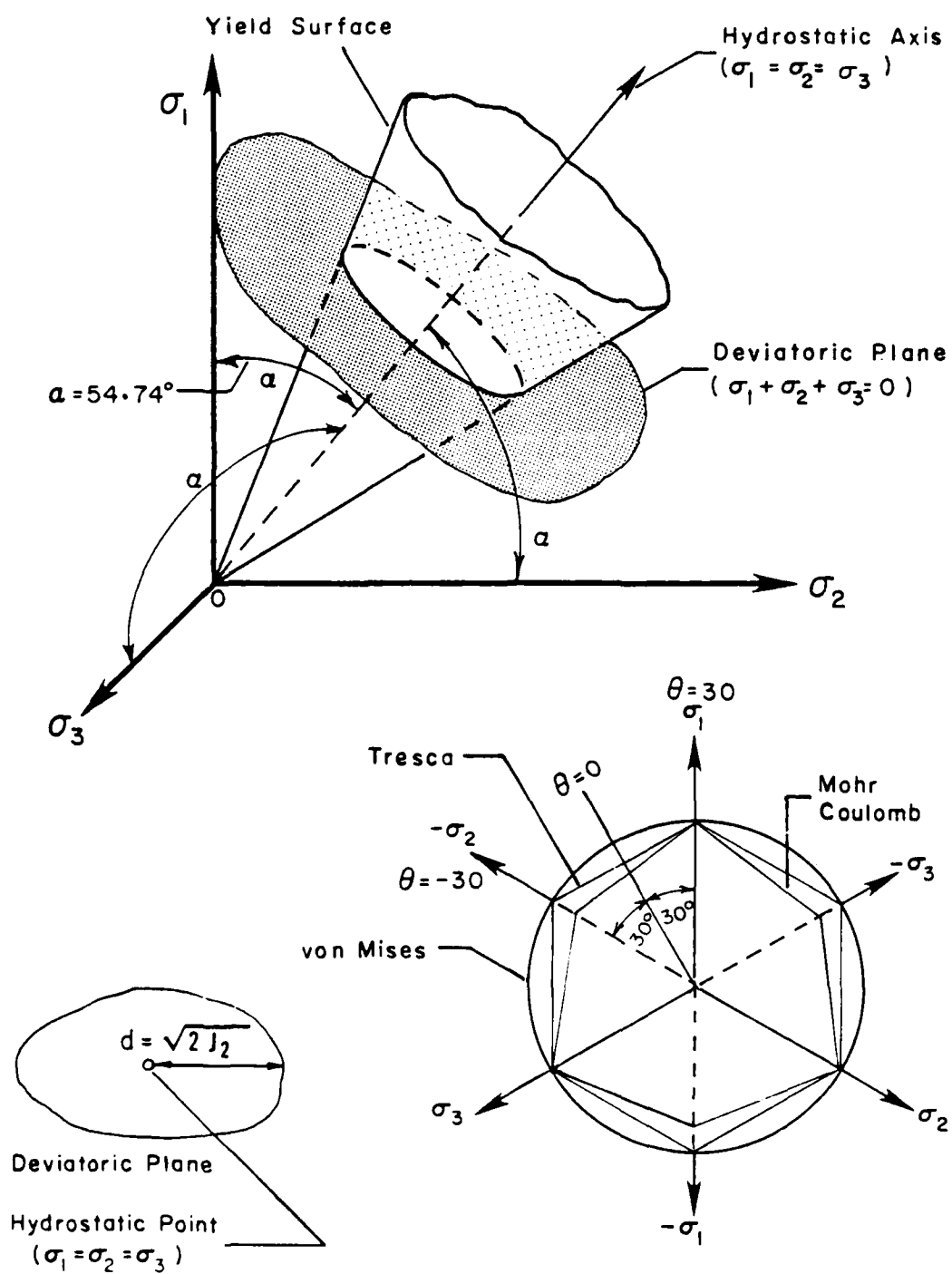


Figure 6. Yield Surface in Heigh-Westergaard Cylindrical Coordinate System.



test, TC or TE of figure 3), the stress point remains on a single deviatoric plane throughout the loading, and this provides a useful method for probing the shape and size of the yield surface's projection on the  $\pi$  plane. The influence of three aspects of loading on the yield/failure criteria is manifest in this Heigh-Westergaard cylindrical coordinate system: a) the shear stress intensity ( $\sqrt{[2J_2]}$ ) is depicted by the length of the vector joining the stress state to the point at which the hydrostatic axis intersects the deviatoric plane; b) the relative magnitude of intermediate principal stress can be calculated directly from the Lode angle  $\theta$  (see equation 37); and finally, c) the effect of confining pressure on the yield/failure of frictional materials is easily visualized by noting the variation in the size and possibly shape of the yield surface's  $\pi$  sections for different levels of mean pressure (or distance along the hydrostatic axis). In summary, we can therefore conveniently put equation 95 in the form  $F(I_1, \sqrt{J_2}, \theta) = 0$  to represent the yield or failure functions for isotropic materials.

The much used Mohr-Coulomb failure criteria (Reference 49) for sand is usually stated as:

$$(\sigma_1 - \sigma_3) + (\sigma_1 + \sigma_3) = \sin \phi, \quad (96)$$

where  $\phi$  is the angle of internal friction. If we combine this equation with equation 41, the yield surface for the Mohr-Coulomb criteria in terms of the stress invariants can be written as:

$$F = \frac{I_1}{3} \sin \phi + \sqrt{J_2} \left\{ \frac{\sin \theta \sin \phi}{\sqrt{3}} - \cos \theta \right\} = 0, \quad (97)$$

and a trace of this surface on the  $\pi$  plane is shown in figure 6. In three-dimensional principal stress space, this yield function plots as an irregular hexagonal pyramid with its apex at the origin for non-cohesive soils. The other two  $\pi$ -plane projections in figure 6 are those of the popular Tresca and Mises yield surfaces used in metal plasticity. Mises (Reference 50) postulated a yield representation of the form

$$F = \sqrt{J_2} - k = 0, \quad (98)$$

where  $k$  is a parameter determining the size of the yield surface (i.e. the yield stress). This criteria says that plastic flow will begin once the load-deformation process produces a critical strain energy of distortion (i.e., the strain energy neglecting the effects of hydrostatic pressure and volume change). On the other hand, Tresca (Reference 51) proposed that the initiation of plastic flow can be correlated to the peak shear stress  $([\sigma_1 - \sigma_3]/2)$ ; by employing equation 41, this maximum shear stress yield criterion may be mathematically expressed as:

$$F = \frac{-1}{\sqrt{3}} \sqrt{J_2} \left[ \sin \left( \theta + \frac{4}{3} \pi \right) - \sin \left( \theta + \frac{2}{3} \pi \right) \right] - k = 0,$$

which simplifies to

$$F = \sqrt{J_2} \cos \theta - k = 0, \quad (99)$$

where  $k$  is again a parameter controlling the size of the yield surface. It is important to note that the functions written in equations 98 and 99 are both independent of the variable  $I_1$  (i.e. the confining pressure) with the implication that yielding is non-frictional. This is, of course, a very unrealistic assumption in the characterization of

drained soil behavior. An approximation to the Mohr-Coulomb law was put forward by Drucker and Prager (Reference 48) as a modification of the Mises yield criterion in the form of a circular cone. For cohesionless soil, this yield function is written as:

$$F = \frac{2 \sin \phi}{\sqrt{3} (3 - \sin \phi)} I_1 - \sqrt{J_2} = 0, \quad (100)$$

where  $\phi$  is the angle of internal friction of the material along a CTC path (see figure 3). Even though the development of the Drucker-Prager yield function was motivated by mathematical convenience, it is widely applied in soil and rock mechanics; however, there is evidence that the Mohr-Coulomb law fits the experimental data better (see, for example, Reference 52).

By examining sketches of the above-mentioned yield criteria and the hydrostatic compression load-unload stress-strain diagram in figure 2, an obvious shortcoming in the soil mechanics application of these yield criteria becomes evident: these yield surfaces are all "open" along the hydrostatic stress axis and will thus predict no plastic strain for loading paths directed out but away from the failure surface. Yet, from the hydrostatic loading plotted in figure 2, we see that considerable irreversible plastic volumetric strain is generated by this stress path. In recognition of this deficiency, Drucker et al. (Reference 53) capped the Drucker-Prager yield surface to reflect the difference between yield and failure in soil. Nowadays, the modern versions of this type of plasticity model are frequently referred to as cap-models (Reference 54).

The development of more sophisticated laboratory equipment and stress-strain data has permitted researchers to refine the functional forms of the yield surface in principal stress space. Using the results of true triaxial tests, Lade and Duncan (Reference 55) have proposed a failure theory which incorporates the third invariant of stress and is written as:

$$F = (I_1^3/I_3) (I_1/p_a)^m - k = 0 , \quad (101)$$

where  $p_a$  is the atmospheric pressure,  $m$  is an exponent explaining deviation from purely frictional response, and  $k$  is a size-controlling parameter of the surface. They also added a spherical cap to this "open-ended" function to account for the yielding during hydrostatic compression.

Matsuoka and Nakai (Reference 56), on the assumption that the shear stress to normal stress ratio reaches a limiting value on the mobilized plane, have derived a quite simple form for the failure criteria for isotropic soils; i.e.,

$$F = \frac{I_1 I_2}{I_3} - k = 0 , \quad (102)$$

where  $k$  assumes the usual role of determining the size of the failure envelope. The mobilized plane concept is a three-dimensional extension of the Mohr-Coulomb criteria which accounts for the influence of intermediate principal stress, and this criteria, together with the Lade surface (equation 101), appear to be gaining wide acceptance as suitable yield/failure criteria for idealized isotropic sands. The Mises, Drucker-Prager, Lade, and Matsuoka surfaces have been shown by

Desai (Reference 57) to be special cases of a completely general third-order polynomial in terms of the stress invariants, and it therefore seems likely that, as more reliable and reproducible stress-strain data becomes available, new failure/yield functions will emerge in the near future.

## 2. Incremental Plastic Stress-Strain Relation

Given a yield surface enclosing an elastic domain, we are now faced with the task of predicting the incremental plastic strain after the stress point penetrates this region. If the yield surface does not coincide with the failure surface, we will expect a finite value of incremental strain when the stress state exits the elastic regime. The subject of this sub-section deals with the computation of the incremental plastic strain or, more generally, the mathematical theory of plasticity. By definition, plasticity theory excludes any influence of the rate of application of stress increment on the predicted plastic strain increment.

In analogy to the flow lines and equipotential lines used in seepage analysis, we can postulate the existence of a plastic potential,  $G$ , in stress space which determines the direction of a plastic strain increment vector,  $d\epsilon^p$ , resulting from a stress increment (Reference 50) ,

$$d\epsilon_{ij}^p = \lambda \frac{\partial G}{\partial \sigma_{ij}} , \quad \lambda > 0 \quad (103)$$

where  $\lambda$  is a scalar factor which controls the magnitude of the generated plastic strain increment and, like the yield/failure

function  $F$ ,  $G$  is a scalar function of stress. Inspection of equation 103 reveals that an isotropic plasticity theory will predict a plastic strain increment vector with principal directions coinciding with those of the stress tensor; recent experimental evidence (Reference 58) indicates that this assumption may not be appropriate for granular materials. The magnitude ( $\lambda$ ) and direction ( $\frac{\partial G}{\partial \sigma_{ij}}$ ) of this plastic strain increment,  $d\epsilon^p$ , depend upon the variables listed in equation 66; i.e., the stress history  $\sigma^t$ , the strain history  $\epsilon^t$ , and any internal variables of significance. Up to this point, three problem statements of plasticity theory have been put forth: a) the determination of the scalar factor  $\lambda$  for computing the magnitude of the strain increment, b) the so-called flow rule or direction of the strain increment vector based on the gradient of a scalar function,  $G$ , constructed in stress space, and c) the representation of the yield surface in stress space. The yield surface concept has already been described so we will continue here by first discussing the plastic flow direction and then lead into the methodology used for calculating the scalar factor  $\lambda$ .

Geometrically, the flow rule can be interpreted as equating the strain increment vector to the exterior normal of a proposed plastic potential; conversely, we can view it as the superposition of experimentally determined plastic strain increment vectors in stress space followed by a back calculation to give a potential function such that the strain increment vectors lie normal to this contrived surface.

Mises (Reference 50) made the assumption that the yield surface and the plastic potential coincide; i.e.,

$$d\epsilon_{ij}^P = \lambda \frac{\partial F}{\partial \sigma_{ij}} , \quad (104)$$

and this suggests a strong connection between the flow law and the yield criterion. When this assumption is made, the flow rule is called associated (i.e., the normality rule), but, if we do not insist upon associating the plastic potential with the yield function (Reference 59), the flow rule is termed non-associated. The implications of the normality rule, it turns out, are far reaching, and it is perhaps best to provide some insight into the structure of the incremental plastic stress-strain relation by summarizing Prager's (Reference 60) treatment of the subject. Essentially, Prager has formulated stipulations, which are to be used in conjunction with the axioms of constitutive theory, to establish admissible plastic stress-strain relations.

The first assumption is designed to preclude the effects of rate of loading, and it says that the constitutive equation

$$d\epsilon^P = d\hat{\epsilon}^P(\underline{\sigma}, d\underline{\sigma}, \underline{g}_n) ,$$

must be homogenous of degree one in the stress increment  $d\underline{\sigma}$ . Recall that homogeneity of order  $n$  ensures that

$$d\epsilon^P = d\hat{\epsilon}^P(\underline{\sigma}^t, \Lambda d\underline{\sigma}, \underline{g}_n) = \Lambda^n d\hat{\epsilon}^P(\underline{\sigma}^t, d\underline{\sigma}, \underline{g}_n), \quad (105)$$

where  $\Lambda$  is a positive constant.

A simple example will clarify this seemingly complex mathematical statement: suppose that an axial stress increment of 1 psi produced a plastic strain increment of .01 % in the axial direction; this means

that if  $\Lambda$  is equal to say 2, a stress increment of 2 psi ( $\Lambda \times 1$  psi) will predict a plastic strain increment of .02% ( $\Lambda \times .01\%$ ). Ideally then, our solution should be independent of the stress increment provided the stiffness change during the stress increment is negligible. A very important particular case of equation 105 is when the function  $\hat{d}\epsilon^p$  is linear; the linearity assumption allows us to write the incremental plastic stress-strain relation in the form

$$d\epsilon_{ij}^p = D_{ijkl} d\sigma_{kl} , \quad (106)$$

where  $\underline{D}$  is a fourth order plastic compliance tensor function of the stress history  $\underline{g}^t$ ,  $n$  plastic internal variables  $q_n$ , and  $m$  discrete memory parameters  $\xi_m$ . In a general sense, the linearity assumption states that if all  $d\sigma_{kl}$  are increased in ratio, all  $d\epsilon_{kl}^p$  are increased in the same proportion.

The second assumption, the condition of continuity, is intended to eliminate the possibility of jump discontinuities in the stress-strain curve as the material's stress state either penetrates the elastic domain (i.e., the yield hypersurface) from within or is unloaded from a plastic state back into the elastic regime. To guarantee a smooth transition from elastic response to elastic-plastic response and vice-versa, a limiting stress vector,  $d\mathbf{g}^t$ , tangential to the exterior of the yield surface should develop no plastic strain increment. The mathematical constraint which results from the satisfaction of this requirement will now be examined. Let us start by assuming that a current stress state,  $\underline{g}$ , lies on the yield surface (i.e., it satisfies the condition  $F(\underline{g}) = 0$ ). An infinitesimal change of stress,  $d\mathbf{g}$ , from



this plastic state [ $F(\underline{g}) = 0$ ] may lead to either of three possible situations:

$$a). \text{ an elastic state (unloading) } \quad \frac{\partial F}{\partial \underline{g}} : d\underline{g} < 0, \quad (107)$$

$$b). \text{ no permanent strain (neutral loading) } \quad \frac{\partial F}{\partial \underline{g}} : d\underline{g} = 0, \quad (108)$$

or

$$c). \text{ permanent strain (loading) } \quad \frac{\partial F}{\partial \underline{g}} : d\underline{g} > 0 \quad (109)$$

where the notation ":" is the double contraction operator (see, for instance, Reference 17) such that the scalar product  $\frac{\partial F}{\partial \sigma_{ij}} d\sigma_{ij}$  is compactly written as  $\frac{\partial F}{\partial \underline{g}} : d\underline{g}$ . Next, we decompose an arbitrary stress

increment,  $d\underline{g}$ , into its components normal ( $d\underline{g}^n$ ) and tangential ( $d\underline{g}^t$ ) to the yield surface

$$d\underline{g} = d\underline{g}^t + d\underline{g}^n.$$

The continuity condition states that the tangential component,  $d\underline{g}^t$ , constitutes a neutral loading, and, hence, does not produce any plastic strains. Consequently, the plastic strain increment magnitude,  $|d\underline{\epsilon}^p|$ , is entirely dependent on the magnitude of the normal component of  $d\underline{g}$  so we may write

$$|d\underline{\epsilon}^p| \propto d\underline{g} : \underline{n} = d\underline{g} : \nabla F / |\nabla F|, \quad (110)$$

where  $\underline{n}$  is the unit normal vector to the hypersurface taken in the direction of increasing  $F$ , and  $\nabla$  is the symbolic operator del which when placed to the left of a scalar function such as  $F(\underline{g})$  denotes the gradient tensor  $\frac{\partial F}{\partial \underline{g}}$ .

In his presentation of the restrictions imposed by the uniqueness condition, Prager (Reference 60) made use of the following boundary value problem: given the instantaneous mechanical state in a body together with a system of infinitesimal increments of surface tractions, find the corresponding stress increments throughout the body. It is then reasonable to demand that plasticity theory predict a unique solution to the problem, but let us assume that the boundary value problem admits two solutions. Say these two solutions resulted in a difference between the stress increments at a given point of the body equal to  $\Delta(d\sigma)$ , and likewise, differences in elastic and plastic strain increments equal to  $\Delta(d\varepsilon^e)$  and  $\Delta(d\varepsilon^p)$  respectively. Now, the two solutions correspond to the same increment of surface tractions, so by the principle of virtual work, we expect the work done on the body (of volume  $V$ ) will be the same for both solutions; i.e.,

$$\int_V [ \Delta(d\sigma) : \{ \Delta(d\varepsilon^e) + \Delta(d\varepsilon^p) \} ] dV = 0 , \quad (111)$$

which means that the integrand must be positive definite. By virtue of Hooke's law, the quantity

$$\Delta(d\sigma) : \Delta(d\varepsilon^e)$$

will always be positive definite so the uniqueness condition reduces to one of showing

$$\Delta(d\sigma) : \Delta(d\varepsilon^p) \quad (112)$$

is positive definite. In the investigation of equation 112, three possible cases must be considered: 1) both solutions result in unloading, 2) both solutions constitute loading, and 3) one solution is an unloading event while the other is a loading process. In the first case,  $d\varepsilon^p$  is zero for both solutions and equation 112 vanishes

trivially. To investigate the second case, we label the two "loading" solutions  $d\bar{g}^{(1)}$  and  $d\bar{g}^{(2)}$  and impose the restriction that the plastic strain increment direction be such that equation 112 is always positive. The limiting scenario occurs when  $d\bar{g}^{(1)}$  and  $d\bar{g}^{(2)}$  are both tangential to the yield surface but directed in an opposite sense; then the only way equation 112 will be positive is if the plastic strain increment is directed along the outward normal to the yield surface. The arguments for case 2 parallel those for case 3, and we can thus conclude that a sufficient condition for uniqueness of a boundary value problem is that the flow rule be associated and that normality of the plastic strain increment apply; that is,

$$d\bar{\epsilon}_{ij}^p \propto \frac{\partial F}{\partial \sigma_{ij}} . \quad (113)$$

By combining the results of: a) the linearity assumption (equation 106), b) the continuity condition (equation 110), and c) the uniqueness condition (equation 113), we can derive the flow rule as:

$$d\bar{\epsilon}^p = \frac{1}{K_p} \frac{\nabla F}{|\nabla F|} \left\{ \frac{\partial F}{\partial \bar{g}} : d\bar{g} \right\} , \quad K_p > 0 \quad (114)$$

where  $K_p$  is a positive scalar quantity known as the generalized plastic modulus; also, this equation applies only when  $F(\bar{g}) = 0$  and a loading event is in process (i.e., equation 109 is satisfied). For non-associative flow, equation 114 can be modified to

$$d\bar{\epsilon}^p = \frac{1}{K_p} \frac{\nabla G}{|\nabla G|} \left\{ \frac{\partial F}{\partial \bar{g}} : d\bar{g} \right\} , \quad K_p > 0 . \quad (115)$$

The quantity

$$L = \frac{1}{K_p} \left\{ \frac{\partial F}{\partial g} : dg \right\} \quad (116)$$

is frequently separated from equations 114 and 115 and is termed the loading function,  $L$  (Reference 4); this separation means that the flow rule may now be condensed to

$$d\epsilon_{ij}^p = L m_{ij} \quad , \quad (117)$$

where  $m_{ij}$  are the components of the unit tensor gradient to the plastic potential  $G$ .

The generalized plastic modulus,  $K_p$ , can be considered as a plastic conjugate to the elastic modulus,  $E$ , which controls the stiffness of the incremental plastic response. In plasticity theory, we must also consider how the magnitude of the scalar  $K_p$  changes with the plastic internal variables  $q_n$  (PIVs). As the stress point penetrates the initial yield surface and moves outward, we can model continued plastic behavior by postulating that this yield surface either: a) undergoes a size change, b) translates, c) rotates, d) changes its shape, or e) experiences any combination of the four previous postulates, such that, after the deformation, the surface satisfies the condition  $F(g + dg) = 0$ . In other words, the stress state went from one plastic state  $[F(g)=0]$  to another plastic state  $[F(g + dg) = 0]$ , and when this requirement is met, the consistency condition is said to be satisfied during plastic flow. This type of behavior is known as work hardening and idealized examples of such response are shown in figures 5f and 5g. This subject is treated separately in the subsection which immediately follows. The various postulates for the expansion, translation, etc. of

the yield surface are called hardening laws, and further discussion of this subject will also be postponed to a later subsection.

We can take two different approaches to obtain the functional relation between plastic modulus and loading history. The first method is simply demonstrated by coupling the stress with the plastic internal variables and writing  $F(\underline{g}, q_n) = 0$ . The consistency condition therefore requires that

$$dF = \frac{\partial F}{\partial \sigma_{ij}} d\sigma_{ij} + \frac{\partial F}{\partial q_n} dq_n = 0 \quad , \quad (118)$$

and if we single out the plastic strain tensor,  $\underline{\epsilon}^p$ , as our only PIV, then we can rewrite the consistency condition as:

$$dF = \frac{\partial F}{\partial \sigma_{ij}} d\sigma_{ij} + \frac{\partial F}{\partial \epsilon_{ij}^p} d\epsilon_{ij}^p = 0 \quad . \quad (119)$$

Substitution of equation 114 into equation 119 leads to

$$dF = \frac{\partial F}{\partial \underline{g}} : d\underline{g} + \frac{\partial F}{\partial \underline{\epsilon}^p} : \frac{1}{K_p} \frac{\nabla F}{|\nabla F|} \left\{ \frac{\partial F}{\partial \underline{g}} : d\underline{g} \right\} = 0$$

from which one observes

$$K_p = - \frac{\partial F}{\partial \underline{\epsilon}^p} : \frac{\nabla F}{|\nabla F|} \quad , \quad (120)$$

which completes the specification of the flow rule. The task of calibrating the plastic stress-strain relation is therefore one of fitting the experimental stress-strain data to obtain the variation of  $F$  with  $\underline{\epsilon}^p$  for use in equation 120. An approach of this type is discussed in some detail in section IV.

The second option for finding the plastic modulus as a function of stress history is to assume that there are a field of nesting (i.e., non-intersecting) yield surfaces in stress space, each of which has a

plastic modulus associated with it (References 61 and 62). Depending upon the loading, a yield surface will translate and/or change its size such that its resulting motion may engage an interior or exterior yield surface which has its own unique set of plastic modulus parameters. In this way, the plastic modulus can vary to reflect the loading history. A model of this type is also discussed in some detail in section III.

Although it will not be pursued here, Prager (Reference 60) also derived the consequences which result from the condition of irreversibility, a fundamental assumption in plasticity theory. From the thermodynamic standpoint, the condition of irreversibility requires a positive rate of entropy production, and an in-depth discussion of this topic, as it relates to soil media, can be found in Jain (Reference 26). More general descriptions of plasticity and thermodynamics considerations can be found in a series of papers by Lubliner (see, for instance, Reference 63).

### 3. Drucker' Stability Postulate

With the mention of work hardening in the previous subsection, it is appropriate to now introduce one of the cornerstones of modern plasticity theory: Drucker's stability postulates.

The meaning of work hardening in the case of a simple axial compression test is just that the stress is a monotonically increasing function of strain which implies that the deformation is stable. Drucker (Reference 1) observes that the definition of work hardening is not a simple picture for more general states of stress and paths of loading where some components of stress may increase while others may

decrease. He then advanced the definition of material stability in terms of the work done by the stress increment on the plastic strain increment. In his 1950 paper, Drucker defines work hardening in the following manner. Consider a material element in which a homogenous state of stress  $\underline{g}$  and strain  $\underline{\epsilon}$  exists. Let an external agency, entirely separate and distinct from the agency which caused the existing state of stress and strain, apply small surface tractions which alter the stress at each point by  $d\underline{g}$  and produce corresponding small strain increments  $d\underline{\epsilon}$ . Next assume that this external agency slowly removes the added surface tractions thus relieving the elastic strain increments  $d\underline{\epsilon}^e$ . Stability implies that positive work is done by the external agency during the application of the set of stresses, or

$$d\underline{g} : d\underline{\epsilon} > 0 , \quad (121)$$

and also, the net work performed by it over the cycle of application and removal is zero or positive; mathematically, this means that

$$d\underline{g} : (d\underline{\epsilon} - d\underline{\epsilon}^e) = d\underline{g} : d\underline{\epsilon}^p \geq 0. \quad (122)$$

It is emphasized that the work referred to is not the total work done by all the forces acting, but it is only the work done by the added set on the displacements which result. The latter postulate (equation 122) can be rephrased to read: work hardening means that useful energy over and above the elastic energy cannot be extracted from the material and the system of forces acting upon it. Upon examination of equation 122 (which is commonly referred to as "stability in the small"), one can immediately conclude that this postulate implies normality of  $d\underline{\epsilon}^p$  to the yield surface. Drucker (Reference 64) extended his postulates by considering the external

agency to apply a finite set of surface tractions to the body with its initial stress state  $\underline{g}^*$  residing within the yield surface at a reference time zero. The external agency first causes the stress state to move to a point,  $\underline{g}$  (at time  $t$ ), exactly on the yield surface; it then gives rise to an infinitesimal loading increment  $d\underline{g}$  (with a corresponding  $d\underline{\epsilon}^p$ ), over an arbitrarily short interval  $\Delta t$ , which now moves the point to a neighboring point outside or on the initial yield surface. Finally, the external agency removes the stress increment  $d\underline{g}$  and returns to  $\underline{g}^*$  (at time  $t^*$ ) along an elastic path. The net work done ( $dW_{net}$ ) by the external agency over the cycle is assumed to be positive and it is equal to the total work during the cycle ( $dW_t$ ) minus the work ( $dW_o$ ) that would be done during the cycle by the initial stress  $\underline{g}^*$ ; i.e.,

$$dW_t = \int_0^t (\underline{g} : d\underline{\epsilon}^e) dt + \int_t^{t+\Delta t} [\underline{g} : (d\underline{\epsilon}^e + d\underline{\epsilon}^p)] dt + \int_{t+\Delta t}^{t^*} (\underline{g} : d\underline{\epsilon}^e) dt \quad (123)$$

However, the net elastic work during the cycle is zero so equation 123 simplifies to

$$dW_t = \int_t^{t+\Delta t} (\underline{g} : d\underline{\epsilon}^p) dt \quad (124)$$

and similarly, we can show

$$dW_o = \int_t^{t+\Delta t} (\underline{g}^* : d\underline{\epsilon}^p) dt \quad (125)$$

Therefore,

$$dW_{net} = dW_t - dW_o = \int_t^{t+\Delta t} [(\underline{g} - \underline{g}^*) : d\underline{\epsilon}^p] dt > 0 \quad (126)$$



and so by Drucker's definition, the following must hold

$$(\underline{g} - \underline{g}^*):d\underline{\epsilon}^P > 0 \quad . \quad (127)$$

With equation 127 (otherwise known as "stability in the large"), convexity of the yield surface can be demonstrated as follows. To satisfy the inequality in equation 127, all vectors  $\underline{g} - \underline{g}^*$  must lie to one side of the hyperplane which is normal to the strain increment vector  $d\underline{\epsilon}^P$ ; this must hold for all points on the yield hypersurface, thus immediately proving that the yield surface is convex. This completes our discussion of Drucker's stability postulate and we now turn our attention to the questions concerning the suitability of the normality rule in soil plasticity.

#### 4. Applicability of the Normality Rule To Soil Mechanics

Jain (Reference 26) concludes that the normality rule applies to materials which are: a) incompressible and their strength is not a function of confining pressure, b) rigid plastic or elastic-perfectly plastic, and c) cohesive. "Standard" materials are categorized as those which follow the normality rule while "non-standard" materials do not follow this rule. The undrained behavior of saturated normally consolidated clays can be considered sufficiently close to "standard" materials. There are, however, two ways in which non-standard materials can make use of the normality rule: the first consists of using a non-associative flow law (equation 115) with the added complexity of finding a plastic potential surface  $G$ , while the second approach of non-associative soil plasticity takes into account any deviation from a

"standard" material by modifying the plastic strain increment vector (i.e., the components  $\frac{\partial F}{\partial \sigma}$  of the normality equation). For this second

alternative, observe from equation 104 that the incremental plastic volumetric strain ( $d\epsilon_{kk}^p$ ) and the incremental plastic deviatoric strain tensor  $d\epsilon_{ij}^p$  may be written respectively as follows:

$$d\epsilon_{kk}^p = \lambda \frac{\partial F}{\partial \sigma_{kk}} \quad (128)$$

and

$$d\epsilon_{ij}^p = \lambda \frac{\partial F}{\partial s_{ij}} \quad (129)$$

In order to bring the analytical result for a "non-standard" material in agreement with the experimental observations, the volumetric component  $d\epsilon_{kk}^p$  must be modified by a factor  $A_1$  and the deviatoric components  $d\epsilon_{ij}^p$  by a factor  $A_2$ ; equations 128 and 129 could then be put in the forms

$$d\epsilon_{kk}^p = \lambda A_1 \frac{\partial F}{\partial \sigma_{kk}} \quad (130)$$

and

$$d\epsilon_{ij}^p = \lambda A_2 \frac{\partial F}{\partial s_{ij}} \quad (131)$$

To clarify the influence of the factors  $A_1$  and  $A_2$ , equations 130 and 131 may specifically be written for the 'triaxial' environment or p-q subspace as:

$$\frac{dv^p}{v} = \lambda A_1 \frac{\partial F}{\partial p} \quad (132)$$

and

$$d\epsilon^p = \frac{2}{3} (d\epsilon_1 - d\epsilon_3) = \lambda A_2 \frac{\partial F}{\partial q} \quad (133)$$

where  $dv^p/v$  is the plastic volume strain and  $d\bar{\epsilon}^p$  is called the plastic equivalent shear strain. A geometric interpretation of equations 124 and 126 is sketched in figure 7. Figure 7a corresponds to the normality rule (i.e.,  $A_1 = A_2 = 1$ ) and figure 7b shows how the volumetric and deviatoric components are modified to change both the magnitude and direction of the resulting plastic strain increment vector. An important consequence of this latter modification is that it results in a non-symmetric incremental compliance matrix (the  $\underline{D}$  matrix of equation 106). Finally, figure 7c illustrates how the magnitude of the plastic strain increment vector may be changed without altering its direction; this is accomplished by setting  $A_1 = A_2 = A$  such that  $A$  is not equal to unity.

Restrictions on the selection of the two factors  $A_1$  and  $A_2$  imposed by stability considerations (of the previous sub-section) have been discussed by Jain (Reference 26), and, he concludes that the modifying factor  $A_2$  must be positive whereas  $A_1$  may take a negative value. Examples of models where these parameters have been employed can be found in the papers by Sture et al. (Reference 65) and Prevost (Reference 7).

## 5. Hardening Rules for Soils

Having reviewed the concepts regarding: a) the initial yield surface, b) the plastic flow laws, and c) the work hardening implications, we complete our discussion of the basic precepts of plasticity theory by surveying the analytical methods used to update the size, the shape, and the location of subsequent yield surfaces during

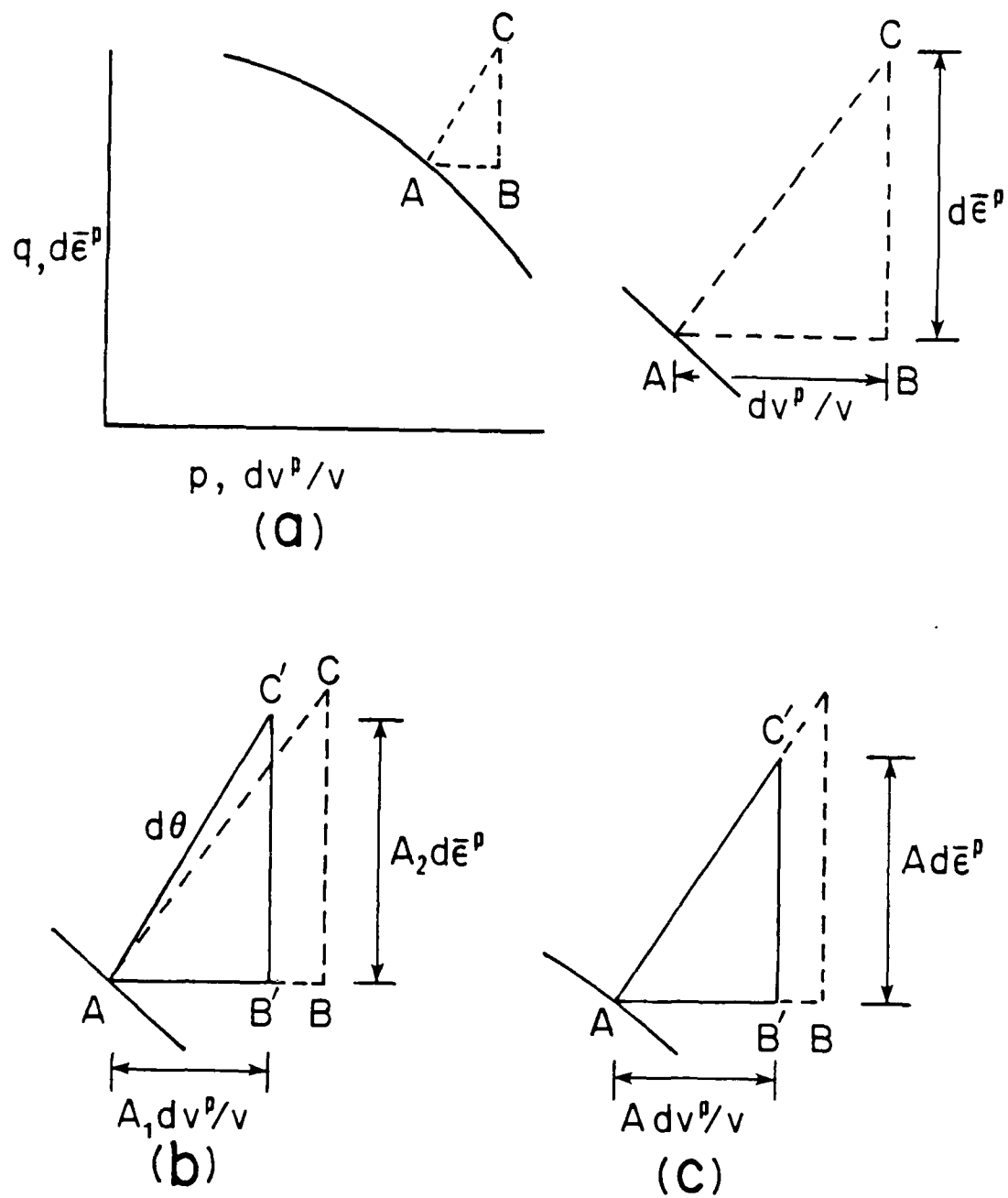


Figure 7. Diagrams Illustrating the Modifying Effects of the Coefficients  $A_1$  and  $A_2$ : (a)  $A_1 = A_2 = 1$ ; (b)  $A_1 \neq A_2$ ; (c)  $A_1 = A_2 = A$  (Reference 26).

work hardening. It is the theoretician's objective to postulate a hardening law (i.e., position/size/shape change of the yield surface) which reflects as closely as possible the history of the deformation. The geometrical properties of a yield surface or a field of surfaces should characterize the current mechanical state of the medium and reflect its loading history.

Let us continue our discussion by denoting the center of a yield surface with the symbol  $\xi$  and by assuming that its size is controlled by the parameter  $k$ , a mathematical equivalent to, say, the radius of a circle. If we adopt the approach suggested in equation 119 to determine the plastic modulus, and disregard the possibility of any shape changes, the yield function can be written in the form

$$F(\underline{g}, \xi, k, q_n) = 0 \quad , \quad (134)$$

where  $q_n$  are the plastic internal variables. For this particular case, the consistency condition will therefore be stated as:

$$dF = \frac{\partial F}{\partial \underline{g}} : d\underline{g} + \frac{\partial F}{\partial \xi} : d\xi + \frac{\partial F}{\partial k} dk + \frac{\partial F}{\partial q_n} dq_n = 0 \quad . \quad (135)$$

Alternatively, if the field of work hardening moduli (or nesting yield surfaces) model is chosen, there is no need to include  $q_n$  as an independent variable in  $F$  since the consistency condition, per se, will not be used to determine the plastic modulus. However, the consistency condition must still be invoked to ensure that the stress point moves to another plastic state ( $F = 0$ ) as the yield surface translates and changes its size. For this type of model, the consistency condition is stated as:

$$dF = \frac{\partial F}{\partial \underline{g}} : d\underline{g} + \frac{\partial F}{\partial \xi} : d\xi + \frac{\partial F}{\partial k} dk = 0 \quad . \quad (136)$$

AD-A162 348

GENERALIZED PHENOMENOLOGICAL CYCLIC  
STRESS-STRAIN-STRENGTH CHARACTERIZATI  
GAINESVILLE DEPT OF CIVIL ENGINEERING  
D SEEREERAM ET AL 27 JUN 85

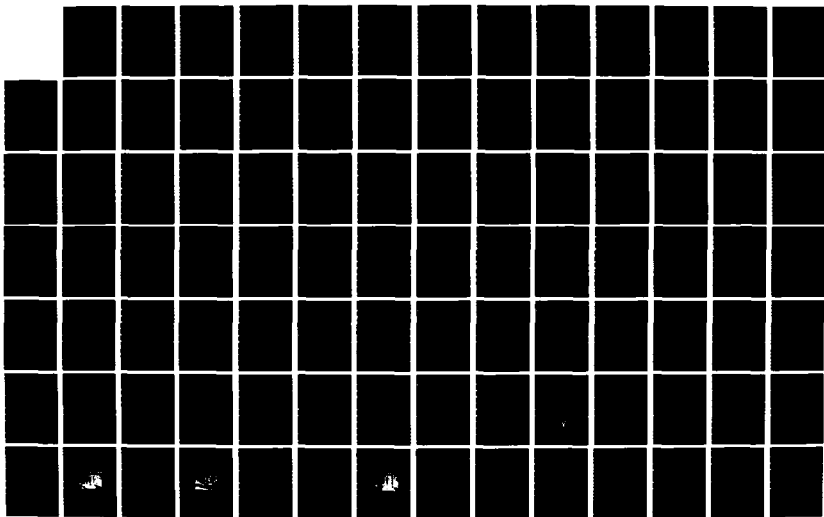
(U) FLORIDA UNIV

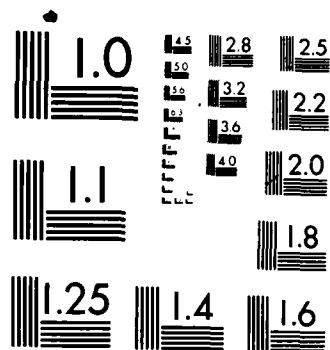
2/3

UNCLASSIFIED

F/G 8/13

NL





MICROCOPY RESOLUTION TEST CHART  
NATIONAL BUREAU OF STANDARDS-1963-A

The simplest work hardening assumption is known as isotropic hardening (Reference 66). In this type of hardening the yield surface is assumed to maintain its shape while only its size may change. This assumption eliminates the translation term,  $\frac{\partial F}{\partial \xi} : d\xi$ , in equation 135, and, in addition, it may be assumed that the size modification is solely a function of the plastic deformation (i.e., plastic strain or plastic work). These postulates form the basis for the critical state model (or density hardening) in soil mechanics (Reference 67); in geotechnical engineering parlance, this is the familiar void ratio (or volume strain) versus the logarithm of the effective confining pressure plot ( $e$  vs.  $\log p'$ ). Here, we assume the size of the yield surface is a function of the plastic void ratio ( $e^p$ ), and using the consistency condition

$$dF = \frac{\partial F}{\partial g} : dg + \frac{\partial F}{\partial k} \frac{\partial k}{\partial e^p} de^p = 0, \quad (137)$$

we obtain the expression for the plastic modulus (see equation 120) in the form

$$K_p = \frac{\partial F}{\partial k} \frac{\partial k}{\partial e^p} (1+e) \frac{1}{|V_F|} \text{tr}(V_F). \quad (138)$$

This class of hardening models is applicable to clays under monotonic loading, and the Cam-clay model (Reference 67) and the cap model (Reference 54) are examples of this particular formulation. These models differ only in the form of the yield function. The disadvantage of this model lies in its inability to simulate cyclic loading, dilatancy, and hardening due to shear strains. The last two shortcomings can be mitigated by the use of combined hardening



(deviatoric and density), a class of hardening not covered in this section but treated fairly extensively in section IV.

For monotonic loading processes, the isotropic hardening model can be successfully applied to the solution of boundary value problems; however, for cyclic loading events, where hysteretic phenomena are of essential importance, the isotropic hardening model does not provide an accurate description. The isotropically hardening surface is usually defined by a large offset value and its interior domain is regarded as elastic. If after initial preconsolidation of a soil specimen, the stress is slightly decreased, reverse plastic flow is experimentally observed with the result that the unload stress-strain curve departs significantly from the elastic curve. In order to account for this effect, Prager (Reference 12) introduced his concept of kinematic hardening in which the center of the yield surface is assumed to translate in the direction of the plastic strain increment vector ( $d\epsilon^P$ ). In the application of this hardening rule, a problem arises: although the yield surface remains rigid in stress space, it may not appear rigid in subspaces. To overcome this difficulty, Ziegler (Reference 68) proposed that the surface translates in the direction of a vector from the center of the yield surface to the loading point [i.e.,  $d\xi \propto (\sigma - \xi)$ ]. Based on experimental observations however, Phillips (Reference 69) has postulated that the yield surface translates in the direction of the stress increment (i.e.,  $d\xi \propto d\sigma$ ). The possible variations on the hardening law are endless, and, for additional discussion of research on hardening, the reader is referred to Naghdi (Reference 15).

Among the topics omitted in this section are the Mroz kinematic hardening rule (Reference 61) and the bounding surface concept (Reference 4). These topics were omitted not because of any lack of importance to soil plasticity; on the contrary, their consideration is central to the presentation of the current research. Accordingly, one of the more sophisticated anisotropic hardening rules is presented in the section immediately following, while the bounding surface philosophy is deferred to section IV.

#### 6. Incremental Elasto-Plastic Stress-Strain Relation

When elastic and plastic strain increments are occurring simultaneously, the constitutive equations must be organized in a compact but general form for computational purposes. The equation for the total strain increment (equation 68) is written as:

$$d\epsilon = d\epsilon^e + d\epsilon^p ,$$

and if our test simulation is stress-controlled (i.e.,  $d\sigma$  is known), we can compute the total strain increment by first combining equations 80 and 81 to obtain the elastic strain increment as:

$$\begin{aligned} d\epsilon_{ij}^e &= d\epsilon_{ij}^e + d\epsilon_{mm}^e \delta_{ij} \\ &= (ds_{ij} + 2G) + \frac{1}{3} (d\sigma_{kk} + 3K) \delta_{ij} . \end{aligned} \quad (139)$$

In tensor notation, we may rewrite equation 139 in the form

$$d\epsilon^e = \underline{D}^e d\sigma , \quad (140)$$

where  $\underline{D}^e$  is the fourth order, incremental elastic compliance tensor.

Equation 140 can then be combined with equation 115 to yield the

expression which can be used to directly compute the total strain increment for a stress controlled test

$$d\epsilon = \underline{D}^e d\sigma + \frac{1}{K_p} \frac{\nabla G}{|\nabla G|} \left\{ \frac{\partial F}{\partial \sigma} : d\sigma \right\} . \quad (141)$$

If, however, a strain controlled test was being simulated, the inverse relation of equation 141 will be needed. The algebraic operations in inverting the stress-strain relation of equation 141 can be carried out by first multiplying both sides of equation 141 by the inverse of the  $\underline{D}^e$  matrix; i.e.,

$$(\underline{D}^e)^{-1} d\epsilon = d\sigma + (\underline{D}^e)^{-1} \frac{1}{K_p} \frac{\nabla G}{|\nabla G|} \left\{ \frac{\partial F}{\partial \sigma} : d\sigma \right\} , \quad (142)$$

and if we replace  $\frac{\nabla G}{|\nabla G|}$  by the unit tensor  $\underline{m}$ ,  $K_p/|\nabla F|$  by the symbol  $K'_p$ , the normalized gradient to the yield function by  $\underline{n}$ , and  $(\underline{D}^e)^{-1}$  by the incremental elastic stiffness tensor  $\underline{C}^e$ , we can compactly rewrite equation 142 as:

$$\underline{C}^e d\epsilon = d\sigma + \underline{C}^e \frac{1}{K'_p} \underline{m} \{ \underline{n} : d\sigma \} . \quad (143)$$

The next step is to multiply both sides of equation 143 by the tensor  $\underline{n}$  as shown below

$$\underline{n} : \underline{C}^e d\epsilon = \underline{n} : d\sigma + \underline{n} : \underline{C}^e \frac{1}{K'_p} \underline{m} \{ \underline{n} : d\sigma \} ,$$

and from this equation we find

$$\frac{1}{K'_p} \underline{n} : d\sigma = \frac{\underline{n} : \underline{C}^e d\epsilon}{K'_p + \underline{n} : \underline{C}^e : \underline{m}} \quad (144)$$

Substitution of equation 144 into 143 gives

$$\underline{C}^e d\epsilon = d\sigma + \frac{(\underline{C}^e : \underline{m}) (\underline{n} : \underline{C}^e)}{K'_p + (\underline{n} : \underline{C}^e : \underline{m})} d\epsilon ,$$

from which we easily see

$$d\bar{g} = \left[ \bar{C}^e + \frac{(C^e : \bar{m}) (\bar{n} : C^e)}{K'_p + (\bar{n} : \bar{C}^e : \bar{m})} \right] d\epsilon \quad . \quad (145)$$

If the flow rule is associated (i.e.,  $\bar{m} = \bar{n}$ ), the stiffness matrix expressed in equation 145 exhibits the major symmetry, but if  $\bar{m}$  is not equal to  $\bar{n}$  (i.e., non-associative flow) the matrix loses its major symmetry and leads to increased computation costs in numerical applications.

### SECTION III

#### ELASTO-PLASTIC ANISOTROPIC HARDENING MODEL OF PREVOST

##### A. INTRODUCTION

The stress-strain behavior of soil is strongly nonlinear, anisotropic, elastoplastic, hysteretic, and path dependent. Although inherently anisotropic materials can be modeled to a certain extent by nonlinear elastic, and isotropically hardening elastic-plastic constitutive models, features such as stress-induced anisotropy in conjunction with rotation of principal stress axes cannot be simulated by these classes of mathematical material models. Alternatively, more general models which merge concepts from isotropic and kinematic plasticity have been developed to realistically simulate the plastic behavior of soil when subjected to complicated three dimensional, and, in particular, cyclic loading paths.

Prevost (Reference 7) has utilized the field of work hardening moduli concept forwarded by Mroz (Reference 61) to develop a set of elasto-plastic anisotropic hardening models for characterizing many categories of soil responses ranging from undrained behavior of saturated clays to drained behavior of sands. In this report, we are only interested in drained behavior of cohesionless soils so we focus strictly on the pressure sensitive version of Prevost models.

## B. FIELD OF WORK HARDENING MODULII CONCEPT

An understanding of the field of work hardening moduli concept is a fundamental prerequisite to any discussion on the anisotropic hardening theories used in modeling soil behavior. This concept is most simply explained by considering the case of a mean normal pressure 'triaxial' test on a plastically incompressible isotropic material (such as the undrained behavior of soil using stress paths TC or TE of figure 3); here, we need only be concerned with the yield surface's projection on the octahedral plane in principal stress space. Suppose we now carry out a series of shear tests starting at the same hydrostatic state but "radially" moving out on the  $\pi$  plane at different Lode angles. For each test, we plot the principal stress difference versus the principal plastic strain difference and note the slope of the curve at different stress levels. By noting the initial slopes of each stress-strain plot, we can assign it the magnitude of the elastic shear modulus  $G$ , from which, we can then separate the elastic strain from the total strains to obtain the plastic components.

Along each of the linear shear paths emanating from the hydrostatic state, we record the decrease of the plastic shear modulus with increasing distance from the starting point. Next, we connect the points of equal plastic shear moduli on all radial paths to form a field of "closed" yield surfaces, each with its associated plastic modulus. Since a point on this plane is characterized by a single magnitude of plastic tangent modulus, the resulting plot of the field of yield surfaces should be non-intersecting or nesting.

For simplicity, we may assume that these locii of iso-plastic shear moduli all form similar curves which can be approximated by circles (or Mises yield surfaces). Also, let us further idealize the model by adopting a purely kinematic hardening rule (i.e., the centers of these yield circles can translate, but their radii do not change). With the location, size, and plastic shear modulus of each yield circle known, we can now simulate the model response for an arbitrary stress path. As we load from the hydrostatic state, the stress point moves out on the deviatoric plane to engage the first yield surface (enclosing the purely elastic domain), activating its plastic modulus in the elasto-plastic constitutive equation (equations 141 or 145). As shearing proceeds, the active yield surface, with the current stress state residing on it, translates toward the second nesting surface in the field such that when both surfaces come into contact, they do not intersect. This condition is satisfied by using Mroz's hardening rule, a topic which will be treated later in this section.

When the second surface is engaged, its plastic modulus replaces that of surface #1 in the constitutive equation, and it also follows a Mroz hardening rule to the third surface. The now deactivated first surface remains attached to the second surface at the point where it initially came into contact with surface #2, and this point is known as the conjugate point. Since the inner surface must satisfy the "nesting" or non-intersecting requirement while staying in contact with the active surface, its translation is dictated solely by the movement of the active surface. If the shear loading continues, and the second surface comes into contact with the third surface in the field, the

same transition process takes place and surface #3 now carries with it surfaces #1 and #2 as it translates toward surface #4 according to the Mroz hardening rule.

If while on surface #4 (or any other surface for that matter), we start unloading back to the hydrostatic stress state along the virgin stress path trajectory, the stress point deactivates surface #4 and returns to the region enclosed by surface #1 (i.e., the elastic domain). Accordingly, the plastic modulus is "infinity" in this region and the response of the material is once again purely elastic. As the unloading continues, the stress point moves toward the opposite end of circle #1 and engages it on the way back to the hydrostatic state of stress. Note that when the stress point exits the elastic region on this unload path, reverse plastic strain are generated. Furthermore, depending on the arrangement of these surfaces prior to the unload, the stress point may encounter several other surfaces during a reverse or re-directed path, and we can therefore see the influence of loading history on anisotropy, which is manifest in the instantaneous configuration of the field of surfaces. In the calibration of the initial field of surfaces, it may turn out that the yield surfaces may not be symmetrically placed with respect to the hydrostatic axis, and this, in essence, reflects the inherent anisotropy of the soil.

This multi-surface concept, simply presented in pressure-insensitive space, provides the fundamental mathematical tools for extending the description to predict the complicated stress-strain-strength behavior of dense sands subject to generalized loading conditions.



Two simplifications of this multi-level memory structure have been introduced in the soil mechanics literature. The first is to consider the existence of only yield surface #1,  $F_1$ , and the outermost or consolidation surface,  $F_p$ . Note that the Mroz translation rule is still in effect for such a two surface configuration. Instead of the field of hardening moduli, we must now prescribe an interpolation rule which describes the variation of the plastic modulus with the distance between the current stress state on surface #1 and its conjugate point on the consolidation surface,  $F_p$ . Such a modified description of the field of work hardening moduli was elaborated independently by Krieg (Reference 70) and Dafalias and Popov (Reference 71). A variation of this concept, known as the bounding surface model, in which the size of the elastic region (yield surface #1) is vanishingly small, will be discussed in detail in the next section. It is important to note here, however, that the degenerate nature of yield surface #1 "frees" the theoretician from the analytical rigor of Mroz's hardening rule, and allows the use of an experimentally verifiable mapping rule to locate the conjugate point on  $F_p$ .

An alternative simplified description of hardening is provided by assuming that the field of hardening moduli inside the consolidation surface,  $F_p$ , is represented by an infinite number of nesting surfaces and the active plastic modulus depends on the ratio of the radius of the instantaneous loading circle and the consolidation surface. A loading surface is defined as the subsequent surface into which an initial yield surface deforms and/or translates such that the loading surface includes the current stress point. If the radius of the loading

surface continue to increase due to a re-direction of the loading program, then the plastic modulus is governed by the ratio of the loading surface radius to the consolidation surface radius. If, on the other hand, the stress path reverses and is directed to the interior of the loading surface, the instantaneous location of this surface is recorded and is now called a stress reversal surface. Prior to the penetration of this stress reversal surface in the unload phase, the plastic modulus is controlled by the ratio of the active loading surface to stress reversal surface radii. Once the stress state exits the domain enclosed by the stress reversal surface, the interpolation rule reverts to its original form. In this way, the memory of a loading event is only erased by another event of greater intensity. Pietrusczak and Mroz (Reference 72) have utilized this mathematical scheme to model the behavior of clay, but it has not yet been applied to sands.

In the following subsections, we describe the essential features of what may be the simplest and most complete statement on elasto-plastic hardening theory: the Prevost Pressure Sensitive Isotropic/Kinematic Hardening Model.

#### C. MODEL CHARACTERISTICS

The pressure-sensitive version of the Prevost model is formulated in terms of directional stress components (i.e., the stress invariants are not used), and associative flow is assumed in the deviatoric subspace. The model does not explicitly involve plastic potentials, although their existence is implied since the computation of the plastic volumetric strain uses a form of equation 130 of the previous

section. Material frame indifference is satisfied in the formulation, but it is not certain whether energy is conserved under all conditions of loading and unloading (Reference 65). The development of the model is based on conventional flow or incremental plasticity theory, and, hence, most of the fundamental postulates of the previous section are merely specialized in this development.

#### D. YIELD FUNCTION

The model employs a yield function of the form

$$F^{(m)} = \frac{3}{2} [\underline{s} - \underline{\alpha}^{(m)}] : [\underline{s} - \underline{\alpha}^{(m)}] + C^2 [p - \beta^{(m)}]^2 - [k^{(m)}]^2 = 0, \quad (146)$$

where  $\underline{s}$  and  $p$  denote the deviatoric stress tensor and the mean stress respectively;  $\underline{\alpha}$  represent the deviatoric tensor components of the center of the yield surface while  $\beta$  locates the surface's center of along the  $p$  axis;  $k^{(m)}$  is the radius of the  $m^{\text{th}}$  yield surface, and  $C$  is the axis ratio of the yield ellipse when projected in  $p$ - $q$  subspace. Prevost frequently set the factor  $C^2$  equal to  $9/2$ , and, in this particular instance, equation 146 simplifies to

$$F^{(m)} = \frac{3}{2} [\underline{q} - \underline{\xi}^{(m)}] : [\underline{q} - \underline{\xi}^{(m)}] - [k^{(m)}]^2 = 0,$$

where the tensor components of the center of a yield surface  $m$  ( $\underline{\xi}^{(m)}$ ) relate to  $\underline{\alpha}$  and  $\beta$  as follows:

$$\underline{\xi}^{(m)} = \underline{\alpha}^{(m)} + \beta^{(m)} \underline{\delta}.$$

With this particular yield axis ratio, the surfaces plot as spheres of radius  $\frac{\sqrt{2}k^{(m)}}{3}$  in stress space.

## E. FLOW RULE

The flow rule is of the form expressed in equation 130 and 131 of the previous section; Prevost (Reference 7) assumes normality in the deviatoric subspace which implies that the function  $A_2$  is set equal to one but its complementary function  $A_1$  of equation 130 is retained to model the plastic volumetric strain response.

In order to facilitate an easy comparison of the formulation reported herein and Prevost's work, most of his notational conventions are adopted; whereupon, the tensors  $\underline{Q}$  and  $\underline{P}$  are the gradient tensors to the yield and plastic potential functions replacing  $\nabla F$  and  $\nabla G$  of the previous section, and,  $\underline{Q}'$  and  $\underline{P}'$  are the deviatoric components of  $\underline{Q}$  and  $\underline{P}$  respectively. These tensors enter the flow rule as:

$$d\varepsilon^P = \frac{1}{K_p} \{ \underline{Q} : d\underline{g} \} \frac{1}{|\underline{Q}|^2} \underline{P} ,$$

and, as a consequence of stating the flow rule in this form, observe that the inverse constitutive relation (equation 145) is now

$$d\underline{g} = \left[ \underline{C}^e + \frac{(\underline{C}^e : \underline{P})(\underline{Q} : \underline{C}^e)}{K_p \{ \underline{Q} : \underline{Q} \} + (\underline{Q} : \underline{C}^e : \underline{P})} \right] d\varepsilon .$$

The non-associativity function of equation 130,  $A_1$ , is assumed to take the form

$$A_1 = 1 + A_3 \frac{\{ \underline{Q}' : \underline{Q}' \}}{|\text{tr } \underline{Q}|} ,$$

where  $A_3$  is a constant multiplied by a term which indicates the variation of the departure from associativity as a function of position along meridional sections of the yield surface. Note, however, that the magnitude of  $A_1$  remains constant on any given octahedral plane and the plastic volumetric strain rate is associated when  $\underline{Q}' = \underline{Q}$ . Since the

non-associativity of the flow is modeled by a single parameter, we can drop the subscript on  $A$ , in the sequel and refer to it as simply the "A" parameter.

A pair of plastic modulus parameters  $h^{(m)}$  and  $B^{(m)}$  characterizes each surface. These parameters are used to calculate the generalized plastic modulus  $K_p$  on a given surface. As in the non-associativity function  $A_1$ , the plastic modulus,  $K_p$ , is assumed to vary along the meridional section of a yield surface while being fixed on any given octahedral plane; to mathematically effect this desired variation, the plastic modulus is given by

$$K_p = h^{(m)} + \frac{\text{tr } Q}{\sqrt{3Q:Q}} B^{(m)},$$

where  $h^{(m)}$  is the plastic shear modulus and  $[h^{(m)} + B^{(m)}]$  and  $[h^{(m)} - B^{(m)}]$  are the plastic bulk moduli associated with  $F^{(m)}$  which are mobilized in consolidation tests upon loading and unloading, respectively. The projections of the yield surfaces onto the deviatoric stress subspace thus define regions of constant plastic shear moduli.

#### F. HARDENING RULE

The field of yield surfaces are assumed to translate and deform isotropically, but, from considerations of Mroz's rule presented earlier in subsection II.B, it is apparent that the hardening cannot be specified arbitrarily. The easier aspect of this hardening rule - i.e., the positioning of interior inactive surfaces - will be presented before the more complicated aspect of updating the location of the active surface as it moves towards its conjugate point.

Say we generalize the yield function to the form

$$F^{(m)} = \hat{F}^{(m)}[g - \xi^{(m)}] - [k^{(m)}]^n = 0, \quad n > 0 \quad (147)$$

where  $n$  is the degree of  $\hat{F}^{(m)}$  in  $[g - \xi^{(m)}]$ . If we further assume that all the yield surfaces are similar we can say that  $\hat{F} = \hat{F}^{(m)}$  for all  $m$ .  $\hat{F}$  is usually chosen as a homogenous function of order  $n$  of its arguments. What does this mean and what are its consequences? The yield function  $\hat{F}$  is said to be homogenous of order  $n$  if the following is satisfied:

$$\hat{F}[\Lambda(g - \xi^{(m)})] = \Lambda^n \hat{F}[g - \xi^{(m)}],$$

where  $\Lambda$  is a positive scalar.

When a surface  $m$  is moving toward a surface  $m+1$ , the stress point on surface  $m$ , say at  $M$ , moves to the corresponding conjugate point on surface  $m+1$ , say at  $R$ , to avoid overlapping. This path of movement is depicted in figure 8 for a field of surfaces drawn in 'triaxial' subspace. Geometrically, it can easily be shown that the tensor linking the center coordinates of surface  $m$ ,  $\xi^{(m)}$ , to the stress point  $g$ , at  $M$ , is directed in the same sense as the tensor connecting the center of surface  $m+1$ ,  $\xi^{(m+1)}$ , to the conjugate stress state at  $R$ , say  $g_R$ .

Mathematically, this may be expressed as:

$$g - \xi^{(m)} = \Lambda [g_R - \xi^{(m+1)}], \quad (148)$$

where  $\Lambda$  is again a positive scalar.

When surface  $m$  comes into contact with surface  $m+1$ ,  $g_R$  coincides with  $g$  and equation 148 becomes

$$g - \xi^{(m+1)} = \Lambda [g - \xi^{(m)}],$$

or

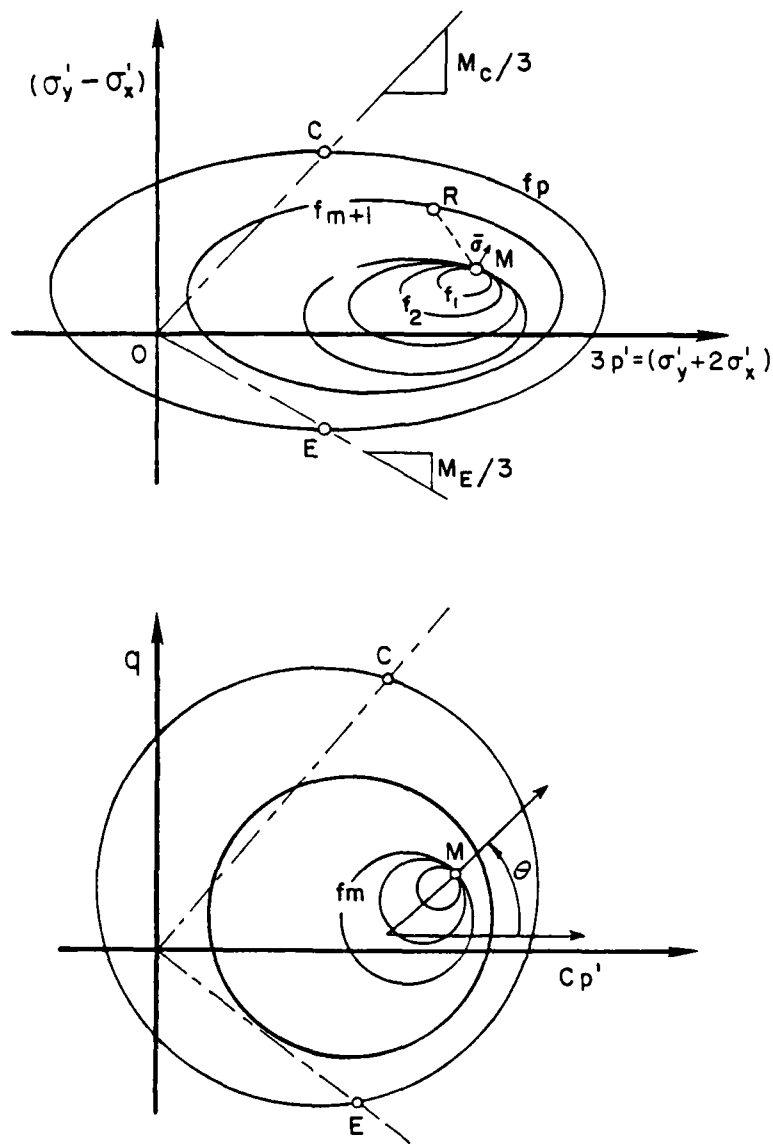


Figure 8. Field of Nesting Surfaces in  $p'$ - $q$  (top) and  $Cp'$ - $q$  subspaces (bottom) (Reference 7).

$$\Lambda = \frac{\sigma - \xi^{(m+1)}}{\sigma - \xi^{(m)}} ; \quad (149)$$

by using equations 147 and 149, we see

$$\begin{aligned} \hat{F} [\sigma - \xi^{(m+1)}] &= \Lambda^n \hat{F} [\sigma - \xi^{(m)}] = [k^{(m+1)}]^n \\ \Lambda^n [k^{(m)}]^n &= [k^{(m+1)}]^n \quad \text{or} \quad \Lambda = \frac{[k^{(m+1)}]}{[k^{(m)}]} , \end{aligned} \quad (150)$$

and

$$\frac{\sigma - \xi^{(m+1)}}{\sigma - \xi^{(m)}} = \frac{k^{(m+1)}}{k^{(m)}} .$$

This equation applies whenever surface  $m+1$  has been engaged and  $m$  now functions as one of the interior inactive surfaces. We can say that whenever we know the location and size of the active surface together with the sizes of the interior surfaces, the location of these interior surfaces can be calculated forthwith; to satisfy the tangency condition at the point of intersection, we have

$$\frac{\sigma - \xi^{(m)}}{k^{(m)}} = \frac{\sigma - \xi^{(m-1)}}{k^{(m-1)}} = \frac{\sigma - \xi^{(m-2)}}{k^{(m-2)}} = \dots \text{etc.}$$

By combining equations 148 and 150, we can derive the expression for the translation direction  $\mu$  joining the current stress state on surface  $F^{(m)}$  to its conjugate point on the next larger surface ( $F^{(m+1)}$ ); that is,

$$\mu = \frac{k^{(m+1)}}{k^{(m)}} [\sigma - \xi^{(m)}] - [\sigma - \xi^{(m+1)}] . \quad (151)$$

The sizes of all surfaces are assumed to expand or contract at the same rate which is governed by the total volumetric strain increment as follows:

$$\frac{dk^{(m)}}{k^{(m)}} = \lambda d\epsilon_v , \quad (152)$$



where  $\lambda$  is an experimentally determined parameter governing the isotropic processes. This equation applies for all yield surfaces (of finite size) in the configuration. Equation 152 can be integrated to directly give the instantaneous yield surface sizes

$$k^{(m)} = k_0^{(m)} \exp(\lambda \epsilon_v), \quad (153)$$

where  $k_0^{(m)}$  are the initial values of  $k^{(m)}$  (at  $\epsilon_v = 0$ ). It is also assumed that the centers of the yield surfaces exterior to the active surface  $F^{(m)}$  move radially according to

$$\begin{aligned} \xi^{(m+1)} &= \xi_0^{(m+1)} \exp(\lambda \epsilon_v) ; \quad \xi^{(m+2)} = \xi_0^{(m+2)} \exp(\lambda \epsilon_v) ; \\ \xi^{(p)} &= \xi_0^{(p)} \exp(\lambda \epsilon_v) , \end{aligned} \quad (154)$$

where  $\xi_0^{(m+1)}, \dots, \xi_0^{(p)}$  are the initial center location of the surfaces  $m+1$  to the consolidation (or outermost) surface  $p$ . It is apparent from equations 153 and 154 that the surfaces shrink in size and move back toward the origin in stress space when the material starts to dilate; this, in effect, simulates a weakening and softening of the soil's structure.

We have specified all but one mathematical aspect of the translation rule: the computation of the magnitude of the incremental translation tensor  $d\mu$  ( $= d\mu \mu$ ) for the active yield surface  $m$ . Numerically, this is accomplished by first defining the translation direction  $\mu$  using equation 151 in which the center location  $\xi^{(m+1)}$  and the sizes  $k^{(m)}$  and  $k^{(m+1)}$  have been previously updated using equations 153 and 154 respectively. To complete this item, we need now only compute the scalar  $d\mu$  by employing the consistency condition.

If an arbitrary stress increment,  $\dot{\mathbf{g}} = \dot{\mathbf{s}} + \dot{p} \hat{\mathbf{g}}$ , is applied, it is expected that the active yield surface will translate and change size

such that the consistency condition is also guaranteed after any translation and size change of this surface. To make for a neater presentation, the implied superscript  $m$ , in reference to the active surface, is omitted hereafter. The attention to detail in this derivation may seem overzealous, but it is considered appropriate since these equations, to our knowledge, appear here for the first time in published literature.

Mathematically, the consistency requirement, after the incremental hardening, may be expressed as:

$$F = \frac{3}{2} [(\underline{s} + \dot{\underline{s}}) - (\underline{\alpha} + \dot{\underline{\alpha}})] : [(\underline{s} + \dot{\underline{s}}) - (\underline{\alpha} + \dot{\underline{\alpha}})] + C^2 [(p + \dot{p}) - (\beta + \dot{\beta})]^2 = [k + \dot{k}]^2 \quad (155)$$

As an aid in seeking the solution, equation 155 may be reorganized to read

$$F = \frac{3}{2} [(\underline{s} - \underline{\alpha}) + (\dot{\underline{s}} - \dot{\underline{\alpha}})] : [(\underline{s} - \underline{\alpha}) + (\dot{\underline{s}} - \dot{\underline{\alpha}})] + C^2 [(p - \beta) + (\dot{p} - \dot{\beta})]^2 = [k + \dot{k}]^2 = k^2 + 2 k \dot{k} + \dot{k} \dot{k} \quad ,$$

which may then be further expanded to

$$\begin{aligned} & \frac{3}{2} [(\underline{s} - \underline{\alpha}) : (\underline{s} - \underline{\alpha})] + \frac{3}{2} [(\dot{\underline{s}} - \dot{\underline{\alpha}}) : (\dot{\underline{s}} - \dot{\underline{\alpha}})] + \\ & 3 [(\underline{s} - \underline{\alpha}) : (\dot{\underline{s}} - \dot{\underline{\alpha}})] + C^2 (p - \beta)^2 + C^2 (\dot{p} - \dot{\beta})^2 + \\ & 2 C^2 (p - \beta)(\dot{p} - \dot{\beta}) = k^2 + 2 k \dot{k} + \dot{k} \dot{k} \quad . \end{aligned} \quad (156)$$

From equation 146, recall that

$$\frac{3}{2} (\underline{s} - \underline{\alpha}) : (\underline{s} - \underline{\alpha}) + C^2 (p - \beta)^2 = k^2 \quad ,$$

so that substitution of this identity into equation 156 leads to

$$\frac{3}{2} [(\dot{\underline{s}} - \dot{\underline{\alpha}}):(\dot{\underline{s}} - \dot{\underline{\alpha}})] + 3 [(\underline{s} - \underline{\alpha}):(\dot{\underline{s}} - \dot{\underline{\alpha}})] + \\ C^2 (\dot{\underline{p}} - \dot{\underline{\beta}})^2 + 2 C^2 (\underline{p} - \underline{\beta})(\dot{\underline{p}} - \dot{\underline{\beta}}) = 2 \underline{k} \dot{\underline{k}} + \dot{\underline{k}} \dot{\underline{k}} . \quad (157)$$

It is convenient to expand some of the parenthetical terms of equation 157 to obtain

$$\frac{3}{2} \dot{\underline{s}}:\dot{\underline{s}} + \frac{3}{2} \dot{\underline{\alpha}}:\dot{\underline{\alpha}} - 3 \dot{\underline{s}}:\dot{\underline{\alpha}} + 3 (\underline{s} - \underline{\alpha}):\dot{\underline{s}} - 3 (\underline{s} - \underline{\alpha}):\dot{\underline{\alpha}} + \\ C^2 \dot{\underline{p}}^2 + C^2 \dot{\underline{\beta}}^2 - 2 C^2 \dot{\underline{p}} \dot{\underline{\beta}} + 2 C^2 (\underline{p} - \underline{\beta}) \dot{\underline{p}} - \\ 2 C^2 (\underline{p} - \underline{\beta}) \dot{\underline{\beta}} - 2 \underline{k} \dot{\underline{k}} - \dot{\underline{k}} \dot{\underline{k}} = 0 . \quad (158)$$

With the translation rate tensor written as:

$$\dot{\underline{s}} = \dot{\underline{\alpha}} + \dot{\underline{\beta}} \underline{\delta} = d\mu \underline{\mu} = d\mu (\text{dev } \underline{\mu} + \frac{\text{tr } \underline{\mu}}{3} \underline{\delta}) ,$$

where dev  $\underline{\mu}$  are the deviatoric components of the tensor  $\underline{\mu}$ ,  $\dot{\underline{\alpha}}$  and  $\dot{\underline{\beta}}$  can now be replaced by  $d\mu \text{ dev } \underline{\mu}$  and  $d\mu \frac{\text{tr } \underline{\mu}}{3}$  respectively in equation 158.

With the translation direction  $\underline{\mu}$  already specified, the objective reduces to one of determining the scalar coefficient  $d\mu$ . This is realized by solving the resulting expression for  $d\mu$  as follows:

$$\frac{3}{2} \dot{\underline{s}}:\dot{\underline{s}} + \frac{3}{2} (d\mu \text{ dev } \underline{\mu}):(d\mu \text{ dev } \underline{\mu}) - 3 \dot{\underline{s}}:(d\mu \text{ dev } \underline{\mu}) + \\ 3 (\underline{s} - \underline{\alpha}):\dot{\underline{s}} - 3 (\underline{s} - \underline{\alpha}):(d\mu \text{ dev } \underline{\mu}) + C^2 \dot{\underline{p}}^2 + \\ C^2 d\mu \frac{\text{tr } \underline{\mu}}{3} d\mu \frac{\text{tr } \underline{\mu}}{3} - 2 C^2 \dot{\underline{p}} d\mu \frac{\text{tr } \underline{\mu}}{3} + 2 C^2 (\underline{p} - \underline{\beta}) \dot{\underline{p}} - \\ 2 C^2 (\underline{p} - \underline{\beta}) d\mu \frac{\text{tr } \underline{\mu}}{3} - 2 \underline{k} \dot{\underline{k}} - \dot{\underline{k}} \dot{\underline{k}} = 0 . \quad (159)$$

Equation 159 is quadratic in  $d\mu$ , and must be solved accordingly; first collect the coefficients of  $d\mu^2$ ,  $d\mu$ , and the constant terms and store them in descriptive variables known as A, B, and C respectively. The result is

$$A = \frac{3}{2} (\text{dev } \underline{\mu} : \text{dev } \underline{\mu}) + C^2 \frac{\text{tr } \underline{\mu}}{3} \frac{\text{tr } \underline{\mu}}{3} , \quad (160)$$

$$B = -3 \dot{\underline{s}} : (\text{dev } \underline{\mu}) - 3 (\underline{s} - \underline{\alpha}) : (\text{dev } \underline{\mu}) - 2 C^2 \dot{p} \frac{\text{tr } \underline{\mu}}{3} - 2 C^2 (p - \beta) \frac{\text{tr } \underline{\mu}}{3} , \quad (161)$$

and

$$C' = \frac{3}{2} \dot{\underline{s}} : \dot{\underline{s}} + 3 (\underline{s} - \underline{\alpha}) : \dot{\underline{s}} + C^2 \dot{p}^2 + 2 C^2 (p - \beta) \dot{p} - 2 \underline{k} : \dot{\underline{k}} - \dot{\underline{k}} : \dot{\underline{k}} . \quad (162)$$

With the coefficients expressed in equations 160, 161, and 162, we can now compactly write equation 159 as:

$$A d\mu^2 + B d\mu + C' = 0 ,$$

from which the solution for the roots are

$$d\mu = \frac{-B \pm \sqrt{B^2 - 4 A C'}}{2 A} . \quad (163)$$

Equation 163 can be conveniently solved by replacing the variable B by an alternate variable  $B' = -B/2$  (i.e,  $B = -2B'$ ). With the alternate variable  $B'$ , equation 163 is now written as:

$$\begin{aligned} d\mu &= \frac{2B' \pm \sqrt{4B'^2 - 4 A C'}}{2 A} , \\ &= \frac{B' \pm \sqrt{B'^2 - A C'}}{A} , \end{aligned} \quad (164)$$

where A and  $C'$  are defined in equations 160 and 162, and

$$\begin{aligned} B' &= -\frac{B}{2} = \frac{3}{2} \dot{\underline{s}} : (\text{dev } \underline{\mu}) + \frac{3}{2} (\underline{s} - \underline{\alpha}) : (\text{dev } \underline{\mu}) + C^2 \dot{p} \frac{\text{tr } \underline{\mu}}{3} + \\ &\quad C^2 (p - \beta) \frac{\text{tr } \underline{\mu}}{3} . \end{aligned}$$

Finally, the root of equation 164 is specified by the condition that the scalar product  $d\mu : [\frac{3}{2} \dot{\underline{s}} + \dot{p} \underline{\underline{s}}]$  be greater than zero, and this final aspect completes the specification of the Prevost isotropic/kinematic hardening rule.

#### F. MODEL CALIBRATION

The last, but perhaps most singular, feature of the Prevost model is its calibration procedure to determine the size and location as well as the plastic modulus and non-associative flow parameters for each surface in the initial configuration. This task can sometimes prove to be more challenging than any other phase, as the writers can attest to, in the actual implementation of the Prevost model.

Complete specification of the model parameters requires the determination of: 1) the initial positions and sizes of the yield surfaces together with their associated plastic moduli, 2) their size or plastic modulus, or both, change as loading proceeds, and 3) the elastic shear,  $G$ , and bulk,  $B$ , moduli (Reference 7). The input stress-strain data is obtained wholly from the results of a monotonic drained conventional triaxial compression test (CTC) and a reduced triaxial extension (RTE) test (the stress paths of which are depicted in figure 3).

In test sample preparation, the soil develops its original anisotropy in the direction of consolidation, and the horizontal direction is thus an isotropic plane ( $xz$  plane) while the axial direction ( $y$  axis) is an axis of rotational symmetry. With this  $n$ -fold axis symmetry and a corresponding calibration stress path which is restricted to the Rendulic (or triaxial) plane, equation 146 simplifies to

$$F^{(m)} = [q - \alpha^{(m)}]^2 + C^2 [p - \beta^{(m)}]^2 - [k^{(m)}]^2 = 0, \quad (165)$$

where

$$q = \sigma_y - \sigma_x,$$

and

$$\alpha = 3 \alpha_y / 2 = -3 \alpha_x = -3 \alpha_z.$$

From both a geometrical and an intuitive standpoint, it is interesting to note the similarity of equation 165 to that of a translated circle of radius  $k$  in a  $C_p$  versus  $q$  coordinate system with a center location at  $[C\beta, \alpha]$ . These circular plots are illustrated in figure 8 where the angle  $\theta$  is also defined. Observe from this figure that we can straight-forwardly write the following equations:

$$q = \alpha + k \sin \theta, \quad (166)$$

and

$$p = \beta + \frac{k}{C} \cos \theta. \quad (167)$$

Substitution of these relations into the 'triaxial' elasto-plastic constitutive equations

$$d\epsilon_v = \frac{dp}{3K} + \frac{1}{K_p} \text{tr}(\underline{P}) \frac{1}{|\underline{Q}|^2} \{Q:dg\},$$

and

$$d\epsilon_{yy} = \frac{1}{2G} ds_{yy} + \frac{1}{K_p} \frac{Q'}{|\underline{Q}|^2} \{Q:dg\},$$

leads to

$$d\epsilon_v/dp = \frac{1}{3K} + \frac{1}{K_p} \{2C \cos \theta + \sqrt{6} A_m \cos \theta |\tan \theta|\} \left\{ \frac{\sin \theta + C \gamma \cos \theta}{3 \gamma} \right\}, \quad (168)$$

and

$$\frac{d\bar{\epsilon}}{dq} = \frac{1}{2G} + \frac{1}{K_p} \sin \theta \{ \sin \theta + C \gamma \cos \theta \}, \quad (169)$$

where  $\gamma = dp/dq$ ,  $d\bar{\epsilon} = d\epsilon_y - d\epsilon_x$ ,  $d\epsilon_v = 2 d\epsilon_x + d\epsilon_y$ , and

$$(K_p)_m = h_m + B_m \cos \theta. \quad (170)$$

The dependence of the model parameter group  $x = K, G, h_m$  and  $B_m$ , and group  $y = \alpha^{(m)}, \beta^{(m)}$ , and  $k^{(m)}$  are assumed to be of the forms

$$x = x_1 \left( \frac{p}{p_1} \right)^n, \quad (171)$$

and

$$y = y_1 \exp(\lambda \epsilon_v), \quad (172)$$

where  $x_1$  and  $y_1$  refer to initial values, and  $\lambda$  and  $n$  are experimental parameters. Note that the dependency of the group  $y$  parameters was alluded to previously in the discussion of the hardening rule.

For most cohesionless soils,  $n$  can be assumed to be equal to 0.5 (Reference 27), and the isotropic hardening parameter,  $\lambda$ , is determined from the results of one-dimensional consolidation tests. It is assumed that these consolidation test results plot as straight lines parallel to the projection of critical state lines on the volumetric strain ( $\epsilon_v$ ) versus the logarithm of the mean normal pressure ( $p$ ) plane. This parameter is then simply determined from the results of  $K_0$ -consolidation soil tests results (Reference 7) as:

$$\lambda = \frac{1}{p_K} dp_K + d\epsilon_v^K, \quad (173)$$

where the subscript/superscript  $K$  refers to  $K_0$ - loading conditions.

If we let  $\theta_C$  and  $\theta_E$  denote the values of  $\theta$  when the stress point reaches the yield surface  $F^{(m)}$  in a CTC (or loading) and an RTE (or unloading) test respectively, equations 166, 167, 168, 169, 170, 171 and 172 can be combined to give

$$\frac{1}{\tan \theta_C} \pm \frac{1}{\tan \theta_E} = \frac{1}{2C} [ 3Y_C (X_C + Y_C) \pm 3Y_E (X_E + Y_E) ] , \quad (174)$$

and

$$\cos \theta_C - \cos \theta_E = R_{CE} (\sin \theta_C - \sin \theta_E) , \quad (175)$$

where

$$\begin{aligned} R_{CE} &= C \{ p_C - p_F \exp[\lambda(\epsilon_V^C - \epsilon_V^E)] \} + \\ &\quad \{ q_C - q_E \exp[\lambda(\epsilon_V^C - \epsilon_V^E)] \} , \\ \frac{1}{X_C} &= (p_C/p_1)^n \frac{d\bar{\epsilon}}{dq} - \frac{1}{2G_1} , \\ \frac{1}{Y_C} &= (p_C/p_1)^n \frac{d\epsilon_V}{dp} - \frac{1}{3K_1} , \end{aligned}$$

and similarly for  $X_E$  and  $Y_E$ , where the subscripts/superscripts refer to CTC and RTE loading conditions, respectively. In equation 174, the plus sign (+) is to be used when  $\tan \theta_C \tan \theta_E$  is less than zero, and the minus sign (-) otherwise.

The next step in the calibration procedure is to tabulate the stress strain data reporting the quantities  $q$ ,  $p$ ,  $\epsilon_V$ ,  $\bar{\epsilon}$  for the CTC and RTE test on the material, both of which start at the same confining pressure ( $p_1$ ). After that, we calculate  $dq/d\bar{\epsilon}$  and  $dp/d\epsilon_V$  at each data point and include these quantities in corresponding columns of the tabulated data sets. With these data, we assign the elastic bulk modulus,  $K$ , and shear modulus,  $G$ , the initial values of the slopes  $\frac{1}{3}$  ( $dp/d\epsilon_V$ ) and  $dq/d\bar{\epsilon}$  respectively. If the magnitudes of these elastic parameters are different for the CTC and RTE tests, the larger magnitude is chosen.

Provided with the following: 1) the isotropic hardening parameter,  $\lambda$ , (equation 173), 2) an estimate of the constant  $n$ , 3) the initial



values of the elastic parameters, 4) the slopes of the CTC and RTE stress paths ( $\gamma_C$  and  $\gamma_E$ ), and 5) an assumed value of the yield axis ratio  $C$ , we now enter the digital CTC stress-strain data and select a representative slope  $dq/d\bar{\epsilon}$  to be used in establishing the first yield surface of the configuration. Using this magnitude of  $dq/d\bar{\epsilon}$ , we next enter the RTE test and search for the corresponding line of data which matches this slope. If an exact correspondence is not found, a simple linear interpolation scheme can be devised. These data are all that is necessary to simultaneously solve equations 174 and 175 for  $\theta_C$  and  $\theta_E$ . For this purpose, note that equation 175 is more conveniently rewritten as:

$$\frac{1}{\tan\theta_C} + \frac{1}{\tan\theta_E} + [2 R_{CE} / (1 - R_{CE}^2)] \left[ \frac{1}{\tan\theta_C \tan\theta_E} - 1 \right].$$

Once  $\theta_C$  and  $\theta_E$  have been calculated, the model parameters associated with  $F^{(m)}$  are simply obtained by combining equations 166, 167, 168, and 169 (Prevost, 1980); namely,

$$\begin{aligned} B_m &= [X_C \sin\theta_C ZC - X_E \sin\theta_E ZE] + [\cos\theta_C - \cos\theta_E] , \\ h_m &= X_C \sin\theta_C ZC - B_m \cos\theta_C , \\ \sqrt{6} A_m &= \frac{1}{|\tan\theta_C|} [3 \gamma_C (X_C/Y_C) - B_m \cos\theta_C] , \\ k_1^{(m)} &= [q_C \exp(-\lambda \epsilon_V^C) - q_E \exp(-\lambda \epsilon_V^E)] + [\sin\theta_C - \sin\theta_E] , \\ \alpha_1^{(m)} &= q_C \exp(-\lambda \epsilon_V^C) - k_1^{(m)} \sin\theta_C , \\ \beta_1^{(m)} &= p_C \exp(-\lambda \epsilon_V^C) - \frac{k_1^{(m)}}{C} \cos\theta_C , \end{aligned}$$

where

$$ZC = \sin\theta_C + C \gamma_C \cos\theta_C ,$$

and

$$ZE = \sin\theta_E + C \gamma_E \cos\theta_E .$$

The procedure is repeated by choosing another magnitude of  $dq/d\bar{\epsilon}$  for the CTC and calculating the parameters associated with the resulting surface. Note that, if it turns out to be more convenient, we could just as well select  $dq/d\bar{\epsilon}$  from the RTE test data and then proceed to find the corresponding data point in the CTC log.

Almost always, the initial configuration of surfaces turn out to be intersecting, but, it usually takes only a slight adjustment in sizes and/or positions to rectify the arrangement. Moreover, it is evident that the degree of accuracy achieved by such a representation of the experimental curves is directly dependent on the number of  $dq/d\bar{\epsilon}$  points or surfaces used to describe the field of work-hardening moduli.

This final aspect completes the presentation of the isotropic/kinematic hardening model of Prevost.

## SECTION IV

### BOUNDING SURFACE PLASTICITY FORMULATION FOR GRANULAR MATERIAL

#### A. GENERAL

The bounding surface concept was proposed by Dafalias and Popov (Reference 71) as a simplified variation of the two surface model which was briefly prefaced in section III. In this theory, the yield surface enclosing the elastic region (i.e., yield surface #1) is assumed to be vanishingly small, thus degenerating to a point. If we adopt the model classification nomenclature of the previous section - i.e., multi-surface, two-surface, infinite surface, etc. -, we can call this type of formulation a one surface model, described solely by an isotropically hardening bounding (or consolidation) surface  $F_c$ . Since the ensuing presentation focuses on a single surface, we can drop the subscript "c" which is used to qualify the yield surface function  $F$ .

Although the bounding surface characterization does not possess an evolutionary law as sophisticated as, say, the isotropic/kinematic hardening model of Prevost, it is a reasonable and computationally less expensive idealization, capable of realistically simulating some loading and unloading tests (Reference 72). One distinct advantage, however, of the bounding surface model is its independence from the analytically rigorous hardening rule of Mroz. This permits the use of any experimentally verifiable and admissible mapping rule to associate the actual stress state to a conjugate point on the bound.

For points within the consolidation surface, the mapping rule's role is two-fold: first, it specifies the plastic strain increment direction as a function of the gradient tensor ( $\nabla F$ ) at the image (or conjugate) point; and secondly, the plastic modulus,  $K_p$ , is assumed to depend on: 1) the plastic modulus at the conjugate point, 2) the Euclidean distance between the actual stress state and the image stress state, 3) any appropriate plastic internal variables, and 4) suitable discrete memory indicators of the loading.

The formulation that follows is based on the formalism of cyclic plasticity as presented in section II (Reference 4). Also, the presentation in this section consists for the most part of original work with all externally derived ideas being acknowledged at first mention.

#### B. DETAILS OF FUNCTION

As discussed in section II.F.1, an assumption of material isotropy means that the bounding surface function,  $F(\bar{\sigma}_{ij}, q_n) = 0$ , can be expressed in terms of the three invariants of the stress tensor:  $\bar{I}_1$ ,  $\sqrt{\bar{J}_2}$ , and  $\bar{J}_3$  (or  $\bar{\theta}$ , where  $\bar{\theta}$  is the Lode angle). The bar over the stress quantities indicate points on  $F = 0$  while  $q_n$  are the  $n$  plastic internal variables (PIVs) used in characterizing the state of the material; the variables  $q_n$  are usually taken to be scalars or components of properly invariant second rank tensors such as inelastic strain. The isotropy assumption further implies a six-fold symmetry in the  $\pi$  plane, and hence, it is only necessary to describe a  $60^\circ$  section for a complete

isotropic representation of a yield/bounding surface in three-dimensional principal stress space (i.e.,  $[-\pi/6] \leq \bar{\theta} \leq [\pi/6]$ ).

# 1. Consolidation portion of piecewise continuous surface

Let us first analytically describe the meridional sections (that is,  $\bar{\theta}$  held constant) of the bounding surface,  $F$ , and then extend the description to include the variation of its projection on the  $\pi$  plane. The meridional section for the region of the surface bounded by the  $I_1$  axis and the critical state line (CSL) is first discussed since its development is much simpler than the mathematical representation of that part of the surface enclosed by the "failure" envelope (or locus of peak stress ratios of the frictional material) and the CSL. In this context, the critical (or characteristic) state is defined as the pre-peak stress ratio at which the plastic volumetric strain rate is zero. Further, note that the sections in the  $\pi$  plane are geometrically similar while those in the meridional section show a scale distortion dependent only on the value of  $\bar{\theta}$ . Once a function  $g(\bar{\theta})$  has been specified to describe the relationship between  $\sqrt{J_2}$  and the Lode angle ( $\bar{\theta}$ ), it is more convenient to use the equivalent octahedral shear stress  $\sqrt{J_2}^*$  ( $= [\sqrt{J_2} / g(\bar{\theta})] = \text{constant}$ ) in the analytical equations of the meridional sections, and to later generalize the description to three dimensional principal stress space by replacing  $\sqrt{J_2}^*$  with the term  $[\sqrt{J_2}/g(\bar{\theta})]$  in the succeeding equations.

An ellipse, with its major and minor principal axes coincident with the  $I_1$  and  $\sqrt{J_2}$  axes respectively, is chosen as the functional form of the section of the bounding surface delimited by the  $I_1$  axis and the

CSL. From figure 9, observe that  $N^*$  ( $= [N/g(\bar{\theta})]$  = constant) is the slope of the critical state line and  $S^*$  ( $= [S/g(\bar{\theta})]$  = constant) is the slope of the limiting "failure" envelope in this equivalent shear stress vs. mean stress sub-space. This selection of the slope of the yield/plastic potential function at the origin of stress space to be equal to  $S^*$  is not absolutely necessary, but it does ensure that the stress state never resides outside a limit envelope.

For normally consolidated clays or loose sands,  $S^*$  and  $N^*$  usually coincide, but for dense sand or highly overconsolidated clays, the material usually starts dilating (i.e., reaches  $N^*$ ) before actually reaching its peak combined stress state (at  $S^*$ ).

$I_0$  is the point at which the bounding ellipsoid intersects the hydrostatic axis while  $Q$  is a parameter used to locate the center of this ellipse on the  $I_1$  axis. Also, as shown in figure 9,  $I_0/Q$  is the  $I_1$  component of the center coordinate of the ellipse, and one may furthermore observe that the semi-diameter of the major axis is equal to  $I_0 - (I_0/Q)$ . At this center coordinate on the  $I_1$  axis, the CSL intersects the bounding ellipse so we can also easily recognize that the magnitude of its conjugate  $\sqrt{J_2}^*$  coordinate is equal to  $N^* (I_0/Q)$ . Given this background information, we can now proceed to mathematically depict the surface in stress-invariant coordinate space.

Recall from elementary analytic geometry that the equation of an ellipse, with its major axis parallel to an arbitrary  $x$  reference abscissa, can be expressed as:

$$F = \frac{(x-h)^2}{a^2} + \frac{(y-k)^2}{b^2} = 1,$$

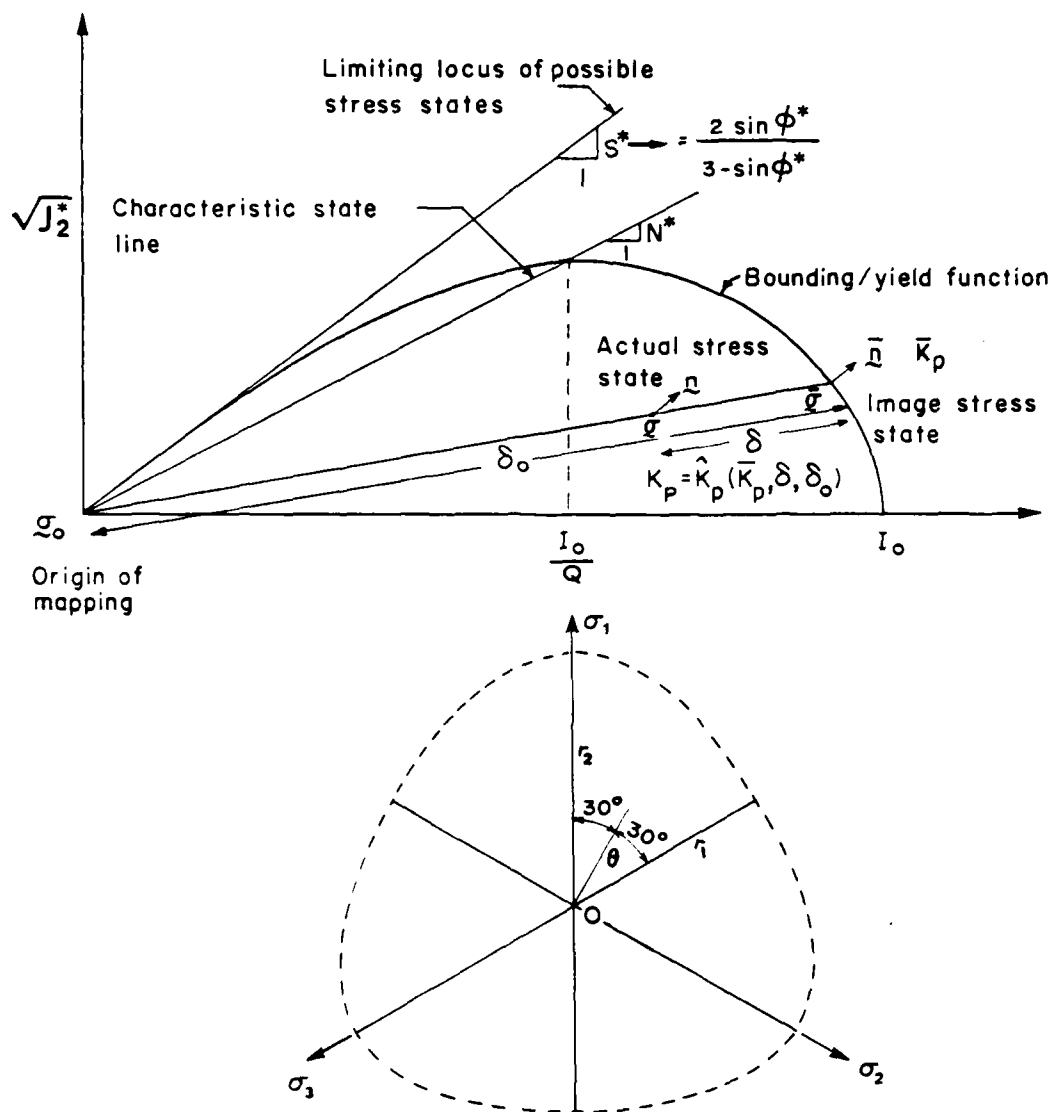


Figure 9. Meridional Section (top) and Octahedral Projection (bottom) of the Bounding Surface Representation.

where  $2a$  and  $2b$  are the major and minor axes respectively, and,  $h$  and  $k$  are the  $x$  and  $y$  coordinates of the center respectively.

Reorganization of the equation above gives rise to

$$F = (x-h)^2 + (a^2/b^2) (y-k)^2 = a^2,$$

and, by identifying  $x = \bar{I}_1$ ,  $h = (I_0/Q)$ ,  $y = \sqrt{J_2}^*$ ,  $k = 0$ ,  $a = I_0 - (I_0/Q)$ ,  $b = N^* (I_0/Q)$  and  $(a/b) = (Q-1)/N^*$ , we can now express the ellipse in this pressure-sensitive invariant stress space as:

$$F = \bar{I}_1^2 - 2 (I_0/Q) \bar{I}_1 + \{(Q-1)/N^*\}^2 \bar{J}_2^* + I_0^2 \{(2/Q)-1\} = 0. \quad (176)$$

Note that the parameter  $Q$  in equation 176 controls the aspect ratio of the ellipsoid's meridional section - it is actually equal to  $\{Q - 1\}$  divided by  $N^*$  -, and it can be regarded as a material parameter, the magnitude of which can be determined by either: a) heuristic methods, b) experience, or c) a back calculation based on the observed plastic strain rate trajectory.

## 2. Dilatation portion of piecewise continuous surface

The meridional segment of the surface, bounded by the CSL and the limiting asymptote (drawn through the origin of stress space and defined by  $S^*$ ) in the positive octant of principal stress space, is next presented. A thorough development of the equation used to describe this portion of the bounding surface is considered appropriate since (to the authors' knowledge) it is introduced in this paper for the first time in the soil mechanics plasticity theory literature.

Let us start by initially considering the following general second order equation (defined for convenience in an arbitrary rectangular



Cartesian x-y coordinate system) to which we shall subsequently apply the relevant constraints:

$$F = a x^2 + b y^2 + c xy + d y + e x + f = 0 . \quad (177)$$

As a first step, we can divide equation 177 by the coefficient of  $x^2$ , "a", and then rename the constants such that  $b = b/a$ ,  $c = c/a$ , etc.; this algebraic operation results in

$$F = x^2 + b y^2 + c xy + d y + e x + f = 0 . \quad (178)$$

Inserting the stress invariant variables in place of  $x$  and  $y$  in equation 178 yields

$$F = \bar{I}_1^2 + b \bar{J}_2^* + c \bar{I}_1 \sqrt{\bar{J}_2^*} + d \sqrt{\bar{J}_2^*} + e \bar{I}_1 + f = 0 . \quad (179)$$

Equation 179 is now subjected to four consecutive constraints such that this function is continuous with the ellipse and satisfies certain boundary stipulations:

a. Constraint #1:  $F = 0$  at  $\bar{I}_1 = \sqrt{\bar{J}_2^*} = 0$ ; this implies that the constant  $f$  is equal to zero, and, as a result, equation 179 reduces to

$$F = \bar{I}_1^2 + b \bar{J}_2^* + c \bar{I}_1 \sqrt{\bar{J}_2^*} + d \sqrt{\bar{J}_2^*} + e \bar{I}_1 = 0 . \quad (180)$$

b. Constraint #2: at  $\bar{I}_1 = \sqrt{\bar{J}_2^*} = 0$ ,  $d\sqrt{\bar{J}_2^*}/d\bar{I}_1 = S^*$ , and this condition establishes that

$$\begin{aligned} d\sqrt{\bar{J}_2^*}/d\bar{I}_1 &= -\partial F/\partial \bar{I}_1 + \partial F/\partial \sqrt{\bar{J}_2^*} \\ &= -(2\bar{I}_1 + c \sqrt{\bar{J}_2^*} + e) + (2b \sqrt{\bar{J}_2^*} + c \bar{I}_1 + d) = S^*, \end{aligned}$$

from which we obtain

$$e = -S^* d . \quad (181)$$

Substitution of equation 181 into equation 180 gives

$$F = \bar{I}_1^2 + b \bar{J}_2^* + c \bar{I}_1 \sqrt{\bar{J}_2^*} + d \sqrt{\bar{J}_2^*} - S^* d \bar{I}_1 = 0 . \quad (182)$$

c. Constraint #3: at  $\bar{I}_1 = (I_0/Q)$ ,  $\sqrt{J_2}^* = N^* (I_0/Q)$ , and substituting this contrived relation into equation 182 furnishes

$$d = (I_0/Q) [1 + bN^{*2} + cN^*] + [S^* - N^*] \quad (183)$$

And now we can substitute 183 into equation 182 to obtain

$$F = \bar{I}_1^2 + b \bar{J}_2^* + c \bar{I}_1 \sqrt{J_2}^* + \frac{(I_0/Q)[1 + bN^{*2} + cN^*]}{[S^* - N^*]} \{\sqrt{J_2}^* - S \bar{I}_1\} \quad (184)$$

d. Constraint #4: at  $\bar{I}_1 = I_0/Q$  and  $\sqrt{J_2}^* = N^* (I_0/Q)$ ,  
 $d\sqrt{J_2}^*/d\bar{I}_1 = 0$

but

$$d\sqrt{J_2}^*/d\bar{I}_1 = -\partial F/\partial \bar{I}_1 + \partial F/\partial \sqrt{J_2}^* = 0$$

which implies that  $\partial F/\partial \bar{I}_1 = 0$ , and therefore

$$2 \bar{I}_1 + c \sqrt{J_2}^* - S (I_0/Q) \frac{[1 + bN^{*2} + cN^*]}{[S^* - N^*]} = 0$$

from which we then see that

$$c = (S^*/N^{*2}) - (2/N^*) - S^* b \quad (185)$$

Finally, the substitution of equation 185 into equation 184 gives the following expression for the bounding surface characterizing the meridional section between the limit asymptote and the CSL:

$$F = \bar{I}_1^2 + b \bar{J}_2^* + \left[ \frac{S^*}{N^{*2}} - \frac{2}{N^*} - S^* b \right] \bar{I}_1 \sqrt{J_2}^* + \frac{(I_0/Q)[\frac{1}{N^*} - bN^*]}{N^*} \{\sqrt{J_2}^* - S^* \bar{I}_1\} = 0 \quad (186)$$

After exhausting all available constraints, inspection of equation 186 reveals that we have eliminated all but one independent parameter (i.e., "b") from the original set (i.e., "a", "b", "c", "d", "e", & "f"). This single distinct parameter can be considered analogous to Q in equation 176 inasmuch as it controls the longitudinal shape of a

certain section of the isotropic bounding/yield function, and, as will be discussed later, it also effectively dictates the direction of the plastic flow rate vector if normality is assumed.

### 3. Range of the parameters "Q" and "b" .

It now remains to specify the allowable range and qualitative significance of the shape controlling parameters Q and b. Theoretically, Q can vary in the range  $1 \leq Q \leq \infty$ , and this is obvious when one recalls that the axis ratio of the ellipse is equal to  $(Q - 1)/N$ . In the past, this value has been assumed to be equal to 2 (Reference 73) or 2.72 (Reference 67), but more recently however, magnitudes of Q closer to 5 have been reported for sand (References 6 and 74). The moderately detailed derivation that ensues determines the restriction on the parameter b for real roots over the range of interest and also sheds some light on the magnitude of "b" at which the canonical form of equation 186 undergoes a transition.

We must now set out to answer the following question: What is the restriction on the magnitude of "b" in equation 186 such that  $\bar{I}_1$  and  $\sqrt{J_2}^*$  are real in the range  $0 \leq \bar{I}_1 \leq (I_0/Q)$ ? Let us start by assuming that  $\bar{I}_1$  is known in equation 186, thus making it possible to solve the resulting quadratic for  $\sqrt{J_2}^*$  as follows:

$$b \bar{J}_2^* + \left\{ \left[ \frac{S^*}{N^{*2}} - \frac{2}{N^*} - S^* b \right] \bar{I}_1 + (I_0/Q) \left[ \frac{1}{N^*} - b N^* \right] \right\} \sqrt{J_2}^* + \left\{ \bar{I}_1^2 - (I_0/Q) \left[ \frac{1}{N^*} - b N^* \right] S^* \bar{I}_1 \right\} = 0 \quad (187)$$

Equation 187 may be rewritten more compactly as:

$$A \bar{J}_2^* + B \sqrt{J_2}^* + C = 0, \quad (188)$$

where

$$A = b \quad , \quad (189)$$

$$B = \left\{ \left[ \frac{S^*}{N^{*2}} - \frac{2}{N^*} - S^* b \right] \bar{I}_1 + (I_0/Q) \left[ \frac{1}{N^*} - bN^* \right] \right\} \quad , \quad (190)$$

and

$$C = \left\{ \bar{I}_1^2 - (I_0/Q) \left[ \frac{1}{N^*} - bN^* \right] S^* \bar{I}_1 \right\} \quad . \quad (191)$$

Solving the quadratic of equation 188 for

$$\sqrt{J_2}^* = \frac{-B \pm \sqrt{(B^2 - 4AC)}}{2A}$$

shows that the roots are real only if  $(B^2 - 4AC)$  is positive for  $0 \leq \bar{I}_1 \leq (I_0/Q)$ . Replacing the proxy relations of equations 189, 190 and 191 into the expression  $(B^2 - 4AC)$  results in

$$\begin{aligned} B^2 - 4AC &= \left\{ \left[ \frac{S^*}{N^{*2}} - \frac{2}{N^*} - S^* b \right]^2 - 4b \right\} \bar{I}_1^2 + \\ &2 \bar{I}_1 (I_0/Q) \left[ \frac{1}{N^*} - bN^* \right] \left[ \frac{S^*}{N^{*2}} - \frac{2}{N^*} + S^* b \right] + \\ &(I_0/Q)^2 \left[ \frac{1}{N^*} - bN^* \right]^2 \geq 0 \quad , \quad \text{for } 0 \leq \bar{I}_1 \leq (I_0/Q) \quad . \quad (192) \end{aligned}$$

We can now further investigate equation 192 by setting  $\bar{I}_1 = 0$  (i.e., its lower limit) and finding the limitation on  $b$  for real values of  $\sqrt{J_2}^*$ ; this operation yields

$$\begin{aligned} (I_0/Q)^2 \left[ \frac{1}{N^*} - bN^* \right]^2 &\geq 0 \\ \left[ \frac{1}{N^*} - bN^* \right]^2 &\geq 0 \\ b &\leq \frac{1}{N^{*2}} \quad . \quad (193) \end{aligned}$$

Equation 193 therefore places an upper bound on the magnitude of  $b$  for real roots, but, still, we must now proceed further to probe the

possibility of a lower bound. This can be accomplished by assigning  $\bar{I}_1$  the value of its upper limit,  $(I_0/Q)$ , in equation 192; this results in the following inequality:

$$\begin{aligned} & \left[ \frac{S^*}{N^{*2}} - \frac{2}{N^*} - S^*b \right]^2 - 4b + 2 \left[ \frac{1}{N^*} - bN^* \right] \left[ \frac{S^*}{N^{*2}} - \frac{2}{N^*} - S^*b \right] + \\ & \left[ \frac{1}{N^*} - bN^* \right]^2 \geq 0 . \end{aligned} \quad (194)$$

Equation 194 gives the same result as equation 193. We can now continue with our query into the possibility of the existence of a lower bound for  $b$  by simply substituting  $b = -\infty$  in equation 194 and testing for the validity of this inequality. This operation can be more tractably accomplished by first dividing equation 194 by  $b^2$  before the proposed substitution; after some simplification, the following result is deduced:

$$\begin{aligned} & (-S^*)^2 + 2(-N^*)(S^*) + (-N^*)^2 \geq 0 \\ & S^{*2} - 2N^*S^* + N^{*2} \geq 0 \\ & (S^* - N^*)^2 \geq 0 \\ & S^* \geq N^* . \end{aligned} \quad (195)$$

We can observe from figure 9 that equation 195 is in fact always true and hence there is no lower bound on the magnitude of the parameter  $b$ .

The next question that we may ask is: At what magnitude of  $b$  does the canonical form of equation 186 change from an ellipse to a hyperbola? Adopting the general procedure for determining the canonical form of 2nd order expressions, we can set the discriminant of equation 186 equal to zero and this produces

$$B^2 - 4AC = [S^{*2}] b^2 + \left[ -2 \frac{S^{*2}}{N^{*2}} + 4 \frac{S^*}{N^*} - 4 \right] b + \left[ \frac{S^{*2}}{N^{*4}} + \frac{4}{N^{*2}} - \frac{4 S^*}{N^{*3}} \right] = 0, \quad (196)$$

from which we can solve the quadratic in equation 196 for b; i.e.,

$$b = \frac{1}{S^{*2}} \left[ \frac{S^{*2}}{N^{*2}} - 4 \frac{S^*}{N^*} + 4 \right]. \quad (197)$$

This magnitude of b computed in equation 197 is the special case for a parabolic equation, but it also identifies the magnitude of b at which the canonical form switches from an ellipse to a hyperbola (i.e., b less than the equality in equation 197 implies a hyperbolic function while b greater than this equality infers an elliptic expression).

#### 4. Inclusion of Bounding Surface Variation on $\pi$ plane

Having presented the meridional sections, the next step is to complete the description by incorporating the variation of  $\sqrt{J_2}$  with the Lode angle,  $\bar{\theta}$ , in equations 176 and 186. Recall that  $\sqrt{J_2}^*$  is equal to  $[\sqrt{J_2} / g(\bar{\theta})]$  in the afore-mentioned equations, and thus, in order to complete the characterization, it is only necessary to specify the functional form of  $g(\bar{\theta})$  and thereafter to replace  $\sqrt{J_2}^*$  by  $[\sqrt{J_2} / g(\bar{\theta})]$  in equations 176 and 186.

The following expression, previously proposed by Gudehus (Reference 75), is adopted (see figure 9) for the yield/bounding representation:

$$g(\bar{\theta}) = \frac{2K}{[1-K] - [1-K] \sin 3\bar{\theta}}, \quad (198)$$

where  $-\pi/6 < \bar{\theta} = \text{Lode Angle} = \frac{1}{3} \arcsin \left[ \frac{3\sqrt{3}}{2} (\bar{J}_3 / \sqrt{J_2}^3) \right] < \pi/6$ .

Inspection of equation 198 shows that  $g(\pi/6) = 1$  and hence

$$\sqrt{J_2}^* = [\sqrt{J_2} / g(\bar{\theta})] = \sqrt{J_2}$$

at  $\bar{\theta} = \pi/6$  (note: this is the case, for example, in the conventional triaxial compression [CTC] test of figure 3). From equation 198, we can also see that  $g(-\pi/6) = K$ , and an example of a test with this particular Lode angle is the CTE in figure 3. We can therefore determine the parameter  $K$  by comparing the friction angles derived from CTC and CTE tests ( $\phi_c$  and  $\phi_e$  respectively). The proof that the parameter  $K$  can be determined from these friction angle data is presented in the sequel. As a first step, note that

$$\begin{aligned}\sqrt{J_2}(\pi/6) &= \sqrt{J_2}^* , \\ \sqrt{J_2}(-\pi/6) &= K \sqrt{J_2}^* ,\end{aligned}$$

and therefore,

$$\sqrt{J_2}(-\pi/6) + \sqrt{J_2}(\pi/6) = K . \quad (199)$$

From elementary soil mechanics, we can write the equations for the slopes of the compression and extension failure envelopes in  $I_1 - \sqrt{J_2}$  space as:

$$\sqrt{[3J_2(\pi/6)]}/p = q/p = 6 \sin \phi_c / (3 - \sin \phi_c) , \quad (200)$$

$$\sqrt{[3J_2(-\pi/6)]}/p = q/p = 6 \sin \phi_e / (3 + \sin \phi_e) , \quad (201)$$

where the subscripts  $c$  and  $e$  refer to compression and extension respectively while  $p$  is the mean stress.

Combining equations 199, 200, and 201, we find that

$$K = \{\sin \phi_e / \sin \phi_c\} \{(3 - \sin \phi_c) / (3 + \sin \phi_e)\} . \quad (202)$$

where, from the purely frictional assumption, it is implicit that  $K$  is independent of the mean normal pressure.

With equations 198 and 202, the function  $g(\bar{\theta})$  is now defined and we are furnished with the necessary information for replacing  $\sqrt{J_2}^* = \sqrt{J_2} /$

$g(\bar{\theta})$  in equations 176 and 186. The ensuing equations result directly from this replacement of variables.

For the region between the  $I_1$  axis and the CSL (i.e., the ellipse),

$$F = \bar{I}_1^2 - 2 (I_0/Q) \bar{I}_1 + \frac{\{(Q-1)/N^*\}^2 \bar{J}_2}{[g(\bar{\theta})]^2} + I_0^2 \{(2/Q)-1\} = 0, \quad (203)$$

and, for the region between the CSL and the failure envelope ,

$$F = \bar{I}_1^2 + \frac{b}{[g(\bar{\theta})]^2} \bar{J}_2 + \left[ \frac{S^*}{N^{*2}} - \frac{2}{N^*} - S^* b \right] \bar{I}_1 \sqrt{\bar{J}_2} \frac{1}{[g(\bar{\theta})]} + (I_0/Q) \left[ \frac{1}{N^*} - b N^* \right] \left\{ \frac{1}{[g(\bar{\theta})]} \sqrt{\bar{J}_2} - S^* \bar{I}_1 \right\} = 0. \quad (204)$$

#### C. COMPUTATION OF THE GRADIENT TENSOR TO THE BOUNDING SURFACE

Having stated the functional form of the bounding surface in three dimensional principal stress space, the next task at hand is to find what is perhaps one of the most important variables in plasticity theory: the gradient tensor to the bounding surface. Generally,  $F$  is a function of the nine independent components of the stress tensor, but the symmetry of the Cauchy stress tensor reduces the number of independent variables to six while the assumption of material isotropy, implicit throughout the previous discussion, further decreases the number of independent variables to the three unique invariants. It is therefore possible to compute the gradient  $\partial F / \partial \bar{g}$  in terms of the three independent variables -  $\bar{I}_1$ ,  $\sqrt{\bar{J}_2}$  and  $\bar{\theta}$  - of  $F$ . We can start by writing the expression for  $\partial F / \partial \bar{g}$  in terms of the chain rule



$$\frac{\partial F}{\partial \bar{\sigma}} = \frac{\partial F}{\partial \bar{I}_1} \frac{d\bar{I}_1}{d\bar{\sigma}} + \frac{\partial F}{\partial \sqrt{\bar{J}_2}} \frac{d\sqrt{\bar{J}_2}}{d\bar{\sigma}} + \frac{\partial F}{\partial \bar{\theta}} \frac{d\bar{\theta}}{d\bar{\sigma}}, \quad (205)$$

where

$$\sin 3\bar{\theta} = \left[ \frac{3\sqrt{3}}{2} (\bar{J}_3 / \sqrt{\bar{J}_2}^3) \right]. \quad (206)$$

From equation 206 we find that

$$\frac{d\bar{\theta}}{d\bar{\sigma}} = \frac{\sqrt{3}}{2 \cos 3\bar{\theta}} \left\{ \frac{\partial \bar{J}_3}{\partial \bar{\sigma}} \frac{1}{[\sqrt{\bar{J}_2}]^3} - \frac{3 \bar{J}_3}{[\sqrt{\bar{J}_2}]^4} \frac{\partial \sqrt{\bar{J}_2}}{\partial \bar{\sigma}} \right\}. \quad (207)$$

Substitution of equation 207 into equation 205 yields (in indicial notation)

$$\begin{aligned} \frac{\partial F}{\partial \bar{\sigma}_{ij}} = \nabla F = & \frac{\partial F}{\partial \bar{I}_1} \frac{\partial \bar{I}_1}{\partial \bar{\sigma}_{ij}} + \left\{ \frac{\partial F}{\partial \sqrt{\bar{J}_2}} - \frac{\sqrt{3}}{2 \cos 3\bar{\theta}} \frac{3 \bar{J}_3}{[\sqrt{\bar{J}_2}]^4} \frac{\partial F}{\partial \bar{\theta}} \right\} \frac{\partial \sqrt{\bar{J}_2}}{\partial \bar{\sigma}_{ij}} + \\ & \left\{ \frac{\sqrt{3}}{2 \cos 3\bar{\theta}} \frac{1}{[\sqrt{\bar{J}_2}]^3} \frac{\partial F}{\partial \bar{\theta}} \right\} \frac{\partial \bar{J}_3}{\partial \bar{\sigma}_{ij}}, \end{aligned} \quad (208)$$

where

$$\frac{d\bar{I}_1}{d\bar{\sigma}_{ij}} = \delta_{ij}, \quad (209)$$

$$\frac{d\sqrt{\bar{J}_2}}{d\bar{\sigma}_{ij}} = \frac{1}{2\sqrt{\bar{J}_2}} \bar{s}_{ij}, \quad (210)$$

$$\frac{d\bar{J}_3}{d\bar{\sigma}_{ij}} = \{a'_{ij}\}^T + \frac{1}{3} \bar{J}_2 \delta_{ij}, \quad (211)$$

in which

$$\bar{s}_{ij} = \bar{\sigma}_{ij} - \frac{1}{3} \bar{\sigma}_{kk} \delta_{ij}$$

and

$$\begin{aligned} \{a'_{ij}\}^T = & \{(\bar{s}_{22}\bar{s}_{33} - \bar{s}_{23}^2), (\bar{s}_{11}\bar{s}_{33} - \bar{s}_{13}^2), (\bar{s}_{11}\bar{s}_{22} - \bar{s}_{12}^2), \\ & (\bar{s}_{23}\bar{s}_{13} - \bar{s}_{33}\bar{s}_{12}), (\bar{s}_{13}\bar{s}_{12} - \bar{s}_{11}\bar{s}_{23}), (\bar{s}_{12}\bar{s}_{23} - \bar{s}_{22}\bar{s}_{13})\}. \end{aligned}$$

In order to find the gradient tensor, we need therefore only to compute the partial derivatives  $\frac{\partial F}{\partial \bar{I}_1}$ ,  $\frac{\partial F}{\partial \sqrt{J_2}}$ , and  $\frac{\partial F}{\partial \bar{\theta}}$  of equations 203 and

204. We find from equation 203,

$$\frac{\partial F}{\partial \bar{I}_1} = 2(\bar{I}_1 - \frac{I_0}{Q}) \quad , \quad (212)$$

$$\frac{\partial F}{\partial \sqrt{J_2}} = 2 \frac{\{(Q-1)/N^*\}^2 \sqrt{J_2}}{[g(\bar{\theta})]^2} \quad , \quad (213)$$

and

$$\frac{\partial F}{\partial g(\bar{\theta})} = -2 \frac{\{(Q-1)/N^*\}^2 \sqrt{J_2}}{[g(\bar{\theta})]^3} \quad . \quad (214)$$

Also, from equation 198, recognize that

$$\frac{dg(\bar{\theta})}{d\bar{\theta}} = \frac{6K(1-K) \cos 3\bar{\theta}}{[1+K] - [1-K] \sin 3\bar{\theta}} \quad , \quad (215)$$

which is to be used in the following relation:

$$\frac{\partial F}{\partial \bar{\theta}} = \frac{\partial F}{\partial g(\bar{\theta})} \frac{dg(\bar{\theta})}{d\bar{\theta}} \quad .$$

In a similar manner to the derivation of equations 212, 213 and 214, we find from equation 204 that

$$\frac{\partial F}{\partial \bar{I}_1} = 2 \bar{I}_1 + \left[ \frac{S^*}{N^{*2}} - \frac{2}{N^*} - S^* b \right] \sqrt{J_2} \frac{1}{[g(\bar{\theta})]} - (I_0/Q) \left[ \frac{1}{N^*} - bN^* \right] S^* \quad , \quad (216)$$

$$\begin{aligned} \frac{\partial F}{\partial \sqrt{J_2}} = & 2 \frac{b}{[g(\bar{\theta})]^2} \sqrt{J_2} + \left[ \frac{S^*}{N^{*2}} - \frac{2}{N^*} - S^* b \right] \bar{I}_1 \frac{1}{[g(\bar{\theta})]} + \\ & (I_0/Q) \left[ \frac{1}{N^*} - bN^* \right] \frac{1}{[g(\bar{\theta})]} \quad , \quad (217) \end{aligned}$$

and

$$\frac{\partial F}{\partial g(\bar{\theta})} = \frac{-2b}{[g(\bar{\theta})]^3} \bar{J}_2 - \left[ \frac{S^*}{N^{*2}} - \frac{2}{N^*} - S^* b \right] \bar{I}_1 \sqrt{\bar{J}_2} \frac{1}{[g(\bar{\theta})]^2} - \frac{(I_0/Q) \left[ \frac{1}{N^*} - bN^* \right]}{[g(\bar{\theta})]^2} \sqrt{\bar{J}_2} \quad (218)$$

It will be useful at this stage of the development to prematurely record two relationships which are extremely important in the subsequent discussion on hardening; these are

a). for the consolidation surface,

$$\frac{\partial F}{\partial I_0} = -2 \frac{\bar{I}_1}{Q} + 2 I_0 \left\{ \frac{2}{Q} - 1 \right\}, \quad (219)$$

and

b). for the dilation domain,

$$\frac{\partial F}{\partial I_0} = \frac{(1/Q) \left[ \frac{1}{N^*} - bN^* \right]}{[g(\bar{\theta})]} \left\{ \frac{1}{[g(\bar{\theta})]} \sqrt{\bar{J}_2} - S^* \bar{I}_1 \right\} \quad (220)$$

#### D. MAPPING RULE LINKING ARBITRARY STRESS STATE TO CONJUGATE POINT

An important attribute of the bounding surface constitutive formulation is the association of the actual stress point,  $\sigma_{ij}$ , to a unique "image" point,  $\bar{\sigma}_{ij}$ , on  $F=0$ . This feature enables us to simulate cyclic stress-strain response by correlating both the plastic loading direction,  $\bar{n}$ , and the plastic modulus,  $\bar{K}_p$ , at the image point  $\bar{g}$  on  $F$ , to the plastic loading vector,  $n$ , and the plastic modulus,  $K_p$ , at the actual stress state,  $g$ . How is this image point,  $\bar{g}$ , defined when the actual stress state does not actually reside on  $F(\bar{g}, q_n)=0$ ? Dafalias (Reference 76) has proposed the radial mapping rule which assumes the existence of an origin in stress space,  $g_0$ , enclosed within the convex bounding surface; once this origin has been selected, the image point

is obtained as the intersection of  $F = 0$  by the straight line passing through the origin and  $\underline{g}$ . This can be expressed analytically as:

$$\bar{\underline{g}} - \underline{g}_0 = \beta (\underline{g} - \underline{g}_0) \quad . \quad (221)$$

From equation 221, it can be easily verified that  $\beta = 1$  when  $\underline{g} = \bar{\underline{g}}$  and  $\beta \rightarrow \infty$  as  $\underline{g}$  approaches  $\underline{g}_0$ . The "simple" mapping rule, in which  $\underline{g}_0 = \underline{0}$ , has been found to give realistic predictions for clays (Reference 77). In order to simplify the presentation of the equations, the "simple" mapping rule is assumed henceforth and equation 221 promptly reduces to

$$\bar{\underline{g}} = \beta \underline{g} \quad . \quad (222)$$

The motivation for the term "radial" mapping becomes more apparent when one observes from equation 222 that the definition of the image point can be interpreted as an imaginary radial (or proportional) loading from the current stress state to the point at which this hypothetical loading program intersects the surface,  $F=0$ ; i.e.,

$$\frac{\bar{\sigma}_{11}}{\sigma_{11}} = \frac{\bar{\sigma}_{22}}{\sigma_{22}} = \frac{\bar{\sigma}_{33}}{\sigma_{33}} = \frac{\bar{\sigma}_{12}}{\sigma_{12}} = \frac{\bar{\sigma}_{13}}{\sigma_{13}} = \frac{\bar{\sigma}_{23}}{\sigma_{23}} = \beta \quad .$$

It is instructive to pause at this point and reflect upon the consequences of not effecting the "simple" mapping rule (i.e.,  $\underline{g}_0 \neq \underline{0}$ ). Say we assume that the bounding surface in figure 9 is used in conjunction with the associated flow rule of plasticity. Consider now that the isotropic sample is then subjected to a hydrostatic consolidation and swell test; based upon theoretical considerations, we would expect our mathematical model to predict a purely volumetric strain rate during the loading and unloading phases. From figure 9, we can note that there is only one location on the bounding surface which

will predict no shear strains and this point is located at the intersection of the elliptic consolidation surface and the  $I_1$  axis. This immediately implies that the origin of mapping must lie somewhere along the  $I_1$  axis. But we must now inquire if this origin of mapping can be specified arbitrarily on the  $I_1$  axis? This question can again be simply answered by examining the expected response for the hydrostatic unloading after the initial spherical loading. Say we had defined the origin at some point  $\gamma I_0$ , where  $\gamma$  ensures that the origin remains within the convex bounding surface (i.e.  $0 \leq \gamma \leq 1$ ), and then we had proceeded to unload the specimen to a magnitude of mean normal pressure which made  $I_1$  less than  $\gamma I_0$ . It is apparent that this hypothetical mapping rule will then put the image stress state on the dilatation surface at the origin of stress space; at this point, the slope of the bounding surface has been defined as  $S^*$  and will always predict a shear strain component! By a process of elimination therefore, we have excluded all but the "simple" mapping rule when associative flow is employed for simulating the response of an isotropic material with this particular bounding surface representation.

The six-dimensional Cauchy stress tensor representation in equation 221 must be re-stated in terms of its invariants for subsequent use in the previously derived isotropic bounding surface function. It is straight-forward from equation 222 that

$$\bar{\sigma}_{kk} = \beta \sigma_{kk} \quad \text{or} \quad \bar{I}_1 = \beta I_1, \quad (223)$$

and it can be further deduced that  $\bar{s}_{ij} = \beta s_{ij}$  which directly implies

$$\sqrt{\bar{J}_2} = \beta \sqrt{J_2}. \quad (224)$$

Inspection of equation 206 reveals that the Lode angle,  $\theta$ , is unaffected by the magnitude of  $\beta$  (i.e.,  $\bar{\theta} = \theta$ ) as shown below

$$\begin{aligned}\sin 3\bar{\theta} &= \left[ \frac{3\sqrt{3}}{2} (\bar{J}_3/\sqrt{J_2}^3) \right] = \left[ \frac{3\sqrt{3}}{2} [(\beta^3 J_3)/(\beta^3 \sqrt{J_2}^3)] \right] \\ &= \left[ \frac{3\sqrt{3}}{2} (J_3/\sqrt{J_2}^3) \right] = \sin 3\theta \quad .\end{aligned}\quad (225)$$

The result in equation 225 indicates that the function  $g(\bar{\theta})$  in equation 198 is insensitive to whether or not the actual stress state is on the bounding surface. If the state of stress is known, we can solve for  $\beta$  by substituting equations 223 and 224 into the appropriate choice of equations 203 or 204. With the "simple" mapping rule, the applicable meridional section (i.e., above or below the CSL) is trivially determined by the ratio  $\sqrt{J_2}/I_1$  of the actual stress state, but, for an arbitrary location of the origin of mapping, the portion of the surface bearing the image point will have to be resolved by checking to see if the straight line passing through the origin,  $g_0$ , and the actual stress state,  $g$ , crosses the CSL while  $F \leq 0$ .

Substitution of equations 223 and 224 into equation 203 leads to

$$\begin{aligned}F &= \beta^2 I_1^2 - 2 (I_0/Q) \beta I_1 + \frac{\{(Q-1)/N^*\}^2 \beta^2 J_2}{[g(\theta)]^2} + \\ &I_0^2 \{(2/Q)-1\} = 0.\end{aligned}\quad (226)$$

With the current state of stress ( $I_1$ ,  $\sqrt{J_2}$  and  $\theta$ ) and the location of the bounding ellipse ( $I_0$ ) known, it is now possible to solve the resulting quadratic equation for  $\beta$  in equation 225. The solution may be written in the condensed manner,

$$\beta = \frac{-B \pm \sqrt{B^2 - 4AC}}{2A} \quad , \text{ with } 1 \leq \beta \leq \infty \quad (227)$$

where

$$A = I_1^2 + \frac{\{(Q-1)/N^*\}^2}{[g(\theta)]^2} J_2 \quad ,$$

$$B = -2 (I_0/Q) I_1 \quad ,$$

and

$$C = I_0^2 \{(2/Q)-1\} \quad .$$

Equation 227 can be validated very easily by substituting into this equation the two coordinates in invariant stress space where we know in advance that the magnitude of  $\beta$  is equal to unity. These two obvious cases occur at the following positions:  $\{I_1 = I_0, \sqrt{J_2} = 0\}$  and  $\{I_1 = (I_0/Q), \sqrt{J_2} = N(I_0/Q)\}$ ; independent insertion of each these coordinate component sets into equation 227 shows that, for both instances, one of the roots of the equation is indeed equal to unity while the other root is less than one. If the reader should actually check these cases, it will be observed that the  $\pm$  operator in equation 227 is important, and hence, in numerical implementation, it is essential to check both roots of equation 227 and then select  $\beta$  as being equal to the root that is greater than or equal to one.

An analogous procedure can be adopted in the derivation and corroboration of the equation for  $\beta$  for the second portion of the piecewise continuous meridional section. We proceed by interchanging in equation 204 the equalities expressed in equations 223 and 224, and obtain

$$F = \beta^2 I_1^2 + \frac{b}{[g(\theta)]^2} \beta^2 J_2 + \left[ \frac{S^*}{N^{*2}} - \frac{2}{N^*} - S^* b \right] \beta^2 I_1 \sqrt{J_2} \frac{1}{[g(\theta)]} + \\ (I_0/Q) \left[ \frac{1}{N^*} - b N^* \right] \beta \left\{ \frac{1}{[g(\theta)]} \sqrt{J_2} - S^* I_1 \right\} = 0$$

which gives the result

$$\beta = \frac{A}{B}, \quad (228)$$

where

$$A = - (I_0/Q) \left[ \frac{1}{N^*} - bN^* \right] \left\{ \frac{1}{[g(\theta)]} \sqrt{J_2} - S^* I_1 \right\},$$

and

$$B = I_1^2 + \frac{b}{[g(\theta)]^2} J_2 + \left[ \frac{S^*}{N^{*2}} - \frac{2}{N^*} - S^* b \right] I_1 \sqrt{J_2} \frac{1}{[g(\theta)]}.$$

It can be easily verified that  $\beta$  is equal to unity for equation 228 when the coordinate components are  $\{I_1 = (I_0/Q), \sqrt{J_2} = N(I_0/Q)\}$ , but remember that, by definition,  $\beta$  is undefined at  $g_0$ ; that is, at  $\{I_1 = 0, \sqrt{J_2} = 0\}$   $\beta \rightarrow \infty$ .

#### E. THE LOADING FUNCTION

From equation 116, recall that the loading function is defined as:

$$L = \frac{1}{K_p} \frac{\partial F}{\partial \bar{\sigma}_{ij}} \dot{\bar{\sigma}}_{ij},$$

where  $K_p$  is the plastic modulus, and this definition implies that the plastic loading direction at a stress state within the bounding surface is defined as  $\nabla F$  at its image stress point (or  $\underline{n} = \bar{\underline{n}}$ ). For a reloading or virgin loading stress path (i.e.,  $\frac{\partial F}{\partial \bar{\sigma}_{ij}} \dot{\bar{\sigma}}_{ij} > 0$ ), the plastic loading

direction is defined as  $\nabla F$  (or  $\underline{n} = \bar{\underline{n}}$ ), but, for a reverse loading event, when  $\frac{\partial F}{\partial \bar{\sigma}_{ij}} \dot{\bar{\sigma}}_{ij} < 0$ , the loading direction is specified as  $-\nabla F$  (or

$\underline{n} = -\bar{\underline{n}}$ ). These assumptions ensure that the loading function is always



non-negative leading to the generation of non-zero plastic strains except for neutral loading where  $\frac{\partial F}{\partial \bar{\sigma}_{ij}} \dot{\sigma}_{ij}$  is equal to zero.

We can therefore compute the loading function,  $L$ , by first substituting equations 223 and 224 into equation 208 and then take the inner product of the resulting second order tensor with  $\dot{\bar{q}}$  to produce

$$L = \frac{1}{K_p} \frac{\partial F}{\partial \bar{\sigma}_{ij}} \dot{\sigma}_{ij} = \frac{1}{K_p} \nabla F : \dot{\bar{q}} = \frac{1}{K_p} \left[ \frac{\partial F}{\partial \bar{I}_1} \delta_{ij} + \frac{\partial F}{\partial \sqrt{J_2}} \frac{1}{2\sqrt{J_2}} s_{ij} + \frac{\sqrt{3}}{2 \cos 3\theta} \frac{1}{\beta} \frac{\partial F}{\partial \theta} \left\{ \frac{1}{[\sqrt{J_2}]^3} \frac{\partial J_3}{\partial \sigma_{ij}} - \frac{3 J_3}{[\sqrt{J_2}]^4} \frac{\partial \sqrt{J_2}}{\partial \sigma_{ij}} \right\} \right] \dot{\sigma}_{ij}$$

which simplifies to

$$L = \frac{1}{K_p} \left[ \frac{\partial F}{\partial \bar{I}_1} \dot{\bar{I}}_1 + \frac{\partial F}{\partial \sqrt{J_2}} \dot{\sqrt{J_2}} + \frac{\sqrt{3}}{2 \cos 3\theta} \frac{1}{\beta} \frac{\partial F}{\partial \theta} \left\{ \frac{\dot{J}_3}{[\sqrt{J_2}]^3} - \frac{3 J_3 \dot{\sqrt{J_2}}}{[\sqrt{J_2}]^4} \right\} \right],$$

and can be finally written in the compact form

$$L = \frac{1}{K_p} \left[ \frac{\partial F}{\partial \bar{I}_1} \dot{\bar{I}}_1 + \frac{\partial F}{\partial \sqrt{J_2}} \dot{\sqrt{J_2}} + \frac{1}{\beta} \frac{\partial F}{\partial \theta} \dot{\theta} \right], \quad (229)$$

where

$$\dot{\theta} = \frac{\sqrt{3}}{2 \cos 3\theta} \left\{ \frac{1}{[\sqrt{J_2}]^3} \dot{J}_3 - \frac{3 J_3}{[\sqrt{J_2}]^4} \dot{\sqrt{J_2}} \right\}.$$

#### F. THE FLOW RULE

With the definition of the loading function  $L$ , we can now write the constitutive relation for the plastic strain rate (equation 117) as:

$$\dot{\epsilon}_{ij}^p = L m_{ij},$$

where  $m_{ij}$  are the components of the unit tensor gradient to the plastic potential.

It is proposed, at this stage in the development of the constitutive model, that the history of the plastic strain tensor,  $(\underline{\epsilon}^p)^t$ , be used as the sole plastic internal variable for characterizing the internal state of the material. Invariant quantities of the plastic strain tensor, analogous to the first invariant of the stress tensor ( $I_1$ ) and the square root of the second invariant of the deviatoric stress tensor ( $\sqrt{J_2}$ ), are selected such that the nine independent components of the symmetric small strain tensor can now be replaced by these two independent plastic state variables. These invariants are: a) the plastic volumetric strain,  $\epsilon_{kk}^p$  (denoted by the symbol  $\xi$ ), and b) the plastic equivalent shear strain defined as:

$$\eta = \int_t \dot{\eta} dt = \int_t \sqrt{\frac{1}{2} \dot{\epsilon}_{ij}^p \dot{\epsilon}_{ij}^p} dt, \quad (230)$$

where  $\dot{\epsilon}_{ij}^p = \dot{\epsilon}_{ij}^p - \frac{1}{3} \dot{\epsilon}_{kk}^p \delta_{ij}$ .

The quantity  $\dot{\eta}$  is known as the generalized or equivalent plastic strain increment (Reference 66) and takes the same invariant form as  $\sqrt{J_2}$  is of the components of the stress tensor  $\underline{g}$ . The equivalent strain  $\eta$  provides a measure of the plastic distortion and it is important to recognize that this quantity is computed by continually summing the positive scalar  $\sqrt{\frac{1}{2} \dot{\epsilon}_{ij}^p \dot{\epsilon}_{ij}^p}$ . This implies that  $\eta$  will not be equal to zero if an element of sand was distorted and then returned to its original shape (i.e.,  $\underline{\epsilon}^p = \underline{0}$ ), but its magnitude will instead reflect the history of plastic distortion  $(\underline{\epsilon}^p)^t$ .

From the flow rule in equation 117 and the plastic strain increment invariants defined above, these following useful relations are obtained:

$$\dot{\xi} = \dot{\epsilon}_{kk}^p = L \, m_{kk} \quad , \quad (231)$$

$$\dot{\epsilon}_{ij}^p = \dot{\epsilon}_{ij}^p = L \left( m_{ij} - \frac{1}{3} m_{kk} \delta_{ij} \right), \text{ or}$$

$$\dot{\epsilon}_{ij}^p = L \, \underline{m}^d \text{ where } \underline{m}^d = \underline{m} - \frac{1}{3} m_{kk} \delta \quad ; \quad (232)$$

$$\dot{\eta} = \sqrt{\left[ \frac{1}{2} L^2 \left( m_{ij} - \frac{1}{3} m_{kk} \delta_{ij} \right) \left( m_{ij} - \frac{1}{3} m_{kk} \delta_{ij} \right) \right]} ,$$

$$\dot{\eta} = L \sqrt{\left[ \frac{1}{2} \left( m_{ij} m_{ij} - \frac{1}{3} m_{kk}^2 \right) \right]} ,$$

but  $\underline{m}$  is a unit tensor, therefore,

$$\dot{\eta} = L \sqrt{\left[ \frac{1}{2} \left( 1 - \frac{1}{3} m_{kk}^2 \right) \right]} \quad . \quad (233)$$

#### G. BACK CALCULATION OF THE PARAMETERS "Q" AND "b"

With the introduction of the scalar quantities  $\dot{\xi}$  and  $\dot{\eta}$  in the previous subsection, it is perhaps instructive to interject at this point in the discussion and inspect the qualitative nature as well as the quantitative significance of the parameters Q and b. Remember that these parameters control the meridional shape of the piecewise continuous bounding surface.

If we assume that the bounding function F is also the plastic potential function (i.e., associative flow), we can attach some relevancy to these parameters since they now effectively control the simulation of dilatancy. Here, dilatancy is defined as the ratio of the plastic volumetric strain rate ( $\dot{\xi}$ ) to the plastic equivalent shear strain rate ( $\dot{\eta}$ ). Several authors [perhaps most notably, Rowe (Reference 78)] have postulated the existence of a unique relationship between the dilatancy and the ratio,  $\sqrt{J_2^*}/I_1$ . Observation of the ratio of plastic volumetric strain rate to plastic equivalent shear strain rate data

from 'triaxial' tests confirm that the dilatancy is approximately constant (see for example, Reference 78), and hence we can make use of this phenomena to provide realistic estimates of the parameters "Q" and "b".

Dividing equation 231 by equation 233 and employing the normality rule of plasticity results in

$$\frac{\dot{\xi}}{\dot{\eta}} = 6 \frac{\partial F}{\partial I_1} + \frac{\partial F}{\partial \sqrt{J_2}^*} . \quad (234)$$

Given the incremental plastic strain tensor and the state of stress ( $I_1, \sqrt{J_2}^*$ ) we can iteratively solve for the parameter "Q" or "b" using the following steps: 1) Assume a magnitude for "Q" or "b" within their respective limits, 2) Solve for  $I_0$  using equation 176 or equation 186 (this choice of equations depends on whether the stress state is above or below the critical state line), 3) With the appropriate gradient tensor equations (i.e., equations 212 and 213 or equations 216 and 217) solve equation 234 for the ratio  $\dot{\xi}/\dot{\eta}$  and compare to the experimental result, and 4) Repeat this procedure with a different estimate of "Q" or "b" until an acceptable tolerance for the ratio  $\dot{\xi}/\dot{\eta}$  in step 3 is achieved.

#### H. THE CONSISTENCY CONDITION

The consistency condition is invoked for the bounding surface to guarantee that the load increment leads from one plastic state to another. This is accomplished by setting

$$\dot{F} = \frac{\partial F}{\partial \bar{g}} : \dot{\bar{g}} + \frac{\partial F}{\partial q_n} \dot{q}_n = 0 ; \quad (235)$$

further, from equation 116, we can verify that

$$L = \frac{1}{\bar{K}_p} \frac{\partial F}{\partial \bar{\sigma}_{ij}} \dot{\bar{\sigma}}_{ij} ,$$

and hence,

$$\frac{\partial F}{\partial \bar{\sigma}} : \dot{\bar{\sigma}} = \bar{K}_p L \quad . \quad (236)$$

By specifying that the rate equations for the  $n$  plastic internal variables be written as:

$$\dot{q}_n = L r_n , \quad (237)$$

we can then restate the consistency condition to read

$$\bar{K}_p L + \frac{\partial F}{\partial q_n} L r_n = 0 ,$$

which when divided through by the loading function,  $L$ , yields

$$\dot{F} = \bar{K}_p + \frac{\partial F}{\partial q_n} r_n = 0 .$$

Hence,

$$\bar{K}_p = - \frac{\partial F}{\partial q_n} r_n \quad . \quad (238)$$

From the flow rule (equation 117), we can see, for example, that if the components of the plastic strain tensor were chosen as the "hidden" variables,  $q_1$ , then  $r_1$  will be represented by the unit gradient tensor to the plastic potential,  $\underline{m}$ .

## I. SELECTION OF PLASTIC INTERNAL VARIABLES

Observe that the location (or size) of the yield/bounding surface can be identified by using a single variable,  $I_0$  which is the point

where the elliptic cap intersects the hydrostatic stress axis. We can therefore express our isotropic hardening law by determining  $\frac{\partial I_0}{\partial q_n}$

[i.e.,  $I_0 = \hat{I}_0(q_n)$  implies  $F(\bar{q}, I_0)$ ] for each of the  $n$  so-called independent "hidden" variables and then use the chain rule to find

$$\frac{\partial F}{\partial q_n} \dot{q}_n = \frac{\partial F}{\partial I_0} \frac{\partial I_0}{\partial q_n} \dot{q}_n,$$

where  $\frac{\partial F}{\partial I_0}$  is computed from either equations 219 or 220. Our task is now

simply the determination of  $\frac{\partial I_0}{\partial q_n} \dot{q}_n$ .

Since overconsolidated clays and dense sands exhibit stable behavior, despite dilatancy, until the peak stress is attained, a refined description of the customary critical state model (or pure density hardening) is required. Enhancement of the density hardening can be achieved by assuming that additional hardening takes place due to the shear action. Three possible approaches for including this distortional hardening aspect are discussed in the following.

#### 1. Combined Hardening Parameter (Strain)

The first alternative that is presented is due to Nova and Wood (Reference 79) wherein they introduced a combined hardening parameter,  $T$ , whose rate is expressed as follows:

$$\dot{T} = \Lambda \dot{\eta} + \dot{\xi}, \quad (239)$$

where  $\Lambda$  is a constant parameter, and,  $\dot{\eta}$  and  $\dot{\xi}$  are defined in equations 231 and 233 respectively. Keeping in mind that the objective is to

compute  $\frac{\partial I_0}{\partial q_n} \dot{q}_n$ , we can state for this particular case that our current

aim is the calculation of

$$\frac{\partial I_0}{\partial T} \dot{T} = \frac{\partial I_0}{\partial T} [\lambda \dot{\eta} + \dot{\xi}] \quad (240)$$

As a general rule, a partial derivative can be found by observing the variation of the value of a function when we give an increment to one independent variable and keep all the other variables constant. In order to evaluate  $\frac{\partial I_0}{\partial T}$  with  $\dot{\eta} = 0$ , we can perform a hydrostatic

consolidation test on a normally consolidated isotropic specimen and observe the relation between  $I_0$  and  $\xi$ ; for this particular case,  $\frac{\partial I_0}{\partial T} = \frac{\partial I_0}{\partial \xi}$ . Experimentally we may observe that there is a unique relationship

between  $I_0$  and  $\epsilon_{kk}|_{\eta=0}$  that can be expressed as:

$$I_0 = [I_0]_{\text{initial}} \exp(\lambda \epsilon_{kk}) \quad (241)$$

and after taking the time derivative of both sides of the equality in equation 241, we find that we can now restate this relationship as:

$$\dot{I}_0 = [I_0]_{\text{initial}} \exp(\lambda \epsilon_{kk}) \lambda \dot{\epsilon}_{kk} \quad (242)$$

By replacing equation 241 in equation 242, we can write the rate equation as:

$$\dot{\epsilon}_{kk}|_{\eta=0} = \frac{1}{\lambda} \frac{\dot{I}_0}{I_0} \quad (243)$$

where  $\lambda$  is a soil constant. This functional form will be recognized by geotechnical engineers as the usual semi-logarithmic relationship between the void ratio and the mean normal effective stress (i.e.,  $e$  vs.  $\log p'$ ).

If we unload the specimen, still under isotropic conditions, we find that the recoverable or elastic part of the volumetric strain rate can be expressed by a relation similar to equation 243 so that

$$\dot{\epsilon}_{kk}^e|_{\eta=0} = \frac{1}{\kappa} \frac{\dot{I}_0}{I_0}, \quad (244)$$

where  $\kappa$  is another constant larger than  $\lambda$ . The irrecoverable or plastic volumetric strain rate is therefore given by

$$\dot{\epsilon}_{kk}^p|_{\eta=0} = \dot{\xi}|_{\eta=0} = \frac{\kappa - \lambda}{\lambda \kappa} \frac{\dot{I}_0}{I_0}, \quad (245)$$

from which we can easily see

$$\frac{\partial I_0}{\partial \xi} = \frac{\partial I_0}{\partial T} = I_0 \frac{\kappa - \lambda}{\kappa - \lambda}, \quad (246)$$

and substitution of equation 246 into equation 240 leads to

$$\frac{\partial I_0}{\partial T} \dot{T} = \frac{\partial I_0}{\partial \xi} [\Lambda \dot{\eta} + \dot{\xi}] = I_0 \frac{\kappa - \lambda}{\kappa - \lambda} [\Lambda \dot{\eta} + \dot{\xi}]. \quad (247)$$

As an aid to understanding this hardening rule, note that equation 247 reflects the assumption that we can write

$$\frac{\partial I_0}{\partial \eta} = \Lambda \frac{\partial I_0}{\partial \xi}.$$

We are still left with determining the parameter  $\Lambda$ , and, in principle, we can perform an analogous test with  $\sqrt{J_2}^*/I_1 = N^*$  such that  $\dot{\xi} = 0$  with the result that the hardening process takes place along the zero-dilatancy line. It should be noted that this process is not unique since the particular stress state  $\sqrt{J_2}^*/I_1 = N^*$  can be reached either during a hardening process or at the end of softening, at the critical state. Note that the critical state (when unlimited deformations can occur without change of stress or volume) may not coincide with



failure. If the critical state is reached after softening, no variation of  $I_0$  is possible because the material has already experienced "infinite" strains when it encountered the "failure" line, but if the material approaches the CSL during a hardening process, we would assume that  $I_0$  can vary. In the former case, we would therefore set the constant  $\Lambda$  equal to zero while  $\Lambda$  will be positive in the latter.

Nova and Wood (Reference 79) suggests an alternative procedure to the difficult determination of  $\Lambda$  through a  $\sqrt{J_2}^*/I_1 = N^* = \text{constant}$  test. Before discussing this alternate method, it will be necessary to introduce some preliminaries; the following stress-dilatancy relationship is foremost:

$$\sqrt{J_2}^*/I_1 = N^* - \mu (\dot{\xi}/\dot{\eta}) \quad , \quad (248)$$

where  $\mu$  is a material parameter. At  $\dot{\xi} = 0$ , we can find  $N^*$  ( $= \sqrt{J_2}^*/I_1$ ), and then subsequently use this parameter to find  $\mu$  from the relation in equation 248. Based upon theoretical considerations presented in their paper, Nova and Wood (Reference 79) have shown that the effective stress path tends asymptotically to a definite value of  $\sqrt{J_2}^*/I_1$  for an undrained test (i.e., no total volume change), and this effective stress path can be depicted in the equation

$$\sqrt{J_2}^*/I_1 = N^* + \frac{\lambda}{\kappa} \mu \Lambda \quad . \quad (249)$$

With  $\kappa$ ,  $\lambda$ ,  $\mu$  and  $N^*$  known from procedures outlined previously, we can therefore get an estimate of  $\Lambda$  by observing the asymptotic difference  $[\sqrt{J_2}^*/I_1 - N^*]$  which occurs during an undrained test.

The final step is the computation of the bounding plastic modulus,  $\bar{K}_p$ , from the consistency condition. This can be simply effected by first substituting equations 231 and 233 in equation 247 to obtain

$$\begin{aligned} \frac{\partial I_0}{\partial T} \dot{T} &= I_0 \frac{\kappa \lambda}{\kappa - \lambda} [\Lambda \dot{n} + \dot{\xi}] \\ &= I_0 \frac{\kappa \lambda}{\kappa - \lambda} [\Lambda L \sqrt{\{ \frac{1}{2} (1 - \frac{1}{3} m_{kk}^2 ) \}} + L m_{kk}], \end{aligned} \quad (250)$$

and then substituting equation 250 into the consistency condition

$$\bar{K}_p L + \frac{\partial F}{\partial I_0} \frac{\partial I_0}{\partial T} \dot{T} = 0$$

which results in the following expression for  $\bar{K}_p$ :

$$\bar{K}_p = - \frac{\partial F}{\partial I_0} I_0 \frac{\kappa \lambda}{\kappa - \lambda} [\Lambda \sqrt{\{ \frac{1}{2} (1 - \frac{1}{3} m_{kk}^2 ) \}} + m_{kk}]. \quad (251)$$

With the form of the yield/bounding surface assumed in this paper, it is possible to solve for the parameter  $\Lambda$  directly from equation 251 without having to perform an undrained test. With an associative flow rule assumption, we find that the dilatancy expression can be stated as:

$$\frac{\dot{\xi}}{\dot{n}} = m_{kk} + \sqrt{\{ \frac{1}{2} (1 - \frac{1}{3} m_{kk}^2 ) \}} = - \frac{1}{S^*}, \quad (252)$$

at failure, but at this point, we would also expect the plastic modulus in equation 251 to go to zero. This means that

$$[\Lambda \sqrt{\{ \frac{1}{2} (1 - \frac{1}{3} n_{kk}^2 ) \}} + n_{kk}] = 0, \quad (253)$$

and combining equations 252 and 253, we find

$$\Lambda = \frac{1}{S^*}.$$

## 2. Combined Hardening (Work)

The second approach that includes the shear action in the isotropic hardening is similar to Nova and Wood's (Reference 79)

combined parameter just described, but, instead of plastic strain, the formulation is based on plastic work,  $W_p$ . In analogy to the synthesized parameter  $T$  employed in the previous development, the plastic work rate is defined as:

$$\dot{W}_p = \underline{s} : \dot{\underline{\epsilon}}^p + \frac{I_1}{3} \dot{\epsilon} \quad (254)$$

Substitution of equation 254 into the consistency criteria results in

$$\begin{aligned} \bar{K}_p L + \frac{\partial F}{\partial W_p} \dot{W}_p &= \bar{K}_p L + \frac{\partial F}{\partial W_p} \left[ \underline{s} : \dot{\underline{\epsilon}}^p + \frac{I_1}{3} \dot{\epsilon} \right] = 0 \\ &= \bar{K}_p L + \frac{\partial F}{\partial I_0} \frac{\partial I_0}{\partial W_p} \left[ \underline{s} : \dot{\underline{\epsilon}}^p + \frac{I_1}{3} \dot{\epsilon} \right] = 0 \quad (255) \end{aligned}$$

Substituting equations 231 and 232 into equation 255 gives

$$\bar{K}_p L + \frac{\partial F}{\partial I_0} \frac{\partial I_0}{\partial W_p} \left[ \underline{s} : L \underline{m}^d + \frac{I_1}{3} L m_{kk} \right] = 0 \quad ,$$

from which we can compute the plastic modulus to be

$$\bar{K}_p = - \frac{\partial F}{\partial I_0} \frac{\partial I_0}{\partial W_p} \left[ \underline{s} : \underline{m}^d + \frac{I_1}{3} m_{kk} \right] \quad (256)$$

The only unknown in equation 256 is the quantity  $\frac{\partial I_0}{\partial W_p}$  which must be calibrated from an estimated relationship based on experimental observations. Lade (Reference 80) and Lade and Duncan (Reference 55) have utilized the plastic work,  $W_p$ , extensively as a hardening parameter and their proposed relationship between plastic work and the mean pressure (or  $I_0$ ) along the virgin hydrostatic compression path takes the form:

$$W_p = C p_a \left[ \frac{I_0^2}{3 p_a^2} \right]^r \quad (257)$$

where  $p_a$  is the atmospheric pressure, and,  $C$  and  $r$  are material parameters which can be determined from a plot of  $\log (W_p/p_a)$  versus  $\log \left[ \frac{I_0^2}{3 p_a^2} \right]$ . The parameter " $r$ " is the slope of the transformed straight line graph while " $C$ " is the magnitude of  $\log (W_p/p_a)$  at  $\left[ \frac{I_0^2}{3 p_a^2} \right]$  equal to 1. By rearranging equation 257 to put  $I_0$  in terms of  $W_p$ , we find

$$I_0 = \sqrt{3} p_a [W_p/(C p_a)]^{5/r},$$

and therefore,

$$\frac{\partial I_0}{\partial W_p} = \frac{\sqrt{3}}{2r C} [W_p/(C p_a)]^{(5/r)-1} \quad (258)$$

Substitution of equation 258 into equation 256 gives the plastic modulus as:

$$\bar{K}_p = - \frac{\partial F}{\partial I_0} \frac{\sqrt{3}}{2r C} [W_p/(C p_a)]^{(5/r)-1} \left[ \underline{s} : \underline{m}^d + \frac{I_1}{3} m_{kk} \right] \quad (259)$$

It is interesting to note that by setting the parameter  $\Lambda$  equal to zero in equation 251, we obtain the commonly used density hardening model while there is no such parameter to give us this control in the analogous plastic work hardening formulation (equation 259). In this regard, the hardening described in terms of the combined strain parameter  $T$  may be preferred over the plastic work formulation just presented.

### 3. Two Parameter Hardening

As a final alternative, it can be assumed that  $\eta$  and  $\xi$  act independently in the yield condition,  $F(\bar{g}, \eta, \xi) = 0$ . A two parameter hardening rule of this type was considered by Prevost and Hoeg (Reference 81) and McVay and Taesiri (Reference 6). Based on

experimental observations by Kondner (Reference 82), Prevost and Hoeg (Reference 81) put forward the following hyperbolic relationship between  $\sqrt{J_2}^*$  and  $\eta$  to describe the hardening of their model's shear yield surface:

$$\sqrt{J_2}^* = \frac{\eta}{a + \eta} [\sqrt{J_2}^*]_{\text{ultimate}} , \quad (260)$$

but we know that  $S^* I_1 = [\sqrt{J_2}^*]_{\text{ultimate}}$ , and hence equation 260 can be written as:

$$\sqrt{J_2}^* = \frac{\eta}{a + \eta} S^* I_1 . \quad (261)$$

From equation 241, we can further see that

$$I_1 = [I_1]_{\text{initial}} \exp(\lambda \xi) , \quad (262)$$

and substitution of this equation in 261 gives rise to

$$\sqrt{J_2}^* = \frac{\eta}{a + \eta} S^* [I_1]_{\text{initial}} \exp(\lambda \xi) ; \quad (263)$$

rearranging, we obtain

$$\frac{\sqrt{J_2}^*}{[I_1]_{\text{initial}}} = \frac{\eta}{a + \eta} S^* \exp(\lambda \xi) . \quad (264)$$

The hardening relationship stated in equation 264 cannot be relied upon exclusively in a single (or piecewise continuous) yield/bounding function representation such as the one considered herein because it does not model any hardening along a hydrostatic compression stress path (i.e.,  $\eta = 0$ ). This feature should not be surprising since Prevost and Hoeg (Reference 81) also used, in conjunction with their shear surface, a singular volumetric surface (i.e., the stress state always resides at the intersection of these two surfaces), governing the yielding of the material during compression.

In order to bypass the deficiency of this hardening rule in transforming from the piecewise discontinuous yield surface depiction to a single continuous yield/bounding function, McVay and Taesiri (Reference 6) adopted the following procedure: they first re-stated the consistency condition in the form

$$\frac{\partial F}{\partial \bar{\sigma}} : \dot{\bar{\sigma}} + \frac{\partial F}{\partial I_0} \frac{dI_0}{d\sqrt{J_2}^*} \bigg|_{\text{CSP}} \frac{\partial \sqrt{J_2}^*}{\partial \eta} \dot{\eta} + f(I_1, \sqrt{J_2}^*) \frac{\partial F}{\partial \xi} \dot{\xi} = 0, \quad (265)$$

where the subscript CSP is an acronym for Calibration Shear Path, and the function  $f(I_1, \sqrt{J_2}^*)$  is selected such that  $f(I_1, \sqrt{J_2}^*)$  is equal to zero along the calibration shear path but equal to unity along the other calibration path which is the hydrostatic consolidation path. This function,  $f(I_1, \sqrt{J_2}^*)$ , can be interpreted as a weighting factor, between zero and unity, for the density hardening term of equation 265.

Along the CSP, a functional representation similar to that used by Prevost and Hoeg (Reference 81) is adopted to model the relationship between  $\sqrt{J_2}^*$  and  $\eta$ ,

$$\frac{\sqrt{J_2}^*}{[I_1]_{\text{initial}}} = \frac{\eta}{a + \eta} S^*, \quad (266)$$

where  $a$  is a constant which controls the initial slope of the assumed hyperbolic shear stress - shear strain curve.

From equation 266 we find

$$\frac{\partial \sqrt{J_2}^*}{\partial \eta} = \frac{a}{(a + \eta)^2} S^* [I_1]_{\text{initial}}, \quad (267)$$

which can be put in the following more convenient format for the consistency condition:

$$\frac{\partial F}{\partial \bar{\sigma}} : \dot{\bar{\sigma}} + \frac{\partial F}{\partial I_0} \frac{dI_0}{d\sqrt{J_2}^*} \bigg|_{\text{CSP}} \frac{\partial \sqrt{J_2}^*}{\partial \eta} \dot{\eta} + f(I_1, \sqrt{J_2}^*) \frac{\partial F}{\partial I_0} \frac{\partial I_0}{\partial \xi} \dot{\xi} = 0. \quad (268)$$

We must now select a calibration shear path (CSP) and evaluate  $\left. \frac{dI_0}{d\sqrt{J_2}} \right|_{\text{CSP}}$ , and then pick a realistic function  $f(I_1, \sqrt{J_2}^*)$  which meets the previously mentioned requirements. McVay and Taesiri (Reference 6) settled upon the conventional triaxial compression (CTC) stress path as their CSP (so the subscript CSP can now be replaced by CTC) and this derivation describes the simple procedure by which  $\left. \frac{dI_0}{d\sqrt{J_2}} \right|_{\text{CTC}}$  is

computed. The equation for the CTC stress path on a normally consolidated sample can be expressed as:

$$\bar{I}_1 = \sqrt{(3\bar{J}_2^*)} + [I_1]_i, \quad (269)$$

where  $[I_1]_i = [I_1]_{\text{initial}}$ ,

and substitution into equation 176 of this unique relationship between the stress invariants gives

$$F = (\sqrt{(3\bar{J}_2^*)} + [I_1]_i)^2 - 2 (I_0/Q)(\sqrt{(3\bar{J}_2^*)} + [I_1]_i) + \{((Q-1)/N^*)^2 \bar{J}_2^* + I_0^2 \{(2/Q)-1\}\} = 0. \quad (270)$$

Taking the total derivative of this equation with respect to  $\sqrt{J_2}^*$  and rearranging, we obtain

$$\left. \frac{dI_0}{d\sqrt{J_2}} \right|_{\text{CTC}} = \frac{A}{B}, \quad (271)$$

where

$$A = 6 \sqrt{J_2}^* + 2\sqrt{3} [I_1]_i - \frac{2\sqrt{3}}{Q} I_0 + 2 \{((Q-1)/N^*)^2 \sqrt{J_2}^*\}$$

and

$$B = \frac{2\sqrt{3}}{Q} \sqrt{J_2}^* + 2 I_0 \{1-(2/Q)\} + \frac{2}{Q} [I_1]_i.$$

These calculations can be carried out in a similar manner for the dilatation portion of the bounding surface (see equation 186), and the result is

$$\left. \frac{dI_0}{d\sqrt{J_2}^*} \right|_{CTC} = \frac{A}{B} \quad (272)$$

where

$$\begin{aligned} A &= 2[3 + b + \sqrt{3} A_1] \sqrt{J_2}^* + [I_1]_i \{2\sqrt{3} + A_1\} + \\ &\quad [1 - \sqrt{3} S^*] A_2 I_0, \\ B &= S^* A_2 [I_1]_i - \sqrt{J_2}^* \{A_2 - \sqrt{3} S^* A_2\}, \end{aligned}$$

where

$$A_1 = \left[ \frac{S^*}{N^{*2}} - \frac{2}{N^*} - S^* b \right],$$

and

$$A_2 = (1/Q) \left[ \frac{1}{N^*} - b N^* \right].$$

The function  $f(I_1, \sqrt{J_2}^*)$  must now be chosen. Recall from equation 269 that the equation of the CTC path is

$$\bar{I}_1 = \sqrt{(3J_2^*)} + [I_1]_i,$$

and we can conveniently re-write this expression in the form

$$\frac{\sqrt{(3J_2^*)}}{[\bar{I}_1] - [I_1]_i} = 1 \quad (273)$$

Observe that when the left hand portion of equation 273 is raised to an arbitrary exponent  $n$ , this quantity is still equal to one along the CTC. This leads us to propose the general relationship

$$f(I_1, \sqrt{J_2}^*) = 1 - \left\{ \frac{\sqrt{(3J_2^*)}}{[\bar{I}_1] - [I_1]_i} \right\}^n \quad (274)$$

One may observe that this expression is equal to one whenever  $\sqrt{J_2}^* [= g(\theta) \sqrt{J_2}^*]$  is equal to zero, and therefore satisfies the requirement



for pure volumetric hardening along the hydrostatic consolidation path. But, is this equation valid for general loading programs? For a monotonic CTC test on a normally consolidated sample,  $[I_1]$  is always greater than  $[I_1]_i$ , and, as a result, the denominator of the power term is always positive for the calibration path. This, however, may not be true for general paths and if the quantity  $([I_1] - [I_1]_i)$  is in fact negative while the exponent  $n$  is an odd integer, the expression for  $f$  can be greater than one. Since we are seeking our range of  $f(I_1, \sqrt{J_2}^*)$  to vary from zero to unity, we will need to allow for this possibility by modifying equation 274 to the following form:

$$f(I_1, \sqrt{J_2}^*) = 1 - \left\{ \frac{\sqrt{(3J_2^*)}}{|[I_1] - [I_1]_i|} \right\}^n. \quad (275)$$

McVay and Taesiri (Reference 6) set  $n$  equal to one but wanted further to decouple completely from the volumetric hardening,  $\frac{\partial I_0}{\partial \xi}$ , when the combined deviatoric/hydrostatic stress state resided above the trajectories of the CTC and Reduced Triaxial Extension (RTE) stress paths. The CTC and RTE stress paths are 120 degrees apart in  $I_1 - \sqrt{J_2}$  space. This requirement can be met by introducing the Heaviside step function in equation 275,

$$f(I_1, \sqrt{J_2}^*) = \left\langle 1 - \left\{ \frac{\sqrt{(3J_2^*)}}{|[I_1] - [I_1]_i|} \right\} \right\rangle. \quad (276)$$

A schematic illustration of this hardening is depicted in figure 10; note that in the regions A and C, combined shear and volumetric hardening is assumed while the hardening in the region B is controlled solely by the shear strain.



We are now furnished with all the information we need for the consistency condition of 268 except for  $\frac{\partial I_0}{\partial \xi}$ ; this hardening can be assumed to take the form of equation 246. For this third hardening option, the plastic modulus on the bounding surface can then be computed as:

$$\begin{aligned} \bar{K}_p = & - \frac{\partial F}{\partial I_0} \left\{ \frac{dI_0}{d\sqrt{J_2}^*} \right\}_{CSP} \frac{\partial \sqrt{J_2}^*}{\partial \eta} \sqrt{\left[ \frac{1}{2} \left( 1 - \frac{1}{3} m_{kk}^2 \right) \right]} \\ & + f(I_1, \sqrt{J_2}^*) \frac{\partial I_0}{\partial \xi} m_{kk} \} . \end{aligned} \quad (277)$$

#### J. LINK BETWEEN THE PLASTIC MODULUS ( $K_p$ ) AND $\bar{K}_p$ AT THE BOUND

The most conspicuous feature of the bounding surface formulation is the definition of the plastic modulus,  $K_p$ , in terms of the plastic modulus at the image point  $\bar{K}_p$ . The generalized plastic modulus,  $K_p$ , can be taken as an experimentally determined function of: i)  $\bar{K}_p$ , ii) the Euclidean distance between  $\bar{g}$  and  $g$  (say  $\delta$ ), iii) the Euclidean distance between  $\bar{g}$  and  $\bar{g}_0$  (say  $\delta_0$ ) and iv) a discrete memory parameter (say  $\alpha$ ) which distinguishes among loading ( $\alpha = 1$ ), reverse loading ( $\alpha = -1$ ), and reloading ( $\alpha = 0$ ) events. In the six-dimensional Cauchy stress manifold, we can compute the Euclidean distances,  $\delta$  and  $\delta_0$ , between the various pairs of stress coordinates as  $\sqrt{[(\bar{\sigma}_{ij} - \sigma_{ij})^2]}$  and  $\sqrt{[(\bar{\sigma}_{ij} - (\sigma_{ij})_0)^2]}$  respectively, and recollecting from equation 222 the 'simple' mapping relationship  $\bar{g} = \beta g$ , we determine

$$\delta = \sqrt{[(\beta \sigma_{ij} - \sigma_{ij})^2]} = (\beta - 1) \sqrt{(\sigma_{ij} \sigma_{ij})} , \quad (278)$$

and

$$\delta_0 = \sqrt{[(\beta \sigma_{ij} - 0)^2]} = \beta \sqrt{(\sigma_{ij} \sigma_{ij})} . \quad (279)$$

We can now postulate a relationship of the form (see, for example, Reference 83)

$$\begin{aligned} K_p &= \bar{K}_p + [(K_p)_o - \bar{K}_p] \left\{ \frac{\delta}{\delta_o} \right\}^Y \\ &= \bar{K}_p + [(K_p)_o - \bar{K}_p] \left\{ \frac{\beta-1}{\beta} \right\}^Y, \end{aligned} \quad (280)$$

where

$$(K_p)_o = K_p \text{ at } \delta = \delta_o,$$

$$\bar{K}_p = K_p \text{ at } \delta = 0,$$

and  $Y$  is a constant parameter; we may express the relationship in an equivalent form (see, for instance, Reference 84):

$$K_p = \bar{K}_p + H(\underline{g}, q_n) \frac{\delta}{\delta_o - \delta} = \bar{K}_p + H(\underline{g}, q_n) (\beta - 1), \quad (281)$$

where  $H$  is a positive 'shape' hardening function of the state. The adjective "shape hardening" describes the role of  $H$  in defining the shape of the stress-strain curves during plastic hardening. In equation 280, we can see that  $K_p = \bar{K}_p$  when the stress point and its image coincide (i.e. when  $\alpha = 1$ ) so we need only concern ourselves further with the differences (if any) that arise from using equation 280 instead of equation 281 in simulating the reload ( $\alpha = 0$ ) plastic modulus. It is also important to note that the continuity condition is satisfied in both constitutive relations (equations 280 and 281) when a loading program proceeds from a reloading to a virgin loading phase.

In both instances in the literature where the bounding surface plasticity model has been used for sand (References 6 and 74), the semi-empirical relations for modeling the unload ( $\alpha = -1$ ) plastic modulus have not included  $\bar{K}_p$  as an independent variable, and as a

result, the general relations presented above are not applicable to this event. Nevertheless, the reverse loading modulus has been modeled as a function of  $\delta$  and  $\delta_0$  and these relations will be presented after the reload modulus is discussed.

Aboim and Roth (Reference 74) adopted a form of equation 281 in their bounding surface constitutive equations for the reload ( $\alpha = 0$ ) plastic modulus; they assumed that  $H(g, g_n)$  was equal to a constant  $H_{r1}$ , and hence their representation was simply

$$K_p = \bar{K}_p + H_{r1} (\beta - 1) \quad . \quad (282)$$

For the reloading path ( $\alpha = 0$ ), McVay and Taesiri (Reference 6) assumed that  $\gamma$  was equal to unity in equation 280 and that the term  $[(K_p)_0 - \bar{K}_p]$  was a constant (say  $H_{r2}$ ) such that the generalized plastic reload modulus relationship could be expressed as:

$$K_p = \bar{K}_p + H_{r2} \frac{\{\beta-1\}}{\beta} \quad . \quad (283)$$

We can now assume an empirical relationship for the reverse loading plastic modulus which is proportional to the relative distance between the stress state and its image stress point. The key differences between the stress reversal modulus and the unload modulus are: i) the continuity requirement is not applicable for reverse loading, and ii) the unload modulus decreases with distance from the bounding surface while we have already shown that the reload modulus decreases as it approaches its image point on the bound. Possible empirical relationships for the case when the discrete memory parameter  $\alpha$  is equal to -1 (reverse loading) arise naturally in the forms:

$$K_p \propto \left\{ \frac{\delta}{\delta_0} \right\}^{-1} \propto \left\{ \frac{\beta-1}{\beta} \right\}^{-1} = H_{u1} \left\{ \frac{\beta-1}{\beta} \right\}^{-1} , \quad (284)$$

or

$$K_p \propto \left\{ \frac{\delta}{\delta_0 - \delta} \right\}^{-1} \propto (\beta - 1)^{-1} = H_{u2} (\beta - 1)^{-1} , \quad (285)$$

where  $H_{u1}$  and  $H_{u2}$  are constants to be determined, together with  $H_{r1}$  and  $H_{r2}$ , by heuristic curve fitting of the experimental hysteresis loops.

From equations 284 and 285, we can observe that the reverse loading plastic modulus goes to infinity at the first load decrement following a virgin loading phase; at this point,  $\beta$  is equal to unity but the discrete memory parameter,  $\alpha$ , is now equal to -1. This case is important since it represents the sole instant when we theoretically have purely elastic strains, thus making it possible to calibrate the elastic constants.

## SECTION V

### LABORATORY INVESTIGATION OF SOIL ANISOTROPY

#### A. INTRODUCTION

Although soils are known to exhibit significant stress-strain-strength anisotropy, detailed quantitative measurements of anisotropic properties have been severely restricted by the limited stress conditions that can be applied with conventional test equipment. The greatest limitation to a detailed study of anisotropic behavior is the inability to have controlled changes of principal stress directions (Reference 10).

Inherent anisotropy studies, using samples prepared in tilted molds, have, in the past, provided quantitative as well as qualitative indications of the influence of anisotropy on the load-deformation response of cohesionless materials (References 35, 43, and 85). It has been pointed out, however, (Reference 86) that the use of tilted samples may lead to non-uniform stresses or strains, depending on the flexibility of the boundary; this potential test flaw suggests a need for alternative test procedures.

Recently, specialized devices, in which the direction of the principal stress axes can be controlled, have shown significant stiffness and strength variation with the relative orientation of the principal stress axes to the material's fabric (References 9, 86, and 87). The hollow cylinder apparatus (HCA) and the directional shear cell (DSC) are the two key types of non-standard equipment presently used in

the controlled exploration of more general stress spaces. These apparatus are by no means ideal or capable of subjecting specimens to completely general stress states, and, with the ever increasing use of supposedly generalized stress-strain models in finite element analysis, the development of improved devices to probe the whole stress-strain spectra takes on added importance.

In this section, attention is devoted to very briefly describing the following experimental devices which provide the source of the measured stress-strain curves: 1) the hollow cylinder apparatus, 2) the directional shear cell, and 3) a series of in-house 'triaxial' tests.

#### B. HOLLOW CYLINDER TEST

In their state of the art paper on Laboratory Strength Testing of Soils, Saada and Townsend (Reference 5) discussed in great detail a large number of static testing devices; included in that paper is an excellent review of the theoretical and practical aspects of the hollow cylinder apparatus.

As part of the data collection phase of this research effort, the results of a series of HCA tests, aimed at investigating inherent anisotropy, on Reid-Bedford sand (at a void ratio of 0.67) were obtained. This test environment is most conveniently described by referring to figure 11 which depicts the state of stress in the "thin", "long" hollow cylinder. The main feature that distinguishes the hollow cylinder test from the conventional solid cylinder test is the application of the shear stress  $\tau_{\theta z}$  which effectively controls the directions of the major and minor principal stresses ( $\sigma_1$  and  $\sigma_3$ ) acting



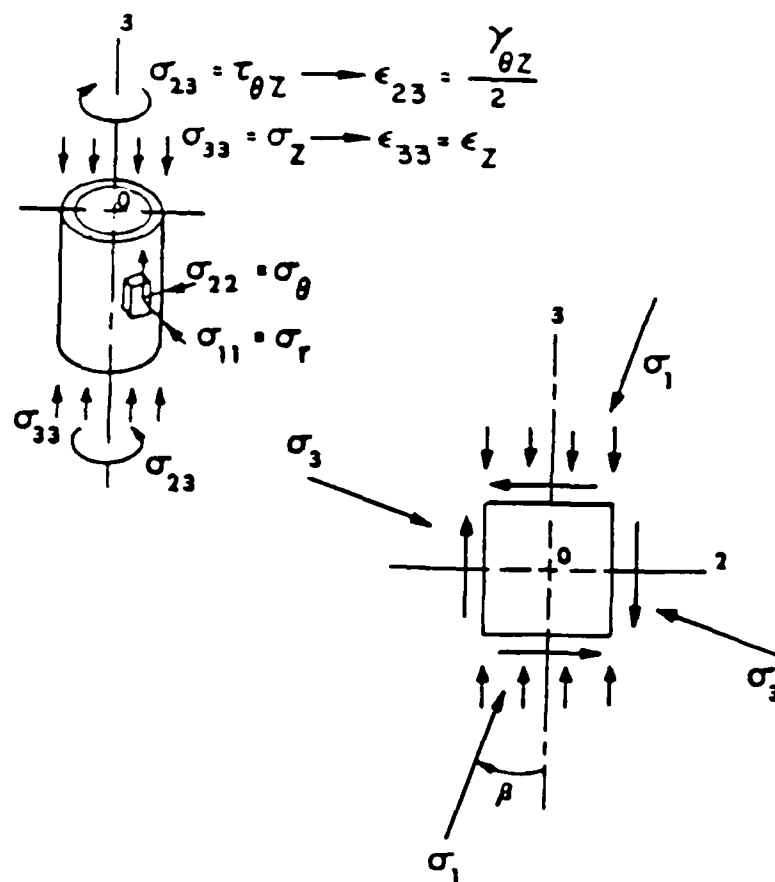


Figure 11. Stress State in Hollow Cylinder Apparatus (Reference 5).

in the vertical plane of the cylinder (i.e.,  $\theta z$  plane). In all these tests, the internal and external cell pressures were always equal, and this suggests that the potential non-uniformities in the radial and circumferential normal stresses were mitigated across the thickness of the specimen. With this special test scenario, note that the cell pressure ( $\sigma_r = \sigma_\theta$ ) is always equal to the intermediate principal stress  $\sigma_2$ .

From figure 11, we see that the change in principal stresses and their directions are given by

$$\Delta\sigma_1 = \frac{1}{2} [\Delta\sigma_z + \Delta\sigma_\theta] + \sqrt{\left[ \frac{1}{2} (\Delta\sigma_z - \Delta\sigma_\theta) \right]^2 + \Delta\tau_{\theta z}^2} , \quad (286)$$

$$\Delta\sigma_3 = \frac{1}{2} [\Delta\sigma_z + \Delta\sigma_\theta] - \sqrt{\left[ \frac{1}{2} (\Delta\sigma_z - \Delta\sigma_\theta) \right]^2 + \Delta\tau_{\theta z}^2} , \quad (287)$$

and

$$\frac{1}{2} \tan 2\beta = \Delta\tau_{\theta z} + [\Delta\sigma_z - \Delta\sigma_\theta] . \quad (288)$$

In the first series of tests, the intermediate principal stress and the angle between the major principal stress and the vertical ( $\beta$ ) were held constant while the samples, inherently possessing an axial axis of rotational symmetry, were monotonically sheared to failure. The angle  $\beta$  varied over the range  $0^\circ$  to  $90^\circ$ ; more specifically, the nominal values of  $\beta$  were  $0^\circ$ ,  $15^\circ$ ,  $31.75^\circ$ ,  $45^\circ$ ,  $58.25^\circ$ ,  $75^\circ$ , and  $90^\circ$ . For this

particular series of tests, note that equations 286-288 simplify to the following:

$$\Delta\sigma_1 = \frac{1}{2} \Delta\sigma_z [ 1 + \sqrt{(1 + 4K^2)} ] , \quad (289)$$

$$\Delta\sigma_3 = \frac{1}{2} \Delta\sigma_z [ 1 - \sqrt{(1 + 4K^2)} ] , \quad (290)$$

$$\Delta\sigma_2 = 0, \quad (291)$$

where

$$K = \frac{1}{2} \tan 2\beta = \Delta\tau_{\theta z} + \Delta\sigma_z . \quad (292)$$

The second series of tests were similar to the first except, now, the mean normal pressure was kept constant. In this case, equations 286-288 reduce to

$$\Delta\sigma_1 = \frac{1}{2} \Delta\sigma_z \left[ \frac{1}{2} + \frac{3}{2} \sqrt{(1 + 4K^2)} \right],$$

$$\Delta\sigma_3 = \frac{1}{2} \Delta\sigma_z \left[ \frac{1}{2} - \frac{3}{2} \sqrt{(1 + 4K^2)} \right],$$

and

$$\Delta\sigma_2 = - \frac{1}{2} \Delta\sigma_z ,$$

where

$$K = \frac{1}{2} \tan 2\beta = \Delta\tau_{\theta z} + \frac{3}{2} \Delta\sigma_z .$$

Again,  $\beta$  assumed the same range and magnitude of values as the constant intermediate principal stress tests.

When dealing with such a variety of tests, it is always convenient to introduce a compact but unmistakably clear notation, and here there is no exception. Adopting Saada's convention (Reference 9), the tests are designated by letters with the following meaning: "D" refers to constant intermediate principal stress; "G" to constant mean normal pressure; "C" and "T" to compression or extension depending on the

direction of  $\sigma_z$ ; and "R" to indicate if the shear stress ( $\tau_{\theta z}$ ) was applied. The numbers refer to nominal values of  $\beta$  during the test. Therefore, a GTR 75, for example, is a mean normal pressure extension test with the major principal stress inclined at an angle of  $75^\circ$  to the vertical. Further, observe that a DC 0 and DT 90 in this classification system are equivalent to the CTC and RTE stress paths respectively of figure 3. Figure 12 shows the stress paths for all tests in the so-called "M.I.T." p-q space (where  $p = \frac{\sigma_1 + \sigma_3}{2}$ , and  $q = \frac{\sigma_1 - \sigma_3}{2}$ ). Although not indicated on this figure, all tests started at an effective confining pressure of 30 psi.

#### C. DIRECTIONAL SHEAR CELL

The Directional Shear Cell (DSC) is a plane strain, flexible boundary stress controlled device which applies varying amounts of normal and shear stresses to the sides of a cubical specimen, thus, in effect, controlling the magnitude and direction of the major and minor principal stresses. Figure 13 presents a diagram of the method used to apply these normal and shear stresses to the sand sample, but, for a more detailed explanation of this device and its operation, the reader is referred to Bekenstein's thesis (Reference 10).

A comprehensive series of DSC tests were carried out at M.I.T. (Reference 10) to investigate: 1) the reproducibility and reliability of the device in simulating supposedly "isotropic shear" tests, and 2)

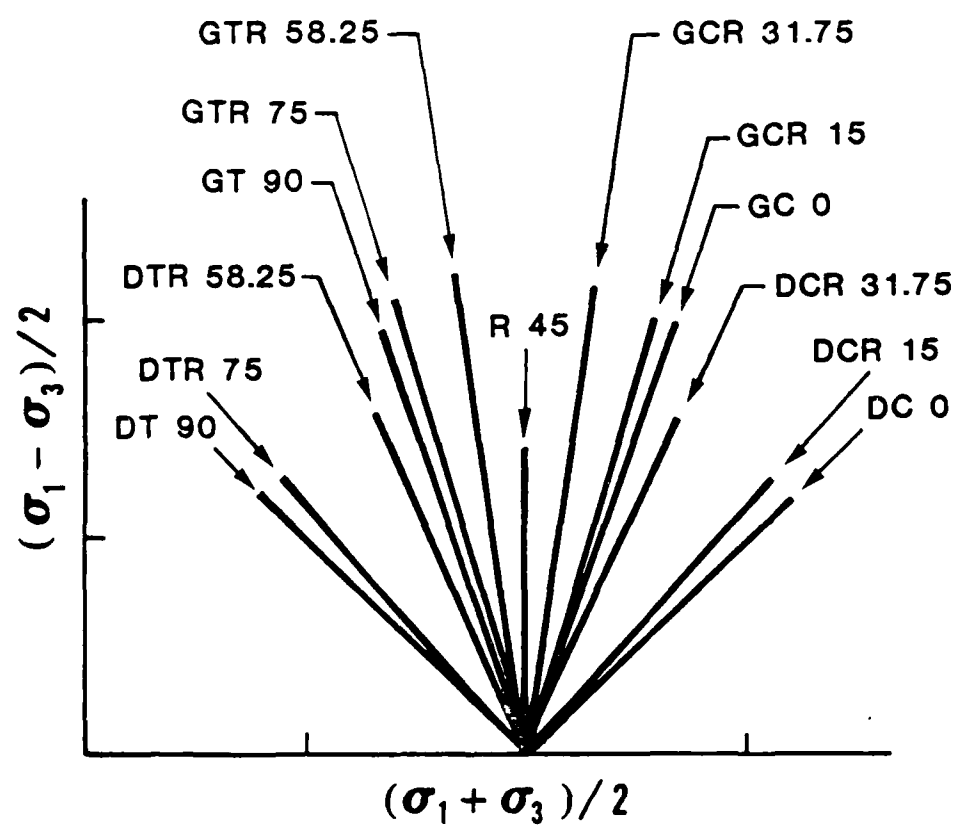
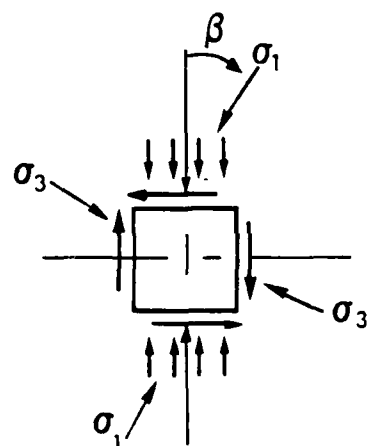


Figure 12. Hollow Cylinder Test Stress Paths (Reference 9).

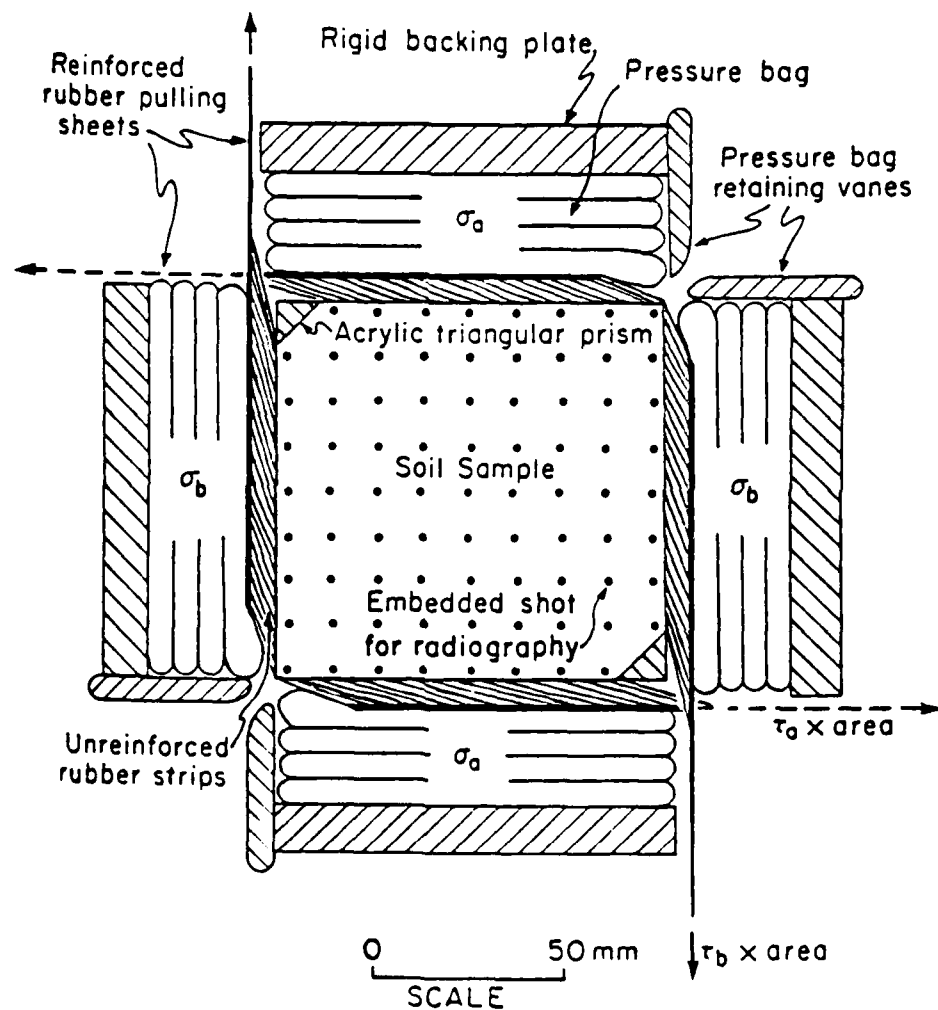


Figure 13. Diagram of Method Used to Apply Normal and Shear Stresses in the Directional Shear Cell (Reference 10).

the influence of stress-induced as well as inherent anisotropy on the stress-strain-strength behavior of both loose and dense Leighton-Buzzard sand.

Isotropic shear tests are defined as monotonically loaded tests wherein the principal stress direction and the minor principal stress ( $\sigma_3$ ) are held constant until failure; the depositional direction is normal to the plane strain sides to negate any effects of inherent anisotropy. This test is schematically illustrated in the monotonic loading phase at the top of figure 14, and, from a theoretical standpoint, it is useful in defining the isotropic stress-strain-strength behavior of the material. Before proceeding further with the discussion, it should be noted that there is never a continuous rotation of principal stress directions during these loading or unloading paths; the mention of this implicit assumption is therefore suppressed in the following.

Induced anisotropy is investigated in two general ways; in the first method, step #1 involves an initial loading, with  $\sigma_3$  constant, to a relatively high, but pre-peak stress ratio  $R (= \sigma_1/\sigma_3)$ . This is then followed by a monotonic unloading to an isotropic stress state ( $R = 1$ ), and finally, with a single jump rotation of the major principal stress direction ( $\psi_B$ ), reloading until failure takes place. This sequence of events is depicted in figure 14. The second method for studying induced anisotropy is illustrated in figure 15 where we note that the principal stress directions ( $\psi_A$ ) during the initial monotonic loading (or induction) phase is not perpendicular to the sides of the specimen.

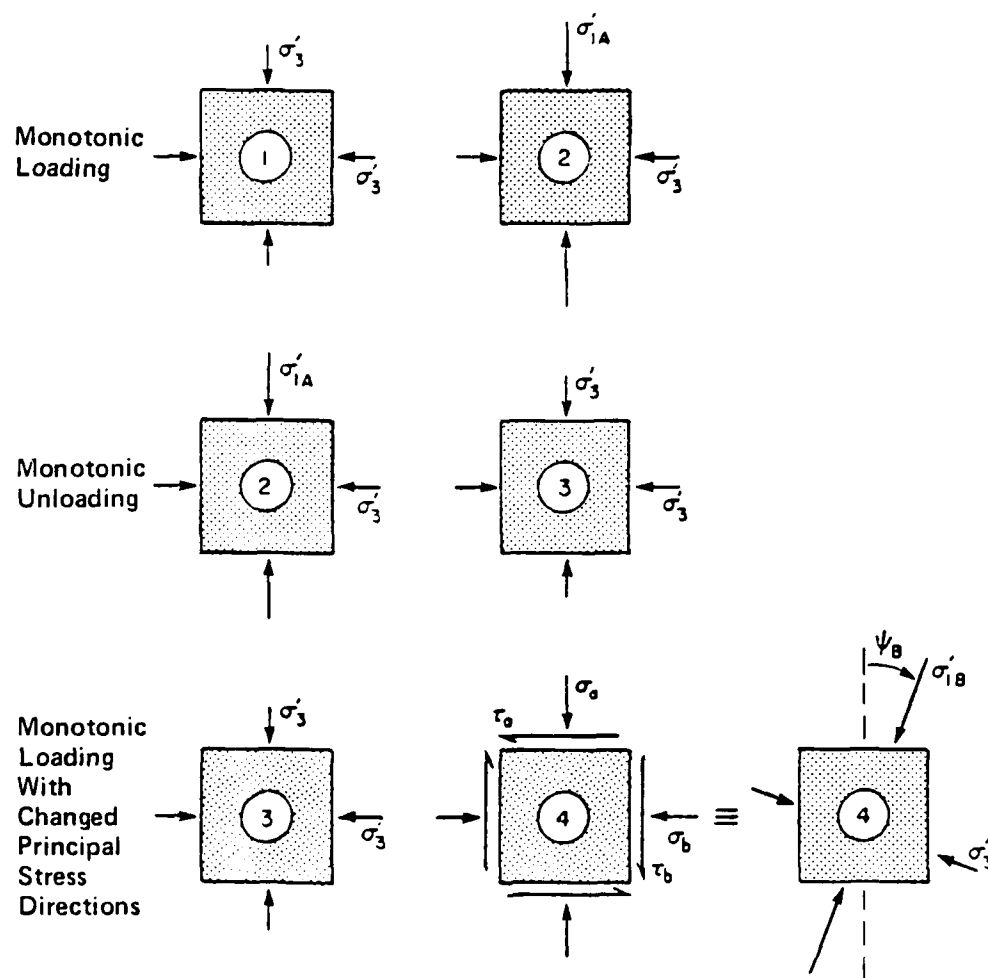


Figure 14. Directional Stress Paths for Jump Rotation Loading Tests;  $\psi_A > 0^\circ$  (Reference 10).



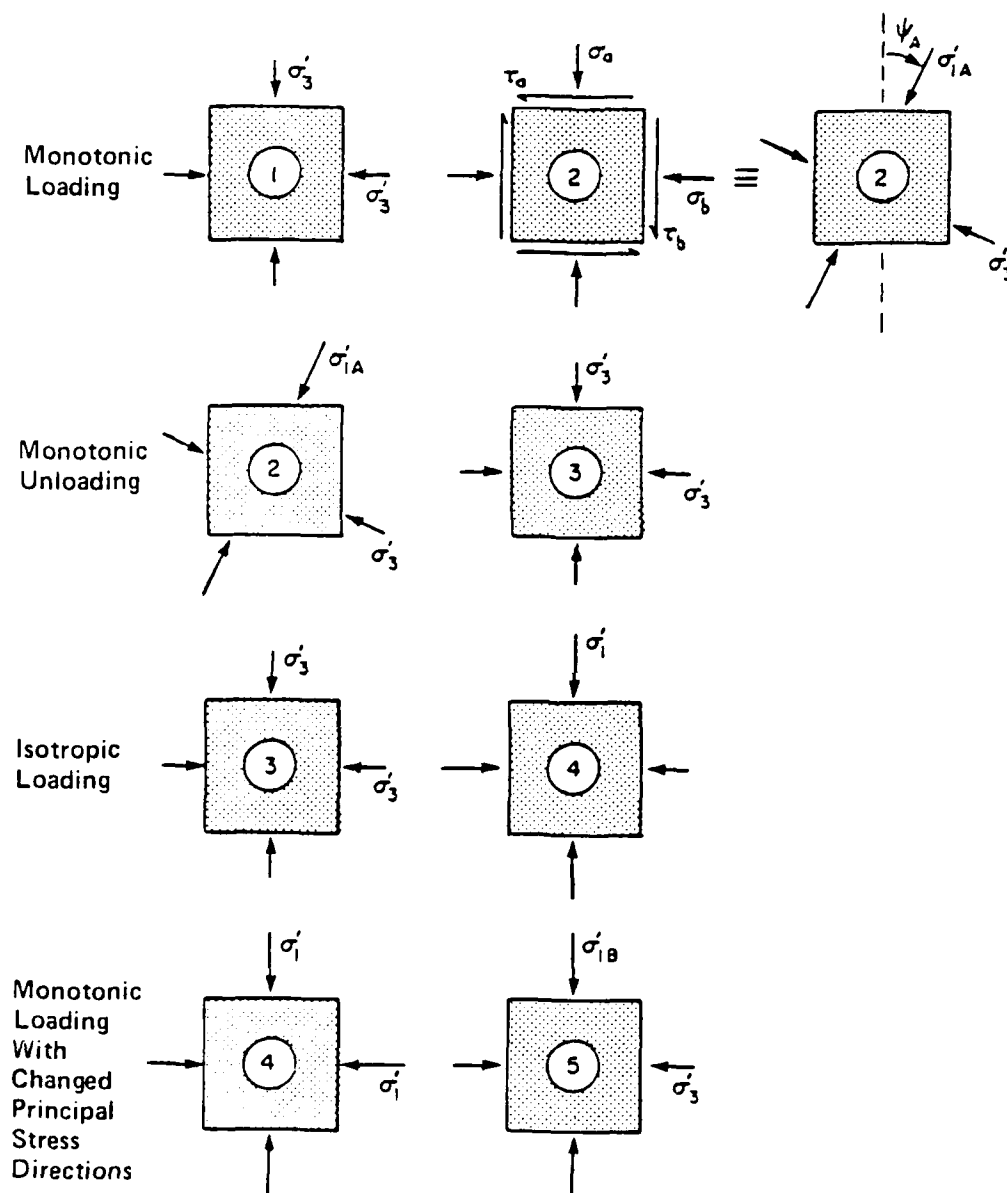


Figure 15. Directional Stress Paths for Jump Rotation Loading Tests;  $\psi_A > 0^\circ$  (Reference 10).

During the reload to failure, however, these principal directions are kept normal to the sides of the cube specimen.

Inherent shear tests were monotonically loaded to failure, but, unlike the induced tests, the samples were oriented so that shear occurred in a plane containing the direction of deposition. Several variations on these tests were carried out, and detailed information regarding this rather comprehensive study of anisotropy in granular materials can be found in Bekenstein's (Reference 10) work.

#### D. IN-HOUSE 'TRIAxIAL' TESTS

Triaxial testing at the University of Florida initiated with the investigation of the shear strength of Reid-Bedford sand at void ratios of 0.57 and 0.67 respectively. The tests were performed at initial effective cell pressures of 25, 35, and 45 psi to bound the pressure range used in the hollow cylinder tests (of the previous subsection). The tests consisted of either increasing or decreasing the axial load while maintaining a constant cell pressure (i.e., CTC and RTE tests respectively of figure 3). Vertical deformation, volume change, and vertical load were measured with a dial gauge, a burette, and a calibrated load cell respectively. Figure 16 is a photograph of a typical specimen after shearing to failure along an RTE path.

In the determination of the strength properties of the Reid-Bedford sand, localized failure modes were predominant for RTE testing (see figure 16). This suggests that the overall strain measurements may not have been representative of the deformation in the local zone. It is postulated that the inherent anisotropy (caused by pluviation through

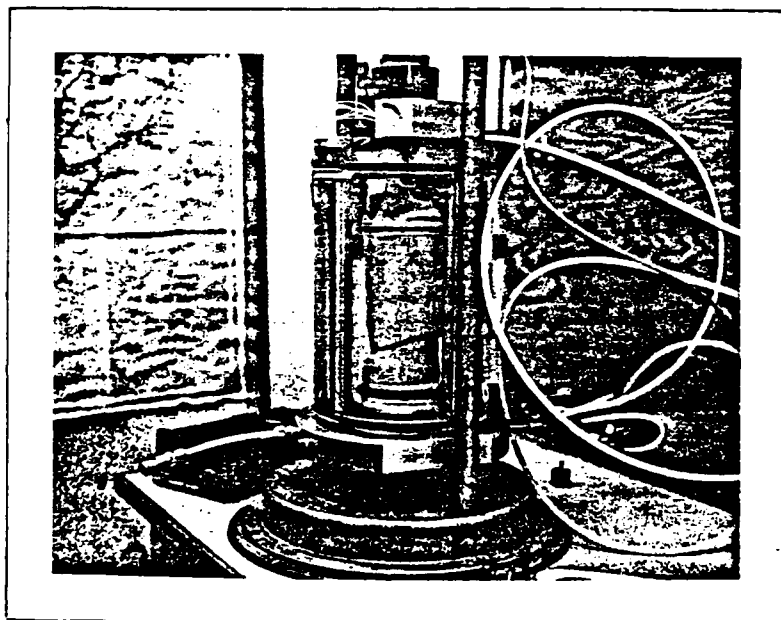


Figure 16. Photograph of Localized Failure of a Solid Cylindrical Specimen after an RTE test.

air) coupled with the fact that dilation occurs only along the small mobilized zones resulted in a net volumetric compression during these unloading tests. This gross behavior, therefore, may not have been representative of the stress-strain response in the region of interest. To correct this problem of possible strain inhomogeneity, the specimen was constructed with a height to diameter ratio of unity while end friction was minimized by coating the bearing caps with teflon spray. These modified RTE tests were deemed acceptable.

Following the conventional strength testing, inherent anisotropy was investigated in the triaxial cell by subjecting "unstrained" samples to spherical loading paths. Owing to the high relative density of the sand, the resulting volumetric compression during consolidation was too small to be accurately measured by the usual burette and dial gauge means; also, the errors introduced by end cap friction may have obscured the volumetric strain measurements. After reviewing alternative corrective measures, linear variable differential transformers (LVDTs) were attached at the top and bottom one-third points of the specimen; this, it was hoped, would eliminate the end effects. The photograph in figure 17 shows a sample with the LVDTs in place prior to testing; figure 18, on the other hand, is a schematic of the test set up used in the chamber. All LVDTs were calibrated to record deformations to the nearest  $\pm 0.0001$  inch; the electrical connections were set up to record the average response of the horizontal pair and the vertical pair of LVDTs.

The second phase of the 'triaxial' anisotropy investigation focused on the observation of the development and demise of stress-induced

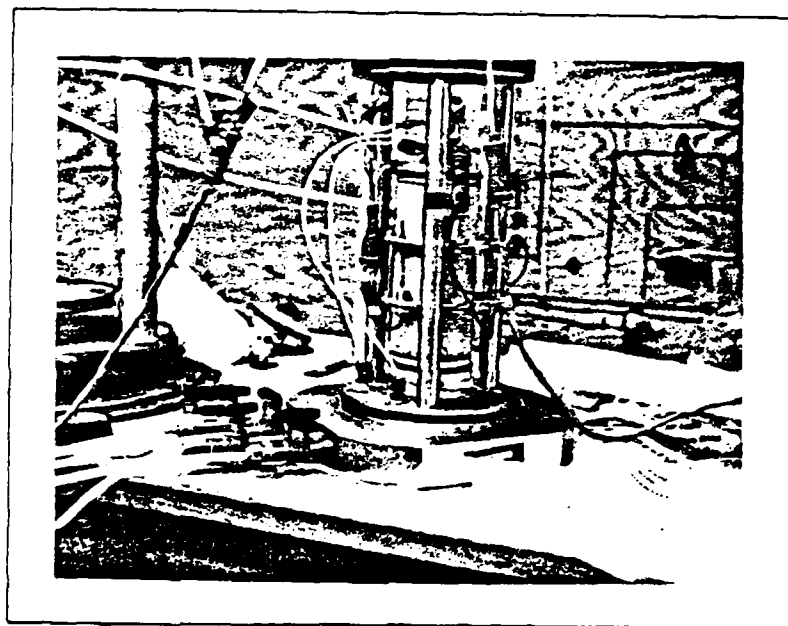


Figure 17. Photograph of Specimen fitted with LVDT Deformation Measurement Devices.

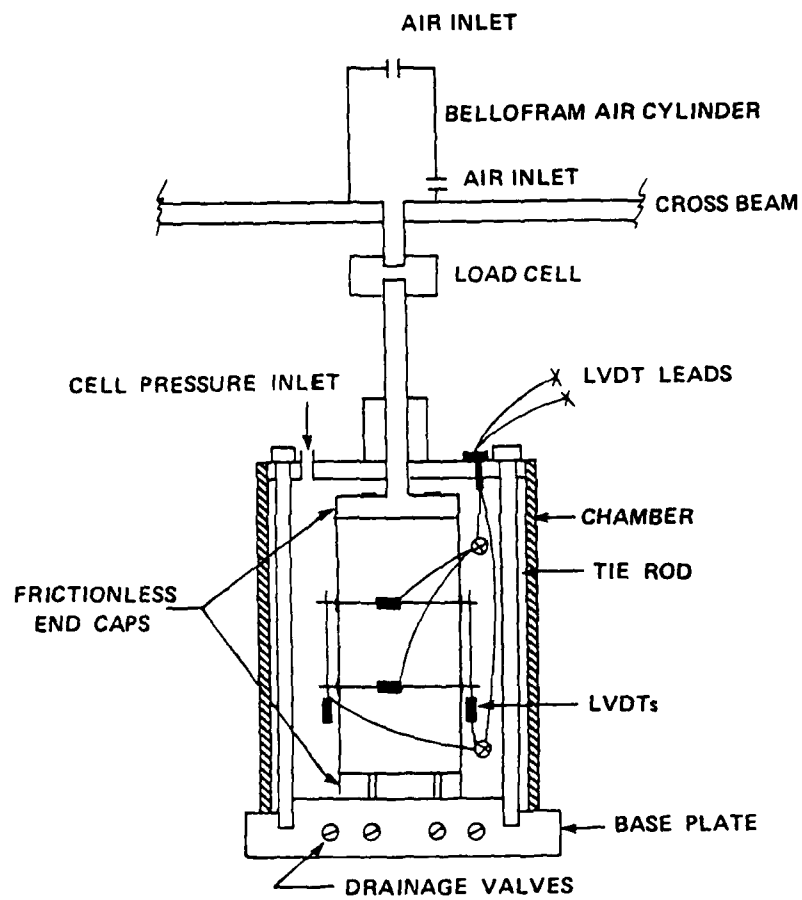


Figure 18. Schematic Illustration of 'Triaxial' Test Apparatus with LVDTs in-place.

anisotropy. These tests simply entailed an axial loading to a prepeak deviatoric stress level, followed by a monotonic unloading back to the original hydrostatic state of stress. The prepeak stress levels selected were 20%, 40%, and 60% of the ultimate shear stress. Finally, after the induction phase, the specimens were loaded spherically while recording the vertical to circumferential strain ratio (i.e.,  $\epsilon_z/\epsilon_\theta$ ). Deviation of this ratio from unity gave an indication of the evolution of the directional stiffness with continued isotropic loading. Again, as in the inherent anisotropy study of the dense sand, sensitivity in deformation measurements was of the essence. To achieve this objective, simultaneous deformation readings were measured using the LVDTs, vertically installed dial gauges, and burette readings. Figure 19 depicts the rather elaborate setup which includes a special (non-conducting) transformer oil in place of water in the chamber. As an aside, it should be mentioned that this series of tests provided considerable insight into the influence of anisotropy, especially as it applies to the cyclic moving wheel stress path (Reference 6).

At the time of this writing, approximately thirty of the above mentioned tests have been carried out. The problems encountered in deformation measurements were unexpected, and consequently, the laboratory testing schedule is somewhat behind. This present series of tests were inaugurated solely for the purpose of gaining insight into the qualitative and quantitative influence of anisotropy. The complexity of the observed behavior suggests that several more basic tests should be carried out before attempting to approximately model the moving wheel stress path in the triaxial chamber. Also, a parallel

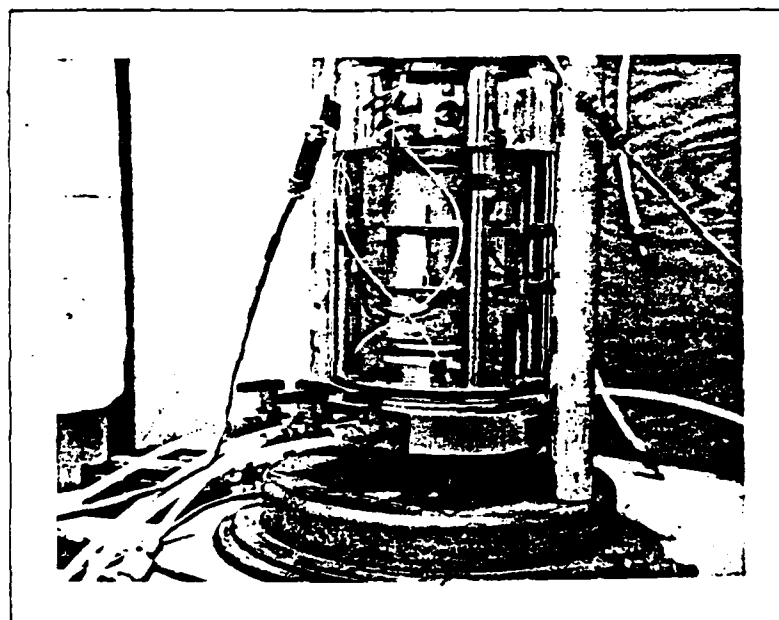


Figure 19. Photograph of Test Apparatus with LVDTs attached to Specimen in Confining Chamber Filled with Oil.



series of tests will have to be performed for the Leighton Buzzard sand to supplement our data base; these data will be requisite in the initialization of the constitutive models prior to predicting the directional shear cell test results.

## SECTION VI

### DISCUSSION OF RESULTS

#### A. GENERAL

The main analytical tasks now completed include: a) the computer coding of the Prevost and Bounding Surface elasto-plastic models which were presented in sections III and IV respectively, and b) a supplementary numerical study of the successive stress states in a soil supporting structure subject to a quasi-static moving wheel load. The Prevost model has been calibrated and used to predict the entire series of measured hollow cylinder test results, but, while the model parameters for the Bounding Surface theory have also been calculated, the present form of its hardening rule has restricted predictions to a limited class of stress paths. Modifications to the hardening rule of the latter are presently under way, however, to permit simulation of a universal plastic stress-strain curve under arbitrary linear loading paths.

Also, secondary computer codes have been written to assist in model calibration and in reduction of both the hollow cylinder and solid cylinder experimental data; the reduction routines also provide information on the influence of principal stress axes rotation on strength as defined by some of the more popular failure criteria for granular media. Finally, study of the stress-strain-strength data obtained from the hollow cylinder test series and some simple exploratory in-house solid cylinder tests has provided insight into how

the presence, relative influence, and evolution of inherent as well as stress-induced anisotropy of sand can be captured in a constitutive model.

#### B. IN-HOUSE 'TRIAxIAL' TESTS

Table 1 is a summary of the physical characteristics of the well-known Reid-Bedford sand which was used for the tests in both the in-house solid cylinder apparatus (SCA) and in Saada's (Reference 9) hollow cylinder apparatus (HCA). In all cases, the nominal void ratio of the specimens was equal to 0.67 (which corresponds to a relative density of 75%), and this parallel study of granular media behavior provides a unique opportunity for comparing and evaluating the influence of these devices on observed response. Accordingly, at appropriate junctures in the ensuing discussion, reference will be made to the differences or similarities which arise from the specimen's shape (i.e., hollow cylindrical or solid cylindrical).

At this point, it is convenient to highlight some useful relations which are applicable to the 'triaxial' environment and to clarify the meaning of the notation used on the axes of the graphs as well as the tables in the sequel. We use

$$q = \sqrt{(3 J_2)} \quad ,$$

$$\bar{\epsilon} = \sqrt{(3 \times \text{2nd invariant of the strain deviator } \underline{e})} \quad ,$$

$$p = I_1/3 = \text{mean stress or mean normal pressure} \quad ,$$

$$p_0 = \text{initial effective mean stress} \quad ,$$

$$p_a = \text{atmospheric pressure} \quad ,$$

$$I_3 = \text{third invariant of } \underline{g} \quad ,$$

TABLE 1. PHYSICAL DESCRIPTION OF REID-BEDFORD SAND

CHARACTERISTIC	DESCRIPTION
Color and Type	Light brown, clean, fine, uniform sand
Grain Shape	Varying from subrounded to subangular
Mineralogy	89% quartz, 9% feldspar, 2% ferromagnesian and "heavies"
Maximum Dry Unit Weight	104.0 pcf
Minimum Dry Unit Weight	86.6 pcf
Granulometric Curve	see figure 20
$D_{60}$ (from figure 20)	0.29 mm
$D_{10}$ (from figure 20)	0.16 mm
Coefficient of Uniformity, $C_u$	1.8
Specific Gravity, $G_s$	2.65 (ASTM D854-58)
Unified Soil Classification	SP
Maximum Void Ratio, $e_{max}$	0.91 (ASTM D-2049)
Minimum Void Ratio, $e_{min}$	0.59 (ASTM D-2049)

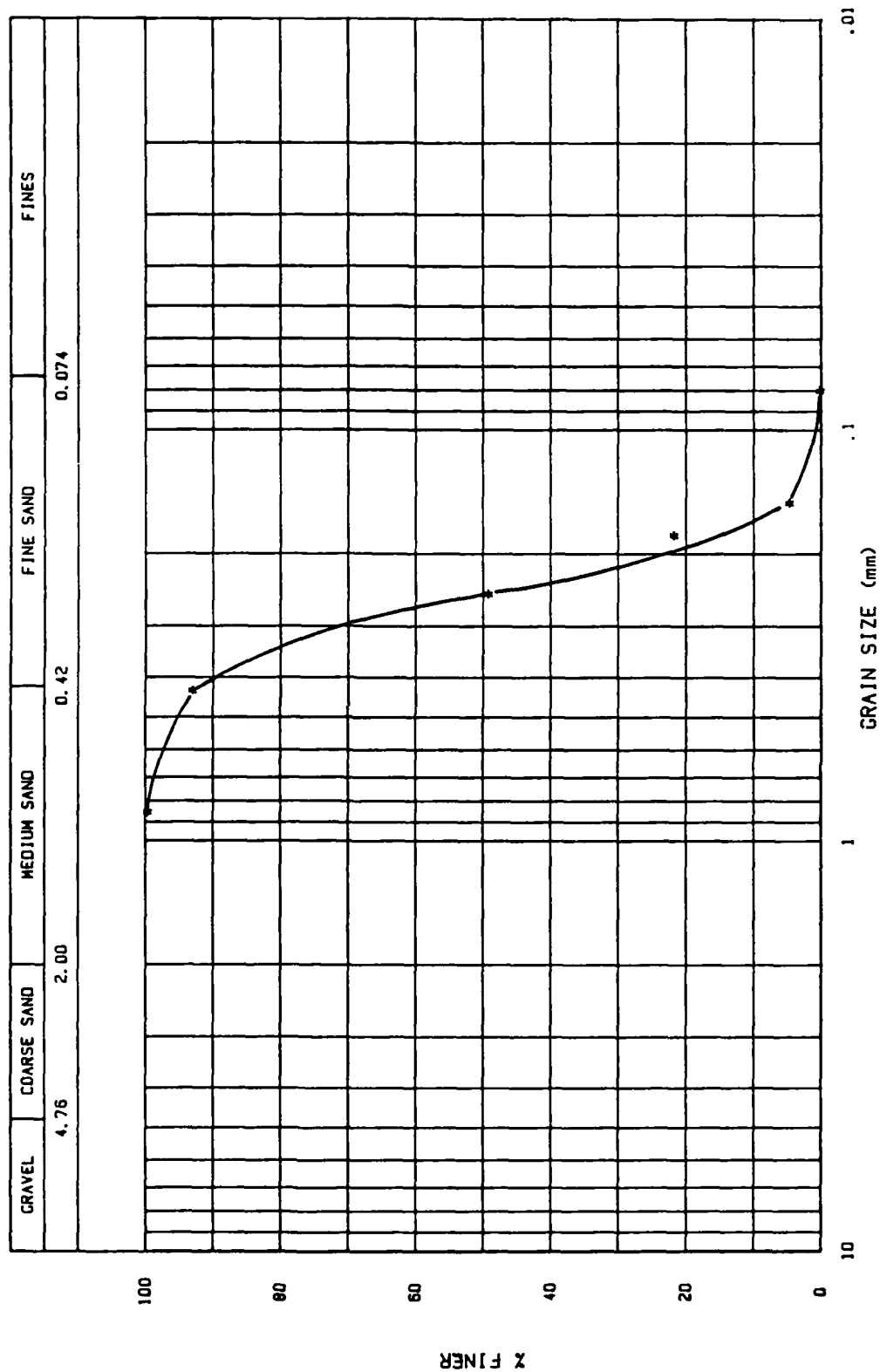


Figure 20. Grain Size Distribution Curve for Reid-Bedford Sand.

$$\epsilon_v = \text{tr} (\underline{\epsilon}) = \text{total volumetric strain} ,$$

and

$$\text{Integral of effective strain increment} = \int_t \sqrt{\frac{1}{2} (\dot{\underline{\epsilon}}:\dot{\underline{\epsilon}})} dt .$$

Note that

$$q = \sigma_1 - \sigma_3$$

and

$$\bar{\epsilon} = \epsilon_1 - \epsilon_3$$

for the stress paths in the 'triaxial' chamber (see figure 3) since either  $\sigma_1 = \sigma_2$  (and  $\epsilon_1 = \epsilon_2$ ) or  $\sigma_2 = \sigma_3$  (and  $\epsilon_2 = \epsilon_3$ ). In the context of the following discussion, the term 'shear' stress is taken to mean a constant multiplied by the octahedral shear stress while an analogous definition holds for the term 'shear' strain.

A series of drained axial compression loading and axial extension unloading tests (i.e., CTCs and RTEs of figure 3) were first carried out to establish the strength of the sand. Initial effective confining pressures of 25, 35, and 45 psi were selected for both the loading and unloading paths. The corresponding series of HCA tests started at 30 psi, and, wherever possible, results of both tests are superposed for comparison.

Figure 21 shows the measured stress paths in p-q subspace for the axial loading tests. The strength parameters computed using the stress states at the end of these trajectories appear as the first four rows in tables 2 and 3; as can be seen, correlation of the strength between the SCA and HCA axial loading tests is excellent.

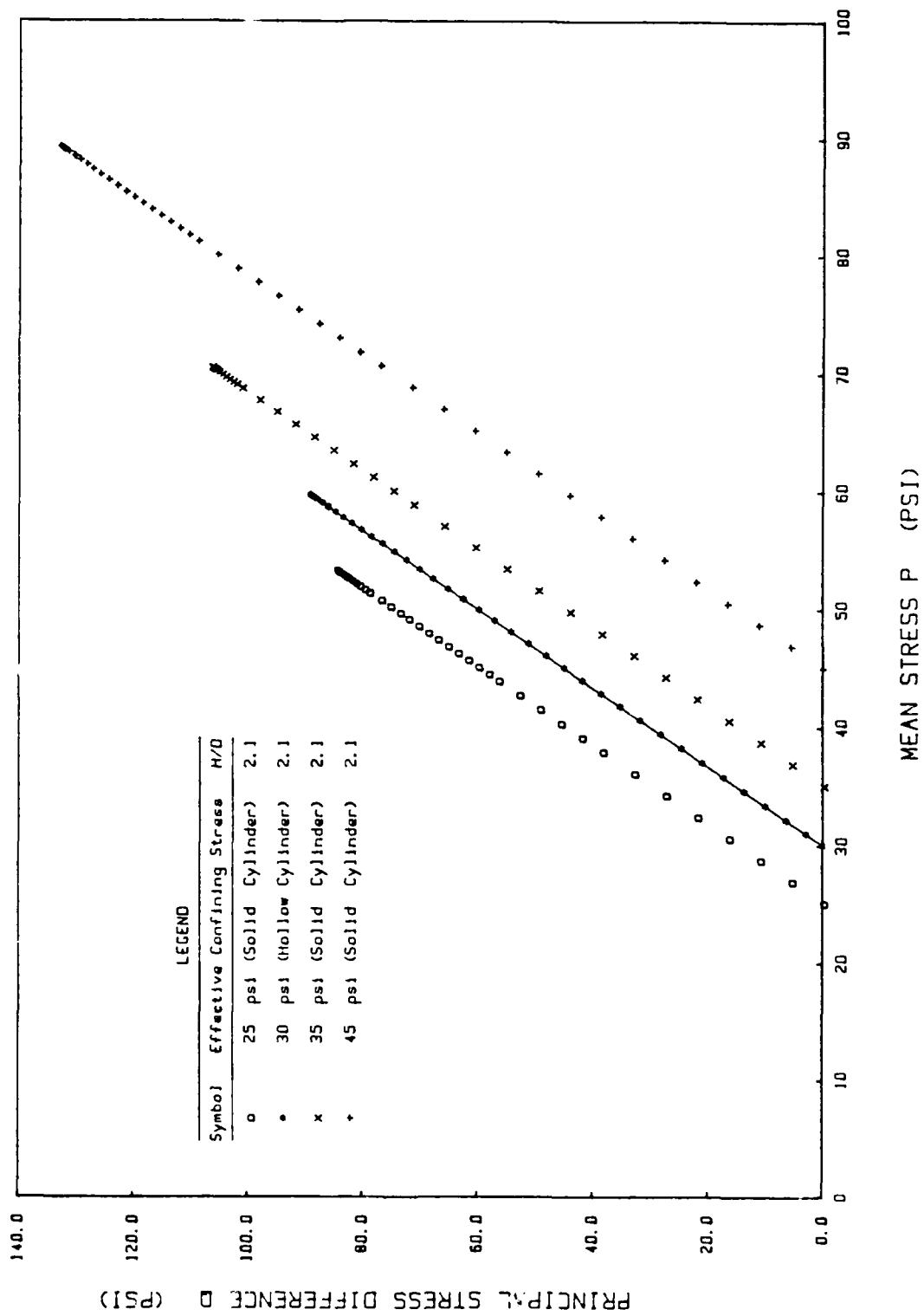


Figure 21. Stress Paths for CTC tests.

AD-A162 348

GENERALIZED PHENOMENOLOGICAL CYCLIC  
STRESS-STRAIN-STRENGTH CHARACTERIZATI  
GAINESVILLE DEPT OF CIVIL ENGINEERING  
D SEEREERAM ET AL 27 JUN 85

(U) FLORIDA UNIV

3/3

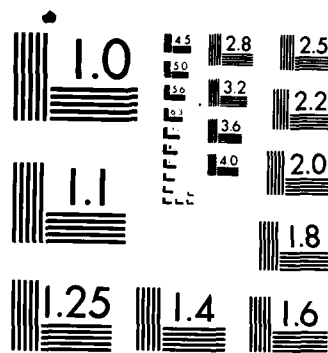
UNCLASSIFIED

F/G 8/13

NL

					END								
					FORMED								
					DTIC								





MICROCOPY RESOLUTION TEST CHART  
NATIONAL BUREAU OF STANDARDS-1963-A

TABLE 2. INFLUENCE OF PRINCIPAL STRESS AXES ROTATION ON STRENGTH

TEST I.D.	DRUCKER-PRAGER'S FAILURE CRITERION $(\sqrt{J_2}/I_1)_f$	MATSUOKA'S FAILURE CRITERION $[-(I_1, I_2)_f - 9] I_3$	MOHR-COULOMB'S FAILURE CRITERION ( $\phi$ , degrees)
Constant Intermediate Principal Stress Tests:			
CTC @25 psi	.306	5.23	38.97
CTC @30 psi or DC 0	.287	4.45	36.71
CTC @35 psi	.291	4.59	37.14
CTC @45 psi	.287	4.42	36.61
RTC	.287	4.43	36.67
DCR 15	.298	5.00	40.39
DCR 32	.294	7.74	49.69
DTR 58	.212	5.81	42.74
DTR 75	.201	5.34	39.49
DT 90	.212	6.64	42.34
Constant Mean Normal Pressure Tests:			
GC 0	.295	4.73	37.57
GCR 15	.315	5.83	42.89
GCR 32	.317	11.22	55.02
R 45	.250	8.22	49.32
GTR 58	.205	5.15	41.00
GTR 75	.185	3.91	35.49
GT 90	.204	5.63	40.00

TABLE 3. SIMPLE MODEL OF FABRIC'S INFLUENCE ON STRENGTH

TEST I.D.	LADE'S FAILURE CRITERION $[(\frac{I_1}{I_3})^3 - 27] (\frac{I_1}{I_3})^m$ $I_3$ $p_a$	ANGLE BETWEEN 2ND SLIP LINE AND WEAK AXIS (degrees)	ANGLE BETWEEN 1ST SLIP LINE AND STRONG AXIS (degrees)
--------------	--	--	--

## Constant Intermediate Principal Stress Tests:

CTC @25 psi	37.06	65	25
CTC @30 psi or DC 0	30.62	65	25
CTC @35 psi	32.07	65	25
CTC @45 psi	31.05	65	25
RTC	28.20	65	25
DCR 15	34.69	50	10
DCR 32	45.87	33	7
DTR 58	26.70	7	33
DTR 75	23.90	10	50
DT 90	29.61	25	25

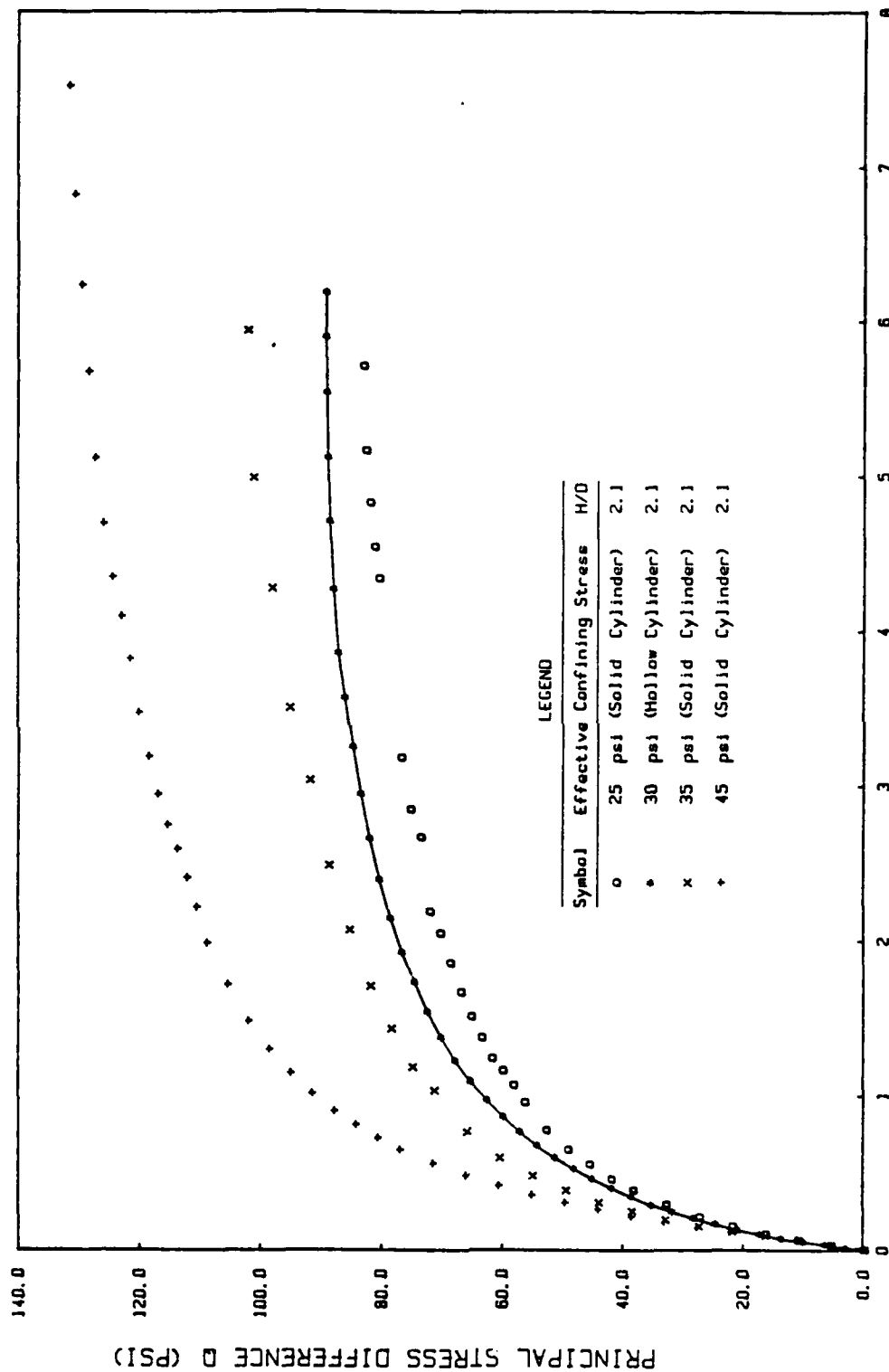
## Constant Mean Normal Pressure Tests:

GC 0	31.72	65	25
GCR 15	40.19	50	10
GCR 32	66.06	33	7
R 45	40.42	20	20
GTR 58	23.91	7	33
GTR 75	17.93	10	50
GT 90	25.58	25	65

Figures 22 and 23 show plots of the shear stress ( $q$ ) vs. shear strain ( $\bar{\epsilon}$ ) and volumetric strain ( $\epsilon_v$ ) vs. mean stress ( $p$ ) respectively for the CTC tests; a comparison of these graphs with the typical behavior depicted in figure 2 indicates that this material behaves like a dense sand, as it should. Inspection of figure 22 shows that there is no apparent difference in the shear stress-shear strain response recorded in the SCA and HCA tests, but, by looking closely at the volume strain vs. mean stress plots in figure 23, we see that the volumetric strains measured in the HCA test are somewhat larger than those in the SCA tests. This difference will become more apparent when the bounding surface predictions of these tests are discussed in a later subsection. Overall, however, there appears to be no significant influence of the specimen's shape on material response for the axial loading tests.

Unlike the loading tests, the response - i.e., stress-strain behavior, volume change characteristics, and strength - of axial unloading tests (RTEs) on sand is significantly affected by the predominant failure mode occurring in the specimen; these may be classed as line failures or zone failures.

In a zone failure, uniform conditions of stress and strain produce multiple failure planes traversing the specimen at angles of  $\pm(45 + \phi/2)$  degrees to the  $\sigma_3$ - direction. This mode of failure was typical of all the axial loading tests. If the strains are non-uniform however, line failure occurs in which two practically solid bodies slide past each other along a single failure plane which is oriented at  $45 + \phi/2$  degrees to the  $\sigma_3$ - direction. The photograph in figure 16 of the



PRINCIPAL STRAIN DIFFERENCE (\*10-02)

Figure 22. 'Shear' Stress vs. 'Shear' Strain for CTC tests.

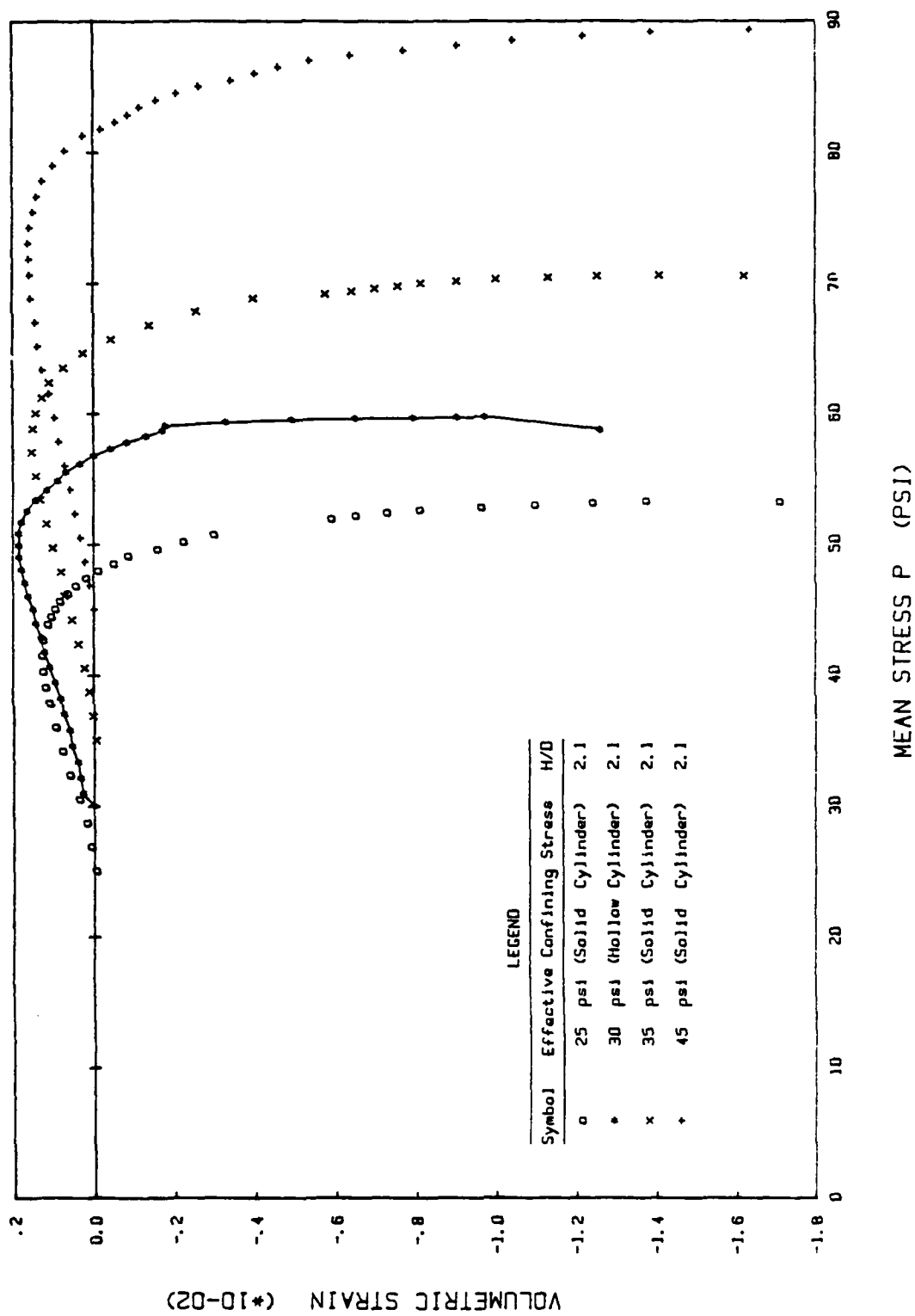


Figure 23. Volumetric Strain vs. Mean Stress for CTC tests.

previous section is a typical example of an RTE line failure obtained using specimens with height to diameter (H/D) ratios of 2.1. As pointed out by Lade (Reference 88),

The stress-strain behavior of a line failure specimen is governed by the relative proportions of elastic and plastic deformation. After initiation of dilation along one or two narrow planes in an extension specimen, failure will eventually occur along these relatively weak planes, and the specimen will only compress elastically. Therefore, the greater the height to diameter ratio of the specimen, the smaller is the percentage of the total volume of sand which is involved in the failure and the larger is the percentage of the volume which will undergo primarily elastic compression. Thus, the average value of strains in line failure specimens depend on the shape of the specimen.

Although the tests in question are unloading tests, one should note that it is possible for anisotropic samples to undergo elastic compression; this will occur, for example, in cross-anisotropic cylindrical specimens if

$$E_y/E_r > \frac{1}{2\nu} ,$$

where  $E_y$  and  $E_r$  are the elastic tangent moduli in the axial and radial (or circumferential) directions respectively, and  $\nu$  is Poisson's ratio. Since the samples used in all experiments were prepared by a combination of pluviation and tapping, it is expected that  $E_y$  will initially be greater than  $E_r$ .

Figure 24 is a plot of the effective stress paths for the series of four RTE tests, each starting at confining pressures of 25, 30, 35, and 45 psi respectively; note that the test at 30 psi had an H/D ratio of unity while the others were at the typical H/D ratio of about 2.1. The

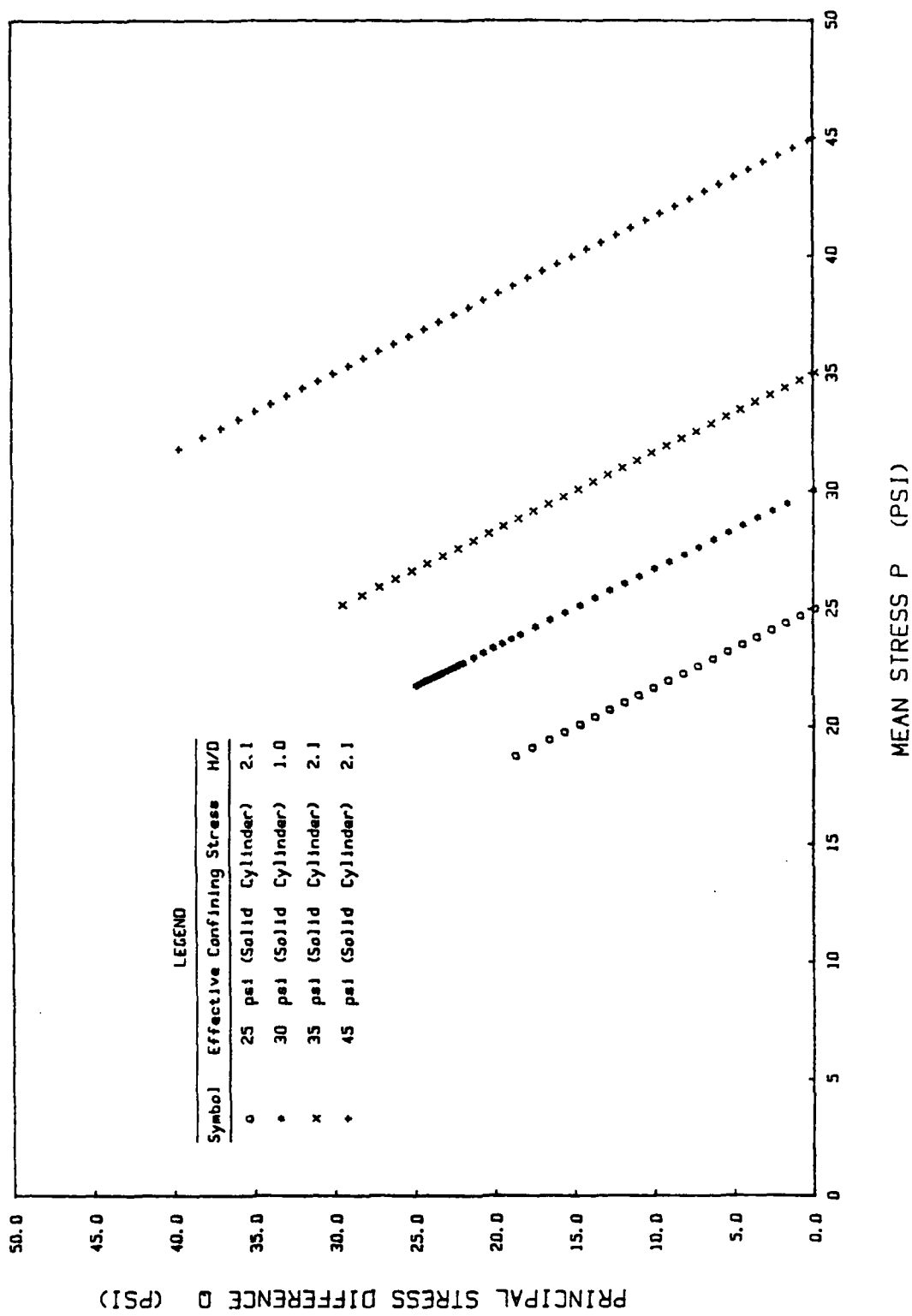


Figure 24. Stress Paths for RTE tests.



test with the H/D ratio of one was characterized by a zone type failure while the other specimens experienced line failure modes upon unloading. There was considerable scatter in the observed strength for these unloading tests, and the test with an H/D ratio of unity was the only one considered acceptable. Further evidence of the marked influence of specimen shape on the observed RTE test response can be seen in the plots of shear stress vs. shear strain (figure 25) and volumetric strain vs. mean normal pressure (figure 26). It is apparent that, because of the severe non-uniformities of strain in the line failure specimens, almost any stress-strain relation can be produced from such specimens depending on their height to diameter ratio, and we therefore recommend extra care in the analysis of the results of unloading tests on solid cylindrical samples of sand.

The stress paths used for the next series of tests were selected primarily for the purpose of providing qualitative and quantitative data on inherent and stress-induced anisotropy. It is anticipated that these simple tests can somehow form a fundamental basis for mathematically modelling the influence of anisotropy on the direction of the plastic flow rate vector. The first test consisted of a spherical loading on a virgin sample which was prepared by pluviation in conjunction with vibration in the direction of deposition. A plot of the axial (or vertical) strain ( $\epsilon_y$ ) versus the circumferential (or horizontal) strain ( $\epsilon_\theta$ ) for this test is presented in figure 27. Superimposed on this graph are the results of a similar test carried out in the HCA; both tests started at a mean normal stress ( $p$ ) of 10 psi and terminated at  $p = 100$  psi. Agreement between the two tests is

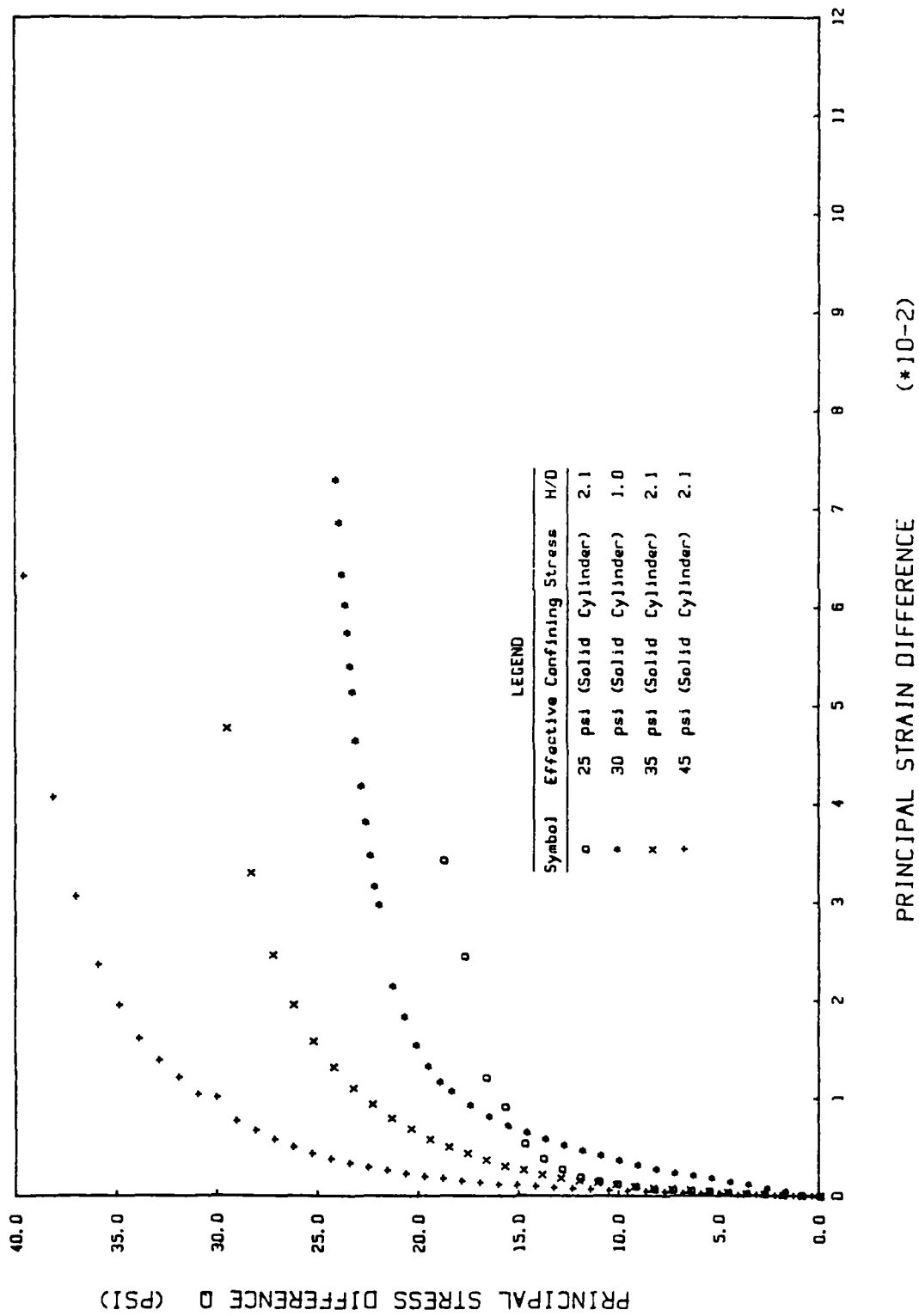


Figure 25. 'Shear' Stress vs. 'Shear' Strain for RTE tests.

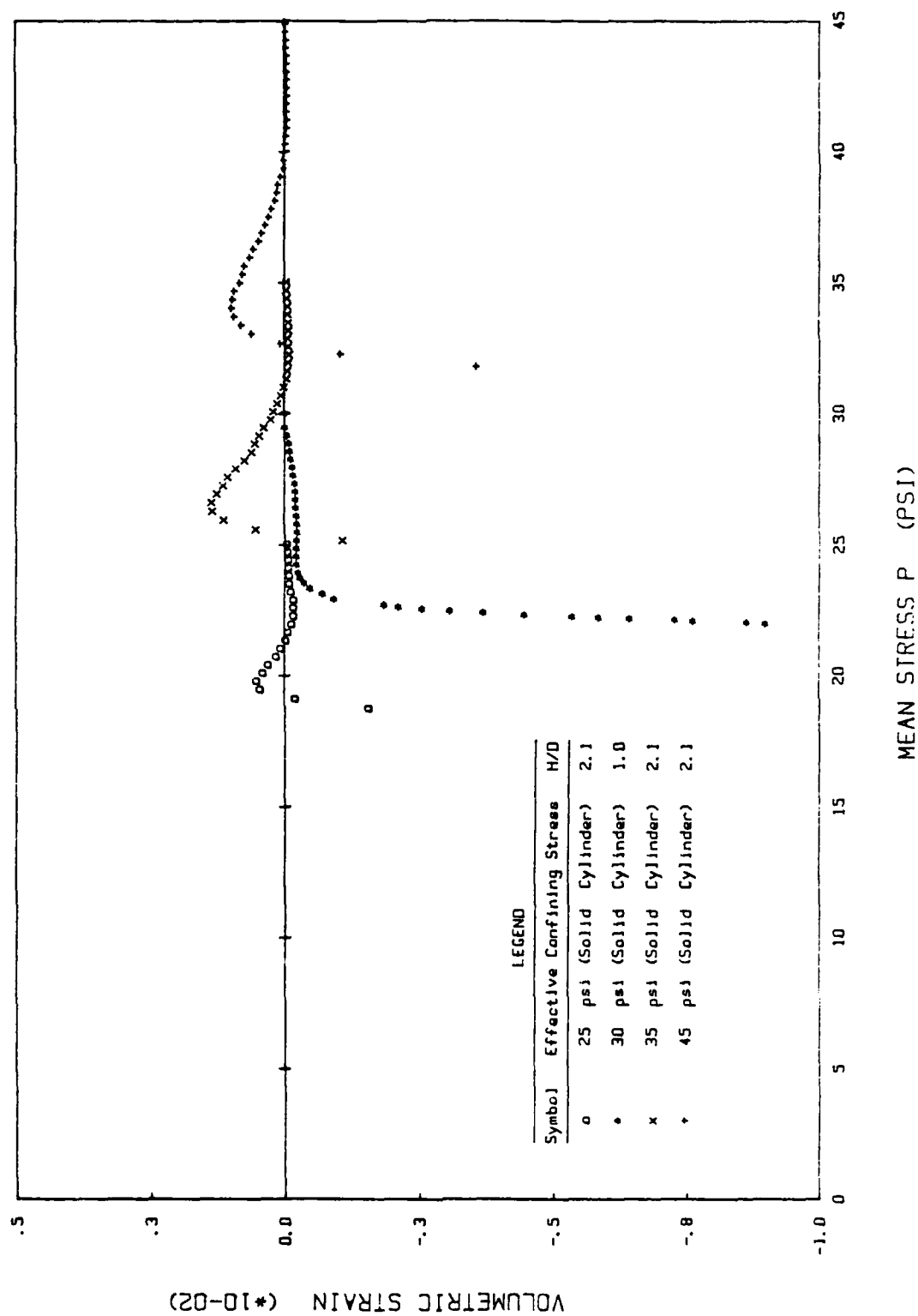


Figure 26. Volumetric Strain vs. Mean Stress for RTE tests.

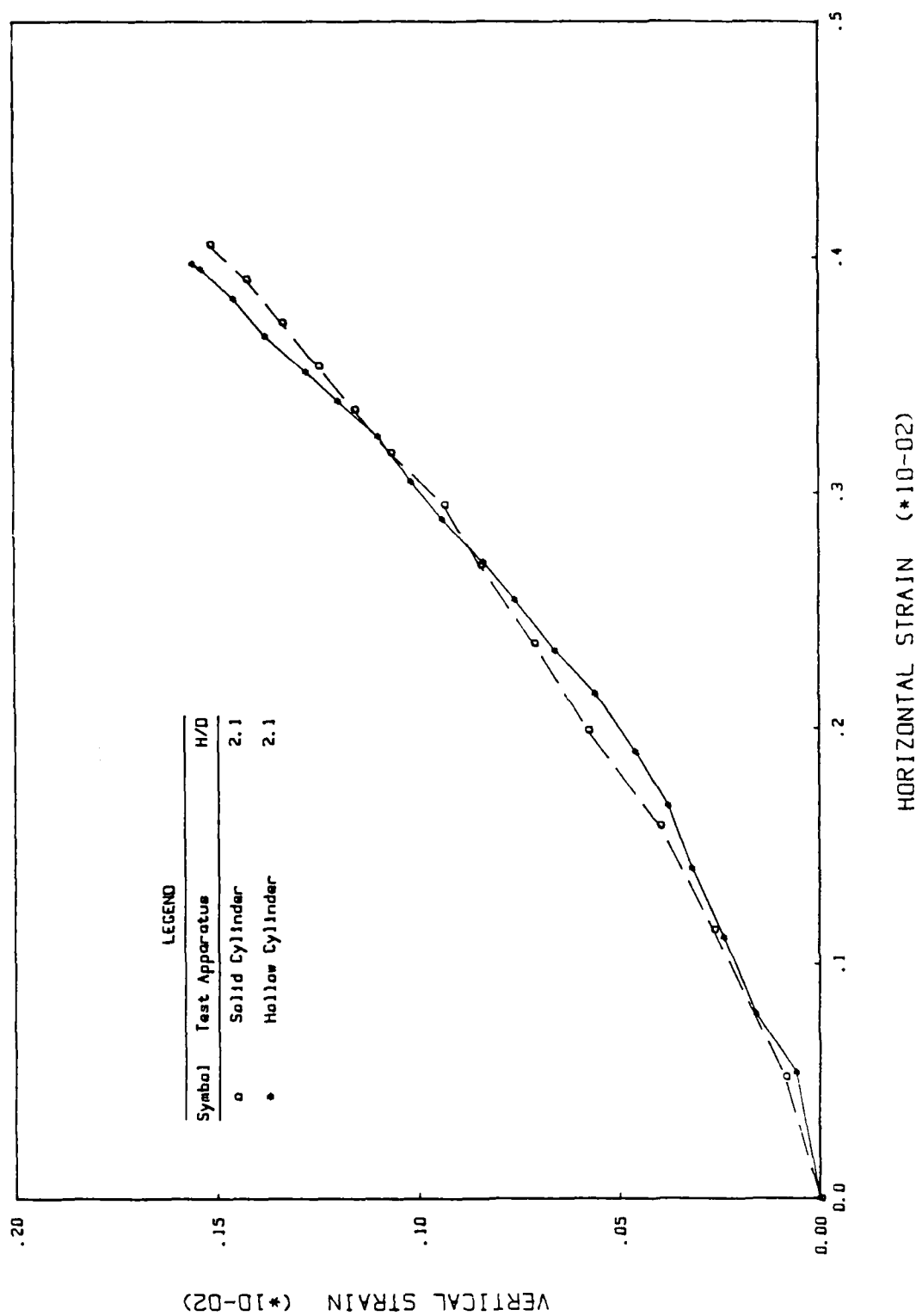


Figure 27. Vertical Strain vs. Horizontal Strain for Hydrostatic Loading on Inherently Anisotropic Specimen.

remarkable. The ratio  $\epsilon_\theta/\epsilon_y$  is, as expected, greater than unity due to the inherent stiffness anisotropy, and its magnitude actually starts at about 6 and decreases to about 3 at the end of the test. It is clear from these results that continued spherical loading of a specimen prepared in this manner does not completely wipe out the influence of inherent fabric on flow.

By using instead a rodding technique during specimen preparation, it may be possible to create a random structure (with a random orientation of the contact normals) which should produce  $\epsilon_\theta/\epsilon_y$  ratios close to unity. But, since most natural deposits of sand do possess some anisotropy due to their natural or artificial formation process, investigation of nearly isotropic specimens may prove to be only of academic interest.

Figure 28 is a plot similar to figure 27 except now the samples have been subjected to some level of deviatoric loading (more specifically, CTC loading) prior to the hydrostatic consolidation. Anisotropy was stress-induced in the specimens up to 15%, 40%, and 60% respectively of the peak deviatoric stress level; at this point, the specimens were unloaded back to an all-round pressure of 10 psi where they were then all subsequently reloaded spherically to  $p = 100$  psi. The results of the last phase of the loading path are plotted in figure 28 together with the data of figure 27 and an idealized isotropic response line to serve as a reference. Again, it is obvious from this graph that the intensity of induced and inherent anisotropy does not diminish significantly under continued spherical loading.

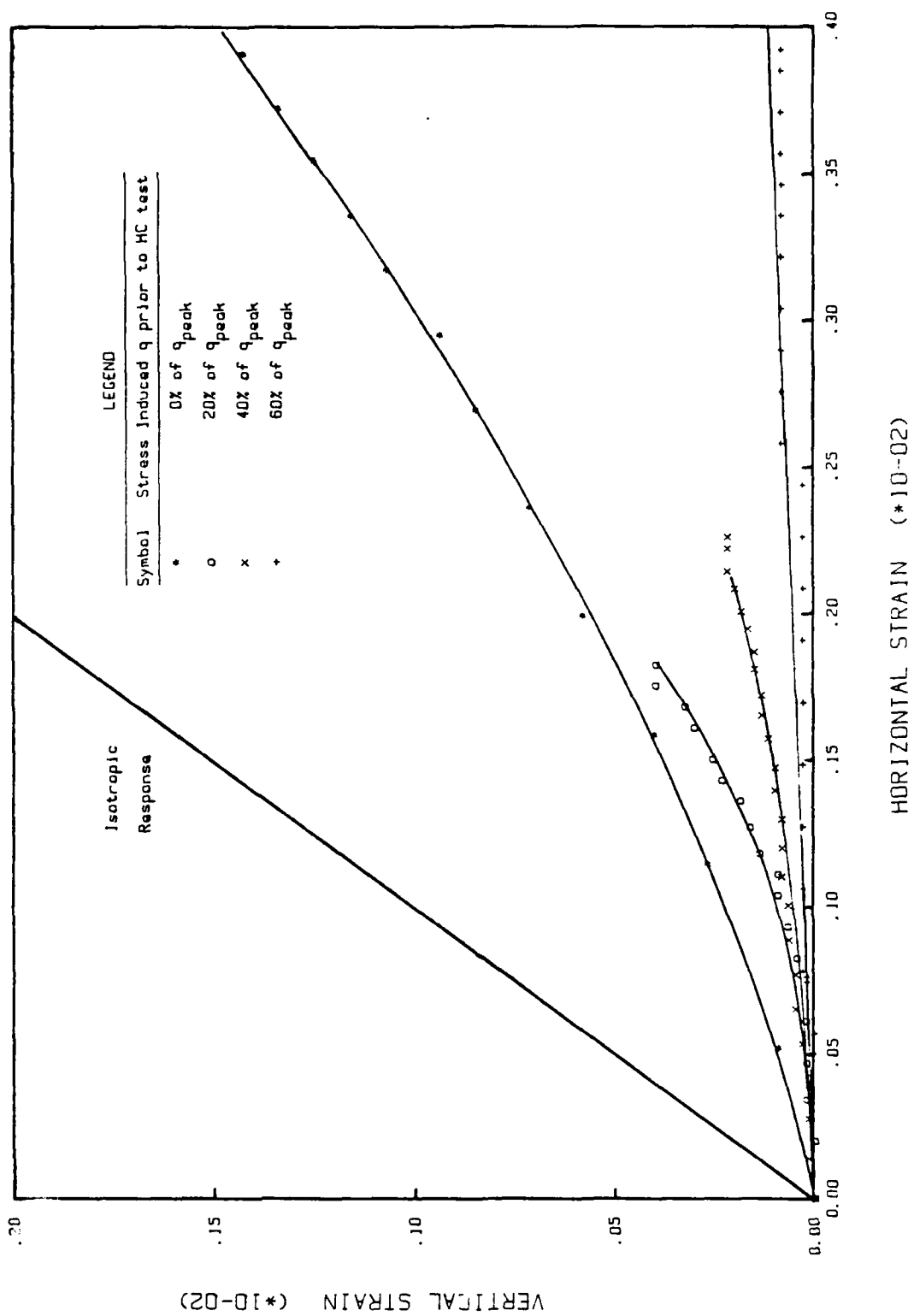


Figure 28. Vertical Strain vs. Horizontal Strain for Hydrostatic Loading on Specimens with Stress-Induced Anisotropy.

### C. HOLLOW CYLINDER TEST RESULTS

The hollow cylinder apparatus (HCA) data has been reduced using the shear stress distribution assumptions outlined by Saada and Townsend (Reference 5); axial displacements, volume change, and twist are converted to the components of the small strain tensor ( $\epsilon$ ) while the generalized stresses (axial load and torque) and the confining pressure are represented by the components of the Cauchy stress tensor ( $\sigma$ ).

Strength parameters for each of the fourteen shear tests have been computed using four different isotropic failure criteria for sand; these yield envelopes were presented earlier in SECTION II and include those of

- 1). Drucker-Prager (Reference 48) in which it is assumed that failure is governed by the ratio of octahedral shear stress to octahedral normal stress;
- 2). Lade (Reference 55) which is an empirically fitted criterion using the first and third invariants of stress;
- 3). Matsuoka (Reference 56) in which he proposes the spatial mobilized plane concept or a limiting value of shear to normal stress on the the plane on which soil particles are on average most mobilized;

and

- 4). Mohr-Coulomb (Reference 49) which is based on a limiting value of shear to normal stress on the plane on which particles are most mobilized (or the plane of maximum obliquity).

The results of this analysis are summarized in tables 2 and 3 using the compact hollow cylinder test identification nomenclature of the

previous section. The exponent "m" used in the calculation of the Lade strength constant was estimated to be equal to .056 (Reference 89).

Before attempting to isolate the influence of inherent anisotropy, it is instructive to explore the following list of possible variables on which the strength constants of tables 2 and 3 may depend:

- 1). the test apparatus is not ideal and there may be varying degrees of non-uniformity in stress and/or strain for the different paths of loading;
  - 2). the strength criterion may not be a good representation of yield in that it may not be able to realistically capture the influence of intermediate principal stress and/or bulk stress;
- and
- 3). induced and inherent anisotropy may produce directional strength and stiffness properties as a result of the relative orientation of the symmetry axes of the applied stress with respect to symmetry axes of the existing fabric. It also seems intuitively reasonable to assume that the extent of this variation will depend on the "deviatoric" intensity of the fabric.

For this preliminary evaluation, we can assume that experiments were perfect and that Lade's failure criterion provides a satisfactory representation of the isotropic failure locus on the octahedral plane. These two assumptions allow us to isolate the variation in strength due to anisotropy by studying the constant mean stress tests. Casual inspection of table 2 reveals that, with the above-mentioned assumptions, inherent anisotropy is clearly an important independent



variable. The general trend in strength variation shows a peak when the maximum compressive stress makes an angle of 32 degrees with the axial (or strongest) direction of the specimen while a minimum strength is observed when this angle is 75 degrees. The discussion in the following paragraph is an attempt to explain this behavior, and this approach, we hope, will provide the framework for mathematically incorporating the strength variation in the Bounding Surface plasticity model.

A crude but preliminary explanation for the observed strength variation was conceived by using a simple slip-line field for materials with friction. Following the usual convention (see, for example, Reference 90), the directions of the first and second slip lines are identified by rotating anti-clockwise and clockwise respectively through an angle of  $45 - \phi_m/2$  from the direction of the major principal stress, where  $\phi_m$  is the mobilized friction angle. Since the inherent fabric anisotropy was created by gravity pouring and a small vertical vibration, we naturally expect the vertical direction to initially be stronger than the horizontal direction owing to the non-spherical density distribution function of contact normals (or any other fabric measure). The postulated model of strength variation then suggests itself: the slip plane which is closer to the weaker direction predominates and this can henceforth be called the critical plane. By completely neglecting the non-critical slip plane, a correlation between the strength and the angle between the critical plane and the weak direction can then be sought. Table 3 presents the data which compares this angle with the Lade strength parameter for an assumed mobilized friction angle ( $\phi_m$ ) of 40 degrees. Remember that we are

focusing only on the mean normal pressure tests and it is implicit that the initial fabric does not change during loading.

This simple sliding picture accounts for the minimum strength we observe at the 58 to 75 degree rotations, and with the plot of figure 29 as an example, there is considerable experimental evidence to support this explanation (References 86, 87, 91, 92, and 93). The data in table 3, however, suggests that angle between the 1st slip line and the strong axis should also be included in the sliding model in order to interpret the peak strength at the 32 degree rotation.

In closing the discussion on observed strength, one should also take note of the deviation of the shear strength as accounted for by pure Coulomb friction; it is common knowledge that the measured friction angle is a combination of surface friction and interlocking friction, the latter decreasing as the confining stress increases because: a) the particles become flattened at contact points, b) sharp corners are crushed, and c) particles break. Of those used herein, only the Lade failure criterion takes into account the curvature of the failure locus on the meridional plane.

Having completed strength, we now proceed to a discussion of stress-strain. Figures 30 and 31 are the shear stress vs. shear strain and volume strain vs. mean stress plots respectively for the constant intermediate principal stress tests in compression space. The shear stress-shear strain plots can be easily fitted with hyperbolas, and this suggests that the simple, but yet powerful, hyperbolic function should be harnessed in a hardening rule which permits modification of the limiting asymptote to model the influence of principal stress axes

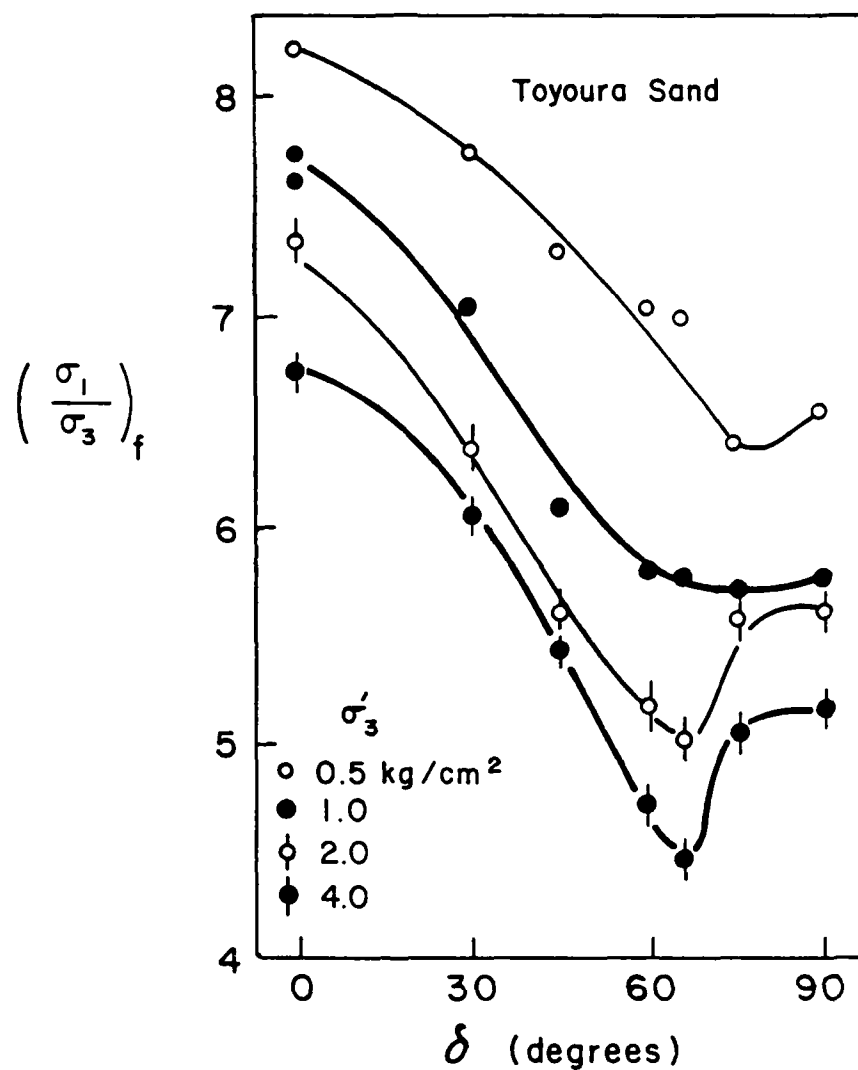


Figure 29. Strength Variation due to Relative Orientation of Eigenvectors of Stress With Respect to those of Fabric (Reference 92).

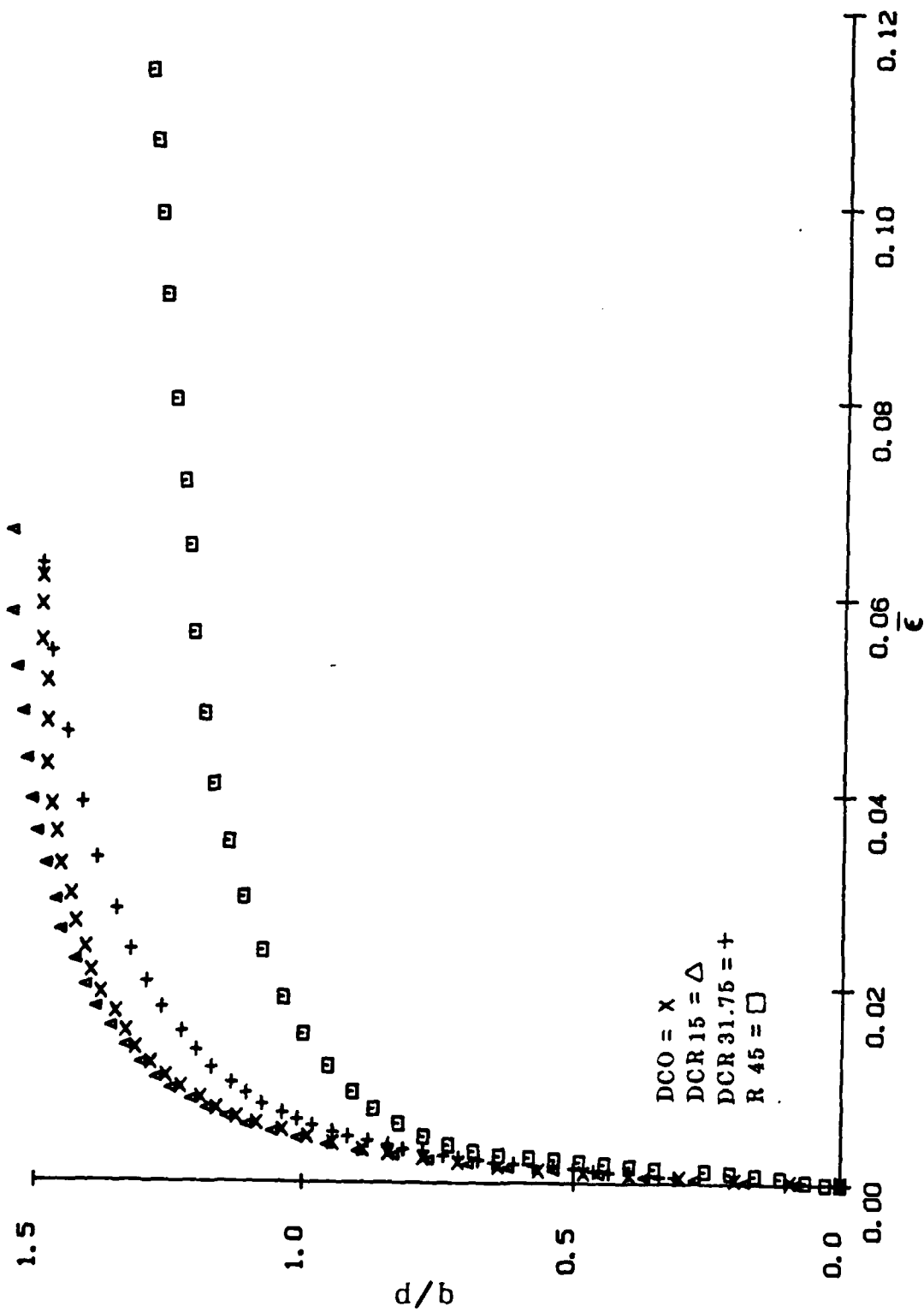


Figure 30. Normalized Shear Stress vs, Shear Strain for the following HCA tests: DC 0, DCR 15, DCR 31.75, and R 45 (data from Reference 9).

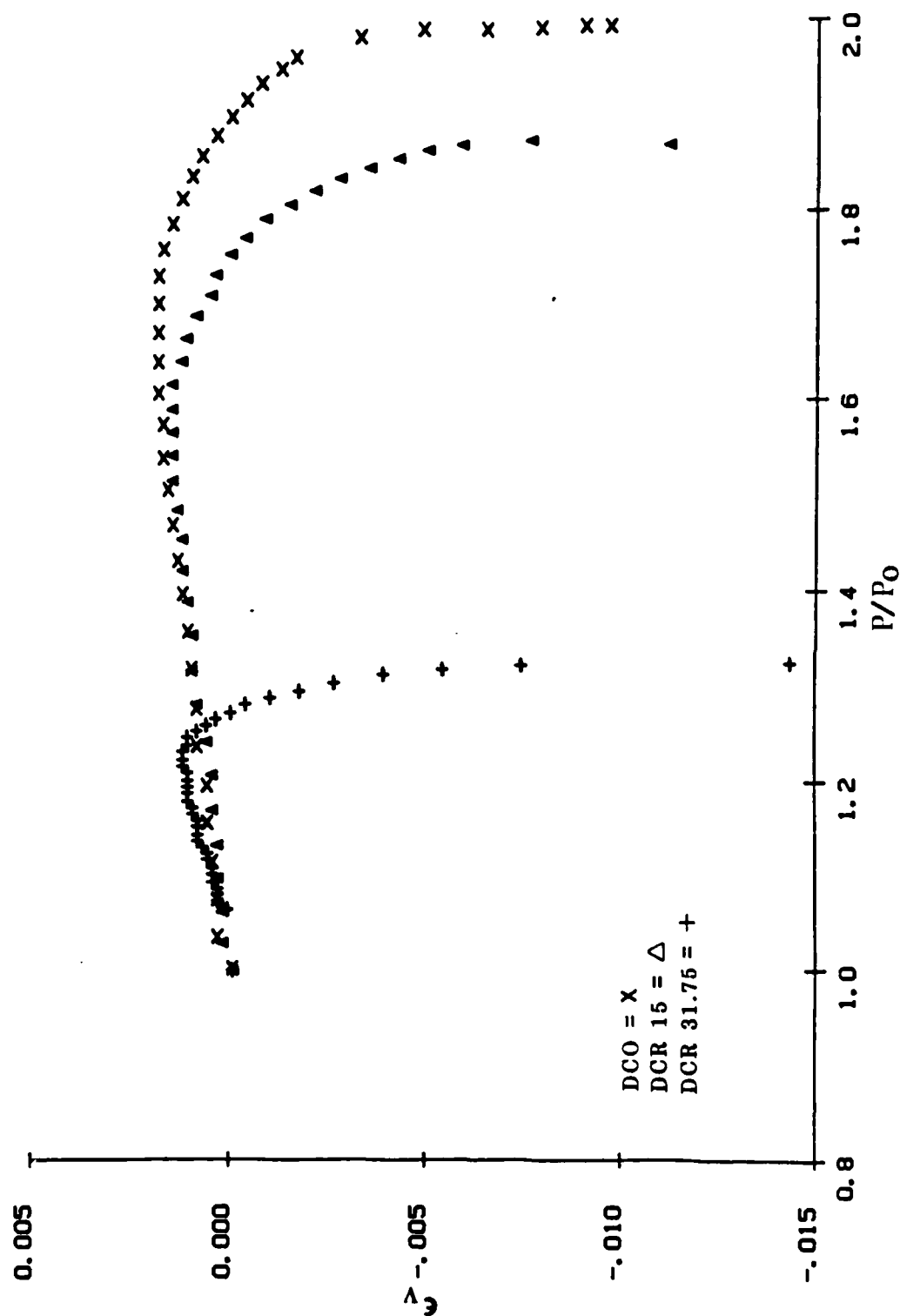


Figure 31. Volume Strain vs. Normalized Mean Stress for the following HCA tests: DC 0, DCR 15, and DCR 31.75 (data from Reference 9).

rotation on strength. The volume change characteristics depicted in figure 31 support the critical state locus hypothesis, which defines a zero dilatancy curve in stress space. For reference, the remainder of the HCA experimental data plots are included in Appendix A.

#### D. PREDICTIONS OF HCA TESTS USING PREVOST'S MODEL

The Prevost isotropic/kinematic model has been calibrated for Reid-Bedford sand using procedures outlined in section III. Although this feature is exactly what this type of model should thrive on, volumetric compression recorded during an unloading test prevents initialization of the Prevost model. This peculiarity, in fact, motivated the study of the sensitivity of the volume change response to the aspect ratio ( $H/D$ ) of the solid cylindrical samples. The sample of height to diameter ratio of unity dilated from the start of the test until failure (see figure 26), and it was thus selected as the unloading calibration path. The parameter,  $\lambda$ , controlling the isotropic hardening process was determined from the results of an extensive series of one dimensional consolidation tests carried out at the U.S. Army Waterways Experiment Station in Mississippi (Reference 94). Table 4 is a summary of the Prevost model parameters which were computed.

Before proceeding with the presentation, the distinction between the terms "prediction" and "postdiction", as implied in this context, must be emphasized. A postdiction will refer to the numerical simulation of a test which was used in deriving the model parameters, so if the model initialization scheme was precise, the experimental data should be reproduced almost exactly. A prediction, on the other

TABLE 4. PREVOST MODEL PARAMETERS FOR REID-BEDFORD SAND

G = 13500 psi, K = 17680 psi, n = 0.5, C =  $3/\sqrt{2}$ ,  $\lambda = 130$ ,  
 initial effective confining pressure = 30 psi,  
 initial void ratio = 0.67,  
 number of yield surfaces used to characterize field = 20

m	$\alpha^{(m)}$	$\beta^{(m)}$	$k^{(m)}$	$h^{(m)}$	$B^{(m)}$	$A^{(m)}$
2	6.408	31.27	6.951	25800	-4766	-.3538
3	8.813	30.94	12.002	22918	-7282	-.5238
4	12.345	31.45	18.028	12205	-4379	-.5792
5	12.867	32.02	21.778	8084	-2904	-.7157
6	15.796	32.43	27.317	5225	-2183	-.7133
7	19.500	34.19	34.345	2873	-1206	-.8528
8	20.001	34.60	36.257	2404	-998	-.8677
9	20.106	35.26	38.134	1963	-783	-.9433
10	23.111	37.66	44.265	1324	-468	-1.085
11	25.289	38.74	48.304	1075	-380	-1.118
12	27.572	40.47	53.206	878	-300	-1.179
13	29.333	41.71	56.713	736	-246	-1.230
14	33.178	44.29	63.402	562	-179	-1.317
15	35.950	46.11	68.734	465	-148	-1.364
16	39.355	48.64	75.509	388	-121	-1.434
17	46.289	54.03	89.040	293	-86	-1.510
18	51.052	59.62	101.946	236	-64	-1.6312
19	63.695	70.81	129.011	143	-37	-1.7759
20	65.566	77.95	144.322	95	-22	-1.8658

hand, refers to the simulation of a loading path other than those used in calibration.

As discussed in section III, the CTC and RTE loading path starting at the same initial confining stress are used to establish the model constants. Postdictions of both these test paths are presented in figures 32 and 34 while the movement of the surfaces during these tests are depicted in figures 33 and 35; each of these loading path recreates its measured response to a reasonable degree of accuracy. In order to minimize numerical discrepancies, 800 load steps were used for each simulation although most solutions were found to be stable when as little as 200 load steps were used.

The true test of the general applicability of a constitutive model, however, is its ability to predict (and not regurgitate its input data). All of the hollow cylinder tests (excluding, of course, the two used in calibration) have been predicted with the Prevost model, and, wherever possible, plots of the initial and final configurations of field of yield surfaces (in  $Cp'-q$  subspace) accompany each prediction. Predictions of the stress paths easily visualized in  $p-q$  stress space - i.e., TC (or GC 0), RTC, and TE (or GT 90) of figure 3 - are shown in figures 36-41 while the remainder have been appended (see appendix B). It is apparent that the model predictions are generally stiffer than the actual response, but it is only fair to point out that the postdictions were also somewhat stiffer than the input data. The



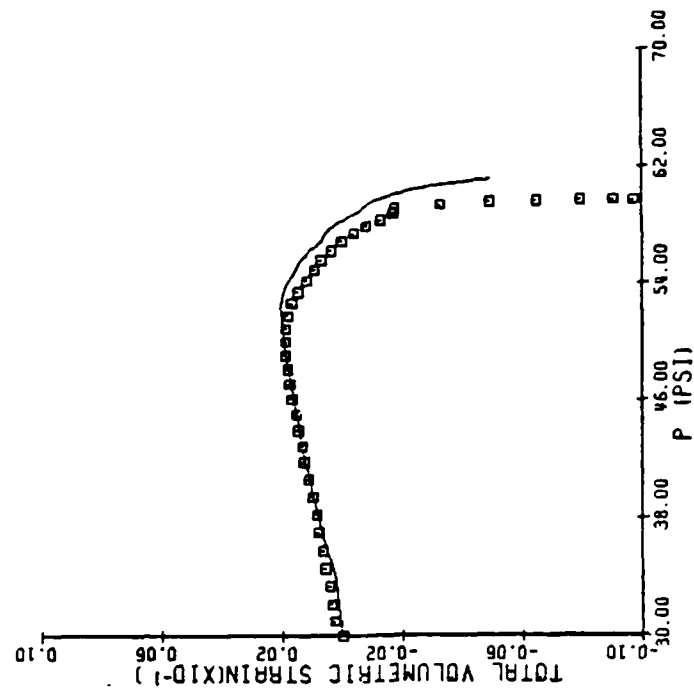
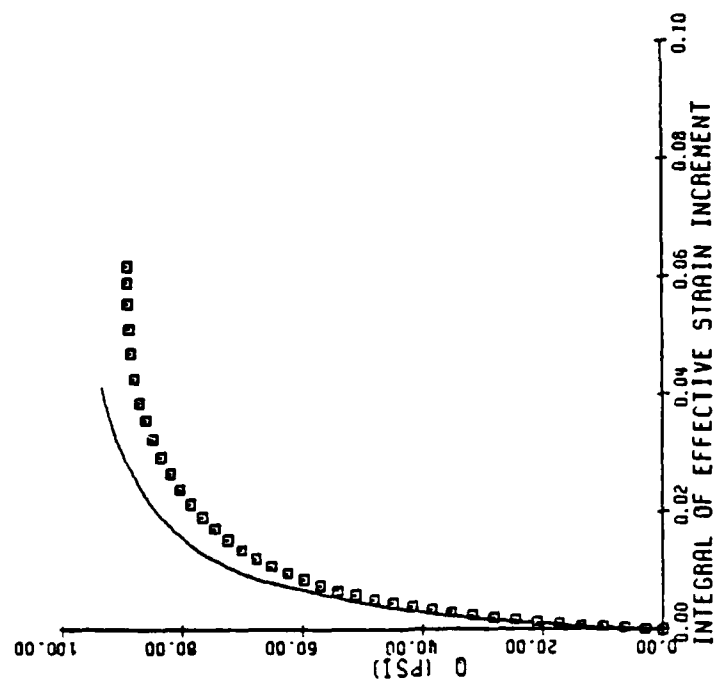


Figure 32. Postdiction of CTC test using Prevost's Model.

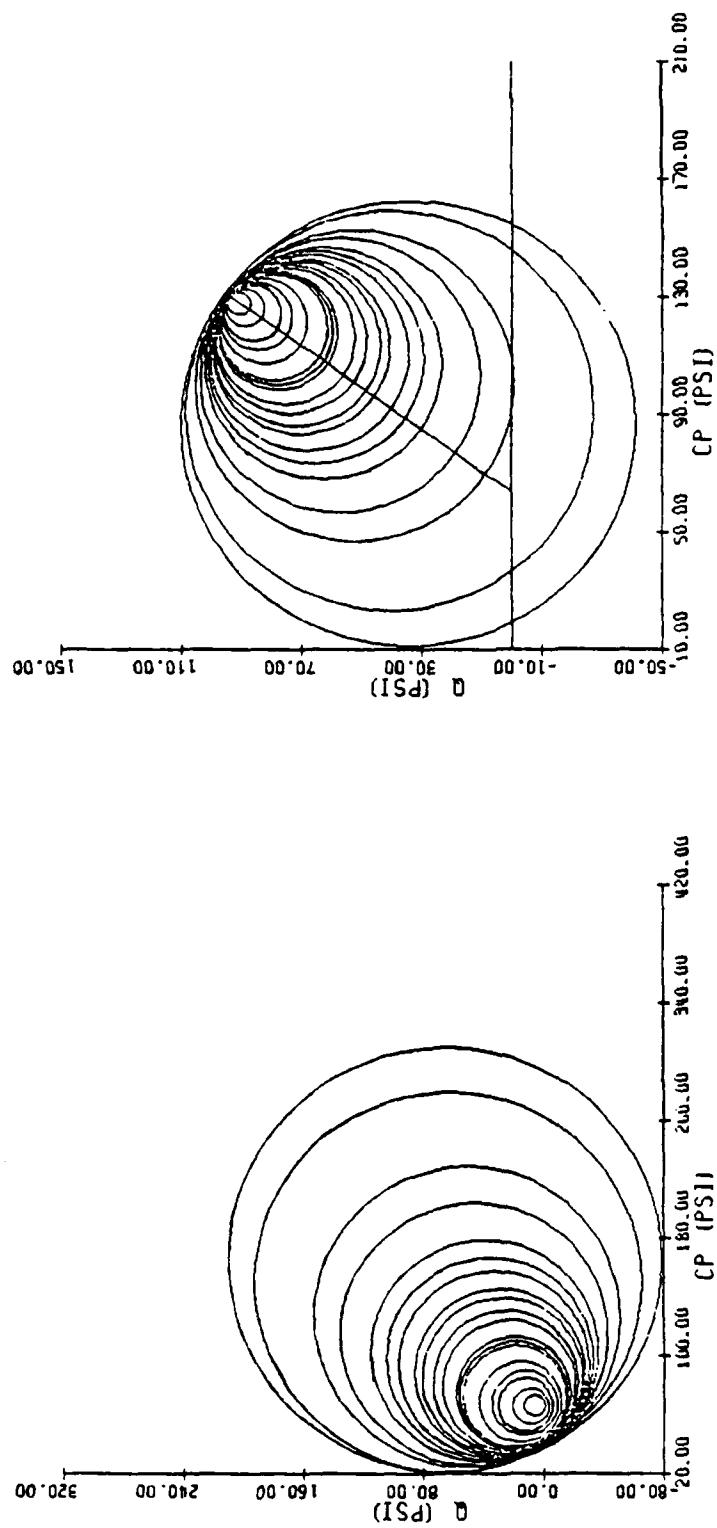


Figure 33. Initial and Final Configuration of Yield Surfaces for CTC simulation.

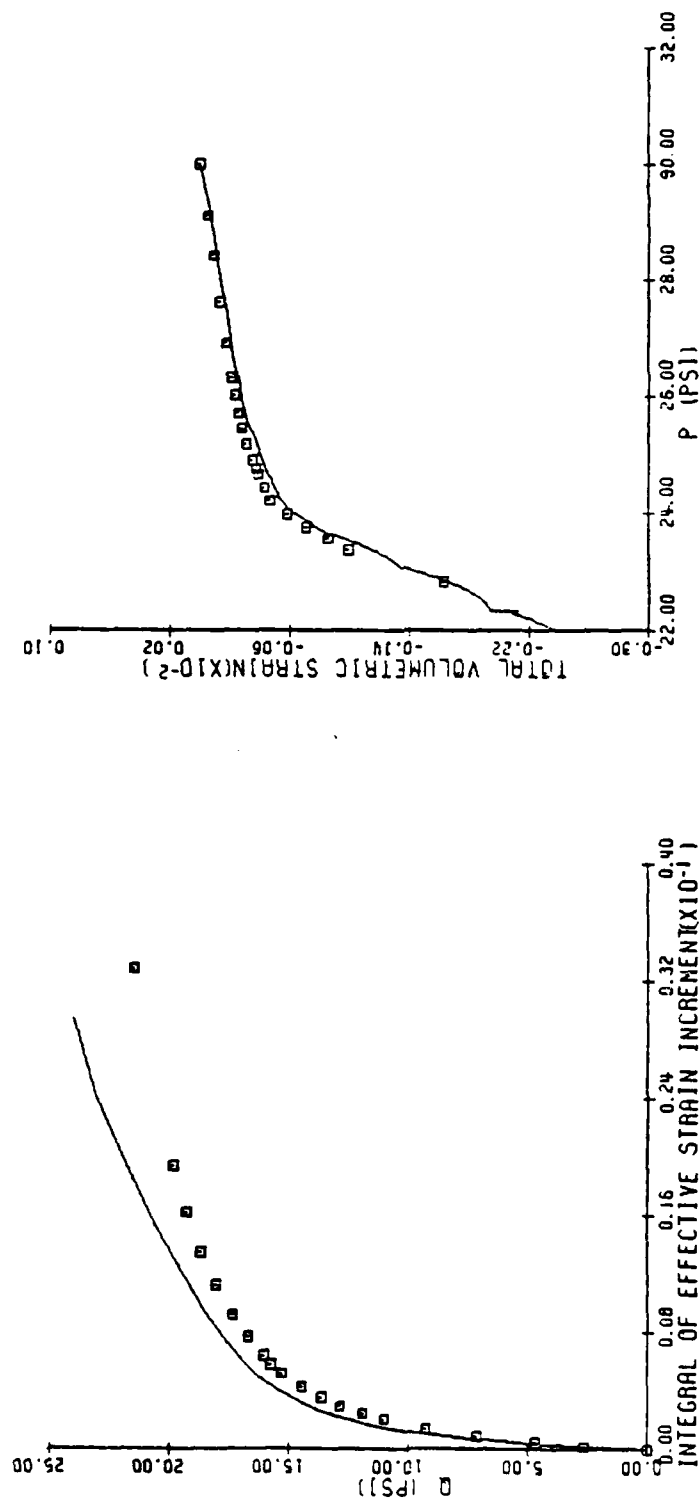


Figure 34. Postdiction of RTE test using Prevost's Model.

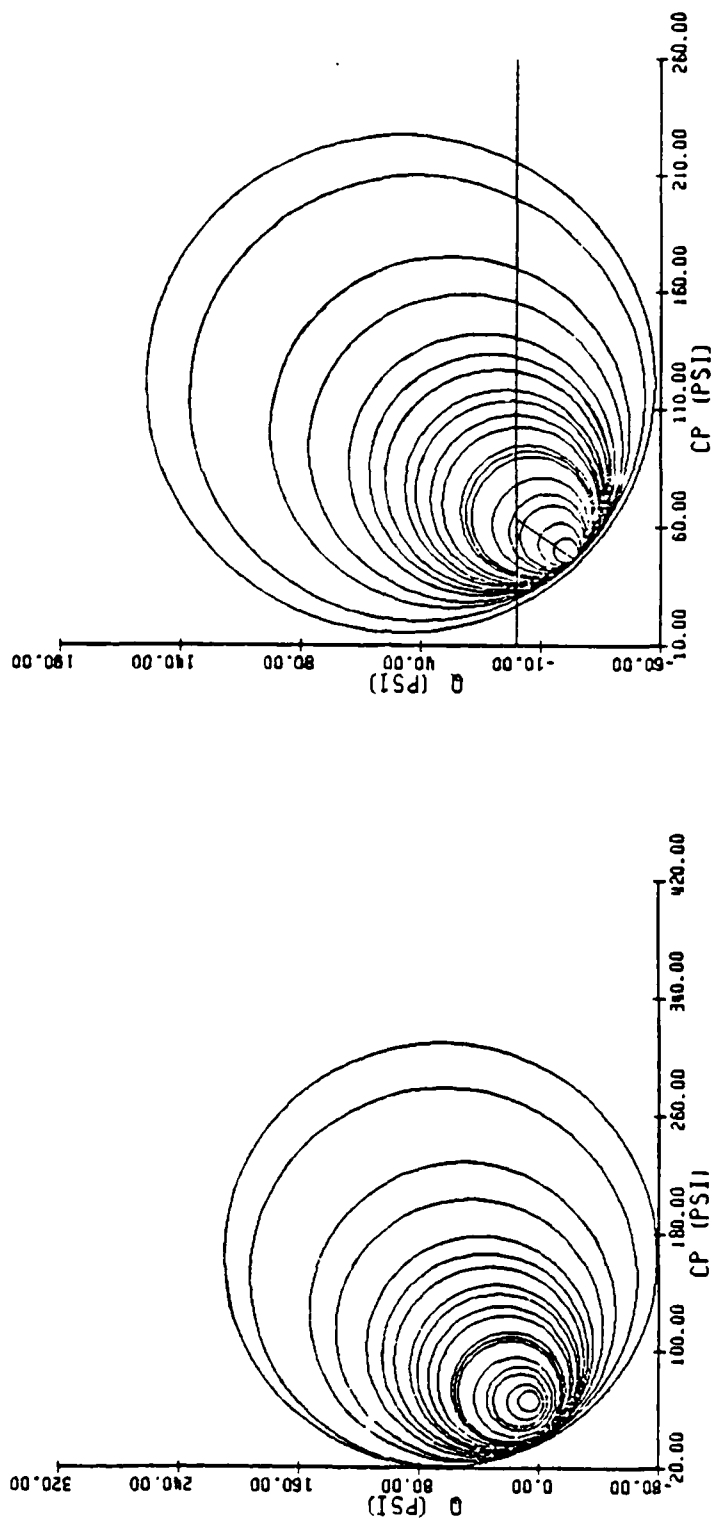


Figure 35. Initial and Final Configuration of Yield Surfaces for RTE simulation.

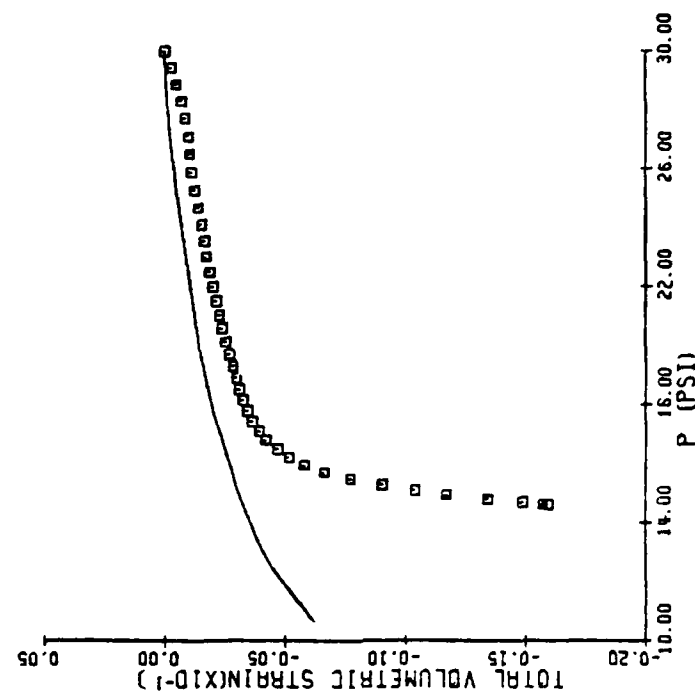
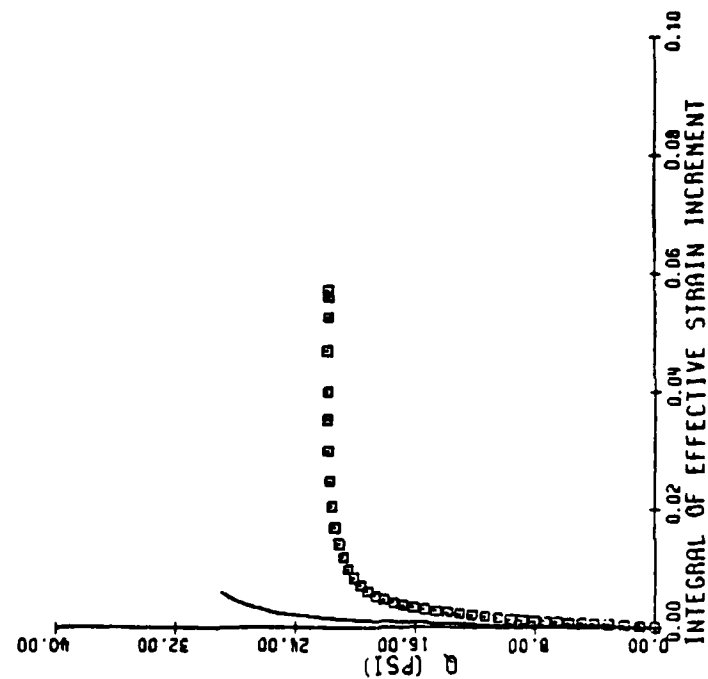


Figure 36. Prediction of RTC test using Prevost's Model.

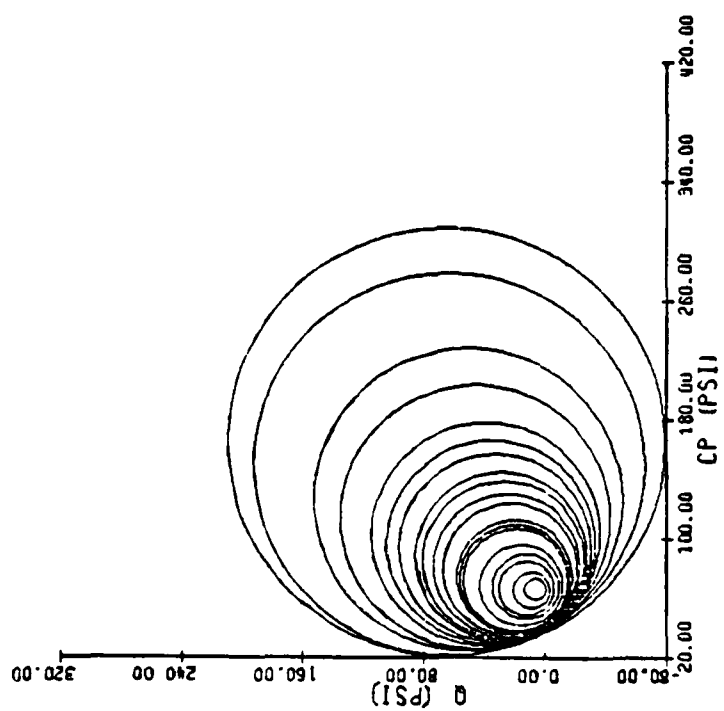
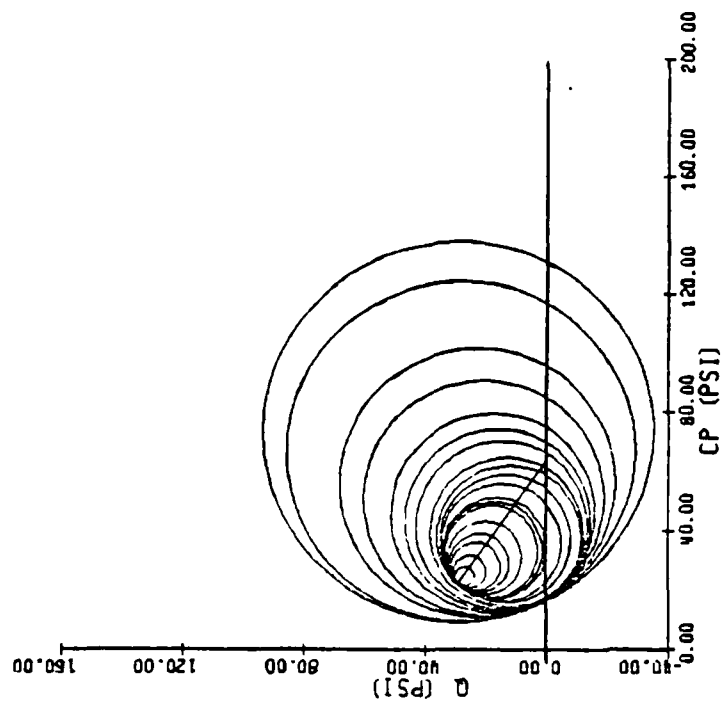


Figure 37. Initial and Final Configuration of Yield Surfaces for RTC simulation.

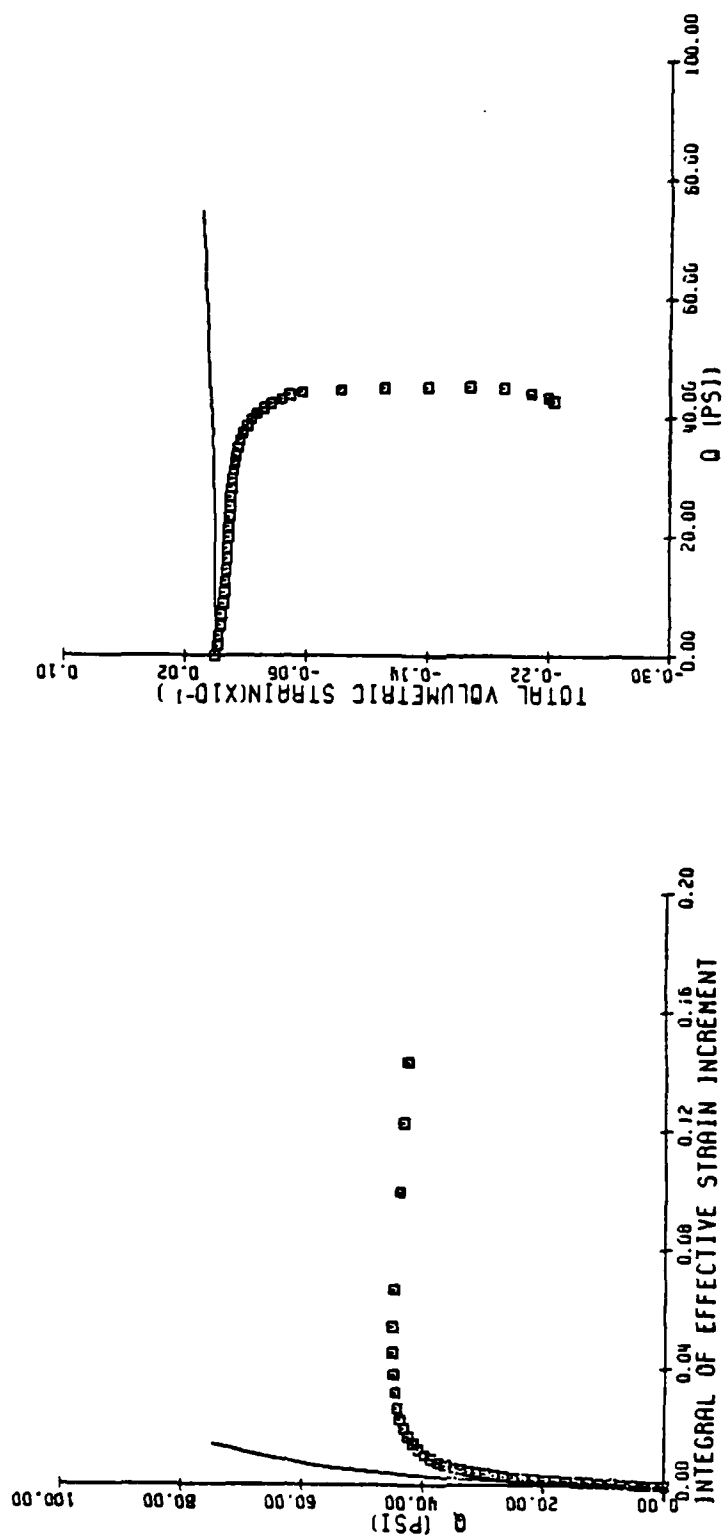


Figure 38. Prediction of GC 0 (or TC) test using Prevost's Model.

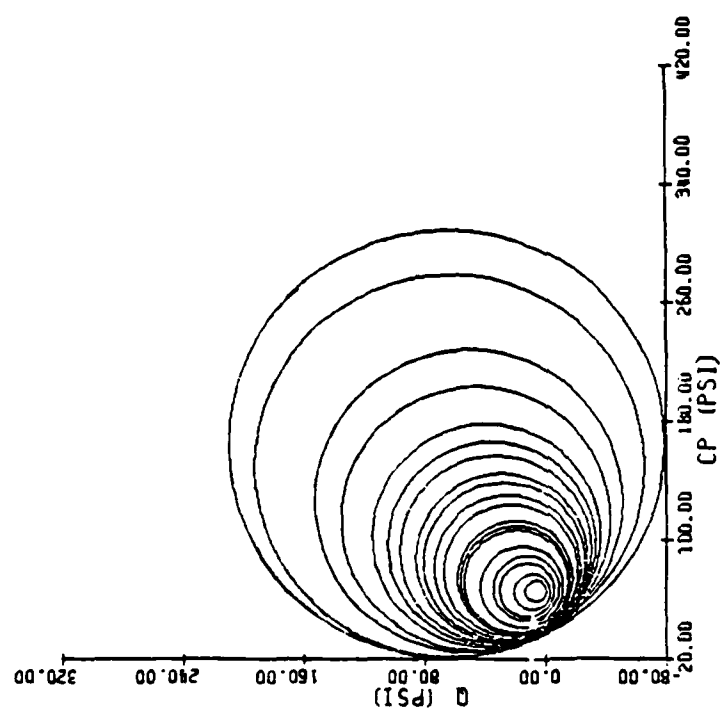
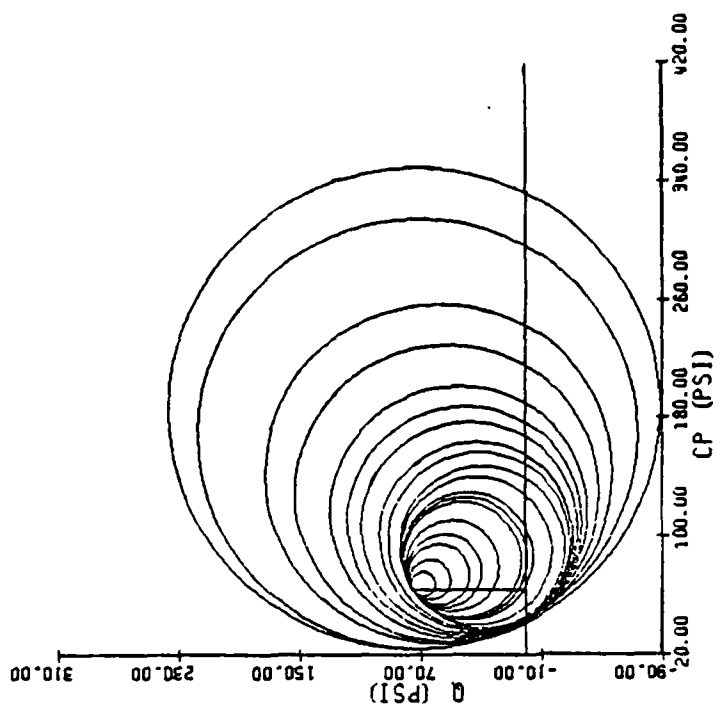


Figure 39. Initial and Final Configuration of Yield Surfaces for GC 0 (or TC) simulation.



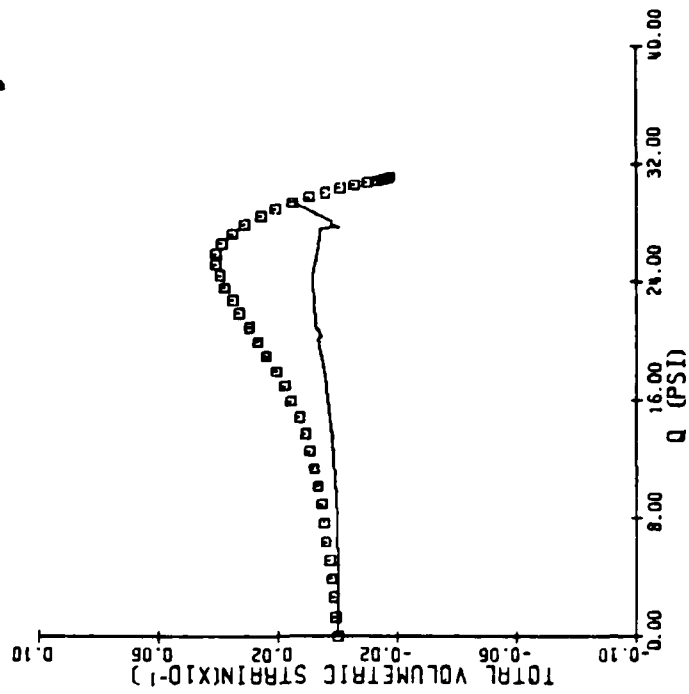
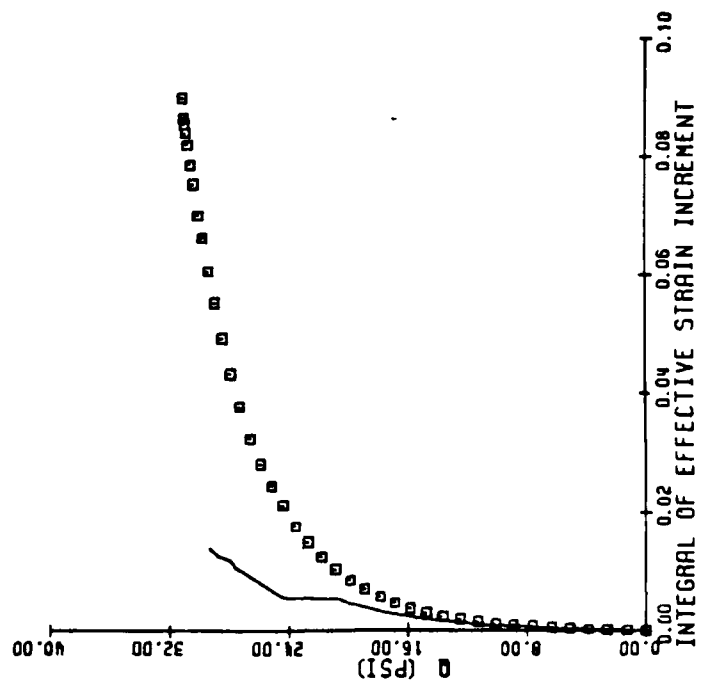


Figure 40. Prediction of GT 90 (or TE) test using Prevost's Model.

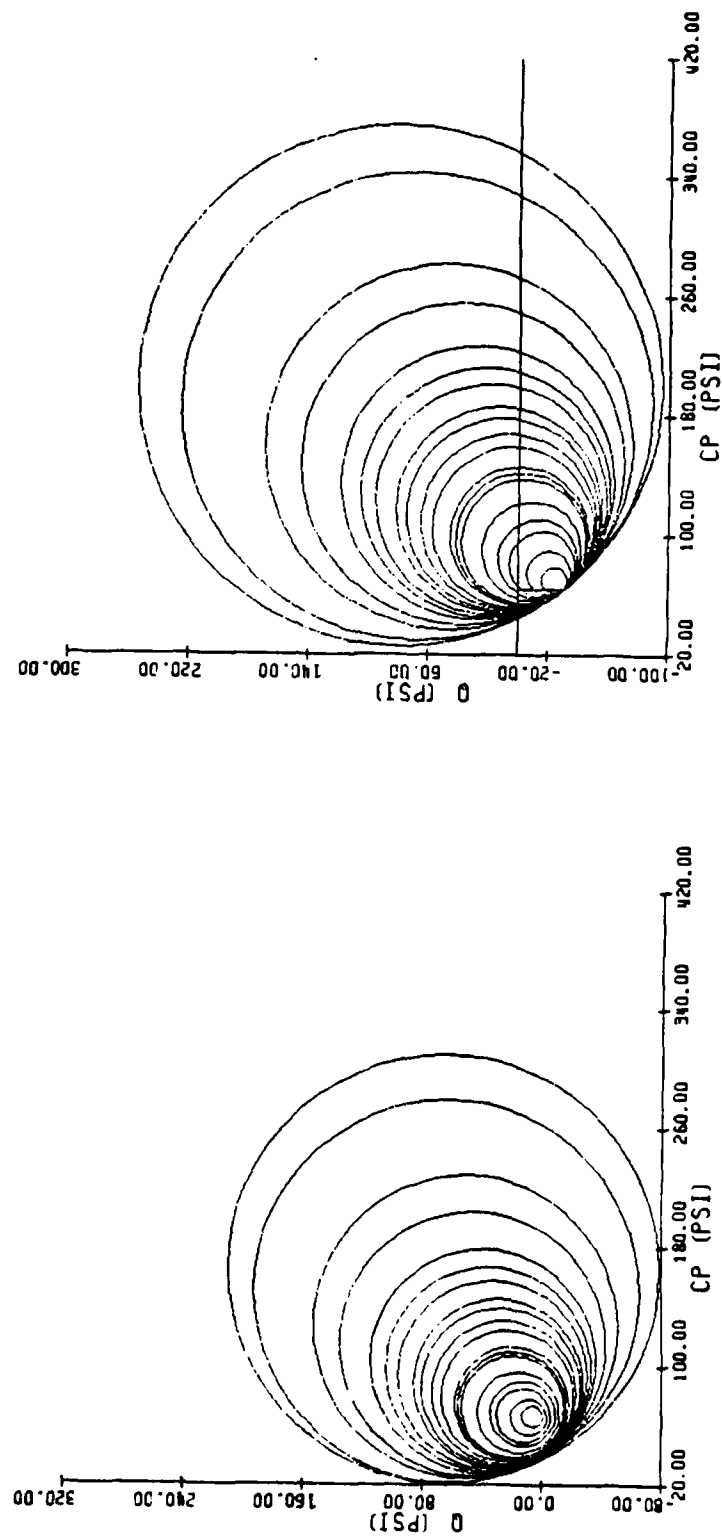


Figure 41. Initial and Final Configuration of Yield Surfaces for GT 90 (or TE) simulation.

writers believe that the general trend of stiff predictions is due to the lack of an explicit incorporation of the failure locus in the formulation.

Further examination of all the plots show that as: a) the principal stress axes of the stress path rotate away from those of the calibration paths, or b) when the stress path itself deviates significantly from either of the calibration paths, the predictions worsen. This statement is best illustrated by inspecting the DCR 15 prediction which is remarkably good because, perhaps, the stress path is, of all tests, the least different from the calibration DC 0 path; the discouraging predictions of the DCR 32 and GCR 15 tests, however, reflect the previous assertion.

#### E. PREDICTIONS OF SOME TESTS USING THE BOUNDING SURFACE MODEL

The bounding surface model used for the predictions herein is still in the embryonic stage of its development. At present, the McVay-Taesiri hardening rule (Reference 6) has been implemented in the model to generate prediction along the conventional triaxial compression and hydrostatic compression stress paths (i.e., the CTC and HC of figure 3). This rule, however, only guarantees that the "universal" plastic shear stress-shear strain curve and the traditional density hardening relation are satisfied for the CTC and HC paths respectively. A modification has been derived, but not yet implemented, which will permit greater flexibility in simulating arbitrary paths. Nonetheless, with a minimum of effort, we show that this adaptable model provides a simple framework for generating rational predictions.

The model parameters were estimated using procedures set forth in section IV, and these parameters are summarized in table 5. All parameters - except the "locking" hardening parameter  $\lambda$  and the unload modulus  $H_u$  which were reckoned from the load-unload HC test - were calculated from a single test: the CTC starting at an effective confining stress of 35 psi. Postdictions of both the load-unload HC test and the calibration CTC are plotted in figures 42 and 43 respectively; the curve-fitted experimental data had high correlation coefficients which is apparent from these graphs.

Predictions of the other three CTC stress paths, starting at 25, 30, and 45 psi respectively, are displayed in figures 44-46. The agreement between the experimental and calculated stress-strain points is remarkable, except for two slight deviations: a) the peak of the simulated CTC test starting at 25 psi falls slightly below the experimental data, and b) the observed volumetric strains for the CTC test @30 psi were somewhat larger than the predicted magnitudes. The apparent discrepancy in the predicted asymptote of the CTC test at @25 psi should, however, be no surprise because, as one may observe from table 2, the measured strength of this test is conspicuously higher than the other CTC tests. On the other hand, the disparity in the volumetric strain prediction of the CTC test @30 psi can be attributed to the device-dependency of the volume change characteristics; recall that the results of a solid cylinder test was used in model initialization while this CTC test @30 psi was carried out in the hollow cylinder apparatus.

TABLE 5. BOUNDING SURFACE MODEL PARAMETERS FOR REID-BEDFORD SAND

PARAMETER DESCRIPTION	MAGNITUDE at e = .67
Elastic Shear Modulus, G	13500 psi
Elastic Bulk Modulus, K	17680 psi
Isotropic "Locking" Hardening Parameter, $\lambda$	325.73
Slope Of Critical State Line, $N^*$	.1900
Isotropic "Shear" Hardening Parameter $S^*$	.6369
Isotropic "Shear" Hardening Parameter A	$3.2178 \times 10^{-3}$
Parameter used to control the Unload Modulus, $H_u$	$1.4000 \times 10^7$
Shape controlling parameter of ellipse, Q	5.00
Shape controlling parameter of dilation surface, b	-10.00

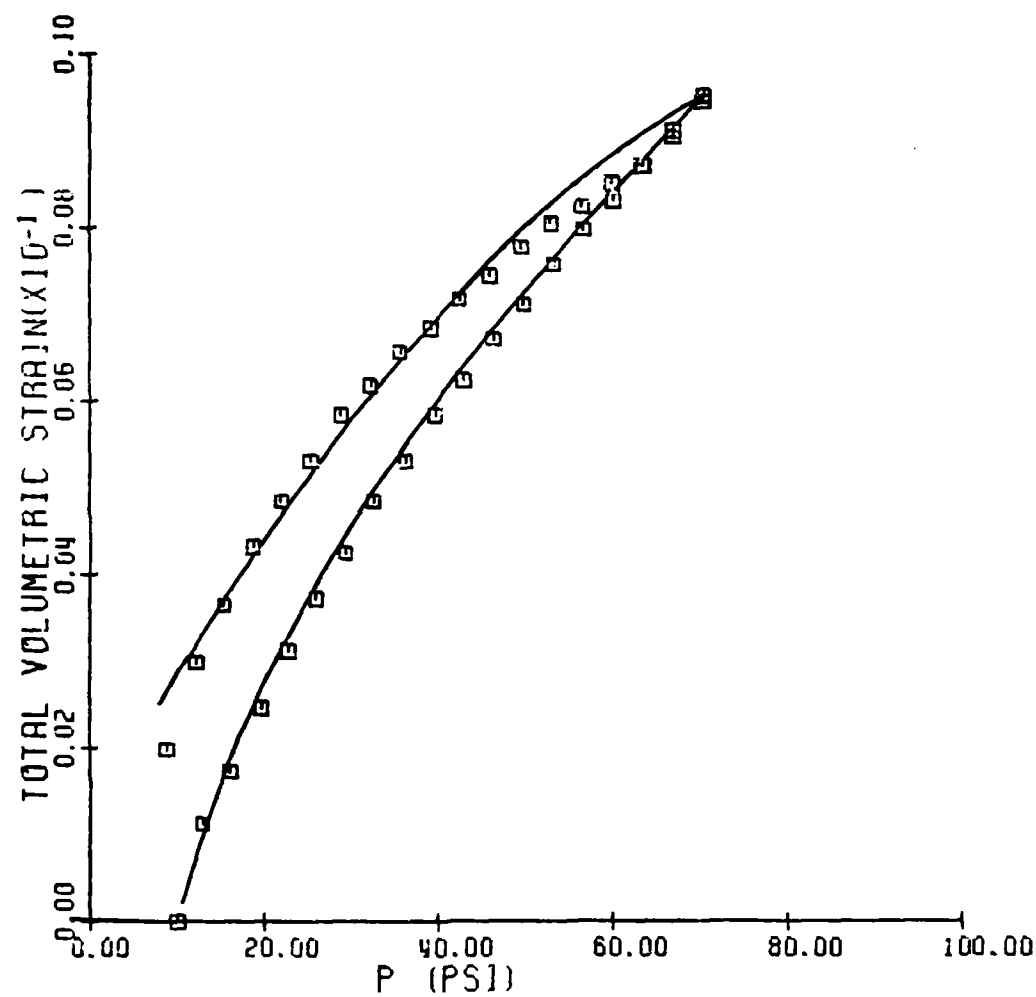


Figure 42. Postdiction of the Load-Unload HC test using the Bounding Surface Model.

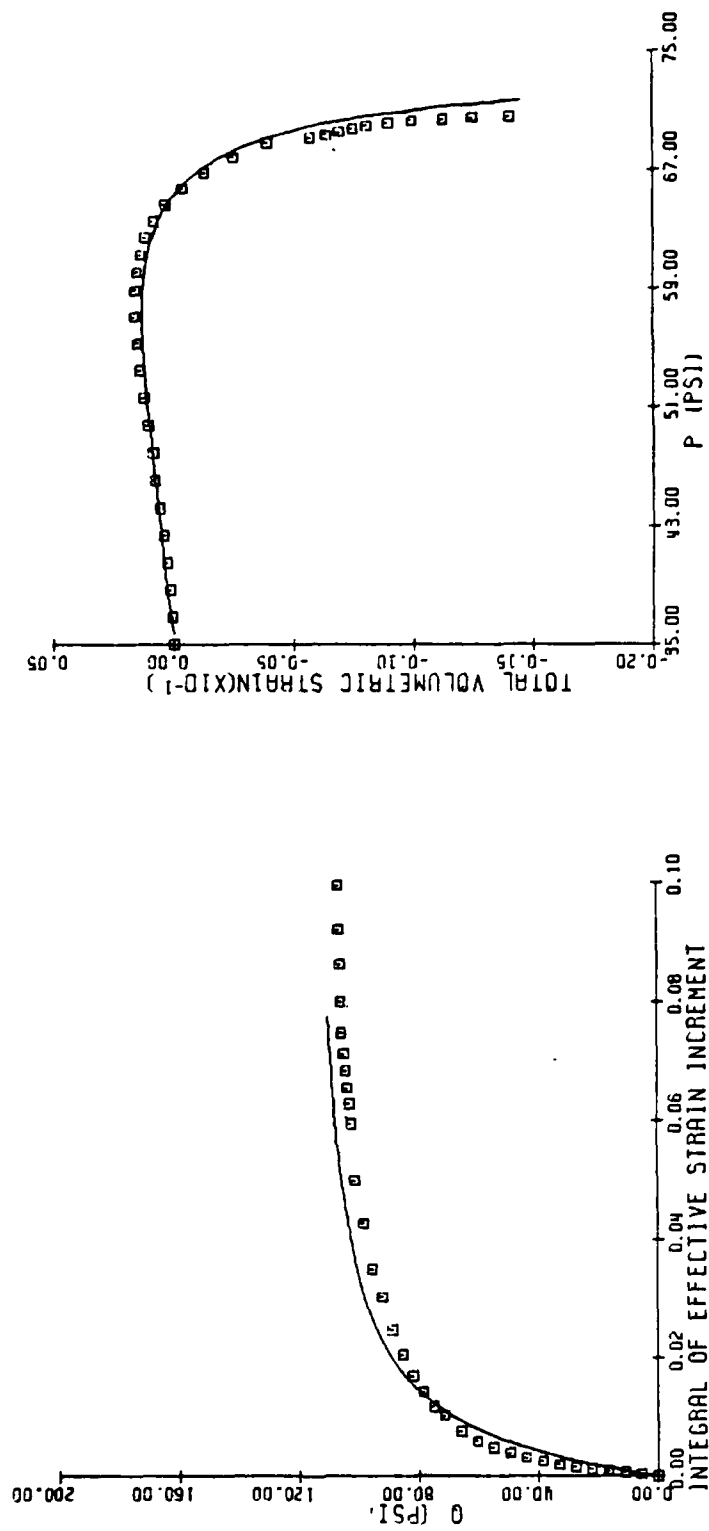


Figure 43. Postdiction of the CIC test @35 psi using the Bounding Surface Model.

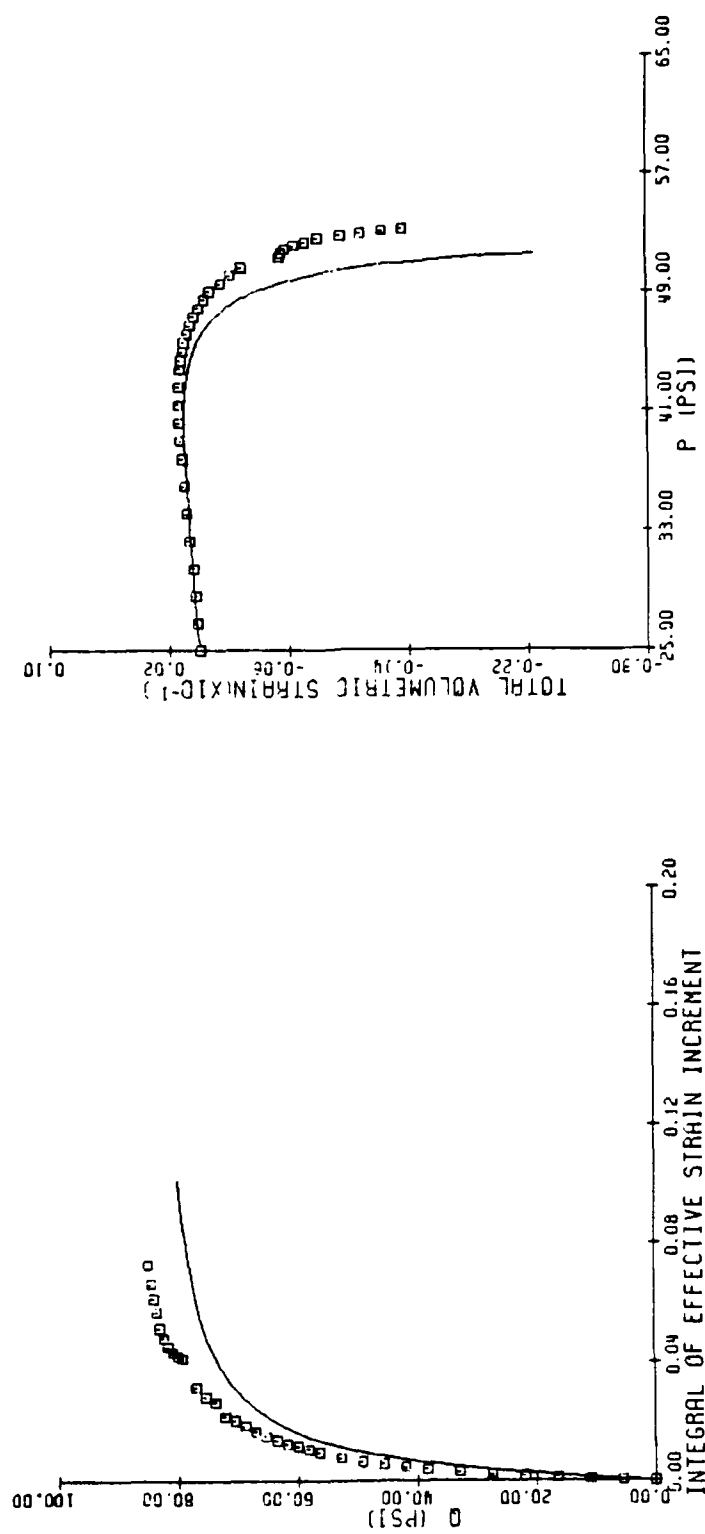


Figure 44. Prediction of the CTC test @25 psi using the Bounding Surface Model.



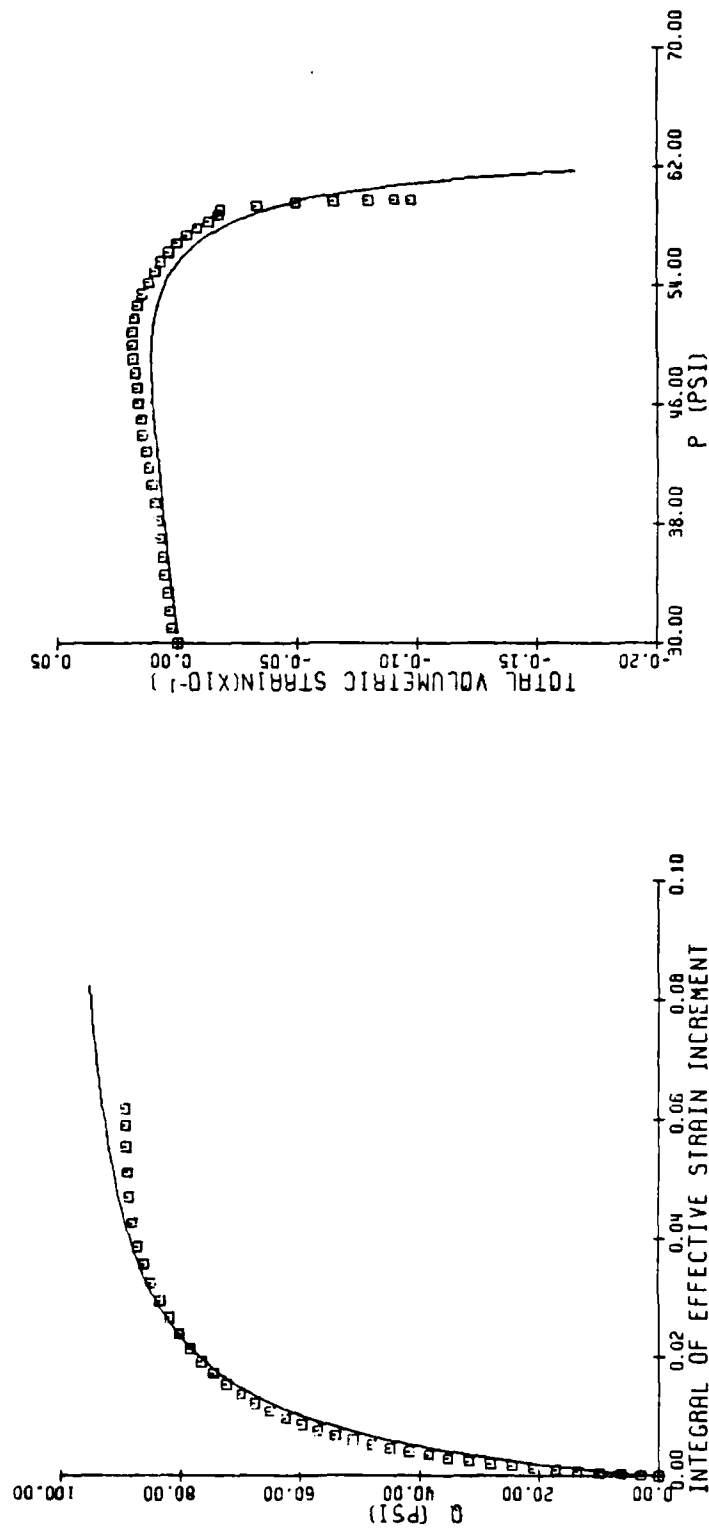


Figure 45. Prediction of the CTC test @30 psi using the Bounding Surface Model.

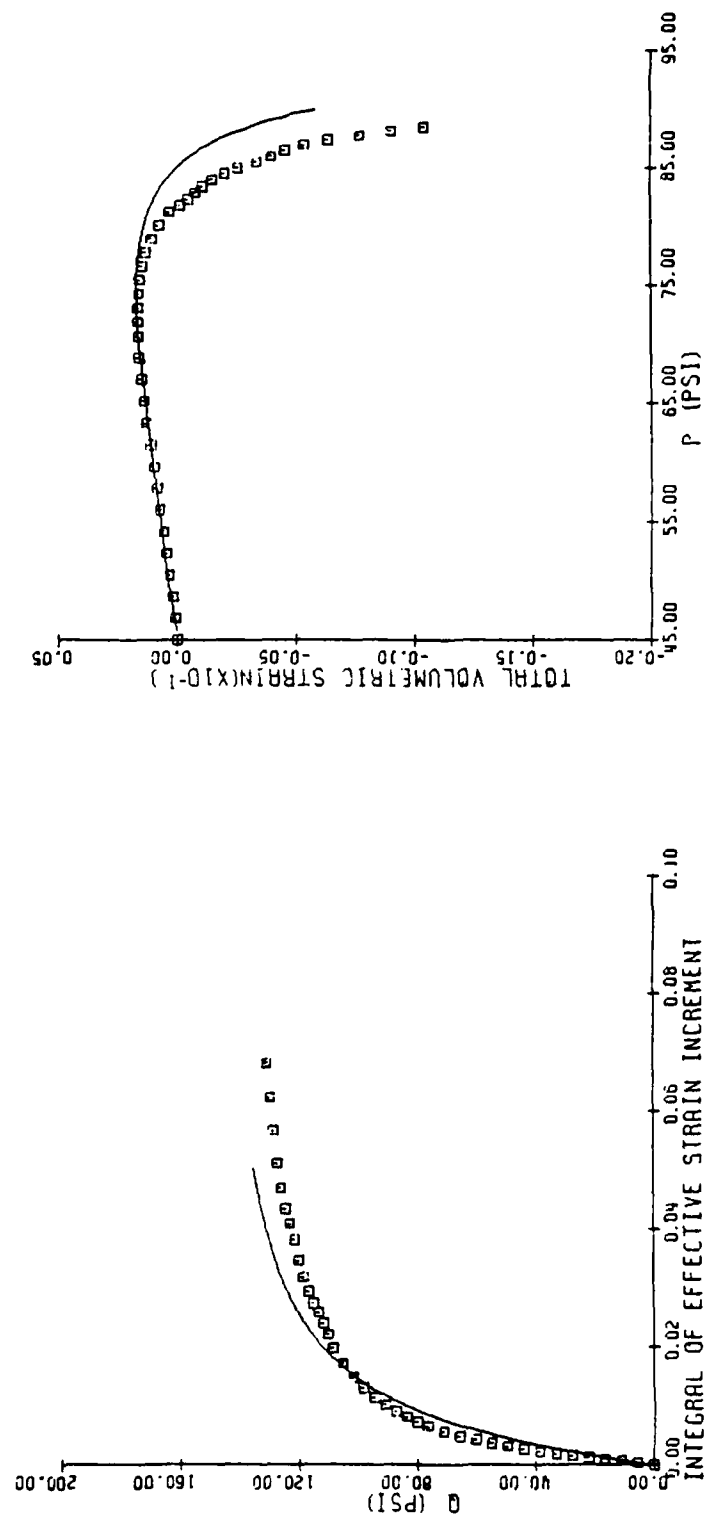


Figure 46. Prediction of the CTC test @45 psi using the Bounding Surface Model.

In closing, it can be said that this series of Bounding Surface postdictions and predictions is good evidence that the characteristic state (or zero dilatancy) line is well defined in stress space, and its inclusion adds considerably to the predictive capability of the model along the CTC.

#### F. ANALYTICAL STUDY OF THE MOVING WHEEL STRESS PATH

An analysis of the stresses in a sandy subgrade was undertaken in order to approximate the stress history of an element of soil as a wheel approaches a point directly above the element and then rolls away from it. This is in the spirit of the stress path method commonly used in estimating settlements of sand (Reference 27).

Initial study of this boundary value problem revolved around the use of a finite element discrete analysis technique which has the flexibility of employing either a linear elastic or the Prevost model as its constitutive assumptions (Reference 95). The results of this preliminary investigation showed only a slight variation in the stresses predicted by both the linear elastic and Prevost models, and it was thus decided that the added complexity and computer cost involved in using Prevost's model over the elastic model was not justified. Consequently, we relied exclusively upon the results of linear elastic analyses; this allowed us to use a simpler and much more economical computational solution technique: the BISAR (Bitumen Structures Analysis In Roads) computer program written specifically for the analysis of layered systems under normal and tangential surface tractions (Reference 96). The theory used in this computer code is

based on the selection of an appropriate stress function involving Bessel functions (Reference 97); the following simplifying assumptions apply: 1) the pavement is a multilayered structure and each layer is linear elastic, homogenous, and isotropic; 2) the interface between layers is continuous (i.e., the frictional resistance between layers is greater than the developed shear force); 3) the bottom layer is of infinite thickness; and 4) all loads are circular and uniform over the contact area.

Figure 47 shows the elastic constants assumed for each layer in the pavement section (Reference 2) as well as the stresses induced by the wheel load at various locations in the sand (subbase) stratum. One may also use the sequence of pictures in this figure to visualize the successive stress states in a soil element as the wheel approaches a point on the surface directly above it. Although not unexpected, the most striking feature of this study was the prediction of a continuous rotation of the principal stress axes during the loading and unloading sequences. Figure 48 depicts this moving wheel stress path in  $p$ - $q$  stress invariant space with the angle between the vertical direction and the major principal stress axis being used to keep track of the material directions. For comparison, plots of the slope of a CTC test path and that of a typical failure curve are also sketched on this figure.

It is conclusive from this theoretical study of the rolling wheel that rotation of the principal stress axes is of primary importance in modelling its effect on pavement rutting. From the writers' point of view, this problem becomes even more provocatively interesting when one

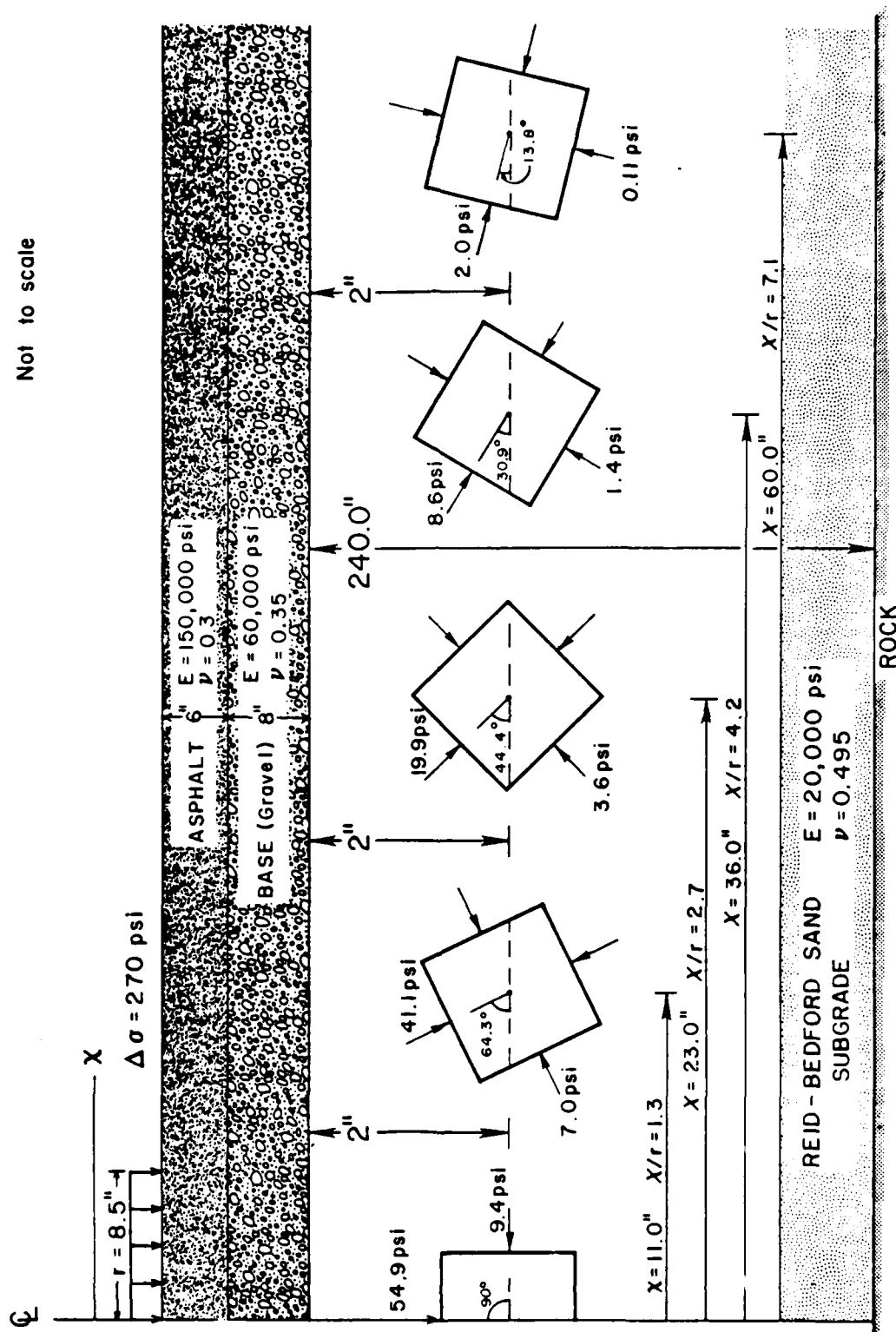
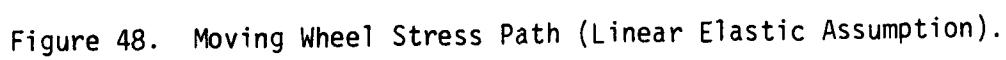


Figure 47. Stresses in a Layered Linear Elastic Medium with a Simulated Wheel Load.



takes note of the fact that, at a recent workshop, none of the "state-of-the-art" soil constitutive models performed well in predicting a test in which the principal stress axes underwent continuous rotation (Reference 98). Arthur et al. (Reference 99) and Ishihara (Reference 100) have emphasized that the rotation of stresses presents experimental and theoretical problems that remain to be solved.

## SECTION VII

### CONCLUSIONS

The conclusions are summarized in the following list:

1. Specimens with line failures yield experimental stress-strain curves which are both unreliable and show considerable scatter; this undesirable failure mode occurs in axial extension tests using solid cylindrical specimens with the typical aspect (height/diameter) ratio of 2.1. Material response during compression loading tests in hollow cylindrical and solid cylindrical specimens are, in general, compatible.
2. Experimental evidence indicates that inherent as well as induced anisotropy has a significant influence on the stiffness, strength, and plastic flow rate direction of granular media. This implies that the isotropy assumption may be too strong for practical problems where it is known that the symmetry axes of the fabric and the stress tensor do not always coincide during loading.
3. An analytical study has shown that the major and minor principal stress axes undergo a continuous ninety degree rotation as a wheel approaches and then passes over an element of soil in the subbase of a pavement structure. In stress invariant space, the slope of this stress



path is not very different from that of the conventional triaxial compression stress path.

4. Although the pressure-sensitive Prevost isotropic/kinematic model reasonably reproduces the response along its calibration paths, the predictions generated by this model along linear non-calibration loading paths were disappointing. This result effectively rules out the use of the Prevost model in simulating the complicated moving wheel stress path.

5. The Bounding Surface model is much simpler to understand and to implement than the Prevost model. Preliminary results from this model are very encouraging, and some possibilities have been proposed as to how the influence of principal stress axes rotation on stress-strain and strength can be incorporated in a future version of this formulation.

## REFERENCES

1. Drucker, D.C. "Stress-Strain Relations in the Plastic Range - a Survey of Theory and Experiment." Office of Naval Research (ONR) Technical Report, Contract N7-onr-358, Graduate Division of Applied Mathematics, Brown University, December, 1950.
2. Barker, W.R. and W.N. Brabston. Development of a Structural Design Procedure for Flexible Airport Pavements. Vicksburg, Mississippi: Soils and Pavements Laboratory, U.S. Army Engineers Waterways Experiment Station, September, 1975.
3. Salkind, M. October 12, 1984 (Comments from Air Force Office of Scientific Research). Personal Communication.
4. Dafalias, Y.F. and E.P. Popov. "Plastic Internal Variables Formalism of Cyclic Plasticity." Journal of Applied Mechanics. Vol. 98, No. 4 (December, 1976): 645-651 .
5. Saada, A.S. and F.C. Townsend. "State of the Art: Laboratory Strength Testing of Soils." in Laboratory Shear Strength of Soil, ed. Raymond K. Yong and Frank C. Townsend. 1916 Race Street, Philadelphia, Pa.: ASTM STP 740, 1980.
6. McVay, M.C. and Y. Taesiri. "Cyclic Behavior of Pavement Base Materials." Journal of the Geotechnical Engineering Division, ASCE, Vol. 111, No.1 (1985): 1-17.
7. Prevost, J.H. "Nonlinear Anisotropic Stress-Strain-Strength Behaviour of Soils." in Laboratory Shear Strength of Soil, ed. Raymond K. Yong and Frank C. Townsend. 1916 Race Street, Philadelphia, Pa.: ASTM STP 740, 1980.
8. Mould, J.C., S.Sture and H.Y. Ko. "Modeling of Elastic-Plastic Anisotropic Hardening and Rotating Principal Stress Directions in Sand." in IUTAM Conference on Deformation and Failure of Granular Materials, edited by P.A. Vermeer and H.J. Luger. P.O. Box 1675, 3000 BR Rotterdam, Netherlands. : A.A. Balkema, 1982.
9. Saada, A.S., Gary Bianchi and Piero Puccini. "The Mechanical Properties of Anisotropic Granular Soils." Colloque International du C.N.R.S. No. 351, Grenoble, France, 1983 .
10. Bekenstein, S. "Directional Shear Tests on Leighton Buzzard Sand," Master's Thesis, Massachusetts Institute of Technology, June, 1980.
11. Yong, R.N. and E.A. Fattah. "Stress-Strain Influence on Soil Compactibility by Rollers." in Proceedings of the Symposium on Limit Equilibrium, Plasticity and Generalized Stress-Strain Applications in Geotechnical Engineering, ed. Raymond Yong and E.T. Selig. New York, N.Y.: ASCE, 1980 .

12. Prager, W. "The Theory of Plasticity: A Survey of Recent Achievements." in Proceedings of the Institution of Mechanical Engineers, (James Clayton Lecture), Vol. 169, No.21 (1955): 41-57.
13. Drucker, D.C. "Stress-Strain Relations in the Plastic Range of Metals - Experiments and Basic Concepts." Rheology. Vol.1 (1956): 97-119.
14. Hodge, P.G., Jr. "The Mathematical Theory of Plasticity." in Elasticity and Plasticity (ed. by J.N. Goodier and P.G. Hodge, Jr.) New York, 1958
15. Naghdi, P.M. "Stress-Strain Relations in Plasticity and Thermoplasticity." in Plasticity, Proceedings of the 2nd Symposium on Naval Structural Mechanics, edited by E.H. Lee and P.S. Symonds, Oxford, England : Pergamon Press, 1960.
16. Eisenberg, M.A. "Studies in the Theory of Plasticity." Doctoral Dissertation, Yale School of Engineering, Yale University, January, 1967.
17. Malvern, L.E. Introduction to the Mechanics of a Continuous Medium. Engelwood Cliffs, New Jersey: Prentice Hall Inc., 1969.
18. Wrede, R.C. Introduction to Vector and Tensor Analysis. 180 Varick Street, New York, N.Y.: Dover Publications, Inc., 1972.
19. Akivis, M.A. and V.V. Goldberg. An Introduction to Linear Algebra and Tensors. Translated and edited by R.A. Silverman, 180 Varick Street, New York, N.Y.: Dover Publications, Inc., 1972.
20. Hay, G.E. Vector and Tensor Analysis. 180 Varick Street, New York, N.Y.: Dover Publications, Inc., 1953.
21. Jaunzemis, W. Continuum Mechanics. New York, N.Y.: The Macmilan Company, 1967.
22. Synge, J.L. and A. Schild. Tensor Calculus. Toronto: University of Toronto Press, 1949.
23. Wylie, C.R. and L.C. Barrett. Advanced Engineering Mathematics. New York, N.Y.: McGraw-Hill Book Co., 1982.
24. Lode, W. "Versuche ueber den Einfluss der mittleren Hauptspannung auf das Fliessen der Metalle Eisen, Kupfer, und Nickel." Zeitschrift fur Physik, Vol.36 (1926): 913-939.
25. Nayak, G.C. and O.C. Zienkiewicz. "Convenient Form of Stress Invariants for Plasticity." Journal of the Structural Division. ASCE, Vol.98, NO. ST4 (April, 1972): 949-954.
26. Jain, S.K. Fundamental Aspects of the Normality Rule. P.O. Box 302, Blacksburg, Virginia, 24060: Engineering Publications, 1980.

27. Lambe, T.W. and R.V. Whitman. Soil Mechanics. New York, N.Y.: John Wiley & Sons, 1969.
28. Cowin, S.C. "Microstructural Continuum Models for Granular Materials." in Proceedings of the U.S.-Japan Seminar on Continuum Mechanical and Statistical Approaches in the Mechanics of Granular Materials, edited by S.C. Cowin and M. Satake, Sendai, Japan: Gakujutsu Bunken Fukyukai, Tokyo, Japan, 1978.
29. Cambou, B. "Orientational Distributions of Contact Forces as Memory Parameters in a Granular Material." in IUTAM Conference on Deformation and Failure of Granular Materials, edited by P.A. Vermeer and H.J. Luger. P.O. Box 1675, 3000 BR Rotterdam, Netherlands. : A.A. Balkema, 1982.
30. Nemat-Nasser, S. and M.M. Mehrabadi. "Micromechanically Based Rate Constitutive Descriptions for Granular Materials." Mechanics of Engineering Materials, edited by C.S. Desai and R.H. Gallagher, New York, N.Y.: John Wiley & Sons, 1984.
31. Gerrard, G.M. "Background to Mathematical Modelling in Geomechanics : The Role of Fabric and Stress History." in Proceedings of the conference on Finite Elements in Geomechanics, edited by G. Gudehus, New York: John Wiley & Sons, 1975.
32. Vermeer, P.A. and H.J. Luger, Editors, IUTAM Conference on Deformation and Failure of Granular Materials (Delft, 31 Aug. - 3 Sept. 1982), P.O. Box 1675, 3000 BR Rotterdam, Netherlands.: A.A. Balkema, 1982.
33. Cowin, S.C. and M. Satake, Editors, Proceedings of the U.S.-Japan Seminar on Continuum Mechanical and Statistical Approaches in the Mechanics of Granular Materials (Sendai, Japan, June 5-9, 1978), Gakujutsu Bunken Fukyukai, Tokyo, Japan, June, 1978.
34. Goodman, M.A. and S.C. Cowin. "A Continuum Theory for Granular Materials." Archive for Rational Mechanics and Analysis, Vol.44 (1972): 321-339.
35. Parkin, A.K., C.M. Gerrard, and D.R. Willoughby. "Discussion on Deformation of Sand in Hydrostatic Compression." Journal of Soil Mechanics and Foundation Engineering, ASCE, Vol.94, No. SM1 (1968): 336-340.
36. Oda, M. "Fabric Tensor for Discontinuous Geological Materials." Soils and Foundations, Vol.22, No. 4 (December, 1982): 96-108.
37. Satake, M. "Constitution of Mechanics of Granular Materials through the Graph Theory." in Proceedings of the U.S.-Japan Seminar on Continuum Mechanical and Statistical Approaches in the Mechanics of Granular Materials, edited by S.C. Cowin and M. Satake, Sendai, Japan: Gakujutsu Bunken Fukyukai, Tokyo, Japan, 1978.

38. Horne, M.R. "The Behavior of an Assembly of Rotund, Rigid, Cohesionless Particles (I & II)." Proceedings of the Royal Society of London, Vol. 286 (1964) : 62-97
39. Gudehus, G. "Gedanken zur Statistischen Boden Mechanik." Baningenieur, Vol.43 (1968): 320-326.
40. Nemat Nasser, S. "On Dynamic and Static Behaviour of Granular Materials." Soil Mechanics - Transient and Cyclic Loads, edited by G.N. Pande and O.C. Zienkiewicz, New York: John Wiley & Sons, 1982.
41. Casagrande, A. and N. Carillo. "Shear Failure of Anisotropic Materials." Boston Society of Civil Engineers. Vol.31, 1944: 74-87.
42. Oda, M., J. Konishi and S. Nemat-Nasser. "Some Experimentally Based Fundamental Results on the Mechanical Behaviour of Granular Materials." Geotechnique, Vol.30, No.4 (1980): 479-495.
43. Oda, M. "The Mechanism of Fabric Change During Compressional Deformation of Sand." Soils and Foundations, Vol.12, No.2 (June, 1972): 1-18.
44. Saleeb, A.F. and W.F. Chen. "Nonlinear Hyperelastic (Green) Constitutive Models for Soils: Theory and Calibration." in Limit Equilibrium, Plasticity and Generalized Stress-Strain in Geotechnical Engineering, ed. Raymond K. Yong and Hon-Yim Ko. New York, N.Y.: ASCE, 1980.
45. Eringen, A.C. Nonlinear Theory of Continuous Media. New York, N.Y.: McGraw-Hill, Inc., 1962.
46. Clough, R.W. and R.J. Woodward. "Analysis of Embankment Stresses and Deformations." Journal of Soil Mechanics and Foundation Engineering, ASCE, Vol.93, No. SM4 (July, 1967): 529-549.
47. Duncan, J.M. and C.Y. Chang. "Non-Linear Analysis of Stress and Strain in Soils." Journal of Soil Mechanics and Foundation Engineering, ASCE, Vol.96, No. SM5 (September, 1970): 1629-1653.
48. Drucker, D.C. and W. Prager. "Soil Mechanics and Plastic Analysis or Limit Design." Quarterly of Applied Mathematics. Vol.10, No.157 (1952): 338-346.
49. Coulomb, C.A. "Essai sur une application des regles de maximis et minimis a quelques problemes de statique, relatifs a l'architecture." Memoires de Mathematique et de Physique, presentes a l'Academie Royale des Sciences, par divers savans, & lus dan ses assemblees, Vol.7 (1773): 343-382.
50. von Mises, R. "Mechanik der plastischen Formaenderung von Kristallen." Zeitschrift fur Angewandte Mathematik und Mechanik, Vol. 8 (1928): 161-185.

51. Tresca, H. "Memoire sur l'ecoulment des corps solides." Memoires presentes par divers savants a l'Academie des Sciences de l'Institut Imperial de France, Paris, Vol.18 (1868): 733-799.
52. Bishop, A.W. "The Strength of Soils as Engineering Materials." Geotechnique. Vol.16 No.2: 91-128.
53. Drucker, D.C., R.E. Gibson and D.J. Henkel . "Soil Mechanics and Work-Hardening Theories of Plasticity." ASCE Transactions, Vol.22, 1957.
54. DiMaggio, F.L. and I.S. Sandler. "Material Models for Granular Soils." Journal of the Engineering Mechanics Division. ASCE, Vol.97, No.EM3 (1971): 936-950 .
55. Lade, P.V. and J.M. Duncan. "Elasto-plastic Stress-Strain Theory for Cohesionless Soil." Journal of the Geotechnical Engineering Division, ASCE, Vol.101, No.GT10 (1975): 1037-1053.
56. Matsuoka, H. and T. Nakai. "Stress-Deformation and Stength Characteristics of Soil Under Three Different Principal Stresses." Proceedings of the Japanese Society of Civil Engineers, Vol. 232 (1974): 59-70.
57. Desai, C.S. "A General Basis for Yield, Failure and Potential Functions in Plasticity." International Journal of Numerical and Analytical Methods In Geomechanics, Vol.4 (1980): 361-375
58. Drescher, A. "An Experimental Investigation of Flow Rules for Granular Materials Using Optically Sensitive Glass Particles." Geotechnique. Vol.26, No.4 (1976) : 591-601.
59. Melan, E. "Zur Plastizitaet des raeumlichen Kontinuums." Ingenieur-Archiv, Vol.9 (1938): 116-126.
60. Prager, W. "Recent Developments in the Mathematical Theory of Plasticity." Journal of Applied Physics, Vol.20, No.3 (March, 1949): 235-241.
61. Mroz, Z. "On The Description of Anisotropic Work Hardening." Journal of Mechanics and Physics of Solids. Vol.15 (1967): 163-175.
62. Iwan, W.D. "On a Class of Models for the Yielding Behavior of Continuous and Composite Systems." Journal of Applied Mechanics, Trans. ASME, Vol. 89, Series E (1967): 612-617.
63. Lubliner, J. "On the Thermodynamic Foundations of Non-Linear Solid Mechanics. " International Journal of Non-Linear Mechanics, Pergamon Press. Vol. 7 (1972) : 237-254 .
64. Drucker, D.C. "A More Fundamental Approach to Stress-Strain Relations." in Proceedings of the 1st U.S. National Congress for Applied Mechanics, ASME (1951): 487-491.

65. Sture, S., J.C. Mould and H.Y. Ko. "Elastic-Plastic Anisotropic Hardening Constitutive Model and Prediction of Behavior for Dry Quartz Sand." Department of Civil Engineering, University of Colorado: Boulder, Colorado, 1984.
66. Hill, R. The Mathematical Theory of Plasticity. Ely House, London: Oxford University Press, 1950.
67. Schofield, A. and C.P. Wroth. Critical State Soil Mechanics. London: McGraw-Hill, 1968.
68. Ziegler, H. "A Modification of Prager's Hardening Rule." Quarterly of Applied Mathematics, Vol.17, No.1 (1959): 55-65.
69. Phillips, A. and G.J. Weng. "An Analytical Study of an Experimentally Verified Hardening Law." Journal of Applied Mechanics, Transactions of the ASME, Vol. 42, No.2, Series E (1975): 375-378.
70. Krieg, R.D. "A Practical Two-Surface Plasticity Theory." Journal of Applied Mechanics, Transactions ASME, Vol.42, Series E (1975): 641-646.
71. Dafalias, Y.F. and E.P. Popov. "A Model of Nonlinearly Hardening Materials for Complex Loadings." Acta Mechanica, Vol.21 (1975): 173-192.
72. Pietrusczak, St. and Z. Mroz. "On Hardening Anisotropy of K. Consolidated Clays." International Journal for Numerical and Analytical Methods in Geomechanics, Vol.7 (1983): 19-38.
73. Roscoe, K.H. and J.B. Burland. "On the Generalized Stress-Strain Behaviour of 'Wet' Clay." in Engineering Plasticity, edited by J. Heyman and F.A. Leckie. Bentley House, P.O. Box 92, 200 Euston Road, London: Cambridge University Press, 1968.
74. Aboim, C.A. and W.H. Roth. "Bounding-Surface Plasticity Theory Applied to Cyclic Loading of Sand." in International Symposium on Numerical Methods in Geomechanics, (ed. R. Dungar, G.N. Pande, and J.A. Studer, Zurich, Switzerland, Sept.13-17, 1982.) P.O. Box 1675, 3000 BR Rotterdam, Netherlands: A.A. Balkema, 1982.
75. Gudehus, G. "Elastoplastische Stoffgleichungen fur trockener Sand." Ingenieur Archiv., Vol.42, 1973.
76. Dafalias, Y.F. "A Bounding Surface Plasticity Model", in Proceedings of the 7th Canadian Congress of Applied Mechanics, Sherbrooke, Canada (1979): 89-90.
77. Dafalias, Y.F. "Bounding Surface Elastoplasticity-Viscoplasticity for Particulate Cohesive Media." in IUTAM Conference on Deformation and Failure of Granular Materials, edited by P.A. Vermeer and H.J. Luger. P.O. Box 1675, 3000 BR Rotterdam, Netherlands.: A.A. Balkema, 1982.

78. Rowe, P.W. "The Stress-Dilatancy Relation for Static Equilibrium of an Assembly of Particles in Contact." Proceedings of the Royal Society of London, Vol. 269 (1962): 500-527.
79. Nova, R. and D.M. Wood. "A Constitutive Model for Sand in Triaxial Compression." International Journal for Numerical and Analytical Methods in Geomechanics, Vol.3 (1979): 255-278.
80. Lade, P.V. "Elasto-plastic Stress-Strain Theory for Cohesionless Soil with Curved Yield Surfaces." International Journal of Solids and Structures, Vol.13 (1975): 1019-1035
81. Prevost, J.H. and K. Hoeg. "Effective Stress-Strain-Strength Model for Soils." Journal of the Geotechnical Engineering Division, ASCE, Vol.101, No.GT3 (March, 1975): 259-278.
82. Kondner, R.L. "Hyperbolic Stress-Strain Response: Cohesive Soils." Journal of Soil Mechanics and Foundation Engineering, ASCE, Vol.89, No. SM1 (January, 1963): 115-143.
83. Mroz, Z. and V.A. Norris. "Elastoplastic and Viscoplastic Constitutive Models for Soils with Application to Cyclic Loading." Soil Mechanics - Transient and Cyclic Loads, edited by G.N. Pande and O.C. Zienkiewicz, New York : John Wiley & Sons, 1982.
84. Dafalias, Y.F. and L.R. Herrmann. "Bounding Surface Formulation of Soil Plasticity." Soil Mechanics - Transient and Cyclic Loads, edited by G.N. Pande and O.C. Zienkiewicz, New York: John Wiley & Sons, 1982.
85. Arthur, J.R.F. and Phillips, A.B. "Homogenous and Layered Sand in Triaxial Compression." Geotechnique, Vol.25, No.4 (1975): 799-815.
86. Symes, M.J., D.W. Hight and A. Gens. "Investigating Anisotropy and the Effects of Principal Stress Rotation and of the Intermediate Principal Stress Using a Hollow Cylinder Apparatus." in IUTAM Conference on Deformation and Failure of Granular Materials, edited by P.A. Vermeer and H.J. Luger. P.O. Box 1675, 3000 BR Rotterdam, Netherlands.: A.A. Balkema, 1982.
87. Arthur, J.R.F., S. Bekenstein, J.T. Germaine and C.C. Ladd. "Stress Path Tests with Controlled Rotation of Principal Stress Directions." in Laboratory Shear Strength of Soil, ed. Raymond K. Yong and Frank C. Townsend. 1916 Race Street, Philadelphia, Pa. : ASTM STP 740, 1980.
88. Lade, P.V. "Localization Effects in Triaxial Tests on Sand." in IUTAM Conference on Deformation and Failure of Granular Materials, edited by P.A. Vermeer and H.J. Luger. P.O. Box 1675, 3000 BR Rotterdam, Netherlands.: A.A. Balkema, 1982.



89. Lade, P.V. and M. Oner. "Elasto-Plastic Stress-Strain Model, Parameter Evaluation, and Predictions for Dense Sand." in Constitutive Relations for Soils (edited by G. Gudehus, F. Darve, and I. Vardoulakis), p. 159, A.A. Balkema, P.O. Box 1675, 3000 BR Rotterdam, Netherlands, 1984.
90. Chen, W.F. Limit Analysis and Soil Plasticity, Elsevier Scientific Publishing Company, New York, 1975.
91. Arthur, J.R.F. and B.K. Menzies. "Inherent Anisotropy in Sand." Geotechnique. Vol. 22, No.1 (1972): 115-128
92. Oda, M., I. Koishikawa, and T. Higuchi. "Experimental Study of Anisotropic Shear Strength of Sand by Plane Strain Tests." Soils and Foundations, Vol.18, No. 1 (1978): 25-38.
93. Konishi, J., M. Oda and S. Nemat-Nasser. "Inherent Anisotropy and Shear Strength of Assembly of Oval Cross-Sectional Rods." in IUTAM Conference on Deformation and Failure of Granular Materials, edited by P.A. Vermeer and H.J. Luger. P.O. Box 1675, 3000 BR Rotterdam, Netherlands.: A.A. Balkema, 1982.
94. Al-Hussaini, M.M. and F.C. Townsend. Investigation of  $K_0$  Testing in Cohesionless Soils. Vicksburg, Mississippi: Soils and Pavements Laboratory, U.S. Army Engineers Waterways Experiment Station, 1975.
95. Hughes, T.J.R. and J.H. Prevost. "DIRT II -- A Nonlinear Quasi-Static Finite Element Analysis Program". California Institute of Technology, Pasadena, CA., U.S.A., 1979
96. Izatt, J.O., J.A. Lettier and C.A. Taylor. "The Shell Group Methods for Thickness Design of Asphalt Pavements." Koninklijke/Shell-Laboratorium, Amsterdam, Holland, 1967.
97. Burmister, D.M. "The General Theory of Stresses and Displacements in Layered Systems." Journal of Applied Physics, Vol.16 (February, 1945): 89-94.
98. Christian, J.T. "State of the Art Report: Generalized Stress-Strain Applications in Geotechnical Engineering." in Proceedings of the Symposium on Limit Equilibrium, Plasticity and Generalized Stress-Strain Applications in Geotechnical Engineering, ed. Raymond Yong and E.T. Selig. New York, N.Y. : ASCE, 1980 .
99. Arthur, J.R.F., K.S. Chua, T. Dunstan and J. Rodriguez. "Principal Stress Rotation: A Missing Parameter." Journal of the Geotechnical Engineering Division. ASCE Vol. 106, No. GT4 (April, 1980): 419-433.
100. Ishihara, K. and I. Towhata. "Effects of Rotation of Principal Stress Directions on Cyclic Response of Sand." Mechanics of Engineering Materials, edited by C.S. Desai and R.H. Gallagher, New York, N.Y.: John Wiley & Sons, 1984.

APPENDIX A  
PLOTS OF HCA EXPERIMENTAL RESULTS

The following are computer plots of the experimental stress-strain data obtained from the Hollow Cylinder Apparatus tests of Saada (Reference 9). The notation applicable to the axes of these graphs has been previously presented in SECTION VI.

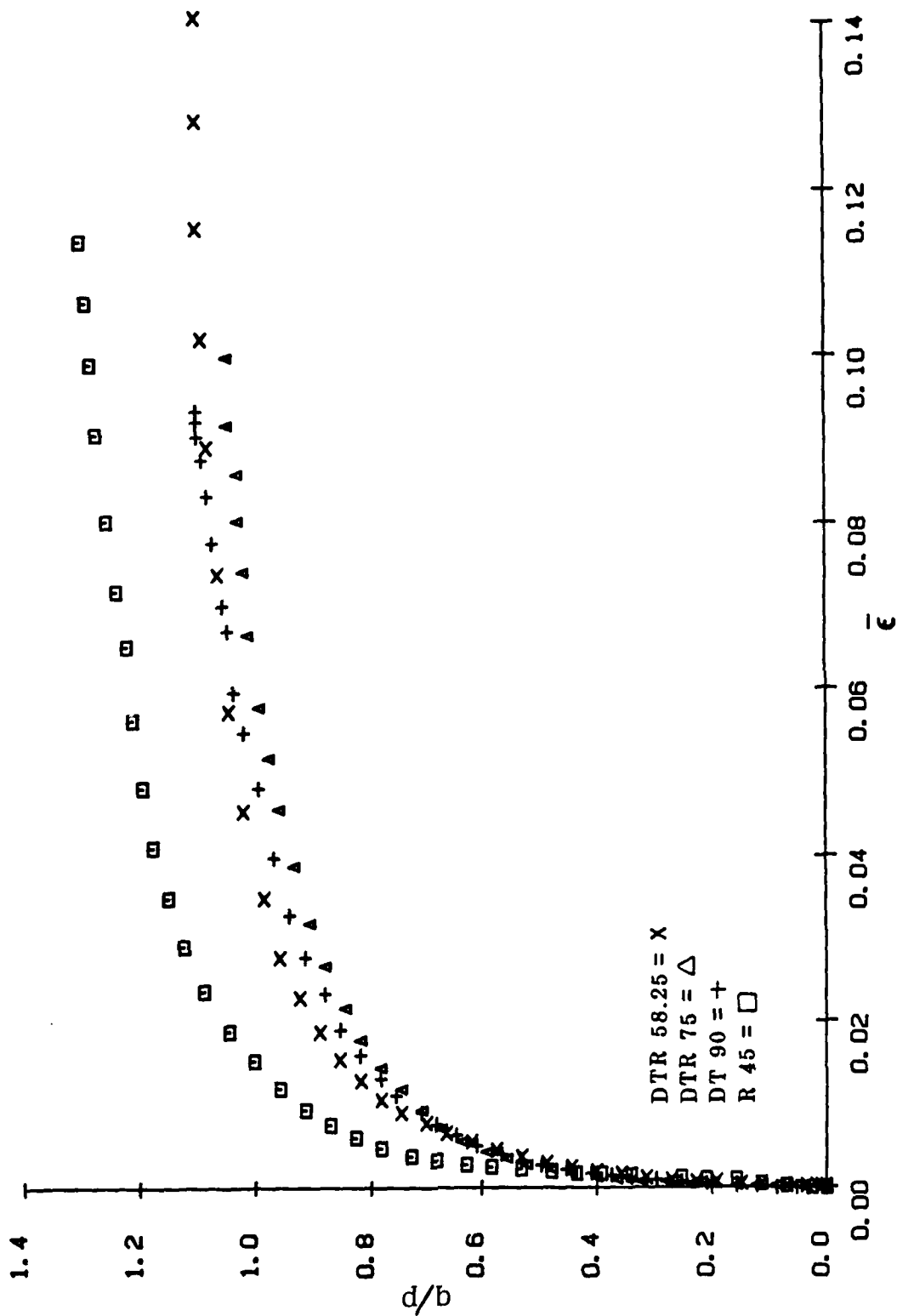


Figure A-1. Normalized Shear Stress vs. Shear Strain for the following HCA tests: R 45, DTR 58.25, DTR 75, and DT 90 (data from Reference 9).

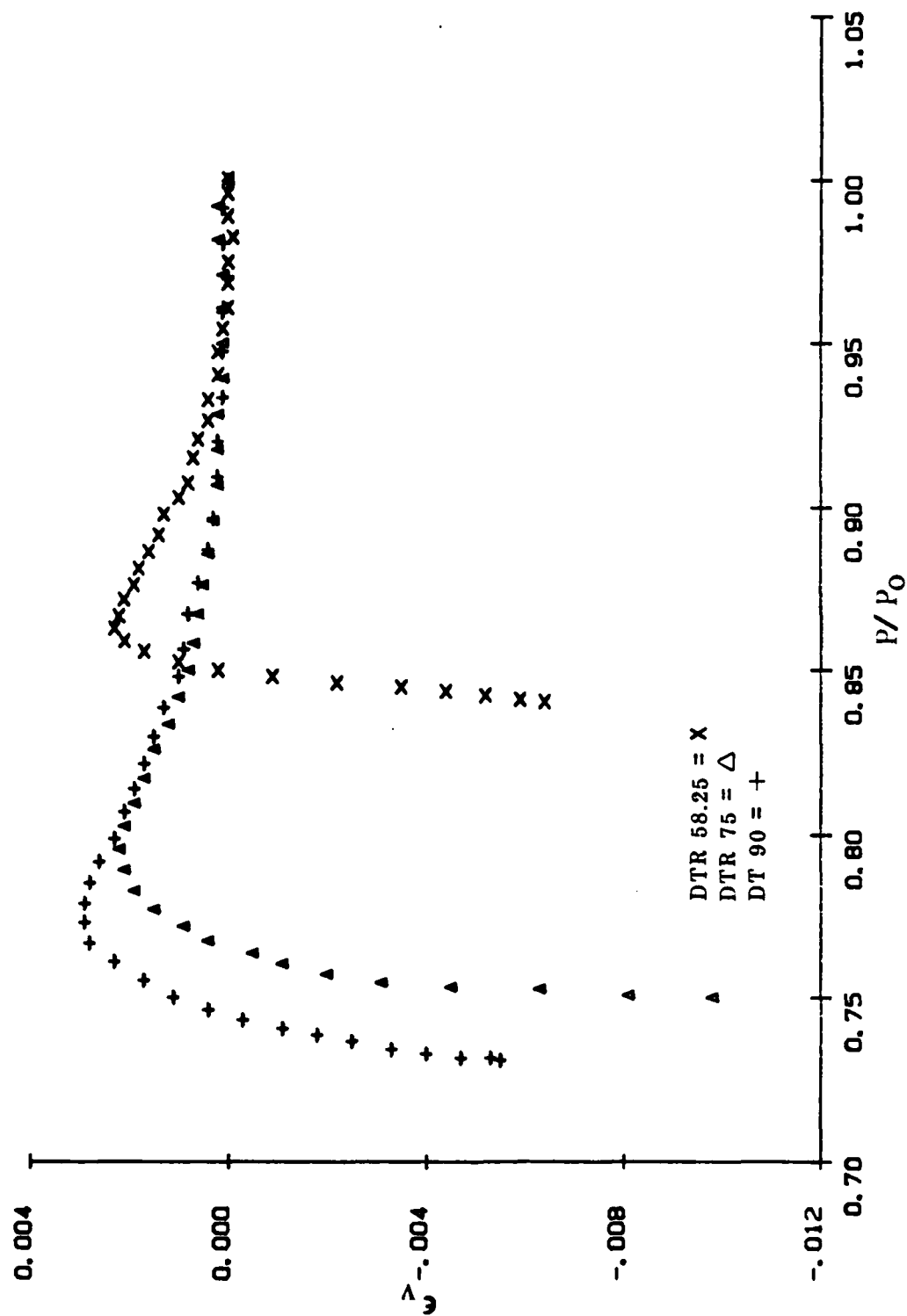


Figure A-2. Volume Strain vs. Normalized Mean Stress for the following HCA tests: DTR 58.25, DTR 75, and DT 90 (data from Reference 9).

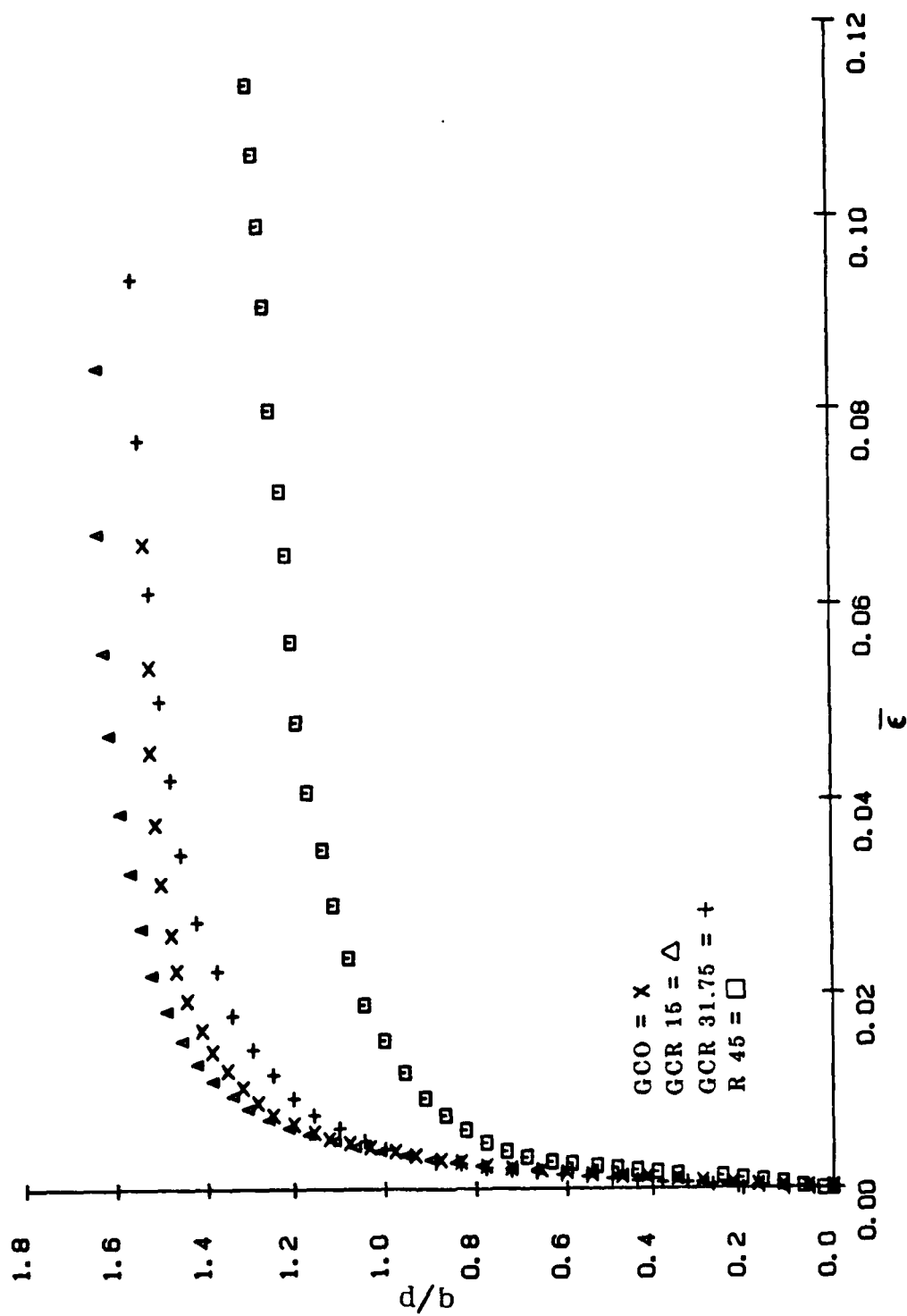


Figure A-3. Normalized Shear Stress vs. Shear Strain for the following HCA tests: GC 0, GCR 15, GCR 31.75, and R 45 (data from Reference 9).

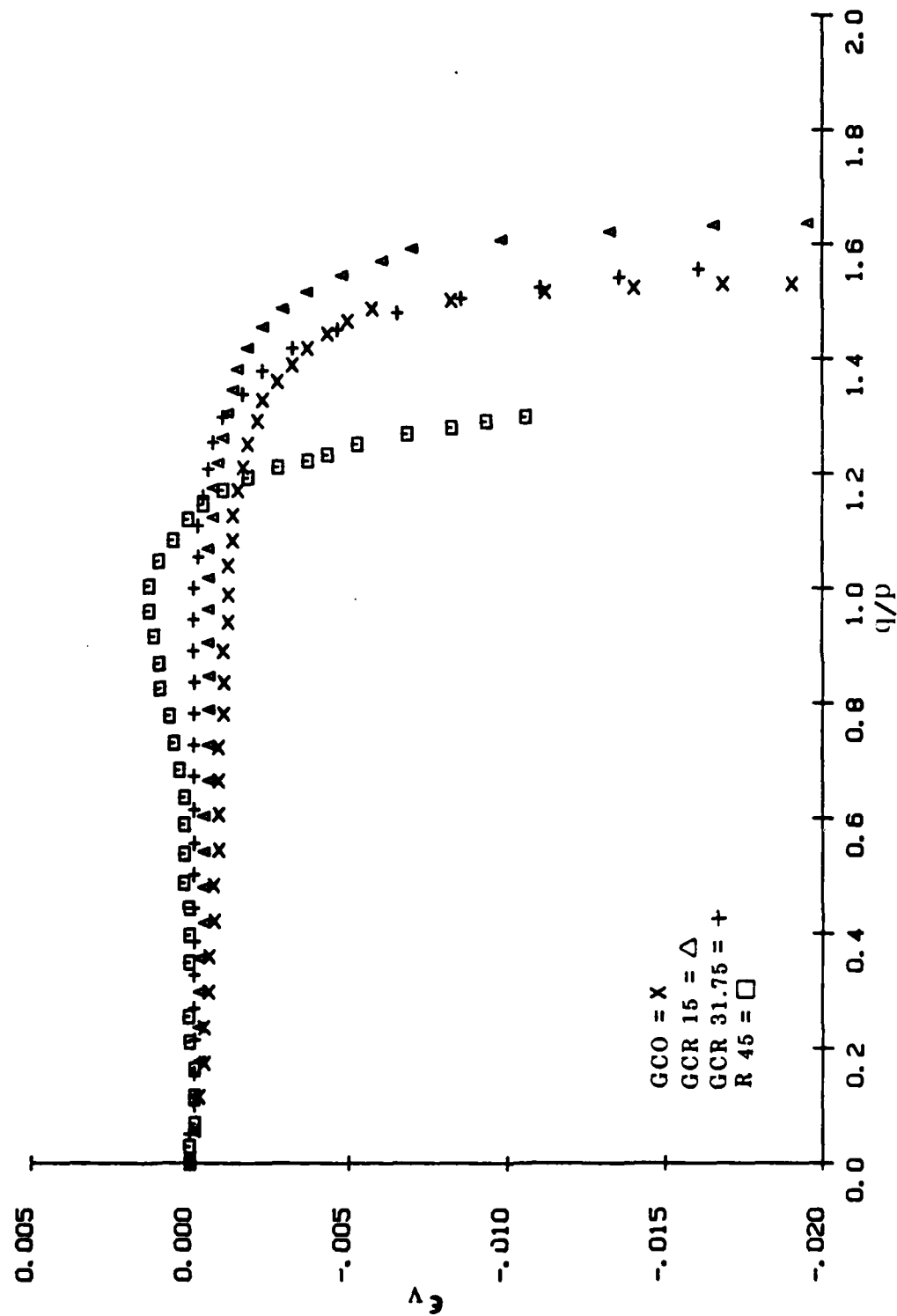


Figure A-4. Volume Strain vs. Normalized Shear Stress for the following HCA tests: GC 0, GCR 15, GCR 31.75, and R 45 (data from Reference 9).

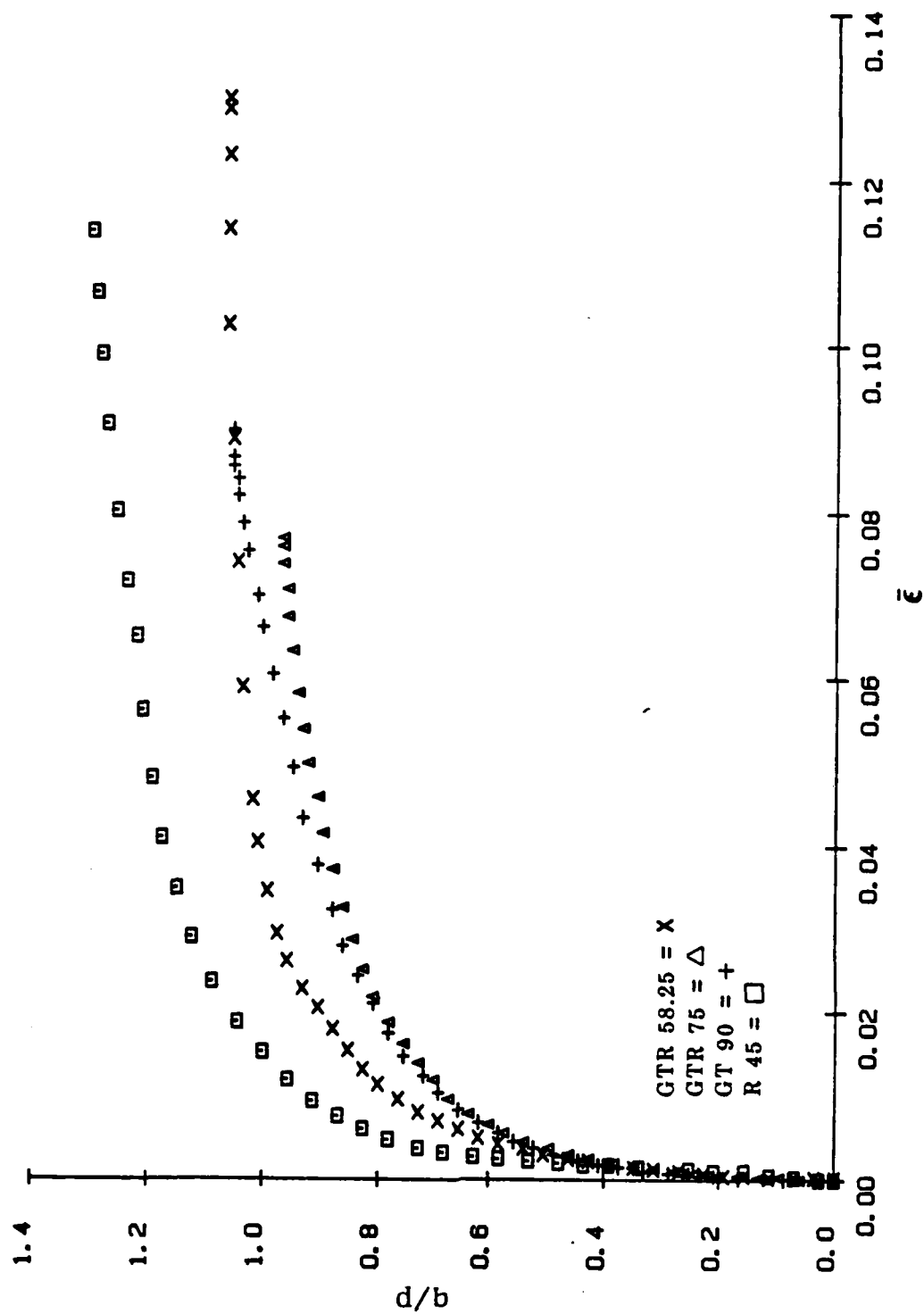


Figure A-5. Normalized Shear Stress vs. Shear Strain for the following HCA tests: R 45, GTR 58.25, GTR 75, and GT 90 (data from Reference 9).

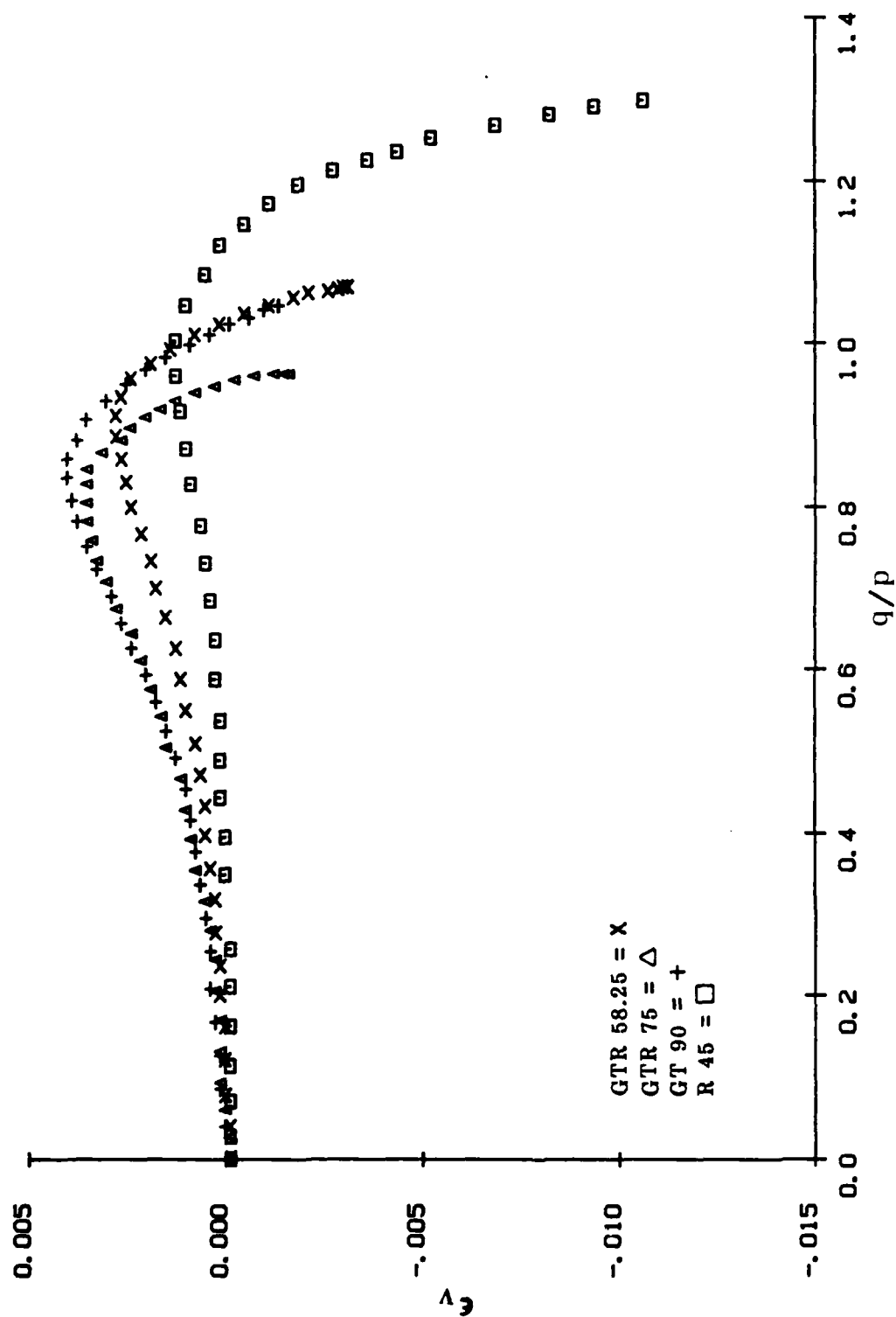


Figure A-6. Volume Strain vs. Normalized Shear Stress for the following HCA tests: R 45, GTR 58.25, GTR 75, and GT 90 (data from Reference 9).



## APPENDIX B

### PREDICTION OF THE HCA TESTS USING PREVOST'S MODEL

This appendix contains plots of the measured Hollow Cylinder Apparatus data (of APPENDIX A) superposed with predictions generated by the Prevost Model.

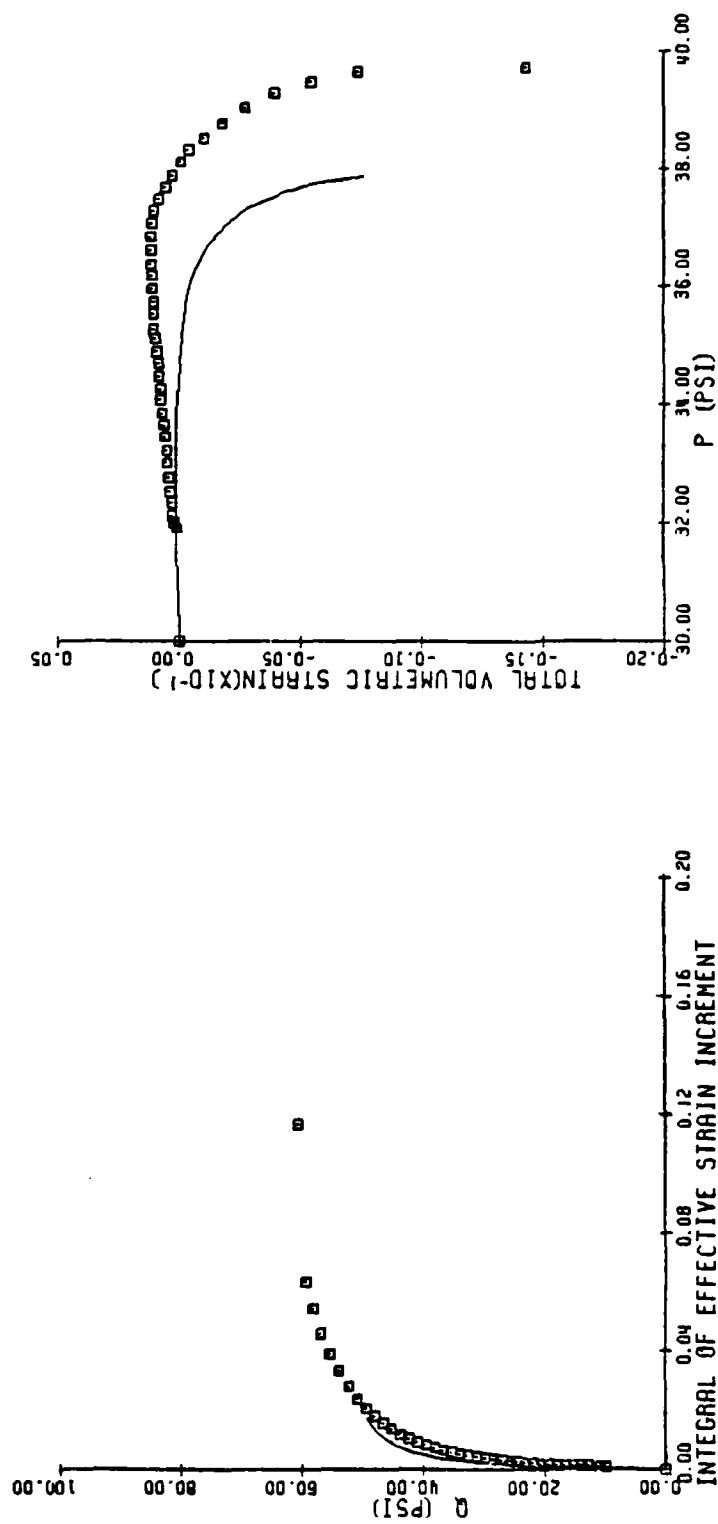


Figure B-2. Prediction of DCR 32 test using Prevost's Model.

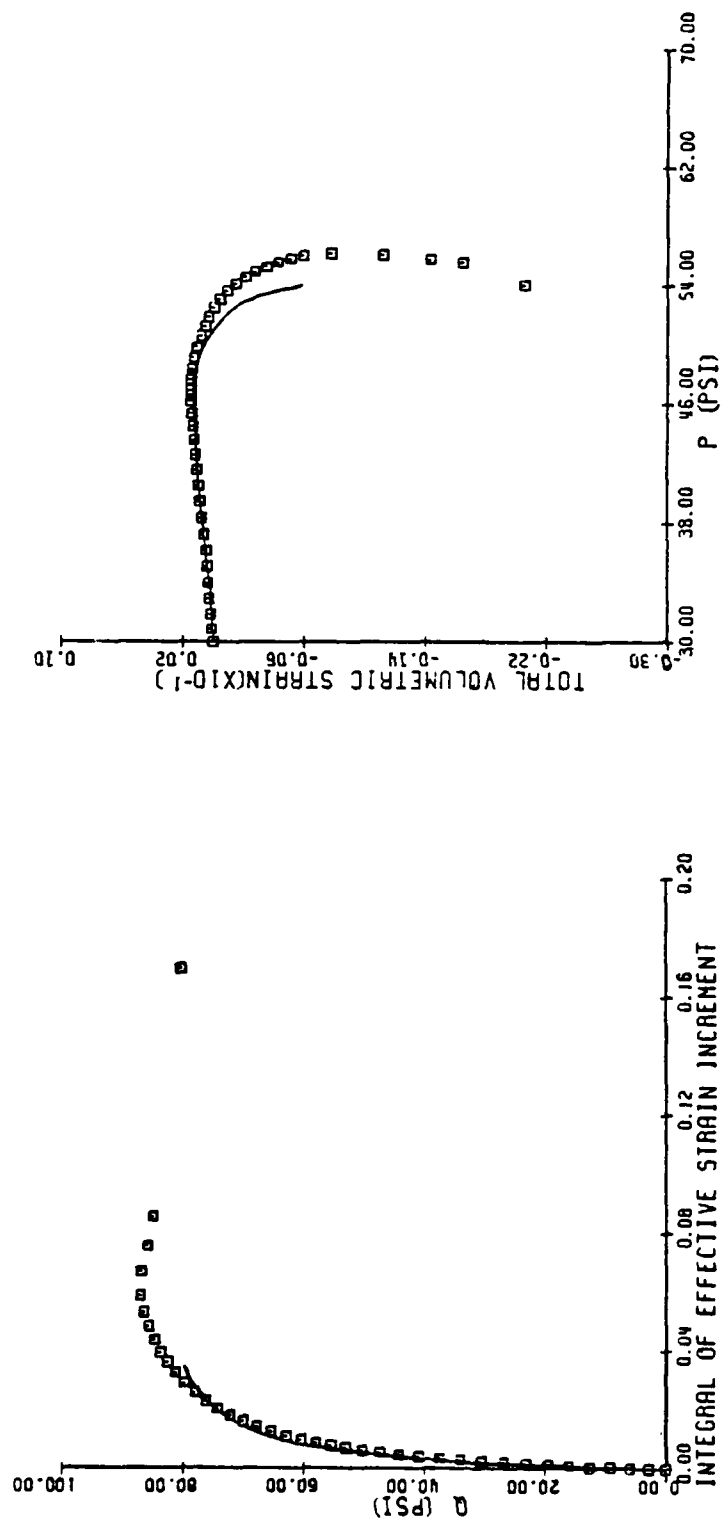


Figure B-1. Prediction of DCR 15 test using Prevost's Model.

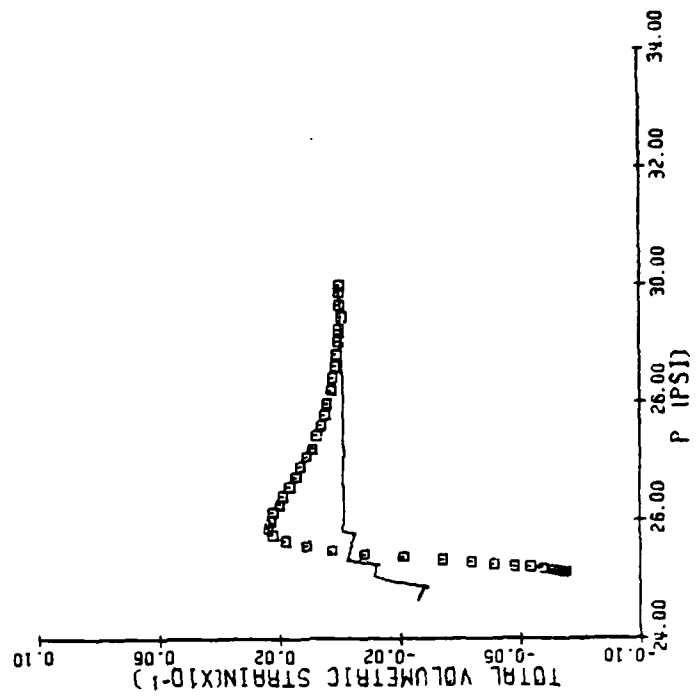
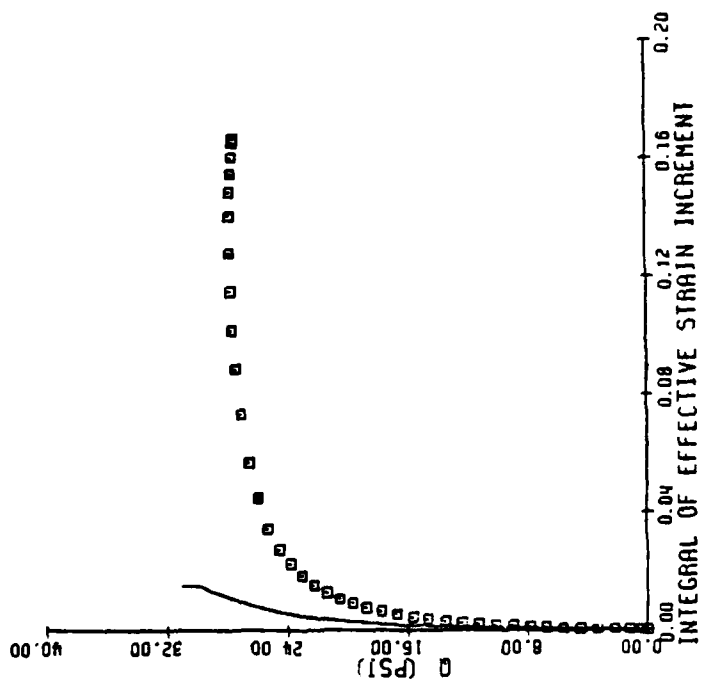


Figure B-3. Prediction of DTR 58 test using Prevost's Model.

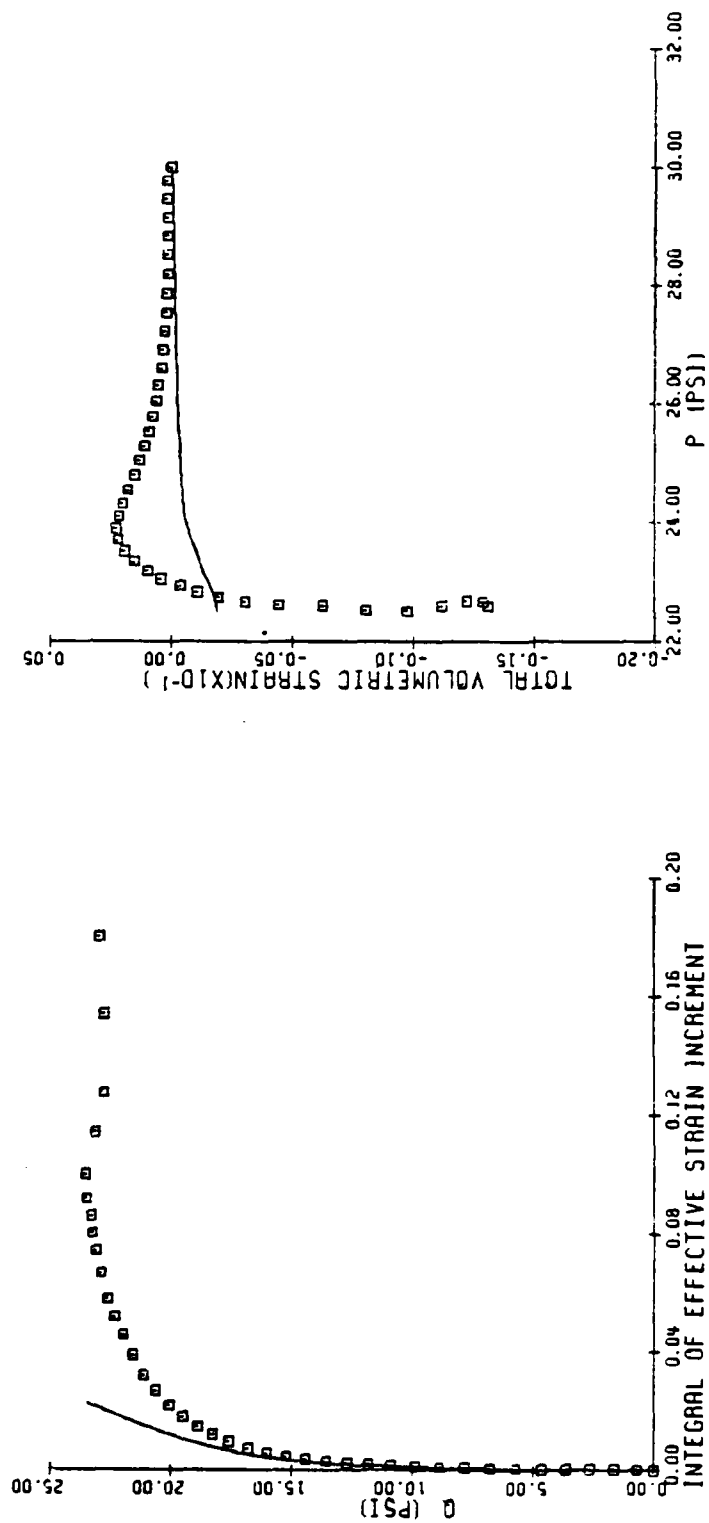


Figure B-4. Prediction of DTR 75 test using Prevost's Model.

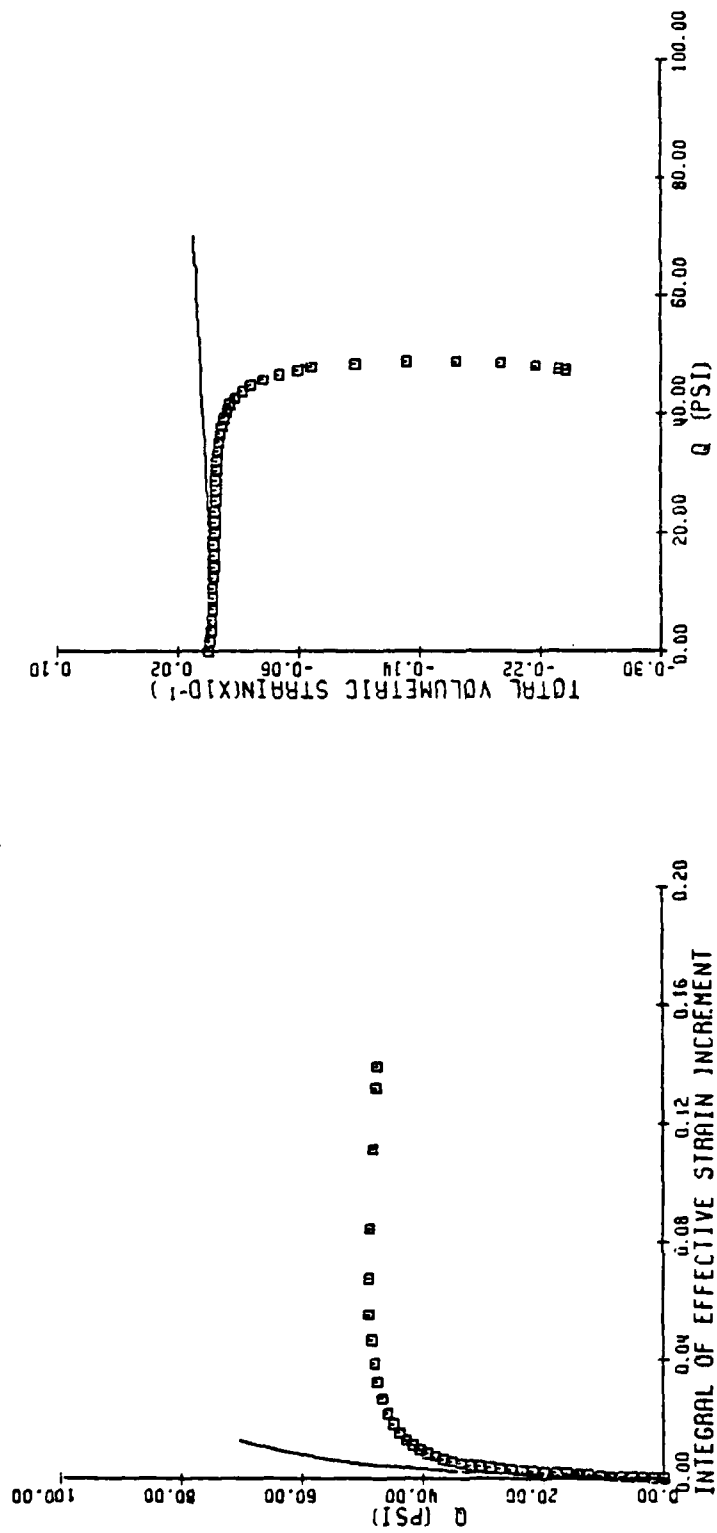


Figure B-5. Prediction of GCR 15 test using Prevost's Model.

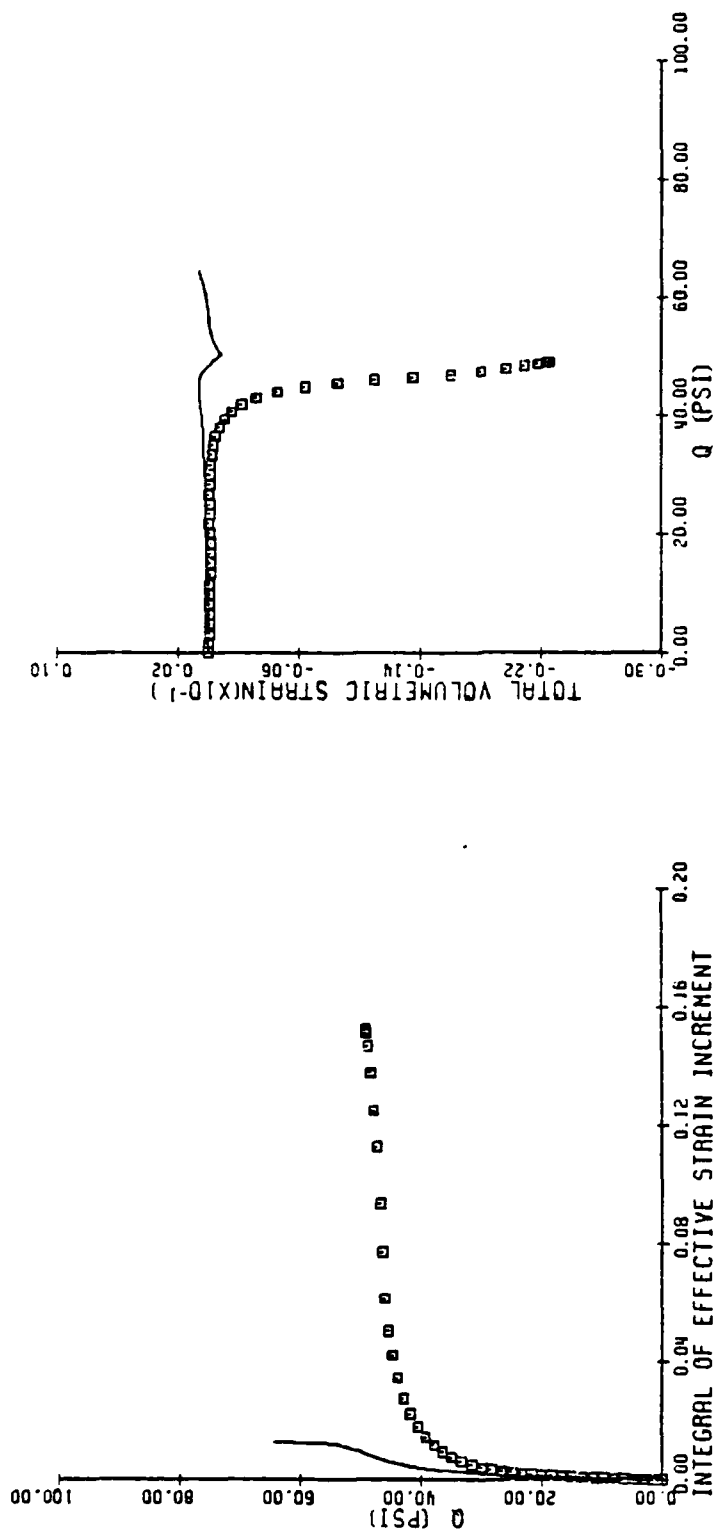


Figure B-6. Prediction of GCR 32 test using Prevost's Model.

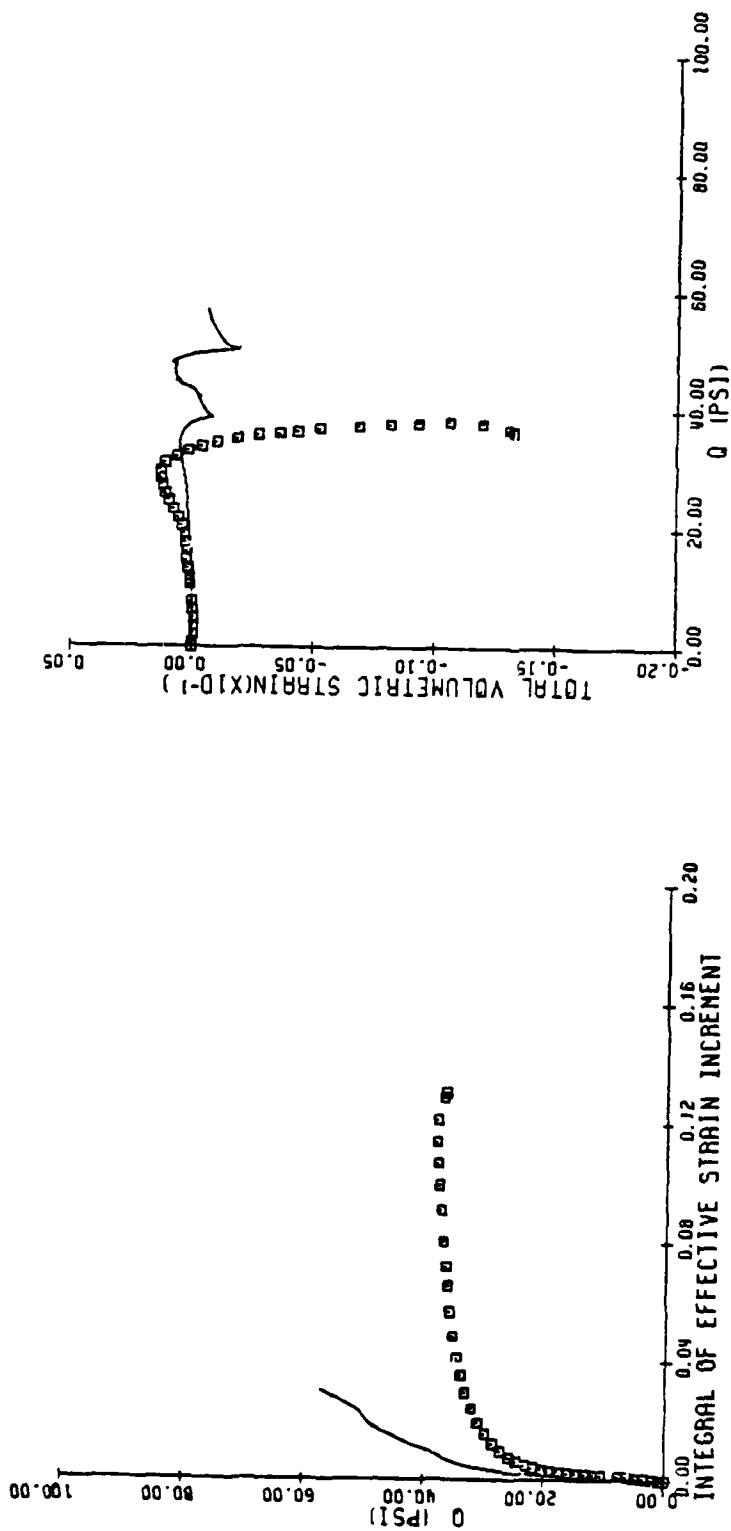


Figure B-7. Prediction of R 45 test using Prevost's Model.



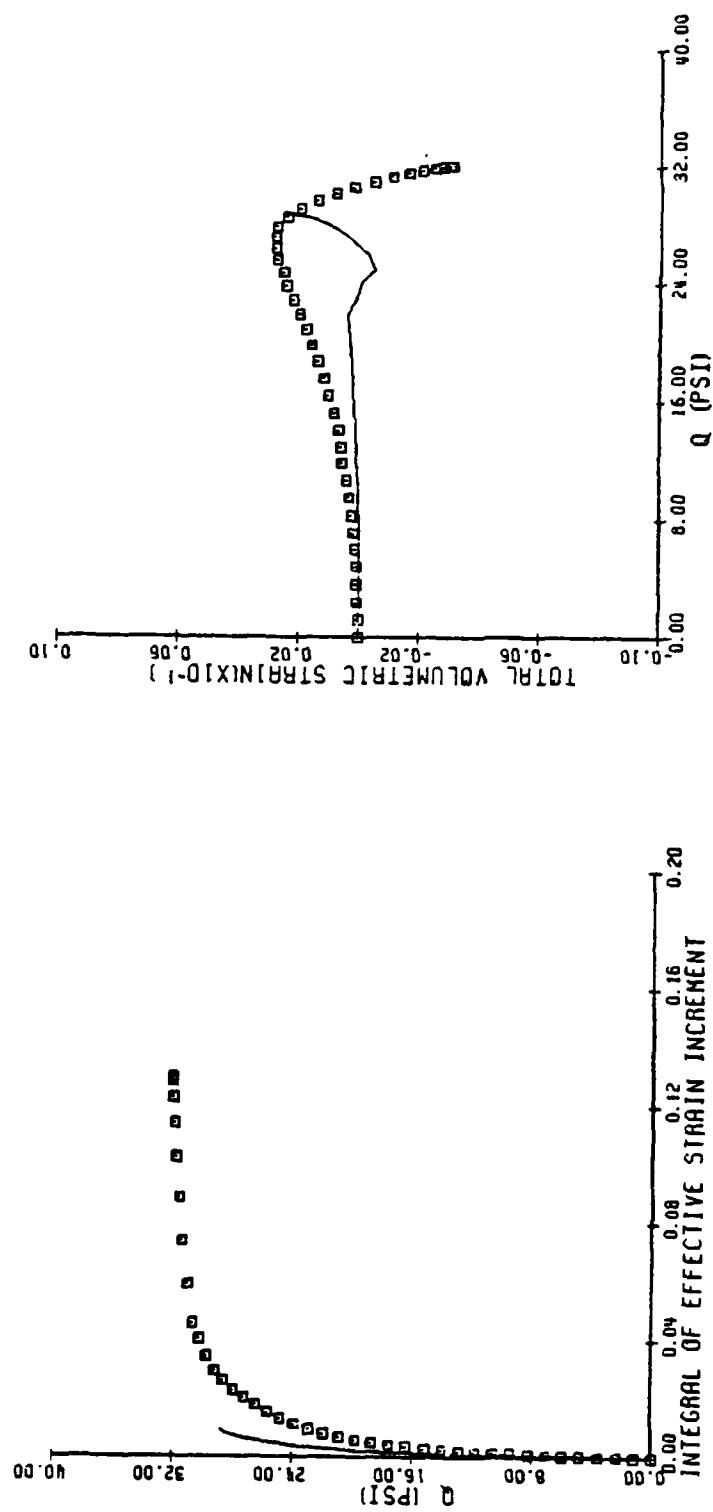


Figure B-8. Prediction of GTR 58 test using Prevost's Model.

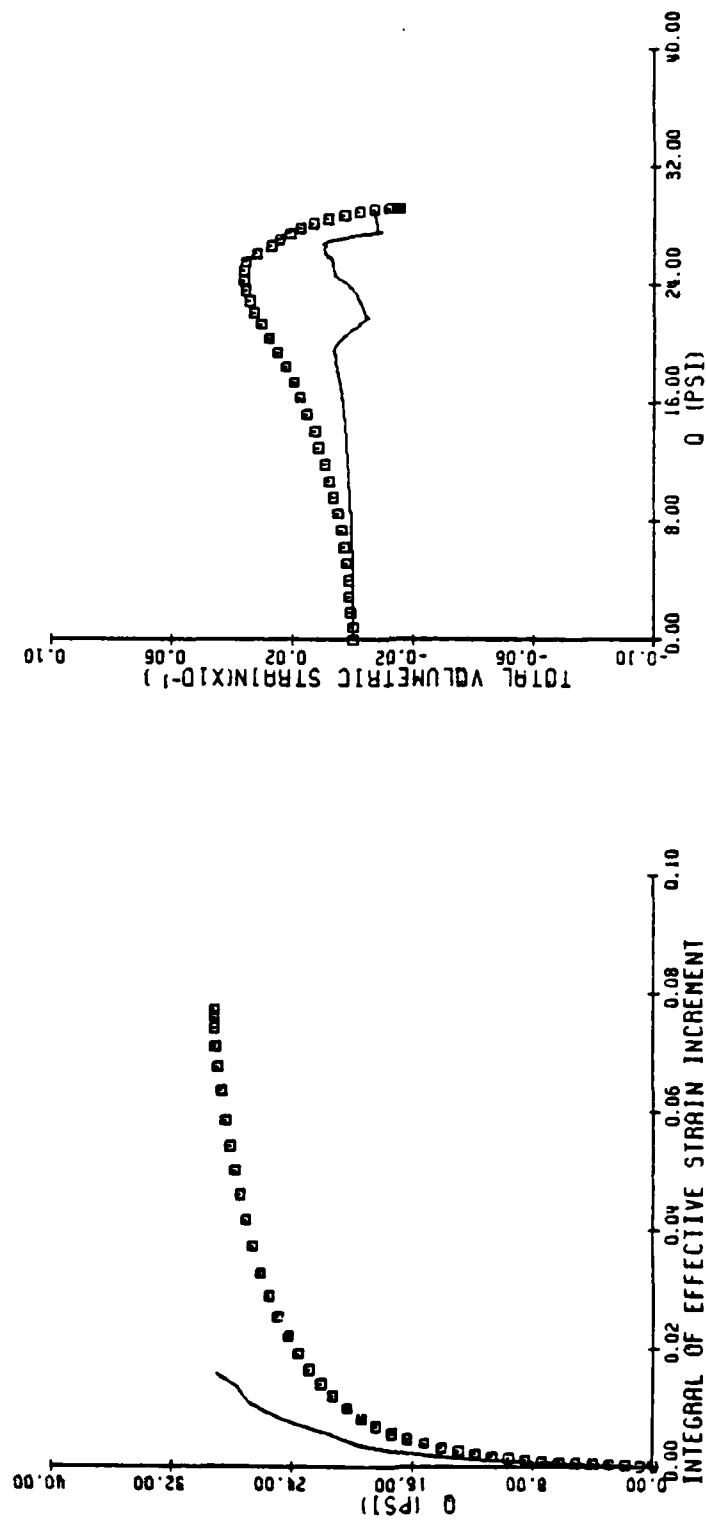


Figure B-9. Prediction of GTR 75 test using Prevost's Model.

**END**

**FILMED**

---

**1-86**

**DTIC**